SEISMIC FRAGILITY ASSESSMENT OF MULTISPAN CONTINUOUS REINFORCED CONCRETE INTEGRAL ABUTMENT BRIDGES

by

Benazir Fatima Ahmed

DEPARTMENT OF CIVIL ENGINEERING
INDIAN INSTITUTE OF TECHNOLOGY GUWAHATI
GUWAHATI-781039, ASSAM, INDIA

SEISMIC FRAGILITY ASSESSMENT OF MULTISPAN CONTINUOUS REINFORCED CONCRETE INTEGRAL ABUTMENT BRIDGES

A Thesis Submitted
In Partial Fulfilment of the Requirements
for the Degree of

DOCTOR OF PHILOSOPHY

by

Benazir Fatima Ahmed

DEPARTMENT OF CIVIL ENGINEERING
INDIAN INSTITUTE OF TECHNOLOGY GUWAHATI
GUWAHATI-781039, ASSAM, INDIA

CERTIFICATE

It is certified that the work contained in the thesis entitled "***Seismic Fragility Assessment of Multispan Continuous Reinforced Concrete Integral Abutment Bridges***", by **Benazir Fatima Ahmed** has been carried out under my supervision and that this work has not been submitted elsewhere for the award of a degree.

Date: 17 May 2021
Place: IIT Guwahati

Dr. Kaustubh Dasgupta
Associate Professor
Department of Civil Engineering
Indian Institute of Technology Guwahati

ABSTRACT

Seismic vulnerability assessment has become a major research area owing to numerous damages and failures in recent earthquakes. The output within a probabilistic framework, i.e., Fragility Curve (FC), expressing the probability of attainment or exceedance of a structural Damage State (DS) at a given level of the earthquake Intensity Measure (IM), effectively aids in seismic disaster mitigation. The present study generates the FCs for a class of multispan continuous reinforced concrete Integral Abutment Bridges (IABs).

For the attributes of the IAB class, analytical models are (a) generated in OpenSees for pier and Pile-Soil System (PSS), (b) developed herein for bearing, and (c) adopted from a past abutment-backfill interaction study for Abutment-Backfill System (ABS). PSS lateral response is evaluated by linking the PSS model with the adopted Strain Wedge Model (SWM) of simulating the pile-soil interaction. The technique (validated with the results of a past test) invovles convergence of SWM with the beam on Winkler Foundation problem of the PSS, achieved herein through the displacement-controlled pushover analysis of the PSS while iterating with the updated soil modulus of subgrade reaction profile obtained from SWM computations in spreadsheets.

144 BS samples are created employing Latin Hypercube Sampling Technique (LHST) over wide ranges of variations for BS structural and geotechnical parameters. For the individual IAB components, attribute-specific capacity (*C*) thresholds corresponding to the Damage States (DSs) are obtained while analysing the respective damage models (developed herein invovling different failure modes and soil-structure interaction aspects relevantly). Repetition for the numerical models of all the samples lead to 144 data values for each DS *C*. Thus, error propagation while adopting past case-specific *C*s, is avoided, as justified by the dispersion of *C* owing to parametric variations. *C* data roughly follow lognormal distribution for PSS, pier and bearing, and uniform distribution for ABS.

Variability in demand (*D*) is incorporated through a set of nine Ground Motions (GMs), selected over wide variations in frequency contents. Component-level *D*s are assessed against the respective DSs, while evolving a few steps beyond the inverse application of the adaptive capacity spectrum method. Adaptive capacity spectra are generated by integrating an automated displacement-based adaptive pushover analysis algorithm code with the numerical models (created using “structural components’ modeling” analogy) of the BS samples in OpenSees. Seismic demand spectra

corresponding to the input GMs are developed using SeismoSignal for the BS damping (evaluated herein) at each component DS. At each of the specified values upto 1.8g to which the IMs (Peak Ground Acceleration (PGA) and pseudo-spectral acceleration at the time period of 0.7s (S_a (0.7s)) of the GMs are scaled, 1296 data values for *D* against each DS are obtained; repetition over the IM range leads to the demand-IM relationship. Data follow lognormal distribution roughly and show more refinement to the fit and lesser dispersions with respect to S_a (0.7s) than PGA. S_a (0.7s) is observed to be more optimal than PGA for abutment-PSS (A-PSS) and ABS, while the change in the IM type has moderate to small and moderate to negligible effects on bearing and pier respectively.

Component-level FCs are derived through Numerical Compution (NC) of fragilities using the just as evaluated *C* and *D* distribution profiles and the traditional Lognormal Formulation (LF). NC is validated while providing similar estimates as by LF, for the approximate lognormal *C* and *D* (with respect to S_a (0.7s)) distributions.With respect to each of the BS DSs (mapped component-level DSs of the same rank), the joint demand cumulative probability surface is generated in MATLAB based on the computed correlations among the component-level *D*s. The BS FC is derived assuming system failure in a series sequence and comparing the samples (102 nos.) of joint demands with 102 quartets obtained through random pairing of individual 102 samples of the mutually independent component-level *C*s; sampling is done employing LHST on the distributions.

For the IAB class, component-level fragilities are mostly higher with respect to PGA and NC compared to S_a (0.7s) and LF. S_a (0.7s) being more optimal than PGA and NC being based on actual *C* and *D* profiles unlike the imposed lognormal fit to data in LF would lead to realistic estimates. A-PSS as well as ABS, bearing and pier follow the order of decreasing level of vulnerability, though bearing is the most vulnerable one upto certain initial ranges of both IMs. BS is more vulnerable than individual components at the respective same DS ranks, while at higher ranks compared to those of the components, it shows more or less vulnerabilities upto certain IM ranges and vice versa beyond.

Heights of bearing, pier and abutment, and pile diameter; and heights of pier and abutment, and pier diameter are found to affect the Sequences of Attainments (SoAs) of the DSs of the components significantly for the respective continuous; and full integral configurations of IABs. The soil friction angle moderately affects both the cases.

As future applications to damage or fragility assessment studies over wide ranges of parametric combinations, generalised expressions with respect to the individual component capacities and trends of SoAs of the DSs of the components are prescribed.

ACKNOWLEDGEMENTS

First of all, I would like to offer my deepest gratitude to The Almighty for letting His Wish in my favour of being a Doctorate. Secondly, I would like take the opportunity to express my sincere and immense gratefulness to my thesis supervisor Dr. Kaustubh Dasgupta for his invaluable guidance and instructions. I am highly indebted to him for his constant willingness and encouragement for discussions as well as efforts, time and patience, which immensely helped in sorting out the issues encountered during the work. His encouragement throughout while attempting new endeavours in line with this dissertation work has led to fruitful accomplishments. His dedication as a mentor, right from providing with the useful but not easily accessible study materials to arranging technical discussions with other professors on many different topics related to the work, has always been motivating. I always admire him for his in-depth knowledge and for being very kind, approachable and down-to-earth.

I would like to thank my doctoral committee members for the comments and valuable suggestions to improve the work quality.

I would like to express my sincere gratitude to the Professors at IIT Guwahati who have been kind enough to spare time out of their busy schedules for the technical discussions on various relevant topics of this dissertation work. The valuable suggestions and knowledge provided by them have been helpful for the smooth accomplishment of the objectives of this work.

I am very much grateful to the professors at IIT Guwahati for imparting their valuable teachings and thus enlightening me about the basics of the subjects required. I would also like to thank all the Civil Engineering departmental staff for their official assistances.

I devote my special thanks to all friends at IIT Guwahati for creating a much-needed jovial atmosphere around. I would like to dedicate my sincere thanks and acknowledgement to some close friends here for being true well-wishers with their criticism and appreciation to build a better me. I express my profound gratitude to all my friends who have always provided a helping hand when needed in any case. I convey my thanks to my seniors for all their valuable advices to improve academically as well as personally during this phase.

I express my heartiest thanks to the few but closest friends, who have been the source

of support and love since many years.

I am extremely indebted to my parents and my younger sister and brother for their immense love and support during this phase. The high expectations that my father put on me have always inspired me to reach for and achieve them as well. The patience they have endured during this long journey is commendable.

I express my gratitude to the Ministry of Human Resource Development, Govt. of India for the financial assistance provided.

I would like to thank everybody who directly or indirectly has helped me toward the accomplishment of the work.

Benazir Fatima Ahmed

TABLE OF CONTENTS

LIST OF TABLES

LIST OF FIGURES

LIST OF ABBREVIATIONS

Abbreviation	Description
ds	: Realization of a DS rank
edp	: Realization of an EDP value
im	: Realization of an IM value
ABS	: Abutment-Backfill System
A-PSS	: PSS at the abutment
BS	: Bridge System
DAPA	: Displacement-based adaptive pushover analysis
DI	: Damage Index
DS	: Damage State
DS1, DS2, DS3, DS4	: 1st, 2nd, 3rd and 4th DSs respectively
EDP	: Engineering Demand Parameter
FAF	: Flow Around Failure
FC	: Fragility Curve
FC-LF	: Fragility Curve-Lognormal Formulation
FC-NC	: Fragility Curve-Numerically Computed
GM	: Ground Motion
IAB	: Integral Abutment Bridge
IACSM	: Inverse application of the Adaptive Capacity Spectrum Method
IM	: Intensity Measure
LF	: Lognormal Formulation
LS	: Limit State
LST	: Limit State Threshold
LST1, LST2, LST3, LST4	: LST values corresponding to 1st, 2nd, 3rd and 4th DSs respectively.
NC	: Numerical Computation
PGA	: Peak Ground Acceleration
PGV	: Peak Ground Velocity
PL	: Performance Level
PLSE	: Parameterised Limit State Expression
PSDM	: Probabilistic Seismic Demand Model
PSS	: Pile-Soil System
SoA	: Sequence of Attainment
SPW	: Soil Passive Wedge
SWM	: Strain Wedge Model

This page has been left intentionally blank

LIST OF SYMBOLS

Symbol	Description
a_i	: i^{th} value of IM in the range (maximum likelihood method)
A, A_u	: Parameter controlling sand FAF, its ultimate value
A_{br}	: Surface area of the bearing pad in plan
A_{b1}, A_{b2}, A_{b3}	: Instants of attainments of ABS LST1, LST2, LST3
$A_{g,pr}$	: Gross area of the pier section
A_{p1}, A_{p2}	: Instants of attainments of A-PSS LST1, LST2
A_{rc}, B_{rc}	: Probabilistic seismic demand model regression coefficients
b_t, b_p	: Ratio of the elastic and the transition stiffness, ratio of the elastic and the post-yield stiffness respectively of the dowel bar
B_{br}	: Breadth of the bearing pad
B_1, B_2	: Instants of attainments of bearing LST1, LST2
$c(a)$	: Median of $S_d(a)$
c_j	: Median IM value for the FC corresponding to j^{th} DS (maximum likelihood method)
C	: Seismic capacity
$C_{i,ab}$, $C_{i,br}$, $C_{i,pl}$, $C_{i,pr}$	: Seismic capacities of ABS, bearing, PSS, pier at respective i^{th} DSs
$\overline{C}$	: Median value of C
d	: Realization of a D value
d_b	: Diameter of the longitudinal bar
d_{brd}	: Diameter of the dowel bar
d_{FAF}	: LST value corresponding to FAF
$d_{i,ab}$, $d_{i,br}$, $d_{i,pl}$, $d_{i,pr}$	: LSTs of ABS, bearing, PSS and pier respectively corresponding to the i^{th} DS, i = 1 to 4
$\overline{d_{i,ab}}$, $\overline{d_{i,br}}$, $\overline{d_{i,pl}}$, $\overline{d_{i,pr}}$	: Respective median values of $d_{i,ab}$, $d_{i,br}$, $d_{i,pl}$, $d_{i,pr}$
d_l, $d_{l,j}$	: Limit displacement, its value corresponding to j^{th} BS sample
D	: Seismic demand
D_g , D_{ss}	: Respective depths of I-girder, superstructure
D_i	: Demand on the i^{th} component
$D_{i,ab}$, $D_{i,br}$, $D_{i,pl}$, $D_{i,pr}$	: Seismic demands on ABS, bearing, PSS, pier in terms of respective EDPs against i^{th} DSs
$D_{i,p}$, $D_{i,q}$	: Respective D values at i^{th} DSs for the p^{th}, q^{th} components
D_{pl}	: Pile cross sectional size
D_{pr}	: Overall depth of the pier section
$\overline{D}$	: Median value of D
$\underline{D}$	: Vector of demands of the bridge components

$\underline{D^T}$: Vector of demands of the bridge components transformed in the lognormal space

$\overline{D_{i,ab}}$, $\overline{D_{i,br}}$, $\overline{D_{i,pl}}$, $\overline{D_{i,pr}}$: Median values of $D_{i,ab}$, $D_{i,br}$, $D_{i,pl}$, $D_{i,pr}$ respectively

$DS_{c,1}$, $DS_{c,2}$,...., DS_{c,n_c} : Respective DSs of the 1st, 2nd , ..., n_c^{th} components

DS_{pr}, DS_{iso}, DS_{BS} : Respective DSs of pier, isolation device, BS

e : Zero-mean random variable

$E_{bf,ik}$: Interslice horizontal force corresponding to k^{th} mobilised surface in logarithmic spiral failure surface model

E_c : Young's modulus of elasticity of concrete

$E_{c,MF}$: Multiplicative factor applied to the empirical expression of E_c

$E_{e,brd}$, $E_{t,brd}$, $E_{p,brd}$: Elastic, transition and post yield moduli of dowel bar

E_{fr}, E_{hyst}, E_{visc} : Frictional, hysteretic, viscous damping in bearing respectively

E_j : j^{th} DS as designated in maximum likelihood method, j = 1,2,3…

E_s, $E_{s,ij}$: Modulus of subgrade reaction, its value at j^{th} soil sublayer corresponding to $\varepsilon_{s,i}$

$E_{s,br_{PL}}$, $E_{fr,br_{PL}}$: Stored energy and energy loss at a PL due to friction in bearing

E_{st} : Young's modulus of elasticity of steel

$\overline{EDP}$: Median value of EDP

f_{brd} : Stress in the dowel bar

$f_{c,pl}$, $f_{c,pr}$: Concrete compressive stress in pile and pier respectively

$f_{c,pl}'$, $f_{c,pr}'$: Normalised values of $f_{c,pl}$ and $f_{c,pr}$ respectively

f_{cc} : Peak compressive stress in core concrete

f_{ck} : Characteristic compressive strength in concrete

$f_{t,brd}$, $f_{y,brd}$, $f_{u,brd}$: Transition, yield and ultimate stresses respectively in dowel bar

$f_{y,pl}$, $f_{y,pr}$: Yield stress in reinforcement in pile, pier respectively

F_{ab}, F_{pl}, F_{pr} : Lateral forces at ABS, pile head, pier respectively

$F_{ab,k}$: Lateral force at ABS corresponding to k^{th} mobilised surface in logarithmic spiral failure surface model

$F_{ab,PL}$: Base shear at the abutment at a given PL

$F_{abf,k}$: Vertical component of $P_{ab,k}$

$F_{bent,PL}$: Base shear at the bent at a given PL

$F_{bp,j}$: Lateral force at the j^{th} bearing-pier assemblage

F_{brd} : Dowel bar shear force

$F_{br,PL}$: Lateral force in bearing at a given PL

$F_j()$: Fragility function corresponding to j^{th} DS

$F_{\max,pl}$, $F_{pl,i}$: Maximum value of F_{pl} , value of F_{pl} with respect to $\varepsilon_{s,i}$

$F_{t,brd}$, $F_{y,brd}$, $F_{u,brd}$: Dowel bar shear forces corresponding to transition, yield, ultimate stresses respectively of the bar

$F_{u,brp}$: Ultimate friction force capacity of the bearing pad

F_{BS}, $F_{BS,PL}$: Total base shear of the BS , its value at a given PL

$F_{BS,k}$: Total base shear of the BS at step k

$FC1_{v|IM_v}$, $FC2_{v|IM_v}$: Probability values at IM_v on the 1st and 2nd FCs respectively

G, $G_{\min}$: Shear modulus of the bearing pad, its minimum value

G_s, $G_{\min,s}$: Shear modulus of sand, its maximum value

h_{br} : Bearing pad thickness

H_{ab}, H_{pr} : Heights of abutment and pier respectively

H_{ab}' : Normalised value of H_{ab}

$H_{ab,k}$: Value of H_{ab} corresponding to the k^{th} mobilised failure surface

H_{spw}, $H_{spw,i}$: Soil passive wedge depth, its value corresponding to $\varepsilon_{s,i}$

$(H_{spw,i})_{BWF}$: $H_{spw,i}$ evaluated from beam on Winkler foundation analysis

$(H_{spw,i})_{SWM}$: $H_{spw,i}$ evaluated from SWM

I_{brd} : Moment of inertia of the dowel bar section

I_{pl} : Moment of inertia of pile

I, I_1 and I_2 : A given input value, input values for the sensitivity analysis

IM_C : IM value corresponding to $\overline{C}$

IM_D : IM value corresponding to $\overline{D}$

IM_{GM} : IM value of of a given GM

IM_m : m^{th} value of IM in the range

IM_v : A given value of IM

k_0 , k_a , k_p : Respective earth pressure at rest, active, passive conditions

$k_{e,brd}$, $k_{t,brd}$, $k_{p,brd}$: Elastic, transition and post yield stiffness respectively of the dowel bar

k_{brp} : Lateral stiffness of the bearing pad

K : Pile stiffness

$K_{e_{bb}}$: Confinement coefficient in pier

$K_{pl\text{-}s}$: Pile-soil stiffness factor

l : Lower limit of the parameter range

L : Longitudinal direction of the bridge

L_{br} : Length of the bearing pad

L_{oh} : Deck overhang length

L_{pl}, L_{sp} : Pile length, span length

L_{pr} : Distance from the column base to the point of contraflexure

L_{ww} : Length of wingwall

$L()$: Maximum likelihood function

$m_{i,k}$: Participating mass of the i^{th} component at step k

M_{brd} : Bending moment at the critical section of the dowel bar

$M_{\max,pl}$, $M_{\max,pl_i}$: Maximum moment in pile, its value with respect to to $\varepsilon_{s,i}$

M_{pr}, $M_{\max,pr}$: Flexural moment in pier, its maximum value

$M_{y,pr}$: Pier bending moment capacity at yield

$M_{BS,k}$: Effective mass of the BS at step k

$M_{1,pr}$: Pier bending moment capacity at first yield

n_{bp}, n_c, n_g, n_{pl}, n_{pr} : Number of bearing-pier systems, components, girders, piles, piers

$n_{c\text{-}p}$, $n_{n\text{-}s}$: Number of primary, secondary components

$n_{br\text{-}DS}$, $n_{pr\text{-}DS}$: Number of simulations where a DS of each of bearing, pier occur

N : Seat length of a girder at the support

O, O_1 and O_2 : A given input value, output values for the sensitivity analysis

OP_{br}, OP_{pr} : Occurrence probabilities of bearing and pier DS respectively

$p\text{-}y$: Soil pressure per unit length of pile versus pile lateral deflection

p_{C_i} , p_{D_i} : Probability per unit value of respective i^{th} capacity, demand bins

P_f : Probability of failure

$P_{ab,k}$: Resultant passive force at ABS corresponding to k^{th} mobilised surface in logarithmic spiral failure surface model

P_{br}, P_{pl}, P_{pr} : Respective axial loads on bearing, pile, pier

$P_{c,i}$: Probability of exceedance of a DS of the i^{th} bridge component

P_{ij} : Probability with respect to (E_j, a_i) in maximum likelihood method

P_{BS}, $P_{i,BS}$: Probability of BS being at or beyond a given DS, P_{BS} at i^{th} DS

P_{LS} : Probability of exceedance of a particular LS

$P[DS|IM]$: Probability of reaching a DS for a given IM

$P[\ ]$: Probability

P_1, P_2, P_3, P_4 : Instants of attainments of LST1, LST2, LST3, LST4 of pier

$q\text{-}z$: Pile tip resistance versus pile vertical deflection

r : Strain hardening ratio

$R_{\mu,str}$: Spectral reduction factor corresponding to μ_{str}

$R_{\xi_{BS,PL}}$: Reduction factor corresponding to $\xi_{BS,PL}$

R^2 : Coefficient of determination

s_t : Tie spacing

S_a , S_d : Spectral acceleration and displacement respectively

S_{ae} , S_{de} : Elastic spectral acceleration and displacement respectively

$S_{a,k}$, $S_{d,k}$: Single degree-of-freedom acceleration, displacement respectively at step k

$S_a(a)$, $\overline{S_a(a)}$: S_a value at IM value of a, its mean

$S_d(a)$: S_d value at IM value of a

$S_{a,C}$, $S_{a,D}$: S_a values corresponding to capacity spectrum, demand spectrum

$S_{a,PL}$, $S_{d,PL}$: S_a , S_d values from the capacity spectrum at a given PL

S_{a1} : Normalised spectral acceleration demand

$S_{a,C_{ij}}$, $S_{a,D_{ij}}$: $S_{a,C}$, $S_{a,D}$ values corresponding to i^{th} BS sample $-$ j^{th} GM pair

${}^{m}S_{a,D_{ij}}$, ${}^{m}S_{d,D_{ij}}$: $S_{a,D_{ij}}$ value against IM_m , S_d value corresponding to $S_{a,D_{ij}}$

SL_{bf} , SL_s : Respective stress levels in backfill, sand around pile

$S_{m,MF}$: Multiplicative factor applied to uncertainty in superstructure mass

S_E : Standard error

S_a (0.7s) : Spectral acceleration at the time period of 0.7s

S_a (0.8s) : Spectral acceleration at the time period of 0.8s

S_1, S_2 : Adjustment factors with respect to the shape of the pile

t–z : Pile skin friction versus pile vertical deflection

T : Transverse direction of the bridge

T_{ab} : Abutment thickness

T_{bf} : I-girder bottom flange thickness

$T_{bf,ik}$: Interslice vertical force corresponding to k^{th} mobilised surface in logarithmic spiral failure surface model

T_C : Characteristic period of the GM

T_d : Deck thickness

T_{tf} : I-girder top flange thickness

T_w : I-girder web thickness

T_N : Bridge natural period

T_{PL} : BS effective period of vibration at a given PL

u : Upper limit of the parameter range

$V_{pr,f}$: Flexural force capacity of pier

$V_{pr,s}^{c}$, $V_{pr,s}^{t}$, $V_{pr,s}^{p}$: Shear capacities contributed by concrete, axial compression and transverse reinforcement respectively

W_{bf} : I-girder bottom flange width

W_d : Deck width

W_{seat} : Bearing seat width

W_{tf} : I-girder top flange width

$W_{tf\text{-}m}$: A multiplier applied to D_g to obtain W_{tf}

$X_{bf,k}$: Horizontal extent of the k^{th} mobilised failure surface from the abutment wall face in logarithmic spiral failure surface model

y_{ab}, $y_{ab,PL}$, $y_{\max,bf}$: ABS displacement, its value at a given PL, its maximum value

$y_{ab,k}$, $y_{br,k}$, $y_{pl,k}$, $y_{pr,k}$: Values of y_{ab}, y_{br}, y_{pl} and y_{pr} at step k

$y_{i,k}$: Displacement of the i^{th} component at step k

y_{br}, $y_{br,PL}$: Bearing displacement, its value at a given PL

$y_{br,j}$, $y_{pr,j}$: Respective displacements of bearing, pier of the j^{th} assemblage

$y_{brp,sh}$, $y_{u,brp_{sh}}$: Shear deformation of the bearing pad and its ultimate value

$y_{brp,sl}$, $y_{u,brp_{sl}}$, $y_{brp,sl_{PL}}$: Bearing sliding displacement, its ultimate value, its value at a PL

$y_{e,pr}$: Elastic relative displacement in pier

y_{gap} : Longitudinal gap closure displacement at the abutment

$y_{\max,bf}$: Maximum displacement capacity of backfill

y_{pl}, $y_{pl,PL}$: PSS displacement, its value at a given PL

$(y_{pl,ij})_{BWF}$: y_{pl} at i^{th} SSL and $\varepsilon_{s,i}$, from beam on Winkler foundation analysis

y_{pr}, $y_{pr,PL}$: Pier displacement, its value at a given PL

y_{pr,f_i} : y_{pr} corresponding to i^{th} flexural DS

$y_{s,pl}$, $y_{m,pl}$, $y_{e,pl}$, $y_{c,pl}$: y_{pl} s (in cm), with s, m, e and c, preceding pl in subscript at slight,

moderate extensive and collapse DSs respectively

$y_{t,brd}$, $y_{y,brd}$, $y_{u,brd}$: Dowel bar deformations corresponding to transition, yield and ultimate strain of the bar

$y_{u,\,pr}$: Ultimate relative displacement in pier

$y_{y,\,ab}$, $y_{u,\,ab}$: Respective yield, ultimate displacements in abutment-backfill

$y_{0,pl}$, $y_{0,\,pl_i}$: Pile head lateral displacement, its value corresponding to $\varepsilon_{s,i}$

$(y_{0,\,pl_i})_{BWF}$, $(y_{0,\,pl_i})_{SWM}$: Respective $y_{0,\,pl_i}$ s, from beam on Winkler foundation approach, SWM

z_j : Depth of the j^{th} SSL

Z_{brd} : Section modulus of the dowel bar

α_{bfr} : Inclination angle of the ultimate Rankine SPW

α_{bft} : Logarithmic spiral arc take-off angle from the backwall bottom

$\alpha_{bf,i}$: Base angle of a backfill slice in backfill

α_{ss}, $\alpha_{ss,m}$: SPW fan angle in SWM, mobilised value

β_C, $\beta_{D|IM}$, $\beta_{EDP|IM}$: Dispersion of C, D and EDP (conditioned on IM) respectively

$\beta_{D|PGA}$: Dispersion in demand with respect to PGA

$\beta_{D|S_a(0.7s)}$: Dispersion in demand with respect to S_a (0.7s)

β_{IM} : Standard deviation of ln(IM)

β_{spw}, $\beta_{spw,m}$: Base angle of SPW, mobilised value

β_t : Total lognormal standard deviation which takes into account the uncertainties related to the input GM, bridge response etc.

χ : Cyclic loading factor

δ_{abf} , $\delta_{abf,i}$: Abutment-backfill interface friction angle, interslice friction angle with respect to i^{th} backfill slice

$\delta_{abf,\,f}$: δ_{abf}, expressed as a fraction of φ_{bf}

$\delta_{\max,\,FC}$: Maximum value of δ_{FC}

δ_{pl} : Pile deflection pattern angle

δ_{FC} : Extent of variation between two FCs

Δ_{sp} : y_{pr} at the onset of concrete cover spalling

Δ_{bb} : y_{pr} at the onset of longitudinal bar buckling

$\Delta y_{bf,\,ik}$: Displacements of the i^{th} soil slice corresponding to k^{th} mobilised surface in logarithmic spiral failure surface model

$\Delta\sigma_h$, $\Delta\sigma_{h,m}$, $\Delta\sigma_{hf}$: Soil horizontal stress change, mobilised value, value at failure

η : Modulus of subgrade reaction

ε_{bf} , ε_{ss} : Respective horizontal strains in backfill, sand around pile

$\varepsilon_{bf,k}$, $\varepsilon_{ss,i}$: ε_{bf} value at k^{th} SL_{bf}, i^{th} value of ε_{ss} in the range

ε_{bff} : Failure strain in backfill

$\varepsilon_{c,\,pl}$, $\varepsilon_{c,\,pr}$: Concrete compressive strains in pile and pier respectively

$\varepsilon_{cu,\,pl}$, $\varepsilon_{cu,\,pr}$: Ultimate values of $\varepsilon_{c,\,pl}$ and $\varepsilon_{c,\,pr}$ respectively

$\varepsilon_{s,\,pl}$, $\varepsilon_{s,\,pr}$: Steel strains in pile and pier respectively

$\varepsilon_{su,\,pl}$, $\varepsilon_{su,\,pr}$: Ultimate values of $\varepsilon_{s,\,pl}$ and $\varepsilon_{s,\,pr}$ respectively

$\varepsilon_{t,brd}$, $\varepsilon_{y,brd}$, $\varepsilon_{su,brd}$: Transition, yield and ultimate strains respectively in dowel bar

$\varepsilon_{y,brd}$, $\varepsilon_{y,pl}$, $\varepsilon_{y,pr}$: Steel yield strains in dowel, pile and pier respectively

$\varepsilon_{ss,50}$, $(\varepsilon_{ss,50})_{42.5}$: Horizontal strain at 50% stress level in sand, value at overburden pressure of 42.5kPa

$\varepsilon_{bf,50}$, $(\varepsilon_{bf,50})_{42.5}$: Horizontal strain at 50% stress level in backfill, value at overburden pressure of 42.5kPa

γ_{br} : Bearing shear strain

γ_{bf} : Unit weight of the backfill

γ_s : Unit weight of the sandy soil

λ : Co-efficient of variation

μ : Mean

μ_{brp} : Coefficient of friction of the bearing pad

$\mu_{brp,MF}$: Multiplicative factor applied to the empirical expression of μ_{brp}

$\mu_{cmax,\,pr}$: Maximum displacement ductility in pier

$\mu_{cy,\,pr}$: Displacement ductility in pier at yield

$\mu_{cy1,\,pr}$: Displacement ductility in pier at first yield

$\mu_{c2,\,pr}$: Pier displacement ductility corresponding to $\Theta_{p2,pr}$ or $\Theta_{p4,pr}$

$\mu_{f\text{-}s,pr}$: Pier ductility at the occurrence of flexure to shear failure

$\mu_{h,pr}$: Cumulative energy ductility in pier

μ_{pr}, $\mu_{pr,PL}$: Displacement ductility in pier, its value at a given PL

$\mu_{pr,b}$: μ_{pr} corresponding to buckling failure of longitudinal bar in pier

$\mu_{pr,\,f_i}$: μ_{pr} corresponding to i^{th} flexural DS

$\mu_{pr,s}$: μ_{pr} corresponding to shear failure in pier

$\mu_{pr,\delta}$: μ_{pr} corresponding to P- δ collapse in pier

μ_{str} : Structural ductility

$\mu_{u,pr}$: Ultimate displacement ductility in pier

μ_{IM} : Mean of IM

υ_{pl} , υ_{pr} : Axial load ratios on pile and pier respectively

ν_s, ν_{bf} : Poisson's ratios of the sand around pile, backfill

$\Phi()$: Lognormal cumulative probability distribution function

φ_{bf} , φ_s : Respective effective friction angles of backfill, sand around pile

$\varphi_{bf}{}'$, $\varphi_s{}'$: Respective normalised values of φ_{bf} , φ_s

$\varphi_{bf,k}$: Mobilised value of φ_{bf} corresponding to k^{th} mobilised surface in logarithmic spiral failure surface model

ϕ : Soil-pile friction angle

$\rho_{i,p\text{-}q}$: Correlation coefficient between p^{th} and q^{th} components at i^{th} DSs

$\rho_{l,pl}$, $\rho_{l,pr}$: Respective longitudinal reinforcement ratios in pile, pier

$\rho_{t,pl}$, $\rho_{t,pr}$: Respective transverse reinforcement ratios in pile, pier

$\rho_{1,ab\text{-}br}$, $\rho_{2,ab\text{-}br}$, $\rho_{3,ab\text{-}br}$: Correlation coefficients between ABS and bearing at respective DS1s, DS2s and DS3s

$\rho_{1,ab\text{-}pr}$, $\rho_{2,ab\text{-}pr}$, $\rho_{3,ab\text{-}pr}$: Correlation coefficients between ABS and pier at respective DS1s, DS2s and DS3s

$\rho_{1,br\text{-}pr}$, $\rho_{2,br\text{-}pr}$, : Correlation coefficients between bearing and pier at respective

$\rho_{3,br\text{-}pr}$, $\rho_{4,br\text{-}pr}$ respective DS1s, DS2s, DS3s and DS4s

$\rho_{1,pl\text{-}ab}$, $\rho_{2,pl\text{-}ab}$: Correlation coefficients between A-PSS and ABS at respective DS1s and DS2s

$\rho_{1,pl\text{-}br}$, $\rho_{2,pl\text{-}br}$: Correlation coefficients between A-PSS and bearing at respective DS1s and DS2s

$\rho_{1,pl\text{-}pr}$, $\rho_{2,pl\text{-}pr}$: Correlation coefficients between A-PSS and pier at respective DS1s and DS2s

σ : Standard deviation

σ_{IM} : Standard deviation of IM

σ_d (a) : Standard deviation of $S_d(a)$

σ_m , $\sigma_{m,\min}$: Normal stress on the bearing pad, its minimum value

$\overline{\sigma_{ov}}$: overburden pressure

ς : Common value of log-standard deviation of FCs of all DS ranks

ς_j : Log-standard deviation of IM for FC at j^{th} DS in maximum likelihood method

ζ, $\zeta_{D_{i,p}}$, $\zeta_{D_{i,q}}$: Dispersion, respective values of ζ for $D_{i,p}$, $D_{i,q}$

ζ_j : Log-standard deviation of $S_d(a)$

τ, τ_m : Pile side shear stress, mobilised value

θ : Median

θ_{IM} : Mean of ln(IM)

Θ_{pr} : Pier end rotation

$\Theta_{p2,pr}$: Plastic hinge rotation in pier with lap splices

$\Theta_{p4,pr}$: Plastic hinge rotation in pier without lap splices

$\xi_{ab,PL}$: Equivalent viscous damping at the abutment at a given PL

$\xi_{A\text{-}PSS,PL}$: Damping in A-PSS at a given PL

$\xi_{bent,PL}$: Equivalent viscous damping for bent at a given PL

$\xi_{bf,PL}$: Damping in backfill at a given PL

$\xi_{bp,j}$: Resultant damping of j^{th} pier-bearing assemblage

$\xi_{br,j}$: Equivalent damping of the j^{th} bearing

$\xi_{BS,PL}$: Equivalent damping of the BS at a given PL

$\xi_{fr,br_{PL}}$: Damping in bearing due to friction at a given PL

$\xi_{hyst,pl_{PL}}$: Hysteretic damping in pile at a given PL

$\xi_{hyst,pr_{PL}}$: Hysteretic damping in pier at a given PL

$\xi_{\min,s}$: Minimum damping ratio in sand

$\xi_{pr,j}$: Equivalent viscous damping of the j^{th} pier with

$\xi_{pl,PL}$: Equivalent viscous damping for pile at a given PL

$\xi_{pr,PL}$: Equivalent viscous damping for pier at a given PL

$\xi_{PSS,PL}$: Equivalent viscous damping for PSS at a given PL

$\xi_{s,PL}$: Damping in sand at a given PL

$\xi_{0,pr}$: Elastic damping in pier

Chapter 1
INTRODUCTION

CONTENTS

1.1 PROBLEM STATEMENT AND MOTIVATION

Bridges, linking the inaccessible areas are the vital elements in a transportation network as well as easing traffic on busy roads by constructing bridges saves time and effort. Apart from direct losses in the event of bridge collapse, its non-functionality due to incurred damages causes indirect losses by hindering the socio-economic activities owing to the consequent traffic disruption. These lifeline facilities must remain operational for executing the post disaster emergency rescue and recovery activities.

Instances of damages/collapses during the recent seismic events like the 1971 San Fernando, 1989 Loma Prieto, 1990 Costa Rica, 1994 Northridge and the 1995 Kobe earthquakes have emphasised the bridges to be seismically sensitive. Since then earthquake-resistant behaviour and design of bridges have been studied extensively in order to learn from these failures. Bridge seismic vulnerability is investigated to be mainly attributed by the factors like (a) inadequate ductile detailing in the flexural plastic hinge zones and shear strength of the bridge components, (b) insufficient shear reinforcement and development lengths at the connections, (c) inadequate ductility/seat widths at bearings etc. As structural system, bridge has very less redundancy leading to increased vulnerability during strong earthquakes (Priestley et al., 1996).

Assessment of seismic vulnerability of bridges has become a major research area in earthquake engineering, since such an a-priori estimation can devise an effective disaster mitigation. It assists in critical pre-earthquake mitigation decisions such as whether a bridge should be open to traffic immediately after an earthquake or demolished or retrofitted as well as the order of retrofit prioritisation for several such bridges in the

network (Bazos and Kiremidjian, 1998) and planning effective alternate routes in case of demolition (Dukes, 2013). In a post-earthquake scenario, it aids in disaster emergency management as it helps the decision makers to find where to focus on relief and rehabilitation resources to be sent (Pradeep, 2013).

Importance of such infrastructure elements in the economic and social context has led to the need for a better evaluation of the seismic vulnerability through a more integrated probabilistic prospective (Zelaschi et al., 2014), since neither the input Ground Motion (GM) nor the structural behaviour can be described deterministically (Elnashai et al., 2004). Hence, the current seismic assessment methods have focused on the development of Fragility Curves (FCs). An FC represents the probabilities of reaching or exceeding a predefined Damage State (DS) (corresponding to any of the different levels of physical damage descriptions, traditionally ranked as slight, moderate, extensive, collapse). DS is attained when the seismic demand (D) placed on the structure is greater than its capacity (C) for that DS, at varying levels of a chosen Ground Motion (GM) Intensity Measure (IM) such as Peak Ground Acceleration (PGA), Peak Ground Velocity (PGV), pseudo spectral acceleration S_a, peak spectral acceleration, Arias intensity etc. The probability is primarily attributed to the different uncertainties in the design and behavior of various bridge components as well as the uncertainties in the earthquake shaking. Fragility statement can be expressed as in Equation (1.1) (where *im* and *ds* are the realisations of IM and DS) and the typical FCs generated for different DSs are depicted in Figure 1.1.

$$\text{Fragility} = P[D \geq C \,|\, IM = im, DS = ds] \tag{1.1}$$

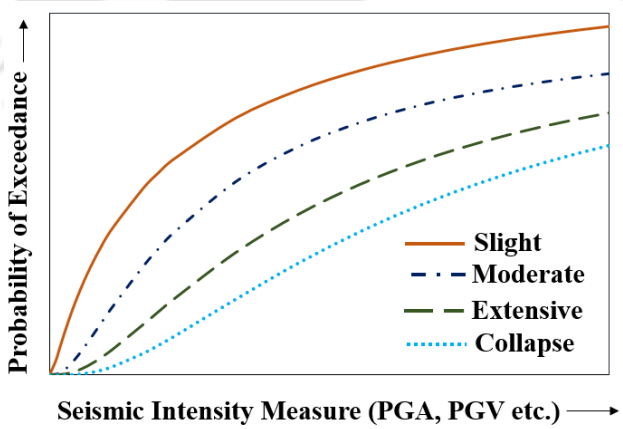

Figure 1.1 Sample fragility curves for different structural damage states.

The intent of this research study is to develop the FCs corresponding to an adopted class of reinforced concrete Integral Abutment Bridges (IABs), with multispan continuous deck supported on multi-column bents through bearings at intermediate locations. This study,

while considering wide variation in the Bridge System (BS) properties and incorporating soil-structure interaction, develops its own damage models for the components and analyses a set of bridge model samples for their inelastic behaviour while subjected to a number of GMs with varying frequency contents. Component-level FCs are generated numerically from the obtained capacity and demand distributions of the components. Finally, the system-level FCs are generated through the evolution of joint demands from all the vulnerable bridge components.

1.2 OBJECTIVES OF THE WORK

The present work focuses on evaluating the component-level and the system-level fragilities of a particular class of IABs owing to very few vulnerability studies of the IAB typology which is gaining worldwide popularity owing to jointless construction, while addressing the identified deficiencies to obtain reliable fragility estimates. Accuracy of the finally derived FCs highly relies on the idealisation of the bridge-foundation-soil system, the adopted seismic analysis method, DS definitions and quantification and identification of an optimal GM IM, which the present work attempts to endeavour at through the following objectives:

1. Analysis of soil-structure interaction and development of damage models for the IAB components.
2. Incorporation of wide variations of geometric, structural detailing and material parameters in the fragility formulation for the class of IABs.
3. Identification of a better IM for IAB.
4. Generation of component-level and system-level FCs employing adaptive capacity spectrum method, correlations existing among the seismic demands of the components and actual distributions of demand and capacity, just as being assessed in the study.
5. Investigation of the comparative vulnerabilities of the individual components as well as the bridge system and the individual components.
6. Development of generalised expressions for the Limit State Thresholds (LSTs) of the component DSs and mathematical expressions with respect to bearing dowel capacities, and investigation of sequences of occurrences of the DSs owing to parametric variations of the IAB components.

1.3 ORGANIZATION OF THE DISSERTATION

The dissertation consists seven chapters with brief outline of the contents as given below:

(a) Chapter 1 provides the general overview of the research topic, objectives of the present work and a brief outline of the chapters of the dissertation.

(b) In Chapter 2, review of the previous research carried out in the field of bridge fragility is discussed, followed by identifying the gap areas and stating the scope for the present work.

(c) Chapter 3 describes the structural attributes of the adopted IAB class, numerical modeling and development of damage models for the IAB components.

(d) In Chapter 4, the uncertainty treatment for the various salient parameters of the IAB components is discussed, leading to the development of probabilistic seismic capacity model and Probabilistic Seismic Demand Model (PSDM) for those components.

(e) In Chapter 5, the probabilistic seismic demand analyses of the IAB components using the adaptive capacity spectrum method are discussed. Thereby, the component-level FCs are derived through numerical computation employing the the capacity and demand dstributions, just as evaluated in the study, and the system-level FCs through the development of the probabilistic seismic joint demand model for the BS.

(f) Chapter 6 presents the development of parameterised expressions for evaluating LSTs over wide ranges of the respective component parameters and evaluation of sequences of attainments of different component DSs owing to parametric variations in geometry and material properties.

(g) In Chapter 7, the entire work is summarised, salient conclusions are drawn, research impacts are highlighted, the scope of future research is outlined and the limitations are laid out.

Chapter 2
LITERATURE REVIEW

CONTENTS

2.1 INTRODUCTION

Research activity in the field of seismic vulnerability assessment of bridges was initiated following the 1971 San Fernando earthquake (Priestley et al., 1996). Following the devastating consequences of the major earthquakes, researches promptly headed in this direction, as a step towards seismic risk mitigation. Assessment of various bridge configurations/classes/inventories have been carried out worldwide, e.g. for the Central and Southeast United States (Choi et al., 2004; DesRoches et al., 2004; Nielson, 2005; Ramanathan, 2012; Sullivan, 2010), for various regions within USA (Dicleli and Bruneau, 1995a, 1995b, 1996; Meng and Lui 2000; Shinozuka et al., 2001; Hwang et al., 2001; Jernigan and Hwang, 2002; Kim and Feng, 2003; Bignell et al., 2005; Kunnath et al., 2006; Pan et al., 2007; Saadeghvaziri and Yazdoni-Motlagh, 2007; Zhong et al., 2008; Zhang et al. 2008; Pan et al., 2010a, 2010b; Kwon and Elnashai, 2010; Brandenberg et al., 2011, Aygun et al., 2011; Seo and Linzell, 2012; Wang et al., 2013; Abdel-Mohti and Peckan, 2013; Zakeri et al., 2014; Jeon et al., 2015), for Canada (Tavares et al., 2012, 2013; Siddiquee, 2015; Mahmoudi (2015); Siddiquee and Alam, 2017) for Italy (Cardone et al., 2007; Franchetti et al., 2008; Tecchio et al., 2011), for Greece (Moschonas, 2009), for Germany (Pottatheere al., 2008), for Hungary (Zsarnoczay et al., 2014; Simon, 2016), for New Zealand (Bradley et al., 2010), for Iran (Nateghi and Shahsavar, 2004; Nicknam, 2011; Langroudi et al., 2011), for Turkey (Avsar, 2009), for Algeria (Kibboua et al., 2014),

for India (Parool et al., 2014), for Taiwan (Chang et al., 2008; Liao and Loh, 2004; Sung, 2013), for Korea (Lee et al., 2007), for Japan (Karim et al., 2001; Tanaka et al., 2010) etc.

Different work carried out on seismic vulnerability assessment of bridges were summarised in review studies like Billah and Alam (2015) listing the bridge components assessed, the adopted Engineering Demand Parameters (EDPs), the employed IMs, uncertainties associated with the parameters and the methodologies, and by Gidaris et al. (2017) displaying the assessed geographic region wise bridge typologies (designed/retrofitted), the employed IMs and the developed fragility models conditioned on simply the IMs or along with other factors like skew angle, bridge parameters etc.

2.2 EVOLUTION OF FRAGILITY CURVES

One of the earliest attempts in the direction of seismic risk analysis of structures was made by Whitmann et al. (1975), following the damages caused by the 1971 San Fernando Earthquake. The penalty in not designing the structure to the elastic response level is that the possibility of minor, repairable damage must be accepted during the design life of the bridge and the benefit is clearly the reduction in the cost (Priestley et al., 1996). In response to implementing more severe design requirements, Whitmann et al. (1975) proposed a procedure called seismic design decision analysis wherein they formulated a systematic framework of providing clear statements of the initial cost required by each of different design strategy and the risk of damages/losses from future earthquakes which are to be balanced. This required the examination in probabilistic terms, of the degree of damage which one earthquake will cause to a particular building system designed according to a particular design strategy. This damage evaluation is repeated for different levels of earthquakes, different design strategies and, where appropriate, for different types of buildings. This formed the founding base of the seismic risk assessment methodology in the form of construction of the damage probability matrix assembling the probability values that various levels of damage will result from earthquakes of various intensities. Funded by the federal emergency management agency for planning the risk mitigation of facilities in California in the face of a major earthquake, the applied technology council headed toward the evaluation of the damage/loss estimates for facilities in California building upon the work of Whitmann et al. (1975), using the matrices and restoration functions in ATC (1985). However, due to non-availability of data from previous earthquakes, the matrices had to be developed based on expert opinion. Data and methodology of ATC (1985) are only applicable for structures in the state of California. In 1991, applied technology council

put forward another report (ATC, 1991) focussing on the seismic vulnerability and impact of disruption of lifelines not only in California, but also in the Conterminous United States. The matrices were modified to obtain continuous damage functions by performing regression of the discrete values of various matrices, which came to be known as FCs.

Major turning point in the field of fragility research can be linked with the availability of the damage distributions reported in post-earthquake surveys after the 1989 Loma Prieta, 1994 Northridge and 1995 Kobe earthquakes. Researchers like Basoz and Kiremidjian (1998); Yamazaki et al. (1999) and Shinozuka et al. (2001) developed FCs empirically through statistical analysis of the damage data obtained from post-earthquake inspection.

The federal agency further came up with a geographical information system based risk assessment software package in the form of HAZUS (1997). Elements of FCs were a combination of performance data (from tests of structural elements), earthquake experience data, expert opinion and judgment. Improved versions of HAZUS (1997) were developed in 1999 and 2003. Over years, the formulation of bridge FCs has historically transitioned from empirical to analytical methods.

2.3 DIFFERENT APPROACHES TO FRAGILTY CURVE GENERATION

Fragility analysis aims at evaluating the conditional probabilities of exceeding a prescribed DS, for varying levels of a GM IM. Over the years, different forms of FCs have been derived by government agencies and research institutes around the world for seismic risk assessment of different classes of structures (Rossetto and Elnashai, 2003). Based on the sources of the earthquake damage data as well as the methodologies of evaluating the fragilites, five generic forms of FCs can been identified. The different FC types, along with their respective advantages and disadvantages have been concisely tabulated in Billah and Alam (2015) and are also discussed as follows:

2.3.1 Empirical Fragility Curve

Empirical FCs use the structural damage distributions reported in post-earthquake surveys as their statistical basis. The observational source is the most realistic, as all practical details of the exposed stock are taken into consideration alongside the soil-structure interaction effects, topography, site, path and source characteristics (Rossetto and Elnashai, 2003). Basoz and Kiremidjian (1998) developed the damage probability matrices using the available damage data from 1989 Loma Prieta and 1994 Northridge earthquakes and derived FCs employing logistic regression. Shinozuka et al. (2001) used the maximum likelihood method to estimate the lognormal parameters to derive the fragility functions

employing the damage data from the 1994 Northridge and 1995 Kobe earthquakes. Yamazaki et al. (1999) used the damage data from the Kobe earthquake to develop empirical FCs for the highway bridges.

Empirically developed FCs seem to be more reliable, as they are based on the more complete GM and actual bridge damage data (Nielson, 2005); however not without limitations. The foremost limitation is that these require a large amount of data for a particular DS of a certain class of structures to get statistically significant results. In practice, this is only achievable through the combination of data from different earthquakes and locations (Rossetto and Elnashai, 2003) or through grouping classes together to get enough data for a given DS and hence reduces the usefulness of FCs (Nielson, 2005). Structural damages and hence FCs are found to be highly dependent on duration, amplitude and the spectral characteristics of the input GM and these FCs cannot introduce various structural parameters and characteristics of input GM due to shortage of enough data (Karim and Yamakazi, 2001). Discrepancies in observations between different inspection teams add up the uncertainty in the developed curves and significantly reduce the reliability of the empirical vulnerability curves (Billah and Alam, 2015). Even, using the same damage data, the derived empirical FCs by two different teams can show significant differences, e.g., those derived empirically by Shinozuka et al. (2001) and Yamazaki et al. (1999) using the 1995 Kobe earthquake damage data, as observed and evaluated quantitatively by Billah and Alam (2015). Also, they are conditioned to subjective or unverifiable definitions of DSs and lack correlation with bridge geometry and structural properties; however, they have been useful in providing a basic form for highway bridge fragilities and motivating analytical fragility work (Mackie and Stojadinovic, 2005).

2.3.2 Expert/Judgement Based Fragility Curve

Expert/Judgement based FCs are based on the opinion of panels of civil engineers with expertise in the field of earthquake engineering in which they are asked to make estimates of the probable damage distributions within a particular population of structures when subjected to earthquakes of different intensities (Rossetto and Elnashai, 2003). These distributions are fit to the expert predictions to represent the range of damage estimate at each GM IM and the probability of exceedance of a specified DS is derived from the resulting distributions and plotted against the IM level to obtain a set of FCs, and the associated uncertainty bounds (Rossetto and Elnashai, 2003). Expert opinion is the predominant source used by most current rehabilitation codes in the U.S.A for the

generation of matrices and FCs, like ATC (1985), ATC (1991) and ATC (1996). Since the experts can be asked to provide damage estimates for any number of structural types, FCs can be easily made to include all the factors affecting the seismic response of different structures (Rossetto and Elnashai, 2003). However, the procedure is totally subjective and depends on the number of experts queried and therefore is based on expertise and experience of the individuals with little correlation to actually observed damage (Ramanathan et al., 2011). It is practically impossible to evaluate the degree of conservatism associated with the judgement-based source and consideration of local structural types, typical configurations, detailing and materials and construction practices, being inherently associated with those FCs preclude their application to other areas (Rossetto and Elnashai, 2003).

2.3.3 Experimental Fragility Curves

Development of bridge FCs using experimental results is not common. Since large-scale experiments involving entire bridge models or full-scale components are expensive, bridge fragility analysis utilising the observed response from shaking table tests has been very limited. Although experimental results provide a basis for defining various damage measures for analytical FCs, their application is still very limited (Billah and Alam, 2015). Based on experimental results from shake table and cyclic load tests on bridge piers, Vosooghi and Saiidi (2012) developed experimental FCs. They developed a probabilistic relationship between experimental damage data and seismic response parameters in the form of FCs. Banerjee and Chi (2013) developed FCs for bridges using damage data obtained from shake table test of a near-full scale bridge. However, lack of adequate data points at all DSs and a weak correlation between geometry and structural properties limit the application of the experimental FCs.

2.3.4 Analytical Fragility Curve

Analytical FCs adopt damage distributions simulated from the analyses of structural models under increasing earthquake loads as their statistical basis (Rossetto and Elnashai, 2003), motivated by the advances in modeling capabilities (Nielson, 2005). These analytical fragility models have received increased attention in the literature in the past decade given their ability to overcome limitations of subjective expert-based fragilities or empirical ones that are constrained by the lack of adequate data (Gidaris et al., 2017). With the advancement in the computational abilities and modelling techniques for inclusion of various response features of the structures like shear-flexure–axial interaction, soil-

structure interaction, interactive confinement on concrete members and reinforcing bar buckling, analytical approaches to FC generation are becoming ever more attractive (Rossetto and Elnashai, 2003). With the use of analytical tools to simulate the earthquake behaviour of any kind of model representing the actual structure, a detailed set of statistical damage data is obtained in order to estimate FCs (Palacios, 2004), surpassing the problems related with limited and incomplete recorded damage data. Analysis techniques can range from simpler elastic spectral analysis to the more complex nonlinear time history analysis. Analyses can result in a reduced bias and increased reliability of the vulnerability estimate for different structures compared to expert opinion (Rossetto and Elnashai, 2003). However, choice of the appropriate analysis method, proper structural idealisation and close to real representation of seismic hazard are prerequisites for the reliability of the derived analytical curves and have to be meticulously dealt with.

2.3.5 Hybrid Fragility Curve

Hybrid vulnerability curves attempt to compensate for the scarcity of observational data, subjectivity of judgemental data and modelling deficiencies of analytical procedures by combining data from the different sources (Rossetto and Elnashai, 2003). These FCs are usually derived from combinations of observed damage statistics with either expert opinion and/or inferences made from experimental tests and/or analytical simulations (Palacios, 2004). ATC (1996) and HAZUS (1999) documents contain FCs of this category. Singhal and Kiremidjian (1996a) included observational data into the derived analytical FCs to obtain hybrid FCs. An important part of this method is the use of weighting system to take into account the reliability of the different data sources (Palacios, 2004), e.g. Singhal and Kiremidjian (1996b) adopted a Bayesian technique to update the analytical curves with the observational damage data. Development of matrices using hybrid method was also adopted by Kappos et al. (1998) involving the existing statistical data from past earthquakes being supplemented by results of inelastic dynamic analysis of appropriate models.

2.4 Basic Features of the Fragility Formulation

GM IM, EDP, Limit State (LS) and the associated uncertainties (discussed below) form the basic key ingredients (mostly associated with the analytical FC) of the fragility framework. Generation of FC involves convolution of the demand model (evaluating the EDPs and linking these to the IMs) and the damage model (gauging the LSs) to obtain the probability of exceedance of a LS for a given IM value. Steps leading to FC generation are depicted in the flowchart in Figure 2.1.

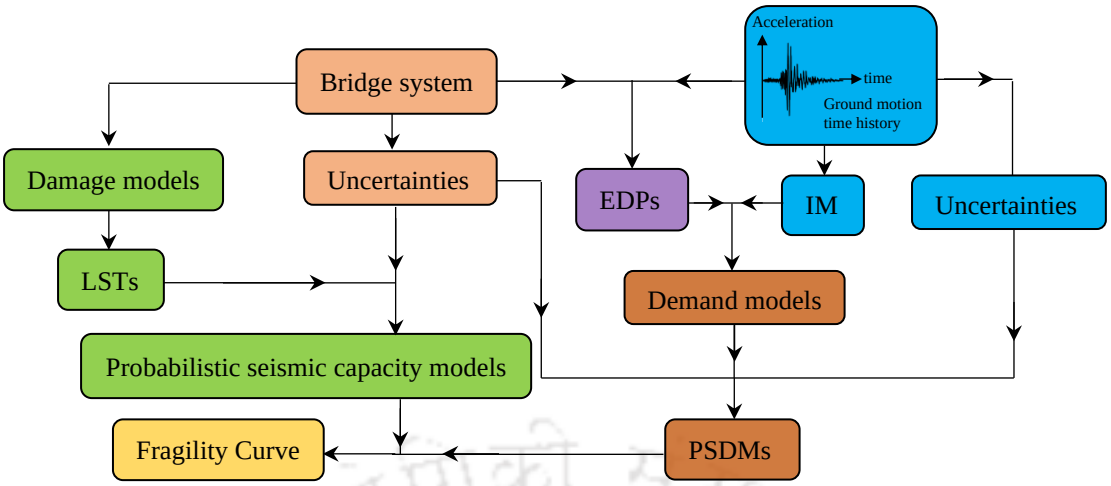

Figure 2.1 Flowchart depicting the bridge fragility generation steps.

2.4.1 Ground Motion Intensity Measure

Earthquake IM refers to the engineering parameter describing a characteristic of a GM or its effect on the structure. GM amplitude, frequency content, duration and numbers of peaks (and even their sequence) in the GM time history above a certain amplitude are some of the important characteristics affecting structural response and damage (Elnashai et al., 2004). IM should represent those GM features and correlate well with the structural response.

Three classes of IMs are used in current practice. The first class contains the traditional IMs describing the earthquake source characteristics and time history record, e.g., strong motion duration, PGA, PGV, peak ground displacement, Arias intensity etc., except the earthquake magnitude and the source to site distance, as they cannot be obtained directly from the accelerogram (Mackie and Stojadinovic, 2005). The second class includes the IMs that describe the time history obtained using a single-degree-of-freedom system filter on the original record, e.g., S_a , pseudo-spectral velocity, response spectrum intensity etc. The third class applies an arbitrary filter to the original time history to obtain more efficient demand models (details in Mackie and Stojadinovic, 2005).

IM should be so selected that it contains more information about the structure of interest such that the uncertainty associated with the demand model is low to achieve optimality (Mackie and Stojadinovic, 2004a). Choosing an optimal IM requires certain qualities to be fulfilled like sufficiency, efficiency, practicality, effectiveness, robustness and hazard computability. Response of a structure subjected to an earthquake GM, characterised by descriptor IM, is designated as EDP (Mackie and Stojadinovic, 2003). The sufficiency condition is satisfied when the estimated EDP distributions depend only on the IM, not upon the properties of the records selected for analysis to avoid biased estimate of structural

response (Baker and Cornell, 2006). IM is termed to be efficient if it can explain a large portion of a GM's effect on a structure, resulting in reduction in the remaining variability in EDP for that given IM (Baker and Cornell, 2006), i.e., $\beta_{D|IM}$. An IM-EDP pair is termed practical if it has some direct correlation with known engineering quantities. It is measured by the regression parameter B_{rc} in the PSDM; a lower value implies a less practical IM (Padgett et al., 2008) and when B_{rc} approaches zero, IM contributes negligibly to the demand estimate. The term proficiency was proposed by Padgett et al. (2008) to measure the composite contribution of practicality and efficiency and serves as a primary factor in the selection process for an optimal IM, calculated as the ratio of B_{rc} and $\beta_{D|IM}$. Effectiveness of IM is determined by its ability to fit a mathematical form to the median trend of EDP. Robustness describes the rate of change of efficiency with some structural parameter such as time period. An IM with a small rate of change is deemed robust (Mackie and Stojadinovic, 2004b). The hazard computability of the IM refers to the level of effort required to assess the probabilistic seismic hazard or determine the hazard curve (Giovenale et al., 2004). IMs, other than PGA or S_a at discrete values (e.g., 1s) in terms of which the hazard maps and curves are readily available, will require more effort.

Mackie and Stojadinovic (2003) found that spectral parameters at the bridge natural period T_N (i.e., S_a and pseudo-spectral displacement S_d) tended to be the most appropriate IM because of their tendency to reduce uncertainty in the demand model. Nevertheless, an IM is to be sought which is necessarily independent of T_N (since T_N gets modified every time), but still exhibits properties of an optimal demand model. Arias intensity does not include this structure-dependent information, but does, however, include the cumulative effect of energy input from the GM. PGA has good correlation only with response of structures with very small T_N s, as it is a spectral quantity for the zero T_N structure. Depending on T_N, a larger PGA does not necessarily indicate larger response and do not produce efficient demand models for structures with longer T_N s. Most of the bridge structures of concern have first mode T_N s between 0.5 and 1.0 sec, thus explaining lack of correlation with PGA, as also advocated in the study by Kafali and Grigoriu (2004) which found PGA to correlate weakly with both observed and theoretically computed structural damages. PGA and peak ground displacement (a similar but displacement based quantity) may have more correlation with response when considering pulse or fling type earthquakes (Mackie and Stojadinovic, 2003). PGV was proposed as a more appropriate IM (being period-independent) for bridges (Mackie and Stojadinovic, 2007). PGV and spectrum

intensity are found to be better IMs for structures in liquefiable soils (Bradley et al., 2010). Mostly used IMs in studies are PGA (as by Hwang et al., 2001; Basoz and Kiremidjian, 1998; Yamazaki et al., 1999; Nielson, 2005; Choine et al., 2015 etc.), $S_a(T_N)$ (like Singhal and Kiremidjian, 1996b; Ramanathan, 2012 at T_N of 0.1s etc.), PGV (e.g., Yamazaki et al., 1999; Bradley et al., 2010), peak ground displacement (e.g., Wang et al., 2013), ratio of PGV to PGA (e.g., Zhong et al., 2008), free-field lateral spreading ground displacement (e.g., Zhang et al., 2008), Arias intensity (e.g., Wang et al., 2013) etc. root mean square acceleration and perceived intensity (e.g. modified Mercalli intensity, Medvedev-Sponheuer-Karnik intensity etc.) may also be employed. Except for spectral quantities, each IM is GM specific and independent of T_N (Mackie and Stojadinovic, 2003).

2.4.2 Demand Model

Seismic demand model describes the effect of GMs on the structural response by establishing a median relationship between EDP and IM along with an associated measure of uncertainty. This is determined using a finite element model and an appropriate analysis method for the structure to obtain the EDP data for the GMs in the selected suite (Mackie and Stojadinovic, 2007). Though, EDP selection is largely dependent on the structure (Mackie and Stojadinovic, 2007), it should be such that it leads to a clearly defined mathematical form of the demand model and which exhibits low uncertainty to satisfy the optimality criterion. In numerical fragility analysis, the structural responses under earthquakes are depicted and monitored by various EDPs (Zhang and Huo, 2009). For the case of highway bridges, the possible EDPs are grouped into 3 categories. Global EDPs describe the overall bridge behaviour such as maximum column displacement, drift ratio, abutment displacement, residual displacements etc. Intermediate EDPs describe the performance of bridge structural components such as maximum column curvature, column moment, shear force in the abutment etc. Local EDPs describe material responses (stress and strain) anywhere of interest in BS (Mackie and Stojadinovic, 2003). Mackie and Stojadinovic (2007) observed global EDPs to typically result in demand models with lower uncertainty. The selected EDPs should have direct and physical correlation with BS damages for obtaining reliable FCs. Previous research has indicated EDP to follow lognormal distribution (Mackie and Stojadinovic, 2004b). Cornell et al. (2002) developed a power law model to represent the relationship between the median EDP, i.e., $\overline{EDP}$ and IM, as in Equation (2.1), where A_{rc} and B_{rc} are the regression coefficients for the EDP

versus IM data, and has been used by many studies like Nielson (2005); Ramanathan (2012); Zhang et al. (2009); Zakeri et al. (2014) etc.

$$\overline{EDP} = A_{rc}(IM)^{B_{rc}}; \quad \ln(\overline{EDP}) = \ln(A_{rc}) + B_{rc}\ln(IM) \tag{2.1}$$

This Lognormal Formulation (LF) has been readily adopted for the probabilistic seismic demand analysis, but is not necessarily the only possible model to express the demand. Detailed discussion on the development of PSDM can be found in Subsection 2.5.2.

2.4.3 Damage Models for the Bridge Components

Damage model (also known as capacity model) correlates the observed damage and the corresponding capacity of a structural component with the level of the applied seismic demand as a function of EDP (Zhang and Huo, 2009). The observable damage is often introduced into the fragility formulation process by determining the capacities at different levels of the structural response (Mackie and Stojadinovic, 2004b). The complex natural phenomena such as concrete cracking and spalling, rebar buckling, transverse reinforcement fracture, loss of shear capacity of bearing, the onset of collapse etc. are identified as structural damages (Mackie and Stojadinovic, 2005). DSs are the identified levels of damages that a BS or its component might experience during seismic loading (Dukes, 2013). Structural response does not always necessarily correlate to physical descriptions of damage/failure; hence damage is described in terms of damage measures which are usually discrete observations of the onset of the DSs (Mackie and Stojadinovic, 2005). Damages are quantified by the LSs and the discrete threshold/limiting values of the LSs for adopted damage measures are termed as Limit State Thresholds (LSTs). Although the DS definitions are discrete, it is assumed that a continuous range of damage exists between the discrete DSs to enable the closed-form computation of the component FCs and also it is essential that the LS definitions use the same metric as the EDPs (Ramanathan, 2012). The subsequent EDPs can then be related to specific values of a damage measure through the use of the damage model (Mackie and Stojadinovic, 2004b). Thus, given the knowledge of EDP, the damage is independent of IM (Baker and Cornell, 2006). Bridge LSTs have a direct influence on the reliability of FCs, since these decide on meeting or exceeding the bridge DS for a given GM IM, therefore have to be evaluated accurately.

LSs can be described using a prescriptive (physics-based) approach, descriptive (judgment-based) approach or by incorporating both using Bayesian updating principles (Nielson, 2005). In the prescriptive (mechanics based) approach, a functional level of the bridge is associated with a component damage and the component LSs are derived from

the level of deformations or curvature demands or any other EDPs that correspond to the physical descriptions of damages. The LSs are set commonly based on experimental tests of structural components or systems or results of analytical methods such as pushover analysis, incremental dynamic analysis. The descriptive (judgemental) approach is based on the post disaster functionality level of the components and is usually in terms of repair cost and downtime (Ramanathan et al., 2012) which would be assigned to the bridge by decision makers (bridge inspectors) for the different DSs, thus making the approach a more subjective one (Nielson and DesRoches, 2007). Other options for LS definitions are evolving, such as the Bayesian updating of these mechanics-based models with subjective data regarding functionality or closure decisions and repair cost implications as adopted by Nielson and DesRoches (2007); Ramanathan et al. (2010). These approaches, however, require significant data for their characterisation regarding historic failures, expert opinion, or field investigation (Tavares et al., 2012). LSs can be characterised by distributions which can assume any form like the normal, lognormal, uniform distributions etc.

Some guidelines provide qualitative descriptions of the DSs for bridges, e.g., HAZUS (2003), as shown in Table 2.1. SEAOC (2009) prescribed the different performance levels and limits (longitudinal and transverse directions of bridge), as shown in Table 2.2. Literature abounds in prescribing the DS definitions and the LSTs or the corresponding numerical expressions in terms of various EDPs, based on experimental/analytical results in their studies for the bridge components. The salient studies on these as discussed below:

Table 2.1 Qualitative Limit States (HAZUS, 2003).

Limit State	Description
Slight	Minor cracking and spalling to the abutment, cracks in shear keys at abutments, minor spalling and cracks at hinges, minor spalling at the column (damage requires no more than cosmetic repair) or minor cracking to the deck
Moderate	Any column experiencing moderate (shear cracks) cracking and spalling (column structurally still sound), moderate movement of the abutment (<2”), extensive cracking and spalling of shear keys, any connection having cracked shear keys or bent bolts, keeper bar failure without unseating, rocker bearing failure or moderate settlement of the approach.
Extensive	Any column degrading without collapse – shear failure – (column structurally unsafe), significant residual movement at connections, or major settlement approach, vertical offset of the abutment, differential settlement at connections, shear key failure at abutments.
Complete	Any column collapsing and connection losing all bearing support, which may lead to imminent deck collapse, tilting of substructure due to foundation failure.

Table 2.2 Deck drift damage limit states (SEAOC, 2009)

Damage states	Damage descriptions	Deck drift (%)	
		Longitudinal	Transverse
Fully operational	First yield	<0.2	<0.5
Operational	Minor local yielding at some piers may occur. No observable fractures. Minor buckling or observable permanent distortion of the bridge members	0.2–0.5	0.5–1.0
Life safety	Hinges form. Local buckling of some elements. Severe joint distortion. Isolated connection failures. A few elements may experience fracture	0.5–1.5	1.0–3.5
Near collapse	Extensive distortion for the structure components and pier panels. Many fractures in connections	1.5–2.5	3.5–5.0
Collapse	-----	>2.5	>5.0

(a) Pier

DSs and the respective LSTs in terms of various EDPs for reinforced concrete circular column piers were prescribed by studies like Kowalsky (2000); Hwang et al. (2001); Elnashai et al. (2004); Choi et al. (2004) (based on tests of similar non-seismically designed columns as in the study) and Nielson (2005) (adopting the limits by Hwang et al., 2001 and converting these to curvature ductility limits); Pan et al. (2007) and Banerjee and Shinozuka (2008); Moschonas et al (2009); Kwon and Elnashai (2010); Ramanathan et al. (2011) (for seismically and non-seismically designed piers as prescribed by Hwang et al., 2001 and Berry and Eberhard, 2003); Ramanathan (2012) (for different design eras, based on experimental results from Sahs et al., 2008); Tavares et al. (2012), Wang et al. (2013) and Mounnarath et al. (2016) (adopting the limits by Hwang et al., 2001 and converting these to curvature ductility limits for the columns in the study); Billah and Alam (2016) (for columns reinforced with shape memory alloy rebars, designated as model 1 through model 5 in the study with respect to different metallic compositions for alloys), adopting the DSs by Hose et al. (2000), etc. and are listed in Tables 2.3 through 2.14 respectively.

Table 2.3 DS description and quantification for pier (Kowalsky, 2000)

Damage state	Damage description	Strain limits	
		Concrete	Steel
Serviceability	Initiation of concrete crushing/ residual crack width >1mm; repair is not needed after the earthquake.	0.004	0.015
Damage control	Concrete is still repairable/incipient buckling of reinforcement; only repairable damage is permitted.	0.018	0.060

Table 2.4 DS description and quantification for pier (Dutta and Mander, 2001)

Damage states	Damage descriptions	Non-seismically designed	Seismically designed	
		Drift limits	Drift limits	Rotational ductility limits
No	First yield	0.005	0.008	1.00
Slight	Cracking and spalling	0.007	0.01	2.01
Moderate	Loss of anchorage	0.015	0.025	6.03
Extensive	Incipient column collapse	0.025	0.05	11.07
Complete	Column collapse	0.050	0.075	23.65

Table 2.5 DS description and quantification for pier (Hwang et al., 2001)

Damage states	Damage descriptions (HAZUS, 1999)	Limit criteria	
		Flexural moment	Displacement ductility
No	No reinforcement steel yielding, minor cracking in concrete	$M_{pr} > M_{1,pr}$	$\mu_{cy1,pr}(=1) > \mu_{pr}$
Slight	Tensional reinforcement steel yielding and visible minor cracking in concrete	$M_{y,pr} > M_{pr} \geq M_{1,pr}$	$\mu_{cy,pr}(=1.2) > \mu_{pr} > \mu_{cy1,pr}$
Moderate	Plastic hinging, but with no failure, extensive concrete cover spalling	$M_{pr} \geq M_{y,pr}$, $\Theta_{pr} < \Theta_{p2,pr}(\Theta_{p4,pr})$	$\mu_{c2,pr}(=1.76) > \mu_{pr} > \mu_{cy,pr}$
Extensive	Disintegration of core concrete, flexural failure	$M \geq M_y, \Theta_{pr} > \Theta_{p2}(\Theta_{p4})$	$\mu_{c\max,pr}(=4.76) > \mu_{pr} > \mu_{c2,pr}$
Complete	$\mu_{\text{cmax},pr} = \mu_{c2,pr} + 3$		$\mu_{pr} > \mu_{\text{cmax},pr}$

Table 2.6 DS description and quantification for pier (Elnashai et al., 2004)

Damage states	Damage descriptions (pier designed according to modern seismic codes)	Displacement limits (pushover analysis)
Undamaged	No damage, no yielding of vertical reinforcement bars	47mm
Slightly damaged	Only minor structural damage and member flexural strength with limited ductility, but no concrete spalling in plastic hinges and that the crack widths remain sufficiently small	64mm
Extensively damaged	Significant structural damage; no service post-earthquake unless significant but feasible repair is undertaken. Rupture of transverse bar or buckling of longitudinal bar should not occur and core concrete in plastic hinges should not need replacement	103mm
No collapse	Extensive damage, repair may not be effective and the structure has to be demolished. Beyond this LS, global collapse is expected due to structure's instability to sustain gravity loads. Strain corresponding to 50% of the compressive strength of concrete and for steel strain, strain of 9% is adopted	142mm

In Table 2.4, against flexural moment M_{pr} and displacement ductility μ_{pr}, $M_{1,pr}$ and $\mu_{cy1,pr}$,

and $M_{y,pr}$ and $\mu_{cy,\,pr}$ are the column bending moment capacities and ductilities at first yield and yielding respectively, Θ_{pr} is the pier end rotation, $\mu_{c2,\,pr}$ is the ductility corresponding to $\Theta_{p2,pr}$ or $\Theta_{p4,pr}$, which are the plastic hinge rotations against $\varepsilon_{c,\,pr}$ (compressive strain in the concrete extreme fibre (ε_c) in pier) of 0.002 or 0.004, with or without lap splices respectively and $\mu_{\mathrm{cmax},\,pr}$ is the maximum ductility (as in FHWA, 1995).

Table 2.7 DS description and quantification for pier (Choi et al., 2004 and Nielson, 2005)

Curvature ductility limits	Slight	Moderate	Extensive	Collapse
Choi et al. (2004)	1	2	4	7
Nielson (2005)	1	1.58	3.22	6.84

Table 2.8 DS description and quantification for pier (Pan et al., 2007 and Basu and Shinozuka, 2008)

Damage states	Pan et al. (2007)		Basu and Shinozuka (2008) (DS definitions from HAZUS, 1999)
	Damage descriptions	Curvature limits (1/m)	Rotational ductility limits
Slight	First yielding of longitudinal bar	0.0028	3.39
Moderate	Column plastic hinge formation	0.0035	4.75
Extensive	Column strength degradation	0.0140	8.43
Complete	Ultimate concrete compression strain	0.0350	-

Table 2.9 DS description and quantification for pier (Moschonas et al., 2009)

Damage states	Damage descriptions	Displacement limits (pushover analysis, based on different ductility $\mu_{u,pr}$ ranges)	
		$\mu_{u,pr} \geq 4$	$\mu_{u,pr} < 3$
Slight	Elastic relative displacement $y_{e,pr}$	$> 0.7 \cdot y_{e,pr}$	$> 0.7 \cdot y_{e,pr}$
Moderate	Ultimate relative displacement $y_{u,pr}$ corresponding to strength drop of first pier, beyond which successive pier fail.	$> 1.5 \cdot y_{e,pr}$	$> y_{e,pr} + 1/3 \cdot (y_{e,pr} - y_{e,pr})$
Extensive		$> 3.0 \cdot y_{e,pr}$	$> y_{e,pr} + 2/3 \cdot (y_{e,pr} - y_{e,pr})$
Collapse		$> y_{u,pr}$	$> y_{u,pr}$

Table 2.10 DS description and quantification for pier (Kwon and Elnashai, 2010)

Damage states	Damage descriptions	Displacement limits (pushover analysis)	
		Longitudinal	Transverse
Serviceability	First yield of vertical reinforcing steel in tension	72	36
Damage control	Achievement of global maximum strength	124	92
Collapse prevention	Achievement of core concrete ε_c of 0.01 leading to 25% loss of concrete stress, which resulted in a significant member strength reduction	500	260

Table 2.11 DS description and quantification for pier (Ramanathan et al., 2011)

Damage states	Curvature ductility limits			
	Slight	Moderate	Extensive	Collapse
Non-seismically designed	1	1.58	3.22	4.18
Seismically designed	1	5.11	7.50	9.00

Table 2.12 DS description and quantification for pier (Ramanathan, 2012)

Design era	Damage states	Damage descriptions	Curvature Ductility limits
Pre 1971 Brittle column	Slight	Cracking	0.80
	Moderate	Minor cover spalling anywhere	0.90
	Extensive	Large shear cracks; major spalling; exposed core; confinement yield (no rupture)	1.00
	Complete	Loss of confinement; longitudinal bar buckling or rupture; core crushing	1.20
1971-1990 Strength degrading column	Slight	Cracking	1.00
	Moderate	Minor cover spalling anywhere	2.00
	Extensive	Major spalling; exposed core; confinement yield (no rupture)	3.50
	Complete	Loss of confinement; longitudinal bar buckling or rupture; core crushing; large residual drift	5.00
Post 1990 Ductile column	Slight	Cracking	1.00
	Moderate	Minor cover spalling concentrated at the top and bottom of the column	4.00
	Extensive	Large shear cracks; major spalling; exposed core; confinement yield (no rupture)	8.00
	Complete	Loss of confinement; longitudinal bar buckling or rupture; core crushing	12.00

Table 2.13 DS description and quantification for pier (Tavares et al., 2012; Wang et al., 2013; Mounnarath et al., 2016)

Damage states	Displacement limits (Tavares et al., 2012)	Drift ratio limits (Wang et al., 2013)	Curvature ductility limits (Mounnarath et al., 2016)
Slight	5mm	0.0076	1
Moderate	7mm	Δ_{sp}/L_{pr} (Berry and Eberhard, 2003)	2.39
Extensive	11mm	$2/3 \cdot \Delta_{bb}/L_{pr}$	7.58
Collapse	30mm	Δ_{bb}/L_{pr} (Berry and Eberhard, 2003)	16.67

In Table 2.13, Δ_{sp} and Δ_{bb} are the displacements at the onsets of concrete cover spalling and longitudinal bar buckling respectively, L_{pr} is the distance from the column base to the point of contraflexure.

Likewise, for both circular and rectangular reinforced concrete column piers, studies like Hose et al. (2000); Berry and Eberhard (2003) (for flexure critical columns bending in single curvature) etc. furnished LSTs, as listed in Tables 2.15 and 2.16 respectively.

LSTs for wall type piers were provided by Karim and Yamazaki (2001) (later used by Nateghi and Shahsavar, 2004) and Liao and Loh (2004) (for square pier too); Bradley et al. (2010); Serdar and Jankovic (2014); Siddiquee (2015) etc., as listed in the Tables 2.17 through 2.20. Mehanny et al. (2014) evaluated the LSTs and found these to be within limits prescribed by SEAOC (2009), defining collapse at 20% loss in pier base shear capacity.

Table 2.14 DS description and quantification for pier (Billah and Alam, 2016)

Damage states	Drift (%) (from incremental dynamic analyses)					Distribution
	model-1	model -2	model -3	model -4	model -5	
Cracking	0.28	0.28	0.28	0.28	0.28	Uniform
Yeilding	1.86	1.80	1.80	1.95	1.21	Lognormal
Spalling	2.88	2.87	2.58	2.68	2.10	Normal
Crushing	5.94	6.05	7.94	5.72	4.84	Gamma

Table 2.15 DS description and quantification for pier (Hose et al., 2000)

Performance level	Qualitative Description	Quantitative Description	Concrete strain	Steel Strain	Pier drift
I- Cracking	Onset of hairline cracks	Cracks barely visible	< 0.0032	< 0.005	<1
II- Yielding	First yield of longitudinal bar	Crack widths < 1mm	0.0032	0.005	1
III- Initiation of local mechanism	Initiation of inelastic deformation. Onset of concrete spalling/diagonal crack development	Crack widths 1-2mm/ Length of spalled region >1/10 cross-sectional depth	0.01	0.019	3
IV- Full development of local mechanism	Wide crack widths/ spalling over full local mechanism region	Crack widths >2mm/ Diagonal cracks >2/3 cross-section depth/ Length of spalled region >1/2 cross-section depth.	0.027	0.048	5
V- Strength degradation	Buckling of longitudinal reinforcement/rupture of transverse reinforcement/ crushing of core concrete	Crack widths > 2mm in concrete core/ Measurable dilation > 5% of the original member dimension	0.036	0.063	8.7

Table 2.16 DS description and quantification for pier (Berry and Eberhard, 2003)

Damage description	Drift limits
Concrete cover spalling	$\frac{\Delta_{sp}}{L_{pr}}(\%) = 1.6\left(1-\frac{P_{pr}}{A_{g,pr}f_{c,pr}}\right)\left(1+\frac{L_{pr}}{10D_{pr}}\right)$
Longitudinal bar buckling	$\frac{\Delta_{bb}}{L_{pr}}(\%) = 3.25\left(1+K_{e_{bb}}\frac{\rho_{t,pr}f_{y,pr}}{f_{c,pr}}\frac{d_b}{D_{pr}}\right)\left(1-\frac{P_{pr}}{A_{g,pr}f_{c,pr}}\right)\left(1+\frac{L_{pr}}{10D_{pr}}\right)$

In Table 2.16, $K_{e_{bb}}$ values are 40 for rectangular and 150 for circular columnns, $f_{y,pr}$ and $f_{c,pr}$ are the yield and peak compressive stresses in transverse reinforcement and concrete respectively, $\rho_{t,pr}$ is the transverse reinforcement ratio, d_b is the longitudinal bar diameter, D_{pr} and $A_{g,pr}$ are the depth and gross area of the column section with axial load P_{pr}.

Table 2.17 DS description and quantification for pier (Karim and Yamazaki, 2001 and Liao and Loh, 2004)

Damage state (HAZUS, 1999)	Karim and Yamazaki (2001)	Liao and Loh (2004)	
	Park-Ang damage index limits = $(\mu_{pr} + \chi\mu_{h,pr})/\ \mu_{u,pr}$	Displacement ductility limits	
		Seismic design	Conventional design
Slight	0.14 < damage index ≤ 0.40	μ_{pr} = 2	μ_{pr} = 2
Moderate	0.40 < damage index ≤ 0.60	μ_{pr} = 4	μ_{pr} = min(1+ ($\mu_{f\text{-}s,pr}$ - 1)/2), 2)
Extensive	0.60 < damage index ≤ 1.00	μ_{pr} = 6	μ_{pr} = min($\mu_{f\text{-}s,pr}$, 3)
Complete	1.0 < damage index	μ_{pr} = 9	$\mu_{f\text{-}s,pr}$ =4.5/ultimate μ_{pr}

Table 2.18 DS description and quantification for pier (Bradley et al., 2010)

Damage descriptions	Cracking	Yielding	Spalling/buckling	Axial failure
Curvature limits (1/m)	0.00055	0.0036	0.0080	0.0150

Table 2.19 DS description and quantification for pier (Serdar and Jankovic, 2014)

Damage states	Damage descriptions (pier designed according to old regulations)	Drift limits
Minor	Minor damages in bridge columns; onset of concrete cover spalling. Functionality can be reduced and repairing cost are not negligible	0.0155
Major	Onset of buckling of longitudinal bars. Duration and repair costs can be significant and bridge functionality loss can happen.	0.063

Table 2.20 DS description and quantification for wall pier (Siddiquee, 2015)

Service states	Damage states	Damage descriptions	Drift limits	
			Pushover analysis	Incremental dynamic analysis
Immediate service	Minimal	Elastic behaviour with minor damage. Full service. $\varepsilon_{c,pr}$ < 0.004; $\varepsilon_{s,pr}$ < $\varepsilon_{y,pr}$.	0.05	0.06
Limited service	Repairable	Inelastic behaviour with moderate damage. At least 50% lane operationality. $\varepsilon_{c,pr}$ < 0.006; $\varepsilon_{s,pr}$ < 0.01.	0.42	0.42
Service disruption	Extensive	Extensive spalling but no concrete crushing/no fracture of hoops or buckling of longitudinal reinforcement; usable for restricted emergency traffic.	0.98	1.02
Life safety	Near Collapse	No bridge collapse; life safety is ensured.	3.05	2.46

In Table 2.17, $\mu_{f\text{-}s,pr}$, $\mu_{u,pr}$ and $\mu_{h,pr}$ are the ductility at occurrence of flexure to shear failure, ultimate displacement and cumulative energy ductilites respectively, χ is the cyclic load factor taken as 0.15. In Table 2.20, $\varepsilon_{s,pr}$ is the pier steel bar strain reaching yield value $\varepsilon_{y,pr}$.

(b) Bearings

Existing bridges have employed a variety of bridge bearings ranging from high type and low type steel bearings, both as fixed and expansion bearings to elastomeric bearings with a plain rubber pad or rubber pads with embedded steel dowels/reinforced with steel laminates. Depending on their material of construction and the mechanism of movability, bearings behave differently and hence their damage mechanisms also differ.

Past studies prescribed bearing DSs based on experimental observations, with the consideration of deck unseating (which is a function of the size of the bearings and the width of the supports (Choi et al., 2004)) as the worst case. Damage descriptions for high type fixed bearing and elastomeric bearings with dowels are provided in Table 2.21. Mander et al. (1996) prescribed LSTs for steel fixed and expansion bearings in longitudinal (L) and transverse (T) directions from their experimental results, as in Table 2.22, which were adopted by studies like Choi et al. (2004), Nielson (2005) and Ramanathan et al. (2011). Mounnarath et al. (2016) adopted the expansion bearing LST prescriptions for the Reston pendulum sliding bearing in their study. LSTs for fixed as well as expansion dowel elastomeric bearings are also available in studies like Choi et al. (2004), Nielson (2005), as in Table 2.22 and were later adopted in studies like Ramanathan et al. (2011).

Table 2.21 DS description for bearing (Mander et al., 1996; Nielson, 2005)

Damage states	Damage descriptions	
	Mander et al. (1996)	Nielson (2005)
	High type fixed bearing	Elastomeric bearings with dowels
Slight	Minor cracks in the concrete pedestal	Noticeable damage but no closure
Moderate	Prying and severe deformation in anchor bolts; initiation of strength degradation	Deck realignment may be required and also implies possible dowel fracture
Extensive	Bond failure of bolts and bearing rocking on the bedding followed by cracking and spalling of concrete cover of the pedestal beneath the masonry plate; subsequent loosening of the nuts and slight raising and bending of the bolts	Dowel fracture is assured and would likely require some degree of repair (girder retention); unrestricted sliding occurs thereafter
Complete	Extensive concrete cover cracking or spalling of the reinforced concrete pedestal; back and forth rocking of bearing due to complete bond failure and even its overturning after the fracture of the anchor bolts beyond a typical seat width	Deck unseating

Table 2.22 DS quantification for bearing (Mander et al., 1996; Choi et al., 2004; Nielson, 2005)

Damage states	Displacement (mm) limit criteria			
	Mander et al. (1996)		Choi et al. (2004); Nielson (2005)	
	Steel fixed bearing (L, T) and expansion bearing (T)	Steel expansion bearing (L)	Fixed dowel elastomeric bearing (L, T)	Expansion dowel elastomeric bearing (L, T)
Slight	1	50	8	30
Moderate	6	100	100	100
Extensive	20	150	150	150
Complete	40	255	255	255

LSTs for different bearing types were provided by Hwang et al. (2001) and Liao and Loh (2011); Pan et al. (2007); Zhang et al. (2008) and Tavares et al. (2012); Avsar (2009); Kwon and Elnashai (2010); Bradley et al. (2010), Ramanathan (2012) and Choine et al. (2014), as in Tables 2.23 through 2.28 respectively.

Table 2.23 DS description and quantification for bearing (Hwang et al., 2001; Liao and Loh, 2011)

Hwang et al. (2001) (Elastomeric bearing with dowel (A307 Swedge bolts))			Liao and Loh (2011) (Plain elastomeric bearing)	
Damage states	Damage descriptions	Shear limit criteria	Damage state (HAZUS, 1999)	Displacement limit criteria (cm)
No	No damage to bolts	$F_{brd} < F_{y,brd}$	Slight	Yield
Yielding	dowel yielding	$F_{y,brd} \leq F_{brd} < F_{u,brd}$	Moderate	10
Failure	dowel broken	$F_{brd} \geq F_{u,brd}$	Extensive	20
			Complete	min (40, 2N/3)

In Table 2.23, F_{brd} is the shear response, $F_{y,brd}$ and $F_{u,brd}$ are the yield and ultimate shear capacities of the bolts in the bearing and N is the seat length of a girder at the support.

Table 2.24 DS description and quantification for bearing (Pan et al., 2007)

Bearing types	Damage descriptions	Displacement limits (mm)
High type rocker bearing	Overturning about the edge of the rocker bottom by rolling off on the masonry plate with the deformation exceeding half the rocker width, which may lead to deck unseating.	153
Low type sliding bearing	Translation of the sliding plate over the bronze plate being larger than half the width of the masonry plate	102

Table 2.25 DS description and quantification for bearing (Zhang et al., 2008; Tavares et al., 2012)

Damage States (HAZUS, 1999)	Zhang et al. (2008) (Lead rubber bearing)	Tavares et al. (2012) Plain elastomeric bearing	
	Shear strain (γ_{br}) limits (%)	Damage limit descriptions	Damage limit descriptions
Slight	γ_{br} >100	Loss of shear capacity	30
Moderate	γ_{br} >150	Displacement exceeds the height of the bearing	60
Extensive	γ_{br} >200	Displacement exceeds 50% of the bearing width or length	150
Complete	γ_{br} >250	Displacement exceeds the bearing full width or length, implying potential unseating	300

Table 2.26 DS description and quantification for bearing (Avsar, 2009)

Damage state	Damage state description (Plain elastomeric bearing)	Displacement limit (mm)
LS1- Serviceability	Friction resisting force holding the elastomeric bearing at its place gets exceeded by seismic force; bearings will thereby be no longer stable and superstructure starts to make permanent displacements leading to minor problems at the bridge	40.5
LS2- Damage control	Due to large horizontal displacement, superstructure girders fall over the pedestal and rests on the cap beam directly. This could cause excessive damage on the asphalt disturbing the traffic flow and affecting the functionality of the bridge	425.0

Table 2.27 DS description and quantification for bearing (Kwon and Elnashai, 2010)

Damage states	Damage descriptions (low type fixed bearings)	Displacement limit criteria (mm)	
		Mean	COV
Serviceability	Occurrence of slippage at bearing plate interfaces and between bearings and structural elements	4	0.25
Damage control	Damages to pintle pins, holes and anchor bolts; attainment of pin lateral shear capacity	7	0.5
Collapse prevention	Loss of lateral resistance of bearing	11	0.75

Table 2.28 DS description and quantification for bearing (Bradley et al., 2010; Ramanathan, 2012; Choine et al., 2015)

Plain elastomeric bearing (Displacement limits)				
Damage states	Bradley et al. (2010)	Damage states	Ramanathan (2012)	Choine et al. (2015)
Minor movement	0.05m	Slight	1in	25.4mm
Unseating	0.25 m	Moderate	4in	101.6mm

(c) Abutment

Most of the past studies provided LSTs for abutment like Tavares et al. (2012); Nielson (2005); Kwon and Elnashai (2010) (adopted by Taskari and Sextos, 2015) e.t.c using the recommendations from Caltrans (1999), identified on the lateral force deformation capacity curves for its components, as in Tables 2.29; 2.30; and 2.31 respectively. LSTs prescribed by Moschonas et al. (2009) and Bradley et al. (2010); and Ramanathan (2012) and Choine et al. (2014) are listed in Tables 2.32; and 2.33 respectively. In Table 2.32, y_{gap}, and $y_{y,ab}$ and $y_{u,ab}$ are the longitudinal gap, and the backfill yield and ultimate displacements.

Table 2.29 DS description and quantification for abutment (Tavares et al., 2012)

Damage states (HAZUS, 1999)	Damage limit descriptions (based on lateral force deformation capacity curve)	Displacement limits (mm) (evaluated based on Caltrans, 1999)	
		Wall	Foundation
Slight	First yield	7	4
Moderate	50% of the ultimate displacement	15	20
Extensive	Ultimate displacement	30	40
Complete	Twice the ultimate displacement	60	80

Table 2.30 DS description and quantification for abutment (Nielson, 2005)

Damage states (HAZUS, 1999)	Damage limit descriptions (based on lateral force deformation capacity curve)	Displacement (y_{ab} mm) limits (based on Caltrans (1999) and Martin and Yan (1995)	
		Passive action	Active action
No	Displacement below half of first yield	$y_{ab} < 7$	$y_{ab} < 4$
Slight	Displacement below first yield-soil yielding	$7 < y_{ab} < 15$	$4 < y_{ab} < 8$
Moderate	Displacement below ultimate deformation	$15 < y_{ab} < 37$	$8 < y_{ab} < 25$
Extensive	Pile in the plastic range	$37 < y_{ab} < 146$	$25 < y_{ab} < 50$
Complete	Displacement greater than twice the ultimate	$146 < y_{ab}$	$50 < y_{ab}$

Table 2.31 DS description and quantification for abutment (Kwon and Elnashai, 2010)

Damage states	Damage descriptions	Displacement limit (mm) (based on Caltrans, 1989)
Serviceability	Soil pressure reaches peak value of 369 kPa	25
Damage control	Incipient damage to the abutments	61
Collapse prevention	Severe traffic disruption due to backwall failure (attainment of wall shear strength due to a large impact from superstructure)	75

Table 2.32 DS description and quantification for abutment (Moschonas et al., 2009; Bradley et al., 2010)

Moschonas et al. (2009)		Bradley et al. (2010)	
Damage states	Limit criteria	Damage states (flexural damages)	Curvature limits (1/m)
Slight	y_{gap}	Cracking	0.00055
Moderate	$> y_{y,ab}+1/3\cdot(y_{u,ab}-y_{y,ab})$	Yielding	0.0036
Extensive	$> y_{y,ab}+2/3\cdot(y_{u,ab}-y_{y,ab})$	Spalling/buckling	0.0080
Collapse	$> y_{u,ab}$	Axial failure	0.0150

Table 2.33 DS description and quantification for abutment (Ramanathan, 2012; Choine et al., 2015)

Damage states	Displacement limits					
	Ramanathan (2012) (inch)			Choine et al. (2015) (mm)		
	Active	Passive	Transverse	Active	Passive	Transverse
Slight	3	1.5	1	25.4	76.1	76.1
Moderate	10	4	4	100	217.5	217.5

(d) Pile-soil system

PSS damages are mostly quantified in terms of pile cap displacement and curvature ductility. The latter relating the peak strains at the pile critical section is a highly localised demand measure whereas, the former gives a better account of overall pile and soil response (Bradley et al., 2009), as it is practically easier to collect post event data on it to assess the pile foundation integrity and performance. Basu and Prezzi (2007) and Mashahiro et al. (2009); Bradley et al. (2010) and Padgett et al. (2013); and Wang et al. (2013) provided PSS DS descriptions and LSTs, as in Tables 2.34; 2.35; and 2.36 respectively. In Table 2.36, P_{pl} is the pile axial load (positive for compression and in kN) with $y_{s,pl}$, $y_{m,pl}$, $y_{e,pl}$ and $y_{c,pl}$ as the pile cap displacements (in cm) for the respective DSs.

Table 2.34 DS description and quantification for PSS (Basu and Prezzi, 2007; Mashahiro et al., 2009)

Damage states	Damage descriptions	Displacement limits
Serviceability	The pile head deflection remains within the tolerable deflection such that no notable residual displacement appears and hence nothing is going to happen in service	0.025 times pile diameter (Basu and Prezzi, 2007) 1% diameter of pile (Mashahiro et al., 2009)
Ultimate	Partial or total collapse, soil resistive stresses attain the limit (yield) value over a substantial portion of the pile length so that plastic flow occurs within the soil mass resulting in large lateral deflections, translation or rotation of pile	-

Table 2.35 DS description and quantification for PSS (Bradley et al., 2010; Padgett et al., 2013)

Bradley et al. (2010)		Padgett et al. (2013)		
Damage states	Curvature Limits (1/m)	Damage states	Damage descriptions (Song et al., 2005) (fixed head concrete pile)	Displacement limits (pushover analysis)
Cracking	0.0003	Slight	Formation of first plastic hinge at pile head	58 mm
Yielding	0.0018	Moderate	Formation of a second plastic hinge along the pile length	82 mm
		Extensive	Attainment of 75% of the ultimate state	120 mm
Failure	0.0090	Collapse	Flexural failure, dictated by limiting curvature in the plastic hinge	160 mm

Table 2.36 DS description and quantification for pile-soil system (Wang et al., 2013)

Damage states	Damage descriptions	Displacement limits (cm) (pushover analysis)
Slight	Attainment of first yield curvature	$y_{s,pl} = 2.15$
Moderate	Attainment of second yield curvature	$y_{m,pl} = 2.949e^{-7}P_{pl}^2 - 4.669e^{-4}P_{pl} + 3.14$
Extensive	Attainment of two-third of the ultimate curvature	$y_{e,pl} = 2.153e^{-7}P_{pl}^2 – 2.962e^{-4}P_{pl} + 8.11$
Collapse	Attainment of the ultimate curvature	$y_{c,pl} = 3.228e^{-7}P_{pl}^2 – 4.440e^{-4}P_{pl} + 12.16$

2.4.4 Uncertainties to be Incorporated in Fragility Formulation

The probabilistic framework leading to the fragility computation inherently requires several uncertainty sources to be considered. These uncertainties are typically classified as aleatoric and epistemic. Aleatoric uncertainty is associated with inherent and inevitable randomness in the system or process and therefore can only be managed and not reduced. Epistemic uncertainty is due to a lack of knowledge, ignorance or course modeling, can generally be reduced with the acquisition of additional information and understanding (Nielson, 2005). In bridge engineering in particular, the most common source of aleatoric uncertainty is associated with the variability in the structural and the underlying soil properties and randomness in seismic GM characteristics. Similarly, epistemic uncertainty is mainly related to decisions made in finite element modeling, e.g. when dealing with synthetic GMs, uncertainty built is attributed to modeling seismological mechanisms, path and site characteristics. Uncertainties exist in bridge geometric, structural and geotechnical material and other parameters affecting the bridge seismic responses and the GM

characteristics. Among all the sources of uncertainty, earthquake-induced GM seems to be the most unpredictable one (Kappos, 2002) and has a significant impact on the variability observed in the structural response (Padgett and DesRoches, 2007). Most studies considered uncertainties in the compressive strength of concrete, yield strength of reinforcing steel, bridge mass, span length, friction coefficient and shear modulus of bearings, strength of dowel bar, gap at the dowels, size of the expansion gap and coefficient of thermal expansion in bearing, deck width, column height and diameter, stiffness of the abutments and foundations, pier longitudinal and transverse reinforcement ratios, foundation and backfill density and shear modulus, BS damping and the angle of incidence of the GM, frequency content, phase, duration etc. of GMs, etc.

FCs for portfolios of structures therefore have to deal with the complexity of considering the uncertainties (Padgett and DesRoches, 2007) associated with those parameters, which are considered as random variables. The variations are estimated based on the published literature as well as engineering judgment (Kwon and Elnashai, 2010) and thereafter empirical cumulative density functions are developed for these variables (Ramanathan et al., 2011). Most studies have used normal and lognormal distributions for the uncertainty characterisation. Kennedy et al. (1980) justified the use of the lognormal distribution by stating it to represent many structural materials and response variables well, given the extreme tails of the distribution is not of a concern, adding that for probabilities greater than 1% can be used reasonably.

2.5 METHODOLOGY OF DEVELOPING ANALYTICAL FRAGILITY CURVE

Many researchers worldwide have opted to develop FCs analytically, owing to the inherent deficiencies of the empirical FCs. Because of the ease and efficiency with which data are generated through analytical approaches, these can be readily applied to various bridge types and geographical regions (with even limited seismic damage records) to generate FCs. Different analytical methods ranging from simple elastic analysis to complex nonlinear time history analysis for simulating the structural response under seismic loading and generating the FCs have been in use. Different representation of seismic hazard is needed based on the chosen procedure (GM parameters, response spectrum, ground motion time histories (Palacios, 2004).

2.5.1 Elastic Analysis

Elastic spectral analysis is the simplest as well as less consuming analytical procedure. Yu et al. (1991) used simple Single degree-of-freedom models and elastic response spectrum

analysis to develop FCs for highway bridges in Kentucky. Jernigan and Hwang (2002) adopted this method to estimate the *C*/*D* ratios for the bridge components, with *C* and *D* determined, as described in FHWA (1995) and from elastic spectral analysis, as specified in AASHTO (1996) respectively. Ten bridge samples were generated by varying nine structural attributes within adopted ranges. Uncertainties in structural capacities are considered by generating 50 samples from the statistical distribution of the mechanistic properties (concrete and steel strength). Variability in demand due to factors like spectral values of input GM and structural damping is accounted for by employing a seismic force factor of which 50 samples were generated assuming it to have a lognormal distribution with a mean value of one and a coefficient of variation of 0.5. The factor is then applied to the seismic response coefficient in the bridge design specification AASHTO (1996). *C/D* ratios for the 50 earthquake-bridge samples are then evaluated for the investigated modes of failure for various components and were assigned to the specified DSs. Damage frequency matrix was calculated and thereby the FCs were generated. The authors advocated the FCs developed by the proposed method to be very well comparable with those developed from other methods, such as nonlinear time history analysis.

2.5.2 Nonlinear Dynamic Analysis

Nonlinear dynamic analysis has been adopted in many past studies like (Choi, 2004; Nielson, 2005; Mackie and Stojadinovic, 2005; Ramanathan, 2012; Hwang et al., 2001; Zhang et al., 2008 etc.) to estimate the seismic demands on the bridge components and thus to generate the FCs. It provides the most reliable solution to the prediction of forces and cumulative deformation demands in every element of the structural system as it accounts for dynamic effects in the structure (Krawinkler and Seviratna, 1998). Generation of demand model, more specifically PSDM employing the dynamic analysis involves the following steps (as stated by Nielson, 2005):

(a) The selected nos. of GMs are randomly paired with the set of analytical models of the BS samples (generated using techniques like the Monte-Carlo sampling or the more refined Latin Hypercube sampling on the probability distributions of the random parameters). Nonlinear dynamic analysis is performed on each of such pairs to obtain the demands on various bridge components in terms of the peak values of the respective EDPs of the components.

(b) Component EDPs are plotted against the corresponding IM values of the GMs to develop the component PSDMs. There are two approaches for generating PSDMs, based

on how the GMs are employed and how the relation between EDP and IM is derived, as discussed below:

(i) Probabilistic Seismic Demand Analysis

Probabilistic seismic demand analysis uses a set of GM records which are either left unmodified or all records are scaled by a constant factor if the unmodified records are not strong enough to induce the structural response level of interest in terms of EDP. The set of IM and their associated EDP values resulting from nonlinear dynamic analysis are sometimes referred to as a cloud, because they form an approximate ellipse when plotted (Baker and Cornell, 2006). While using the probabilistic seismic demand analysis, a parametric approach is adopted, where one assumes that the random variable EDP has some probability distribution. Generally, the choice of a distribution is made based on past experience and statistical tests exist to identify when a dataset is not well represented by the specified distribution (although with a small dataset it is difficult for such methods to confidently identify a lack of fit). Most studies assumed the EDP data to have lognormal distribution when conditioned on IM. Thus the relationship between the conditional mean of EDP and the IM is linear in log space, and the conditional dispersion of the EDP is constant. These often provide a reasonable estimate of the mean value of ln(EDP) over a small range, yielding the model as in Equation (2.2) where, A_{rc} and B_{rc} are constant coefficients to be estimated from the regression analysis on the cloud of PSDA data and e is a zero-mean random variable representing the remaining variability in ln(EDP) for a given IM. If e is assumed to have a constant variance for all IM values, then the lognormal standard deviation $\beta_{EDP|IM}$ (commonly referred to as the dispersion) of the simulation data can be estimated from the logarithmic correlation between the median value $\overline{EDP}$ and IM, as in Equation (2.2) where *edp* and *im* are the realisations of EDP and IM respectively, with subscript i for the i^{th} GM record. It is to be noted that the assumption of constant variance is reasonable over a small range of IM, but usually less appropriate for a wide range of IM. The demand fragility (i.e., the probability $P[\ ]$ that EDP exceeds any specified value on a given value *im* of IM) becomes a simple lognormal cumulative probability distribution function $\Phi()$ (Mackie and Stojadinovic, 2004b), as in Equation (2.3).

This formulation has been adopted in many studies like Nielson (2005); Zhang et al. (2008); Ramanathan (2012) etc. One such cloud representation, when the evaluated EDP data is plotted against the IM values, is shown in Figure 2.2(a), as obtained by Baker and Cornell (2006) in their study for the maximum interstorey drift ratio (adopted as the EDP)

against S_a (0.8s) (spectral acceleration at T_N of 0.8s) (taken as the IM) in their study. However, this widely used model is not necessarily the only one to express the demand.

(ii) Incremental Dynamic Analysis – Also known as the scaling approach, the GMs are scaled to selective IM levels corresponding to prescribed seismic hazard and analysis is performed at different hazard levels (Zhang et al. 2008). The resulting plot of EDP versus IM when all the GMs are scaled to a particular IM value looks like a stripe. When the procedure is repeated over a range of IM values, multiple stripes of data are obtained, which together are termed an incremental dynamic analysis (Vamvatsikos, 2002). One such data of multiple stripes is shown in Figure 2.2(b), as obtained by Baker and Cornell (2006) for the maximum interstorey drift ratio (adopted as the EDP) against S_a (0.8s) (taken as the IM) in their study.

$$\ln(\overline{EDP}) = \ln\left(A_{rc}\right) + B_{rc}\ln\left(IM\right) + e;$$

$$\beta_{EDP|IM} \cong \sqrt{\frac{\sum_{i=1}^{N}\left(\ln\left(edp_i\right) - \left(A_{rc} + B_{rc}\ln\left(im_i\right)\right)^2\right)}{n_{GM} - 2}} \tag{2.2}$$

$$P\left[EDP \geq edp \,|\, IM = im\right] = 1 - \Phi\left[\frac{\ln\left(edp\right) - \ln\left(\overline{EDP}\right)}{\beta_{EDP|IM}}\right]$$

$$= 1 - \int_0^{edp} \frac{1}{\sqrt{2\pi}\cdot\beta_{EDP|IM}\cdot edp}\cdot\exp\left[-\frac{[\ln(edp) - \ln(A_{rc}(im)^{B_{rc}})]^2}{2(\beta_{EDP|IM})^2}\right]\mathrm{d}(edp) \tag{2.3}$$

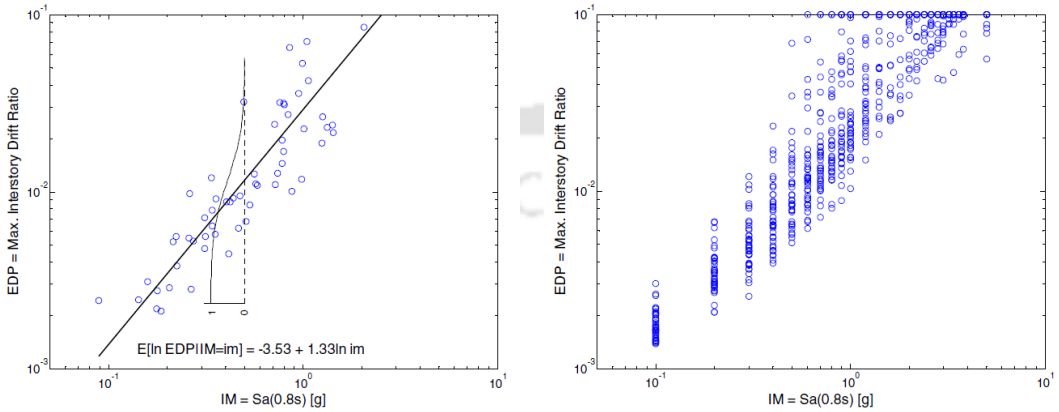

(a) (b)

Figure 2.2 EDP versus IM data (a) Cloud representation in probabilistic seismic demand analysis and (b) Stripe representation in incremental dynamic analysis (Baker and Cornell, 2006) (presented with permission granted by the first author).

While using incremental dynamic analysis, PSDM uses non-parametric approach which does not require assumptions about the distribution of the data (Lehmann and D'Abrera, 1998). This approach has the advantage being robust when the data do not fit a specified parametric distribution (Baker and Cornell, 2006). The occurrence ratio of a specified DS using the analysis can be computed and directly used as the damage probability at the given IM level, as the ratio of the number of damage cases over total number of simulation cases (Zhang et al., 2008), as in Equation (2.4).

$$P\left[EDP \geq edp \middle| IM\right] = \frac{\text{no. of damage cases}}{\text{total no. of simulation cases}} \tag{2.4}$$

In most cases, probabilistic seismic demand models generated employing incremental dynamic analysis can be fitted with a normal as well as lognormal cumulative probability distribution functions, as in Equations (2.5) and (2.6) where σ_{IM} and μ_{IM}; β_{IM} and λ_{IM} are standard deviations and mean of *IM* and ln(IM) values respectively required to reach a specified DS based on the normal and lognormal distributions respectively.

$$P\left[EDP \geq edp \middle| IM\right] = \int_{-\alpha}^{IM} \frac{1}{\sqrt{2\pi}\cdot\sigma_{IM}} \cdot \exp\left[-\frac{(im-\mu_{IM})^2}{2\sigma_{IM}^2}\right] \mathrm{d}(im) \tag{2.5}$$

$$P\left[EDP \geq edp \middle| IM\right] = 1 - \int_{0}^{IM} \frac{1}{\sqrt{2\pi}\cdot\beta_{IM}\cdot im} \cdot \exp\left\{-\frac{\left[\ln(im)-\lambda_{IM}\right]^2}{2\beta_{IM}^2}\right\} \mathrm{d}(im) \tag{2.6}$$

Unlike probabilistic seismic demand analysis, in incremental dynamic analysis, σ_{IM} is usually not constant over the range of IMs and also the mean value of ln(EDP) is not a linear function of ln(IM). Its advantage over probabilistic seismic demand analysis is that it is a direct method if response at only a single IM level is of interest. However, if the response estimates are needed at many IMs, incremental dynamic analysis potentially requires more structural analyses than the cloud approach (Baker and Cornell, 2006). Incremental dynamic analysis has been used by AmiriHormozaki et al. (2014), Tehrani and Mitchell (2013), Mahmoudi (2015), Ghazali et al. (2019), Sangadji et al. (2017) etc.

Seismic fragility generation involves the convolution of demand and capacity models. FC can be derived using a closed form solution (conveniently for lognormal capacity and demand distributions) where, $\overline{D}$ and $\overline{C}$ denote the median values and $\beta_{D|IM}$ and βc denote the dispersions of demand and capacity *D* and *C* respectively. Thus the probability P_{LS} of exceedance of a particular LS, i.e., when the corresponding capacity is less than/equal to

the imposed demand $D = d$ at $IM = im$, can be expressed in Equation (2.7) (Cornell et al., 2002) as,

$$P_{LS} = P[D \geq C \,|\, IM] = P[C \leq D \,|\, D = d]P[D = d] \tag{2.7}$$

Assuming lognormal distribution for both the demand and capacity, we have the expression for P_{LS}, as in Equation (2.8). P_{LS} can be obtained in terms of IM by employing Equation (2.1) to obtain the relation between $\overline{D}$ and $\overline{C}$ respectively with the corresponding IM values i.e., IM_D and IM_C causing them, as in Equation (2.9). Thereafter substituting Equation (2.9) in Equation (2.8), the final form of P_{LS} is shown in Equation (2.10) as,

$$P_{LS} = \Phi\left(\frac{\ln(d/\overline{C}}{\beta_C}\right)\left(1-\Phi\left(\frac{\ln(d/\overline{D})}{\beta_{D|IM}}\right)\right) = \Phi\left(\frac{\ln(\overline{D}/\overline{C})}{\sqrt{\beta_C^2+\beta_{D|IM}^2}}\right) \tag{2.8}$$

$$\ln(\overline{D}) = \ln(A_{rc}) + B_{rc}\ln(IM_D)\,; \quad \ln(\overline{C}) = \ln(A_{rc}) + B_{rc}\ln(IM_C) \tag{2.9}$$

$$P_{LS} = \Phi\left(\frac{\ln(IM_D)-\ln(IM_C)}{\frac{\sqrt{\beta_C^2+\beta_{D|IM}^2}}{B_{rc}}}\right) \tag{2.10}$$

Other than the regression analyses on the EDP-IM data to obtain the two parameter lognormal distribution of probabilistic seismic demand model, maximum likelihood method can be also used to estimate the parameters of lognormal probability distribution (i.e., the median and the log-standard deviation) describing the FCs. Maximum likelihood method was employed by Shinozuka et al. (2001), which was later adopted by Kim and Feng (2003); Banerjee and Shinozuka (2008); Yi et al. (2007). FCs can be constructed for any number of DSs where, for the j^{th} DS, c_j and ς_j are the median and log-standard deviation of the IM value corresponding FC, accompanied by goodness-of-fit-test. Shinozuka et al. (2001) estimated the FC parameters by integrating the DS information with that of the adopted IM within the fragility function $F_j()$ (Equation 2.11) and making use of maximum likelihood method. From FC definition and with the assumption that log-standard deviation is common to the FCs of all ranks as ς, one determines $P_{ij} = P(a_i, E_j)$, i.e., the probability that a BS sample will be in the DS E_j when subjected to IM (PGA as in Shinozuka et al., 2001) equal to a_i, as in Equation (2.11). The likelihood function $L()$, as in Equation (2.12), thereby estimates c_j and ς through a straightforward optimization algorithm, with x_{ij} is 1

if the DS E_j occurs in that bridge sample subjected to a_i and is 0 otherwise. The Equations (2.11) and (2.12) are expressed (in Shinozuka et al., 2001) as,

$$F_j\left(a_i;c_j;\varsigma_j\right)=\Phi\left[\frac{\ln\left(\frac{a_i}{c_j}\right)}{\varsigma_j}\right];\quad \begin{aligned} P_{i1}&=P\left(a_i,E_1\right)=1-F_1\left(a_i;c_1;\varsigma\right),\\ P_{i2}&=P\left(a_i,E_2\right)=F_1\left(a_i;c_1;\varsigma\right)-F_2\left(a_i;c_2;\varsigma\right),\\ P_{i3}&=P\left(a_i,E_3\right)=F_2\left(a_i;c_2;\varsigma\right)-F_3\left(a_i;c_3;\varsigma\right),\\ P_{i4}&=P\left(a_i,E_4\right)=F_3\left(a_i;c_3;\varsigma\right) \end{aligned} \tag{2.11}$$

$$L\left(c_1,c_2,c_3,\varsigma\right)=\prod_{i=1}^{n}\prod_{j=1}^{4}P_j\left(a_i,E_j\right)^{x_{ij}};\ \frac{\partial \ln L\left(c_1,c_2,c_3,\varsigma\right)}{\partial c_j}=\frac{\partial \ln L\left(c_1,c_2,c_3,\varsigma\right)}{\partial \varsigma}=0 \tag{2.12}$$

2.5.3 Capacity Spectrum Method

Since, the FCs developed using nonlinear dynamic analysis require a lot of computational effort, as an alternative, many researchers preferred and adopted a simpler and more practice-oriented nonlinear static analysis procedure in the form of the capacity spectrum method. The method was developed in 1970s for seismic vulnerability of buildings and is used to find a correlation between earthquake GM and building performance (Freeman, 1998). This method has been extended for fragility analysis of bridges by many researchers (Shinozuka et al., 2001; Bignell et al., 2005; Ballard and Sedarat, 1999; Cardone et al., 2007; Moschonas et al., 2009; Chang et al., 2008; Mohtashami and Shooshtari, 2013; Casarotti and Pinho, 2007). It basically identifies the structural performance by superimposing the seismic demand spectrum onto the capacity spectrum of the structure and locating the performance point as discussed below:

(a) Capacity Spectrum

Capacity spectrum or the capacity diagram is the equivalent Single degree-of-freedom representation of the capacity curve of the multi degree-of-freedom structure, obtained by transforming it into spectral acceleration-displacement response spectrum co-ordinates. Capacity curve, more specifically the pushover curve represents the variation of the total base shear of this structure with the displacement at the control node within the structure. Thereby, capacity spectrum is modeled using participation factor for the vibrating mode of the multi degree-of-freedom structure and the modal mass of the equivalent single degree-of-freedom system (Chopra and Goel, 1999).

Capacity curve is derived from the nonlinear static analysis like pushover analysis in which the multi degree-of-freedom structure is subjected to monotonically increasing lateral forces or displacements at the nodes with an invariant distribution until the structure

reaches a predetermined target displacement or collapse. However, this invariant load pattern might fail to keep track of the structure's dynamic characteristics change after the formation of the first local plastic mechanism. Consequently, it cannot account for damage accumulation and resulting modification of the modal parameters, which might considerably affect the response characteristics of a given structure. An improved version of pushover analysis in the form of modal pushover analysis procedure was developed by Chopra and Goel (2002), which resulted in improved accuracy in the estimation of seismic response of structures with higher mode effects. However, it still retained the application of the invariant force distribution. Nevertheless, the conventional pushover analysis has been employed by Shinozuka et al. (2001) and Moschonas et al. (2009), while generating the FCs through capacity spectrum method.

In order to overcome the limitations of conventional pushover analysis, an enhanced version referred to as adaptive pushover analysis, where the load vectors are progressively updated to consider the change in system modal attributes during inelastic phase, is developed, with different variants by Gupta and Kunnath (2000); Elnashai (2001) and Antoniou and Pinho (2004a), (2004b). Thus, the time-variant distributions of inertia forces are more closely followed up leading to conceptually more correct results. It accounts for both higher mode contributions as well as alteration of the local resistance and modal characteristics of the structure, as induced by the progressive accumulation of damage. Site- or record-specific spectral shapes can also be explicitly considered in the scaling of forces, so as to account for the dynamic amplification that expected GM might have on the different vibration modes of the structure (Pinho et al., 2005). The adaptive pushover analysis algorithm by Antoniou and Pinho (2004a) adapts the load (force vector) to be applied to the structure at each analysis step by carrying out the eigenvalue analysis considering the instantaneous nonlinear structural stiffness and the mass matrix. However, despite the apparent superiority, the force-based adaptive pushover procedure provides a relatively minor advantage over its traditional counterpart, particularly the estimation of deformation patterns of buildings, which are poorly predicted by both types of analyses. Antoniou and Pinho (2004b) argued that application of displacements, rather than forces, in an adaptive fashion, with the possibility of updating the displacement loading pattern according to the structural properties of the model at each step of the analysis, can be a conceptually appealing nonlinear static analysis tool. The study showed Displacement-based Adaptive Pushover Analysis (DAPA) technique to comparatively provide greatly improved predictions, throughout the deformation range, of the dynamic responses for

different types of structures. DAPA procedure features the best overall behaviour, despite the slight under prediction of the deformed shape values, with the lowest values of scatter. Recently, DAPA was extended for a preliminary verification of the assessment of a series of concrete bridge configurations by Casarotti and Pinho (2007) and the responses were found to be in a very good agreement in the majority of cases with those obtained by the nonlinear dynamic analysis.

Within adaptive pushover analysis perspective, Casarotti and Pinho (2007) revised capacity spectrum as adaptive capacity spectrum, which features two types of "adaptiveness". Firstly the pushover analysis algorithm is fully adaptive and secondly the 'equivalent single degree-of-freedom adaptive capacity curve' is derived step-by-step by calculating the equivalent single degree-of-freedom displacement $S_{d,k}$ and acceleration $S_{a,k}$ based on the actual deformed shape at each analysis step k till BS failure, with the expressions in Equation (2.13) as,

$$S_{d,k} = \frac{\sum_i m_{i,k} y_{i,k}^2}{\sum_i m_{i,k} y_{i,k}};\ S_{a,k} = \frac{F_{BS,k}}{g M_{BS,k}} \quad \text{and} \quad M_{BS,k} = \frac{\sum_i m_{i,k} y_{i,k}}{S_{d,k}} \tag{2.13}$$

where, $F_{BS,k}$ and $M_{BS,k}$ are the base shear and effective mass of BS, and $m_{i,k}$ and $y_{i,k}$ are the participating mass and displacement respectively of the i^{th} component.

This method, referred to as adaptive capacity spectrum method, was employed by Cardone et al. (2007) for generating the bridge FCs. Employing multimode adaptive capacity spectrum analysis for the integral bridges in their study, Mohtashami and Shooshtari (2013) concluded adaptive capacity spectrum method as a robust FC development tool.

(b) Seismic Demand Spectrum

Seismic demand in earthquake-resistant design is basically represented by strength, displacement, hysteretic or input energy spectrum (usually inelastic). These spectra not only depend on the characteristics of the expected GM at the site, but also on the nonlinear characteristics of the structural system (Vidic et al., 1994). Most studies have adopted inelastic strength and displacement spectra as the seismic demand spectra. Strength spectrum or the elastic pseudo-acceleration spectrum is the graphical variation of the elastic spectral acceleration S_{ae} with T_N of the structure and is transformed as acceleration-dislacement response spectrum by replacing T_N with the elastic spectral displacement S_{de} against the corresponding S_{ae} values using Equation (2.14).

To account for the inelastic structural behaviour, effective damping values are applied to the elastic response spectrum, resulting in damped linear elastic response spectrum. The damped response spectrum imitates inelastic response spectrum by relating the elastic damping ratios to the ductility ratios μ_{str} s (ratio between the maximum and the yield displacements of the structure) for various characteristics of hysteresis behaviour. Many researchers have adopted different forms of spectral reduction factors $R_{\mu,str}$ (the ratio of elastic strength demand to inelastic strength demand) representing the hysteresis energy dissipation of ductile structures for a specified μ_{str}, which is to be applied to the elastic response spectrum to obtain the inelastic response spectrum. For instance, in Newmark and Hall (1982), $R_{\mu,str}$ values of $1/\sqrt{2\mu_{str}-1}$ and $1/\mu_{str}$ in the constant acceleration and velocity portions respectively of the response spectrum are applied. For an inelastic Single degree-of-freedom system with bilinear force-deformation characteristics, Vidic et al. (1994) provided the $R_{\mu,str}$ values considering the characteristic period T_C of the GM typically defined as the transition period at the junction of constant acceleration (short period range) and the constant velocity (medium period range) segments of the spectrum, in Equation (2.15) with the expressions as,

$$S_{de} = S_{ae}\left(\frac{T_N}{2\pi}\right)^2;\quad S_a = \frac{S_{ae}}{R_{\mu,str}};\ S_d = \frac{\mu_{str} S_{de}}{R_{\mu,str}} \tag{2.14}$$

$$R_{\mu,str} = (\mu_{str}-1)\frac{T_N}{T_C}+1 \text{ for } T_N < T_C;\quad R_{\mu,str} = \mu_{str} \text{ for } T_N > T_C \tag{2.15}$$

To obtain the seismic demand spectrum in terms of overdamped response spectrum, Cardone et al. (2007) calculated the equivalent viscous damping for the bridge system (pier-deck assemblages) for each chosen Performance Level (PL) or DS based on the Jacobsen's equations (Equation 2.16), specialised to the actual mechanical behaviour of the bridge components (bearing and pier). In Equation (2.16), $\xi_{br,j}$ is the equivalent damping of the j^{th} bearing at its displacement and force levels $y_{br,PL}$ and $F_{br,PL}$ respectively due to the energy losses of E_{visc}, E_{hyst} and E_{fr} through viscous, hysteretic or frictional behaviour in a cycle of amplitude $y_{br,PL}$. $\xi_{pr,j}$ is the equivalent viscous damping (Kowalski et al., 1995) of the j^{th} pier with $\xi_{0,pr}$ and $\xi_{hyst,pr}$ as the elastic and hysteretic dampings respectively corresponding to μ_{pr} and the strain hardening ratio r.

$$\xi_{j,br} = \frac{E_{visc}+E_{hyst}+E_{fr}}{2\pi \cdot F_{br,PL}\cdot y_{br,PL}};\quad \xi_{j,pr} = \xi_{0,pr}+\xi_{hyst,pr} = 0.05+\frac{1}{\pi}\left(1-\frac{(1-r)}{\sqrt{\mu_{pr}}}-r\mu_{pr}\right) \tag{2.16}$$

Resultant damping $\xi_{bp,j}$ of j^{th} pier-bearing assemblage is computed by combining the damping of j^{th} bearing and pier in proportion to the respective displacements $y_{br,j}$ and $y_{pr,j}$, as in Equation (2.17). Finally the equivalent damping $\xi_{BS,PL}$ for BS is obtained by weighing the dampings of all the n_{bp} number of bearing-pier systems in proportion to the corresponding force levels, $F_{bp,j}$ with respect to the total base shear F_{BS} (Equation 2.17). Proper reduction factor $R_{\xi_{BS,PL}}$ is calculated based on $\xi_{BS,PL}$, with which the 5% damped normalised response spectrum is reduced to obtain the overdamped response spectrum, with the following general form, shown in Equation (2.17) as,

$$\xi_{bp,j} = \frac{\xi_{br,j} y_{br,j} + \xi_{pr,j} y_{pr,j}}{y_{br,j} + y_{pr,j}};\ \xi_{BS,PL} = \frac{\sum_{j=1}^{n_{bp}} \xi_{bp,j} F_{bp,j}}{\sum_{j=1}^{n_{bp}} F_{bp,j} (= F_{BS})};\ R_{\xi_{BS,PL}} = \sqrt{\frac{7}{2 + \xi_{BS,PL}}} \qquad (2.17)$$

(c) Performance Point

When capacity spectrum and seismic demand spectrum are superimposed on each other, the relationship between *D* and *C* is readily apparent. If the capacity curve can intersect and cross the demand envelope, the structure can survive the earthquake (Freeman, 1998). The graphical intersection of the two curves, i.e., the performance point determines the PL or DS of the structure for that earthquake, providing estimates of the inelastic acceleration and displacement demand on the structure. Determination of performance point requires iterations so as to match the ductilities at the this point obtained on the demand spectrum and the capacity spectrum within a given tolerance (Casarotti and Pinho, 2007). The iterative procedures can be found in details in ATC (1996). Performance point, determined graphically are depicted in Figures 2.3(a) and 2.3(b), as by capacity spectrum method in ATC (1996) and by adaptive capacity spectrum method developed by Casarotti and Pinho (2007) respectively. Though their purpose is the same, there are some essential differences between the two, as pinpointed by Kappos et al. (2012). Capacity spectrum method (essentially applied to buildings) uses code-mandated damped elastic or inelastic acceleration-displacement response spectrum and the forced based conventional pushover curve considering elastic mode shapes or assumed deformed shapes and the capacity curve is derived based on the displacement of the reference node. Adaptive capacity spectrum method (developed with bridge application in mind, though can be applied to buildings as well) uses elastic overdamped response spectrum, either code-defined or site-specific and uses the more reliable displacement based adaptive pushover curves. The single degree-of-

freedom capacity curve is calculated step by step based on the actual deformed pattern without reference to any predefined shapes and not built on the displacement of a specific physical location.

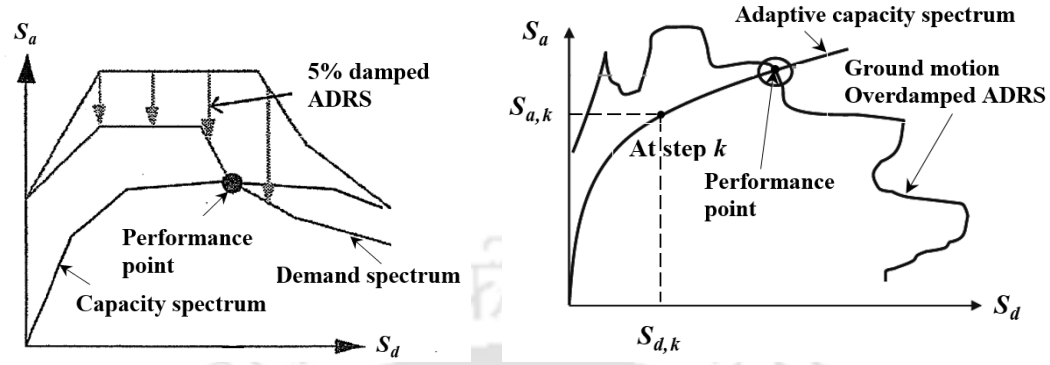

(a) (b)

Figure 2.3 Determination of the performance point using (a) ATC (1996) and (b) Casarotti and Pinho (2007).

(d) Derivation of Fragility Curves using Capacity Spectrum Method

Employing capacity spectrum method, FC can be generated by two ways:

(1) The first method follows the usual procedure of determining the performance point of the structure under a predefined seismic IM (for e.g., a given PGA) by an iterative procedure based on bilinear idealisation of either the conventional capacity spectrum or the adaptive capacity spectrum. To account for uncertainties (Subsection 2.4.4), in earthquake and structural parameters, the mean and mean ± standard deviation seismic demand spectrum can be generated considering a suite of GM histories (sorted by the IM specific to the purpose) and bridge samples respectively. Then the capacity spectrum constructed for each bridge sample is merged with the mean and mean ± standard deviation demand spectra for a particular IM value (Shinozuka et al., 2001). Hence three performance points with three corresponding spectral displacements $\overline{S_a(a)}$ and $\overline{S_a(a)} \pm \sigma_d(a)$ are defined for each bridge sample for an IM value of a, which are a function of a since the demand spectrum from which these are evaluated, depend on the GM histories sorted by a. The two parameters, median $c(a)$ and standard deviation $\zeta(a)$ of the lognormal distribution for the spectral displacement $S_d(a)$ can be obtained from Equation (2.18) as,

$$\overline{S_d(a)} = c(a)\exp[\{(a)\}^2/2]\,;\ \{\sigma_d(a))\}^2 = \{\overline{S_d(a)}\}^2[\exp(\{\zeta(a)\}^2)-1] \qquad (2.18)$$

Thereafter, the probability $P_j(a, d_l)$ that the sample bridge j will have a DS exceeding the limit displacement d_l is given by Equation (2.19). The fragility $F(a, d_l)$ against the IM value of a at the DS corresponding to d_l can be estimated by taking all bridge samples in that IM

group under consideration, shown in Equation (2.19) as,

$$P[S_d(a) \geq d_l\ ] = P_j(a, d_l) = 1 - \Phi\left[\frac{\ln(d_{l,j}/c_j)}{\zeta_j(a)}\right];\ F(a, d_1) = \frac{\sum_{j=1} P_j(a, d_l)}{j} \qquad (2.19)$$

(2) The second method, developed by Cardone et al. (2007) is described by Kappos et al. (2012) as the inverse application of the adaptive capacity spectrum method (IACSM). The method evaluates the seismic IM values of the expected GMs, corresponding to the pre-determined DSs of the structure, identified by given performance points or PLs on the capacity curve of the bridge. With the performance points fixed, the associated viscous damping ratios for the bridge components can also be evaluated, if the inelastic deformed shapes of the bridge corresponding to the respective PLs are already known. Hence, this method is only applicable in case of adaptive capacity spectrum method, where the inelastic deformed shapes are simultaneously evaluated at the analysis steps. Hence, compared to the first method, it is not iterative and does not require bi-linearisation of the capacity curve. By properly combining the damping contributions of the bridge components, $\xi_{BS,PL}$ can be directly evaluated and the corresponding seismic demand spectrum is obtained from the 5% damped elastic response spectrum using a proper reduction factor based on $\xi_{BS,PL}$. IM value associated to each PL, e.g., PGA_{PL} can be calculated analytically as the ratio between the acceleration on the capacity curve $S_{a,PL}$ with respect to that PL ($S_{d,PL}$ being the correposnding spectral displacement) and the normalised spectral acceleration $S_{a1}(T_{PL}, \xi_{BS,PL})$ at the effective period of vibration T_{PL} and $\xi_{BS,PL}$, in Equation (2.20) as,

$$PGA_{PL} = \frac{S_{a,PL}}{S_{a1}(T_{PL}, \xi_{PL})/PGA_{PL}}\ ;\ T_{PL} = 2\pi\sqrt{\frac{S_{d,PL}}{g \cdot S_{a,PL}}} \qquad (2.20)$$

IM value associated with each PL, can be evaluated graphically by properly translating the overdamped normalised response spectrum to intercept the adaptive capacity spectrum in the selected PL (Figure 2.4a). IM value evaluated against the given PL, represents the median threshold value of the associated GM. Starting from these values, a series of FCs can be developed, one for each PL. FC is expressed by a standard lognormal cumulative probability function Φ, as in Equation (2.21) where, the left hand side represents the DS probability being equal to or exceeding the selected PL for a given PGA value. PGA_{PL} is the median threshold value of PGA associated with the DS and β_t is the total lognormal standard deviation which takes into account the uncertainties related to the input GM, bridge response, etc. FC evaluated for a particular PL is shown in Figure 2.4(b).

$$P\left(DS \geq PL \middle| PGA\right) = \Phi\left[\frac{1}{\beta_t} \ln\left(\frac{PGA}{PGA_{PL}}\right)\right] \tag{2.21}$$

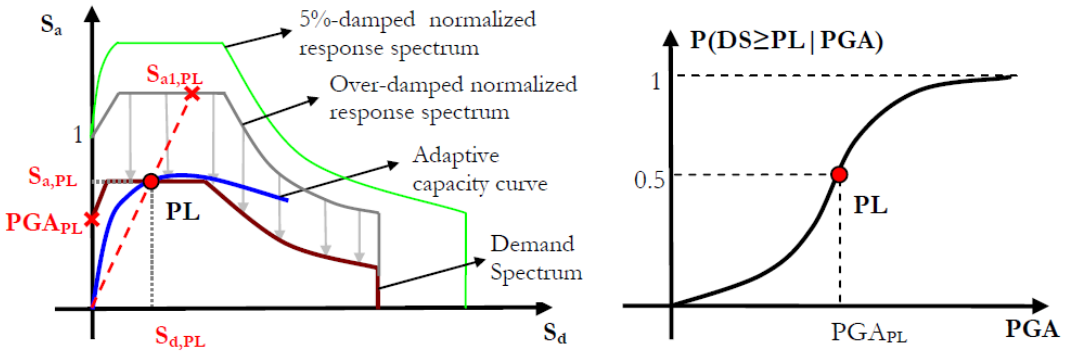

(a) (b)

Figure 2.4 (a) Evaluation of PGA and (b) FC for a given PL (Cardone et al., 2007).

2.6 SYSTEM FRAGILITY CURVE

Although the component level FCs give indication of the most vulnerable components in BS, the general assessment of vulnerability for the BS must be made by combining the effects of its various components. In fact, often the BS vulnerability is strongly affected by the coupling between simultaneously developing damage modes in different components (Taskari and Sextos, 2015) and therefore is controlled by different components at different DSs. Therefore, it is necessary to combine the FCs for the components into a FC for the entire bridge (Tavares et al., 2012). Nielson and DesRoches (2007) found BS to be more fragile than any of the individual components, ignoring the fragility contributions of which can lead to a misrepresentation of the overall BS fragility and can result in errors as large as 50% at higher DSs. Hence the logical step that succeeds the determination of component fragilities is to integrate these to enable the macroscopic view of the overall bridge as a system (Ramanathan et al., 2011).

BS fragility can be derived based on functionality or repair cost after earthquakes (Mackie and Stojadinovic, 2005) or be generated as a union of the component level fragilities using a joint PSDM (Nielson, 2005). BS can be assumed as a series as well as a parallel combination of the individual components (Zhang and Huo, 2009) and many studies evaluated the BS fragilities considering either of the assumptions.

The series approximation for BS assumes that a given BS DS is achieved if any component *X* or component *Y* exhibits the associated level of damage, i.e. if at least one bridge component achieves a particular DS, the overall BS is deemed to achieve that level

of damage (Tavares et al., 2012). The probability that the BS is at or beyond a particular DS, i.e., P_{BS} is the union of the probabilities of each of the n_c number of components exceeding the same DS, i.e., $P_{c,i}$ and the global DS (DS_{BS}) is dictated by the largest one of the DS*s* at the component level ($DS_{c,i}$ s), as in Equation (2.22). The lower and upper bounds of P_{BS} for a serial system (Equation 2.23) correspond to completely correlated components and uncorrelated components respectively. The expressions are shown as,

$$P_{BS} = \bigcup_{i=1}^{n_c} P_{c,i} \; ; \quad DS_{BS} = \max(DS_{c,1}, DS_{c,2}, ..., DS_{c,n_c} \tag{2.22}$$

$$\max_{i=1}[P_{c,i}] \le P_{BS} \le 1 - \prod_{i=1}^{n_c}[1 - P_{c,i}] \tag{2.23}$$

On the other hand, if a BS is assumed as a parallel system, then it will reach a specific all the components have reached that DS. The failure probability is computed as the intersection of component probabilities and DS_{BS} is dictated by the smallest DS at component level (Equation 2.24). The lower and upper bounds (Equation 2.25), corresponds to independent components and completely correlated components respectively. The expressions are obtained as,

$$P_{BS} = \bigcap_{i=1}^{n_c} P_{c,i} \; ; \quad DS_{BS} = \min(DS_{c,1}, DS_{c,2}, ..., DS_{c,n_c}) \tag{2.24}$$

$$\prod_{i=1}^{n_c} P_{c,i} \le P_{BS} \le \min[P_{c,i}] \tag{2.25}$$

These bounds are often very wide, which imply the significance of correlation between the components. In reality, a BS is neither a parallel nor a serial system and the responses of the components are often correlated with each other to some extent. Thus, the global DS is located in between these limits. The first-order bounds which assume either the total correlation or complete independence between the components, is thus not able to provide an accurate estimation of the failure probability of the BS. Nevertheless, first order bounds considering the series systems was adopted by Choi et al. (2004) and found that the lower bound representing with fully stochastically dependent components provides unconservative estimate for the fragilities of the considered bridges. Similarly, the upper bound assumes that the components are all statistically independent and was found to provide a conservative BS fragility estimate. As the difference between the bounds decreases, the upper bound estimate of the BS fragility becomes more appropriate. To account for seismic risk from multiple failure modes, second-order reliability was adopted by Pan et al. (2007) where some correlation was evaluated and found to yield narrower

bounds than the commonly used first-order reliability method, thereby a single estimate for the second order fragility could be approximately obtained. Since, the evaluation of the joint probability of more than two events is computationally difficult, those approximate bounds have been proposed as an alternative to the more computationally demanding Monte-Carlo simulation to get the system FC.

For including the effects of multiple bridge components, Nielson (2005) attempted the BS fragility estimation through the development of a joint probabilistic seismic demand model, which can be obtained using Monte Carlo or any other numerical simulation. This approach recognises some level of correlation to exist between the D_is placed on the various n_c number of bridge components during a given earthquake (i =1 to n_c), incorporation of which is important for fragility analysis when a vector of EDPs is utilised. Thus, demand on BS is simply the joint demand on the components. If $\underline{D} = (D_1, D_2, ..., D_{n_c})$ represents the vector of the demands, then the vector $\underline{D^T} = \ln \underline{D}$ represents the vector of component demands in the transformed lognormal space. Since, the marginal component demands D_is are lognormally distributed, the transformed demands D_i^T are normally distributed in the transformed space. Joint probabilistic seismic demand model is formulated in this space by assembling the vector of means of the transformed demands and the covariance matrix. Covariance matrix considers the correlation coefficients between ln(D_i)s and not D_is. Correlation coefficients between the component demands are obtained by using the results of nonlinear time history analysis and the resulting covariance matrix is then assembled. A Monte Carlo simulation is used to compare the realisations of D_is (from conditional joint normal distribution in the transformed space) and statistically independent component capacities to calculate P_{BS}. Samples are drawn from the damage and capacity models and the probability of D exceeding C is evaluated for an IM value and the procedure is repeated for increasing IM values. Regression analysis is used to estimate the median c_i and dispersion ς_i of the IM for the i^{th} DS characterising the BS fragility (Ramanathan, 2012) using Equation (2.26) as,

$$P[DS_i \text{ or greater } | IM] = \Phi\left[\frac{\ln(IM) - \ln(c_i)}{\varsigma_i}\right] \tag{2.26}$$

The proposed FC methodology thus eliminates the need to rely on BS fragility bounds and their associated restrictions. It should be noted that the specifics on its application will vary depending on the type of bridge being considered (Nielson and DesRoches, 2007).

Though the above researches have suggested some methodologies for the BS fragility evaluation, however, the component fragilities should be combined in such a way that they have similar consequences at the BS level in terms of functionality and repair consequences (Nielson, 2005; Ramanathan, 2012). The major challenge lies in being able to group components that have similar consequences at the BS level in terms of functionality and repair consequences. In order to be able to address the aforementioned concerns, two classes of components viz., primary and secondary were proposed by Ramanathan (2012). Primary components are defined as those that affect the vertical stability and load carrying capacity of the bridge. Extensive or complete damage to these components might lead to closure of the bridge. Column damage and deck unseating belong to this category. Secondary components may be defined as the ones that do not affect the vertical stability of the bridge, failure of these components will only lead to restrictions on the travel speed and traffic conditions on the bridge and will not force closure of the bridge, e.g., shear key, abutment. Thus, the primary components contribute to all the BS DSs, while secondary components contribute to the initial BS DSs. Following this principle, contribution of the component-level DSs, as assigned to the BS DSs by Zakeri et al. (2014) are presented in Table 2.37. The BS FCs were derived considering the correlations between components as shown in Equation (2.27) (Zakeri et al., 2014) where, $n_{c\text{-}p}$ and $n_{c\text{-}s}$ are the total number of primary and secondary components respectively and j is 1, 2, 3, 4 corresponding to the slight, moderate, extensive, and complete DSs, respectively. Here the probability of exceeding the BS j^{th} DS, $P[DS_j|IM]$ is typically computed as the probability of the union of events $E_j[DS_j|IM]$ in which the i^{th} bridge component reaches or exceeds j^{th} DS.

In the study by Zhang and Huo (2009), BS DS is defined as composite behaviour of the component DSs while assigning weighing ratios to the individual component DSs, based on the relative importance for load carrying and the repairing cost. The component, costing more to be repaired hence should carry more weight. This study considers weighting ratios of 0.75 and 0.25 to piers and isolation devices respectively for the corresponding DSs as DS_{pr} and DS_{iso}, as in Equation (2.28). However, since either excessive bearing displacement or column collapse damage ($DS = 4$) can result in the collapse of a single span or the entire bridge, a serial mechanism is therefore adopted for the collapse damage.

Mackie and Stojadinovic (2005) proposed a new system of bridge-level performance objectives based on loss of bridge performance in terms of traffic load carrying capacity, loss of lateral and vertical load capacity, as in Table 2.38.

Table 2.37 Assignment of component level damage with BS damage state (Zakeri et al., 2014)

Limit state	Component-level limit state		System-level limit state
	Primary component	Secondary component	
Slight	DS1	DS2	DS1
Moderate	DS2	DS3	DS2
Extensive	DS3	DS4	DS3
Complete	DS4	N/A	DS4

$$P[DS_j \mid IM] = \begin{cases} P[\bigcup_{i=1}^{n_{c-p}} E_{primary\_i}(DC_j \mid IM)]\ ;\ j = 4 \\ P[\bigcup_{i=1}^{n_{c-p}} E_{primary\_i}(DC_j \mid IM)] + \\ \qquad\qquad ;\ j \le 3 \\ P[\bigcup_{i=1}^{n_{c-s}} E_{secondary\_i}(DC_{j+1} \mid IM)] \end{cases} \tag{2.27}$$

$$DS_{BS} = \begin{cases} \text{int}(0.75DS_{pr} + 0.25DS_{iso}) \\ 4 \end{cases} ; \quad \begin{matrix} DS_{pr}\ ,\ DS_{iso} < 4 \\ DS_{pr} \text{ or } DS_{iso} = 4 \end{matrix} \tag{2.28}$$

Table 2.38 Proposed performance levels using bridge-level damage variables (Mackie and Stojadinovic, 2005)

Objective name	Traffic capacity remaining (volume)	Loss of lateral load carrying capacity	Loss of vertical load carrying capacity
Immediate access	100%	< 2%	< 5%
Weight restriction	75%	< 2%	< 10%
1 lane open only	50%	< 5%	< 25%
Emergency access only	25%	< 20%	< 50%
Closed	0%	> 20%	> 50%

2.7 GAP AREAS

- Although there are numerous studies on fragility evaluation of different bridge types and configurations, work on IABs is limited to its seismic performance like Sritharan et al. (2005); Frosch et al. (2009); Burke Jr. (2009). Only a few studies have focused on estimating the fragility of IABs like Zakeri et al. (2013); Ramanathan (2012); Choine et al. (2014) etc.
- Though some work has been done on the seismic vulnerability assessment for buildings, almost no work for BSs in India has been carried out till now. Although a study exists on fragility evaluation of simply supported multispan bridges on steel bearings specific

to Northern India by Parool and Rai (2015), so far no study has been carried out on seismic vulnerability of IAB configuration.

- Most of the studies have evaluated the fragilities pertaining to the particular bridge inventories of the respective areas or regions, with given bridge characteristic properties. Such FCs are structure specific and are generally not applicable to BSs over wide variations in geometry, design detailing and material properties.
- Soil-structure interaction being imminent in case of bridge founded on soft soils, precise estimations of damages, the respective LSTs and thus fragilities call for detailed modeling and analysis of bridge-foundation-soil system. These requirements have been incorporated in very few studies like Ledezma (2007); Bradley et al. (2010); Brandenberg et al. (2011); Kwon and Elnashai (2010); Aygun et al. (2011); Padgett et al. (2013); Wang et al. (2013) etc. Hence, PSS LSTs are prescribed only in very few studies while accounting for soil-structure interaction. Thus, in case of IABs where soil-structure interaction is significantly influential, variation in geotechnical parameters poses additional incongruity, which had not been accounted for.
- No generalised forms for LSTs for bridge components exist, except a few attempted studies like Stefanidou and Kappos (2017). Hence, inconsistencies exist in case of adoption of Limit States (LSs) of the bridge components, as these are case-specific being based on particular properties of the components in the respective studies; however, application of such case-specific LS results to another study with different component parameters might lead to erroneous fragility estimates.
- Most of the studies while evaluating PSDMs have used the popular power law model based on assumption of lognormal distribution for demand and capacity. However, in reality, distributions for capacities and demands are not always truly lognormal. Studies with fragility formulation considering arbitrary distributions for structural seismic capacities and demands are lacking in literature.
- Very few studies like those by Nielson (2005) and Ramanathan (2012) have attempted to evaluate BS fragilities considering correlations among the component demands. The BS fragility formulation in those studies is again based on the assumption of lognormal distribution. Hence, studies assessing BS fragilities considering arbitrary distributions have not been carried out.

- Very few studies like Cardone et al. (2007) have carried out fragility analysis considering adaptive capacity spectrum method. Most of the studies have employed different forms of nonlinear time history analysis, which are computationally demanding. Adaptive capacity spectrum method though relatively simpler, can be a more practical approach to fragility generation, without sacrificing the accuracy in the fragility estimates.
- Very few studies like Mackie and Stojadinovic (2004b) and Ramanathan (2012) have investigated the optimality of IMs in the fragility formulations. Studies considering particular bridge configurations should also investigate which IMs are more optimal for the adopted ones, other than PGA, which is commonly adopted in most of the studies.

2.8 SCOPE OF PRESENT WORK

- Since work on seismic fragility of bridges in India is scanty, particularly with absence of any study exclusively on IABs, seismic fragility assessment of an IAB, any existing one or some hypothetical form, can to be carried out.
- Wide ranges of practical variations in geometric, structural detailing and structural as well as geotechnical material parameters can be incorporated for identifying the influential parameters regarding the performance of IABs as well as creating sub-bins and investigating the comparative vulnerabilities.
- Damage models for the individual components can be developed, incorporating different failure modes as well as soil-structure interaction, so as to able to evaluate the DS LSTs specific to particular set of parameters and over wide ranges of the respective parameters. Subsequently, generalised expression, i.e., the relationship among the LST and the parameters can be developed employing the LST data onbtained through the analyses of the damage models over wide ranges of parametric variations. Those expressions, when well validated, can be directly applied to evaluate the expected LST values for any set of parameters within the adopted ranges without analysis repetition each time, rather than past case-specific ones.
- Computation of component fragilities can be carried out with a different approach, which will be applicable for arbitrary distributions for seismic capacities and seismic demands than adopting the traditional lognormal formulation and likewise at BS level.
- Component fragilities can be evaluated by carried out adaptive capacity spectrum method, which is considered as an efficient alternative to nonlinear time history analysis.

The assessed demand and the fragility estimates can be compared with those obtained using nonlinear time history analysis to examine the suitability of its applicability.

- Optimality of various IMs can be explored. For instance, in a study considering IAB configuration, suitability of other available IMs like S_a, PGV, peak ground displacement etc., other than PGA can be investigated.

Chapter 3

ATTRIBUTES AND NUMERICAL MODELING OF THE ADOPTED BRIDGE CLASS

CONTENTS

3.1 INTRODUCTION

Every bridge has its own structural attributes leading to its unique seismic behaviour. Nonetheless, bridges do have some characteristics (like number of spans, type of superstructure and substructure, skew etc.) similar in some aspects. Consequently, it is possible to classify bridges into some groups based on their similar structural properties and thus with expected similar seismic behaviour to arrive at the common sets of FCs. Organising the bridge population into different bridge classes through various bridge classification methods paves the way for evaluating the seismic vulnerability with respect to a given class. This study deals with the seismic vulnerability evaluation of a particular class of IABs resulting in FCs specific to the adopted class.

3.2 DESCRIPTION AND ATTRIBUTES OF THE ADOPTED BRIDGE CLASS

An IAB typology corresponds to bridge superstructure without any movable joint (thus eliminating significant post construction maintenance problems) between the spans and between the span and the abutment. Bearings may or may not be present at the abutment, based on which IAB has two variants, namely (a) full and (b) semi IAB. In full IAB, the superstructure is directly connected to the substructure such that during lateral movements, they move together into and away from the backfill. In semi IAB, only the backwall portion of substructure is directly connected with the superstructure and the beams rest on bearings

placed on a stationary abutment stem (White, 2007).

With respect to the IAB typology, the present study adopts the continuous configuration with an aim to study all the major components as in a conventional bridge and thus not avoiding bearing unlike the full integral configuration. Thus, the study works around three span continuous cast-in-situ reinforced concrete deck – precast prestressed I-girder bridges, supported intermediately on reinforced concrete bents through elastomeric bearings and fully integral abutments at the ends with compacted dense sand as the backfill. Foundations below each pier and backwall consist of a group and a row respectively of fixed head reinforced concrete square piles on loose sandy soil. Typical elevations in the longitudinal and transverse directions are shown in Figures. 3.1 and 3.2 respectively

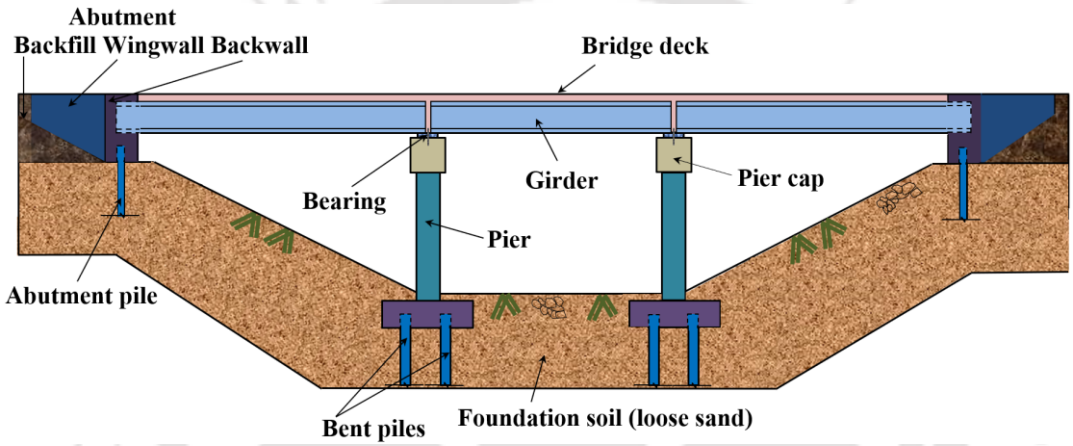

Figure 3.1 Typical configuration (elevation in the bridge longitudinal direction) of the multispan continuous integral abutment bridge adopted in the study.

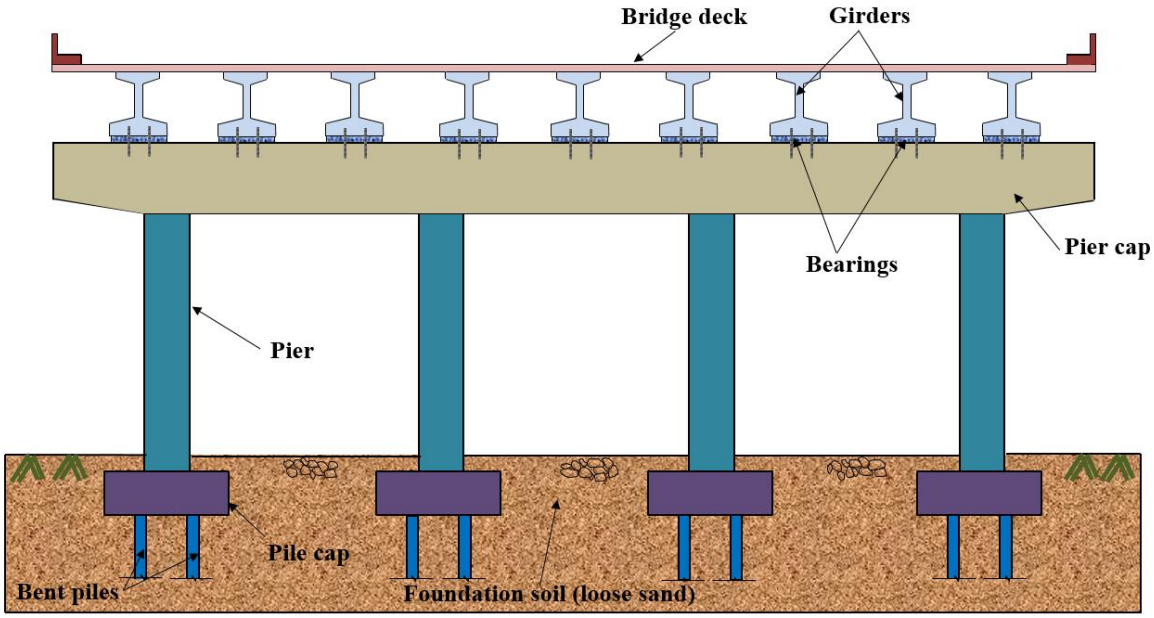

Figure 3.2 Typical configuration (elevation in the bridge transverse direction) of the multispan continuous integral abutment bridge adopted in the study.

The seismic design philosophy for the adopted bridge involves possibility of plastic hinges in piers as well as abutment-piles and pier-piles during severe earthquake shaking Abutment elements like backwall and wingwall are to be designed to resist the immediately mobilised backfill soil pressure, as the bridge moves under seismic loading and the bearing elements to undergo inelastic deformations. The attributes of the various components are described in the sections as below:

3.2.1 Bridge Superstructure

The study considers precast prestressed concrete (being the predominant form for beams in IABs, as per the European Survey reported in White 2007) I-girder with cast in situ concrete deck. In case of prestressed/precast concrete fully IABs (referred to as simply IABs hereafter), the maximum individual value of the span length L_{sp} can range from 60-200m according to the USA agencies' report mentioned in White (2007), which also listed the range of the maximum allowable total bridge length to be 150-1175m. Hence the number of spans n_{sp}s for IABs can be interpreted to be varying from three to six in general. Span lengths L_{sp}s adopted for cast-in-situ slab supported on precast prestressed girders generally range between 20m to 40m according to Kumar and Babu (2016) while Priestley et al. (1996) recommends L_{sp} of 12-35m. As mentioned in Avsar (2009), the feasible length of an I-girder is limited to 40m or less.

Superstructure depth D_{ss} and I-girder depth D_g (which becomes the deck thickness T_d when deducted from D_{ss}) are evaluated based on D_{ss}/L_{sp}. For prestressed/precast girder, D_{ss}/L_{sp} is usually kept as 0.05 for simply supported and 0.04 for continuous spans, as per Kumar and Babu (2016) while as per Ramanathan (2012), the permissible D_{ss}/L_{sp} is 0.05 for multispan continuous concrete I-girder bridges. They also recommend the girder spacing as 2 to 3m and $1.5D_{ss}$ respectively. Number of girders n_g is based on the deck width W_d, girder spacing and the deck overhang length L_{oh}, with W_{tf} as the I-girder top flange width). The expression for L_{oh}, as adopted from DOT, Minnesota, is mentioned as,

$$6\text{inches} \leq L_{oh} \leq \text{smallest of } \{D_g, 40\% \text{ of girder spacing}, 32\text{inches}+0.5W_{tf}\} \quad (3.1)$$

3.2.2 Bearing

At the bent locations, the superstructure is supported on elastomeric bearings, being typical of concrete girder bridges (Zakeri et al., 2014). The elastomeric bearing in the study is one of a fixed type consisting of a rubber pad with two reinforcing bars of Grade Fe-415 (IRC 2011) passing through it. While utilising prestressed concrete girders that bear on elastomeric pad, a diaphragm is placed between the ends of the girders (Comisu, 2005) and

the pad is placed centrally below it (depicted in the bridge longitudinal direction, as in Figure 3.3(a). Bars while passing through it are embedded into the cap beam at one end and loosely inserted into the underside of the diaphragm at the other end (typical arrangements in both the bridge longitudinal (*L*) and transverse (*T*) directions are depicted in Figures 3.3(a) and 3.3(b) respectively.

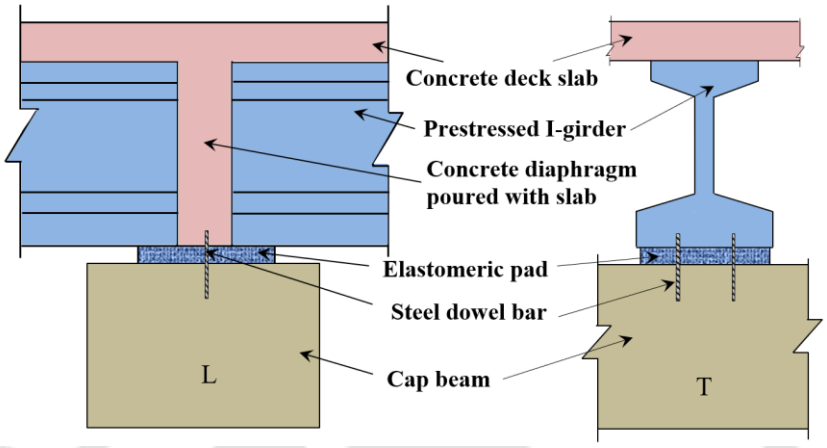

(a) (b)

Figure 3.3 Arrangements of bearing in (a) longitudinal and (b) transverse directions.

Rubber bearings are considered to be axial and rotationally rigid (Stanton and Roedar 1982), while comparatively flexible in shear. Bottom surface of the pad being in contact with the top surface of the concrete cap beam, the bearing transfers a proportion of the shear force through friction along the rubber-concrete interface until the pad ultimate friction force capacity $F_{u,brp}$ is exceeded. With the loss of grip on the interface, the pad slips along the interface (Figure 3.4(a)) indefinitely till it topples about the cap beam edge and falls off. However, it will be held in place by the dowel bars until the seismic force is strong enough to cause the bars to fracture against the ultimate flexural force capacity $F_{u,brd}$ (Figure 3.4(b)). The constituents work in parallel, for case in point, with a resisting force ($F_{u,brp}$ + $F_{u,brd}$) (Figure 3.4(c)) at the instant of sliding.

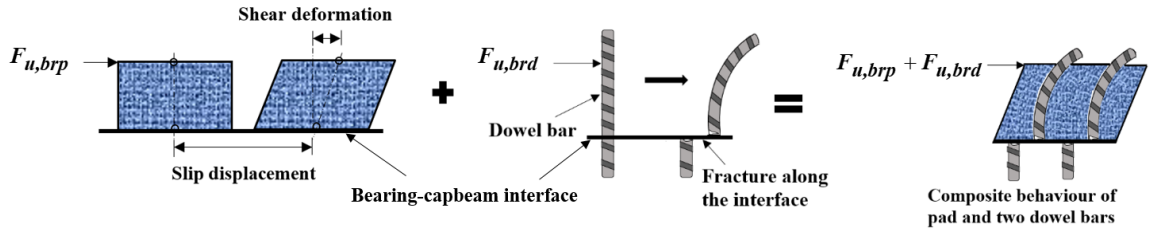

(a) (b) (c)

Figure 3.4 Seismic behaviour of (a) pad, (b) dowel bar and (c) bearing assembly.

(a) Lateral load resisting mechanism of the rubber pad

Under lateral loading, the pad undergoes shear deformation $y_{brp,sh}$ till the ultimate value

Under lateral loading, the pad undergoes shear deformation $y_{brp,sh}$ till the ultimate value $y_{u,brp_{sh}}$ against $F_{u,brp}$ (with respect to its coefficient of friction μ_{brp}), with stiffness k_{brp} governed by its shear modulus G, thickness h_{br} and plan area A_{br} (for bearing pad of length L_{brp} and breadth B_{brp}), as in Equation (3.2a). With the exceedance of $F_{u,brp}$, the pad is free to slide (with the loosening of its grip on the concrete surface) and undergoes sliding displacement $y_{brp,sl}$ at a constant force $F_{u,brp}$. μ_{brp} is dependent on the normal stress σ_m resulting from the axial load P_{br} from the superstructure (Schrage 1981), as explained by Equation (3.2a). Cut-outs provided through the pad, being just as sufficient for projecting the bars having diameter d_{brd}, is considered insignificant in the capacity estimation. It is to be noted that $y_{brp,sh}$ as well as $y_{brp,sl}$ are obtained in terms of the bearing top node displacement. The expressions are shown as,

$$y_{u,brp_{sh}} = k_{brp} F_{u,brp};\quad k_{brp} = \frac{GA_{br}}{h_{br}};\quad \mu_{brp} = 0.05 + \frac{0.4}{\sigma_m};$$
$$F_{u,brp} = \mu_{brp} P_{br};\quad \sigma_m = \frac{P_{br}}{A_{br}} \tag{3.2a}$$

Employing the expressions for k_{brp}, $F_{u,brp}$, μ_{brp} and σ_m in $y_{u,brp_{sh}}$ (Equation (3.2a)), the final expression for $y_{u,brp_{sh}}$ in Equation (3.2b) is obtained as,

$$y_{u,brp_{sh}} = (0.05\sigma_m + 0.4)\frac{h_{br}}{G} \tag{3.2b}$$

The pad lateral force deformation capacity curve is elastic perfectly plastic, with an initial linear path with stiffness k_{brp} upto the point ($F_{u,brp}$, $y_{u,brp_{sh}}$), followed by a zero stiffness path until its ultimate sliding displacement $y_{u,brp_{sl}}$ at the point ($F_{u,brp}$, $y_{u,brp_{sl}}$).

(b) Lateral load resisting mechanism of the dowel bars

For moderate seismic loading, behaviour of dowel bars is usually in the inelastic range. However, modeling a dowel as a beam resting on elastic and cohesionless foundation is still the most expedient way to describe the mechanism (DesRoches et al., 2003). Dowel, loaded in shear in front of the joint, is supported by the concrete contact bearing pressure in the plane through it along the part embedded in the concrete element (Figure 3.5). This loading condition results in considerable flexural deformation and stresses normally in dowel (Khandelwal, 2015).

Typical dowel arrangement for these bearings (as in Figure 3.3) mechanises the beam action rather than the dowel action (Taylor, 1969) when subjected to shear force. However,

Hwang et al. (2001) considered shear failure of the 1-in. diameter A307 (mild steel) swedge bolts and employed the double shear test results performed on such bolts by Mander et al. (1996) in their study. The beam action implies the dowel bar to resist the load F_{brd} with a typical cantilever action corresponding to the loading applied at a distance equal to the joint height h_{br} from the interface till it fractures abruptly at $F_{u,brd}$. Dowel is assumed to be weak enough as compared to the surrounding concrete such that the concrete bearing stresses (Figure 3.5) developed at the joint face in the plane through the dowel are quite low by the time $F_{u,brd}$ gets developed in the bar.

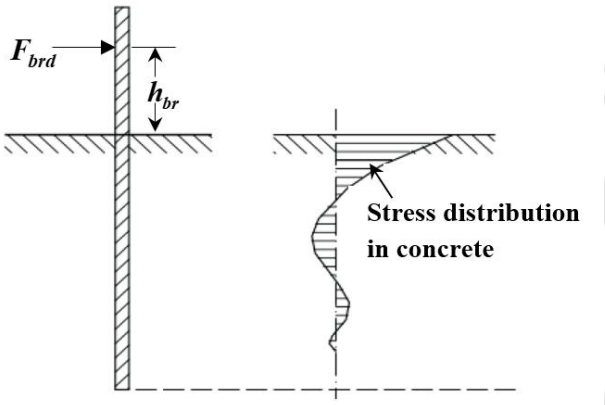

Figure 3.5 Stresses in the surrounding concrete of the embedded dowel (Khandelwal, 2015).

This condition is simulated through the application of static lateral force F_{brd} at a height h_{br} equal to the pad height from the bottom (pad-cap beam interface) which is considered as fixed (following DesRoches et al., 2003). As the loading is continued monotonically, the bar deforms in cantilever mode till its most critical section (adjacent to the interface) reaches $F_{u,brd}$ resulting in fracture and subsequent separation at the interface. Based on this numerical model and with known stress-strain (f_{brd}, ε_{brd}) characteristics (Figure 3.6) of the bar, the forces $F_{t,brd}$, $F_{y,brd}$ and $F_{u,brd}$, and the corresponding deformations $y_{t,brd}$, $y_{y,brd}$ and $y_{u,brd}$ (against the transition, yield and ultimate points of the stress-strain curve) at the loading point of the dowel bar (as evaluated in Appendix A) are expressed in Equations (3.3) and (3.4) respectively. In Figure 3.6, OA, AB and BC represent the elastic, transition and post yield portions with $E_{e,brd}$, $E_{t,brd}$ and $E_{p,brd}$ as the elastic, transition and post yield moduli. In the figure, $f_{t,brd}$, $f_{y,brd}$ and $f_{u,brd}$, and $\varepsilon_{t,brd}$, $\varepsilon_{y,brd}$ and $\varepsilon_{su,brd}$ are the transition, yield and ultimate stresses and strains respectively.

Dowel lateral force deformation capacity curve can be plotted by following the path, as depicted in Figure 3.7, with stiffness $k_{e,brd}$, $k_{t,brd}$ and $k_{p,brd}$ upto points ($F_{t,brd}$, $y_{t,brd}$), ($F_{y,brd}$, $y_{y,brd}$) and ($F_{u,brd}$, $y_{u,brd}$) respectively, as depicted in Figure 3.7 (expressions for $k_{e,brd}$, $k_{t,brd}$

and $k_{p,brd}$ are evaluated in Appendix A).

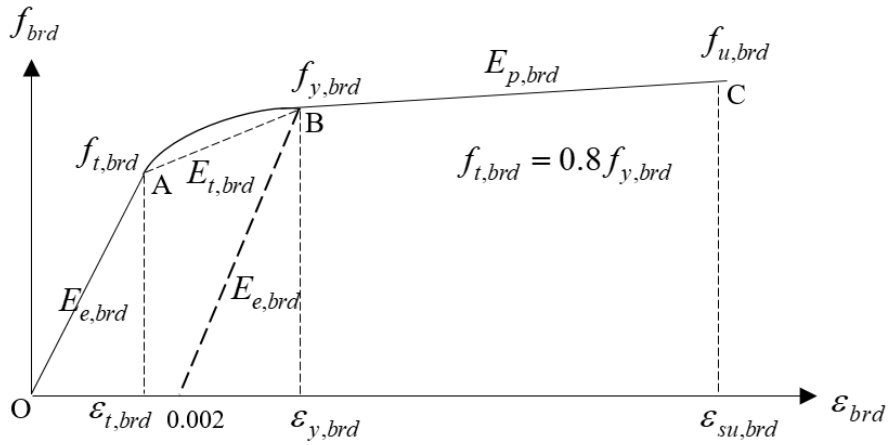

Figure 3.6 Stress-strain relationship of reinforcing bar.

$$F_{t,brd} = \frac{0.8 f_{y,brd} d_{brd}^3}{10.18 h_{br}};\ F_{y,brd} = \frac{f_{y,brd} d_{brd}^3}{10.18 h_{br}};\ F_{u,brd} = \frac{f_{u,brd} d_{brd}^3}{10.18 h_{br}} \tag{3.3}$$

$$y_{t,brd} = \frac{0.8 h_{brd}^2 f_{y,brd}}{1.5 d_{brd} E_{e,brd}};\ y_{y,brd} = \frac{h_{brd}^2 f_{y,brd}}{1.5 d_{brd} E_{e,brd}} + \frac{0.00133 h_{brd}^2}{d_{brd}};$$

$$y_{u,brd} = \frac{0.00133 h_{brd}^2}{d_{brd}} + \frac{h_{brd}^2}{1.5 d_{brd}} \left(\varepsilon_{su,brd} - 0.002 \right) \tag{3.4}$$

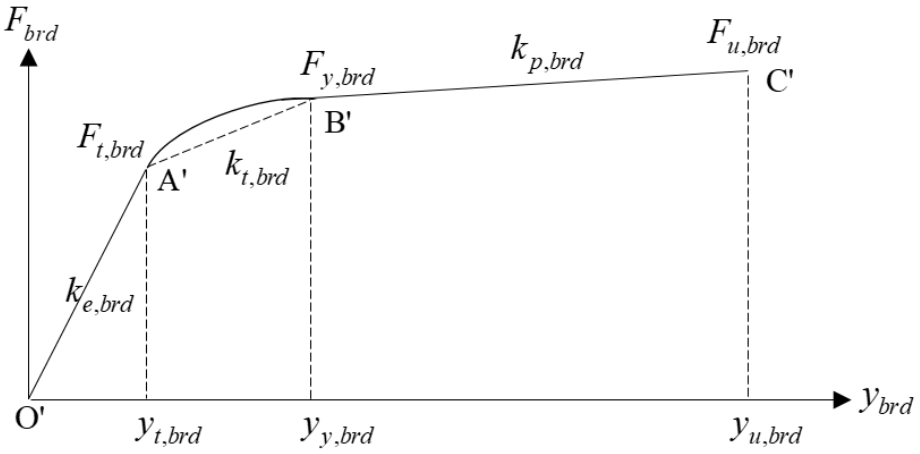

Figure 3.7 Force-deformation curve for the dowel bar.

(c) Resultant load force deformation characteristic for the bearing

With parallel combination of the constituent lateral force deformation capacity curves (Figure 3.8(a)), derived numerically for given values of the respective parameters, the resultant lateral force deformation capacity curve for the bearing is generated, as depicted in Figure 3.8(b).

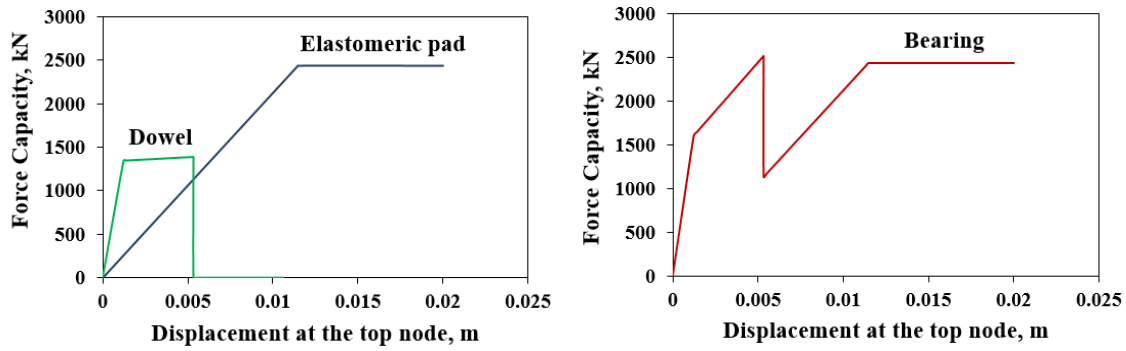

(a) (b)

Figure 3.8 (a) Individual force displacement responses of the pad and the dowels and (b) resultant force displacement response of bearing.

However, the shape as well as the magnitude of the bearing lateral force deformation capacity curve is affected by variation in the properties of the constituents. For instance, keeping the values of $f_{y,brd}$ and $f_{u,brd}$, $\varepsilon_{su,brd}$, G, d_{brd} as 415MPa, 485MPa, 0.145, 1200 kN/m^2 and 0.025m respectively, the values of h_{br}, σ_m, P_{br} and A_{br} in a bearing sample (designated as sample *A*) are changed from 0.150m to 0.040m, 2268 kN/m^2 to 1493.83 kN/m^2 , 91 to 131 kN, 0.04m^2 to 0.0875m^2 respectively to form the sample *B*. The individual lateral force deformation capacity curves are shown in Figures 3.9(a) and 3.9(b) for samples *A* and *B* respectively, where F_{br} (in kN) and y_{br} (in m) represent the force and displacement with respect to both the bearing constituents. The combined effects of the changes in those parameters have shifted the displacements of both the constituents at salient points to lower values, while the respective force capacities have increased for sample *B* with respect to sample *A*. The sequence of attainments of the pad ultimate friction force capacity, dowel yielding and fracture gets altered; while for sample *A*, the friction capacity is reached prior to dowel fracture, it is the vice versa for sample *B*. This in turn, has affected the path profile of the bearing lateral force deformation capacity curve along with the magnitude, as reflected in the respective lateral force deformation capacity curves of samples *A* and *B* (Figures 3.9(c) and 3.9(d)). Further, in case of sample *C*, where, d_{brd} is changed to 0.04m, keeping the values of other parameters same as in sample *B*, the dowel force capacity is increased while the instant of the dowel fracture is shifted to even smaller value as compared to sample *B* (Figures 3.9(e) and 3.9(f)).

3.2.3 Column-Bent

The adopted bridge class in the study corresponds to multicolumn bents with the number of piers n_{pr} engulfing upto four. Ranges of pier diameter D_{pr} and W_d are divided into four sub-ranges, categorising the bents into four Column Bent Types (CBTs), as 1CBT, 2CBT,

3CBT and 4CBT consisting of one, two, three and four piers respectively in the study. W_d range is based on accommodating the elements like kerb, crash barrier, footpath and railing, for two/four lane road and highway bridges (Table 3.1) in Indian context (IRC 2000a). W_d and D_{pr} sub-ranges, as listed in Table 3.2 are fixed considering Ramanathan (2012), which also shows the increase in n_{pr} and the consequent decrease in D_{pr} with the increase in W_d.

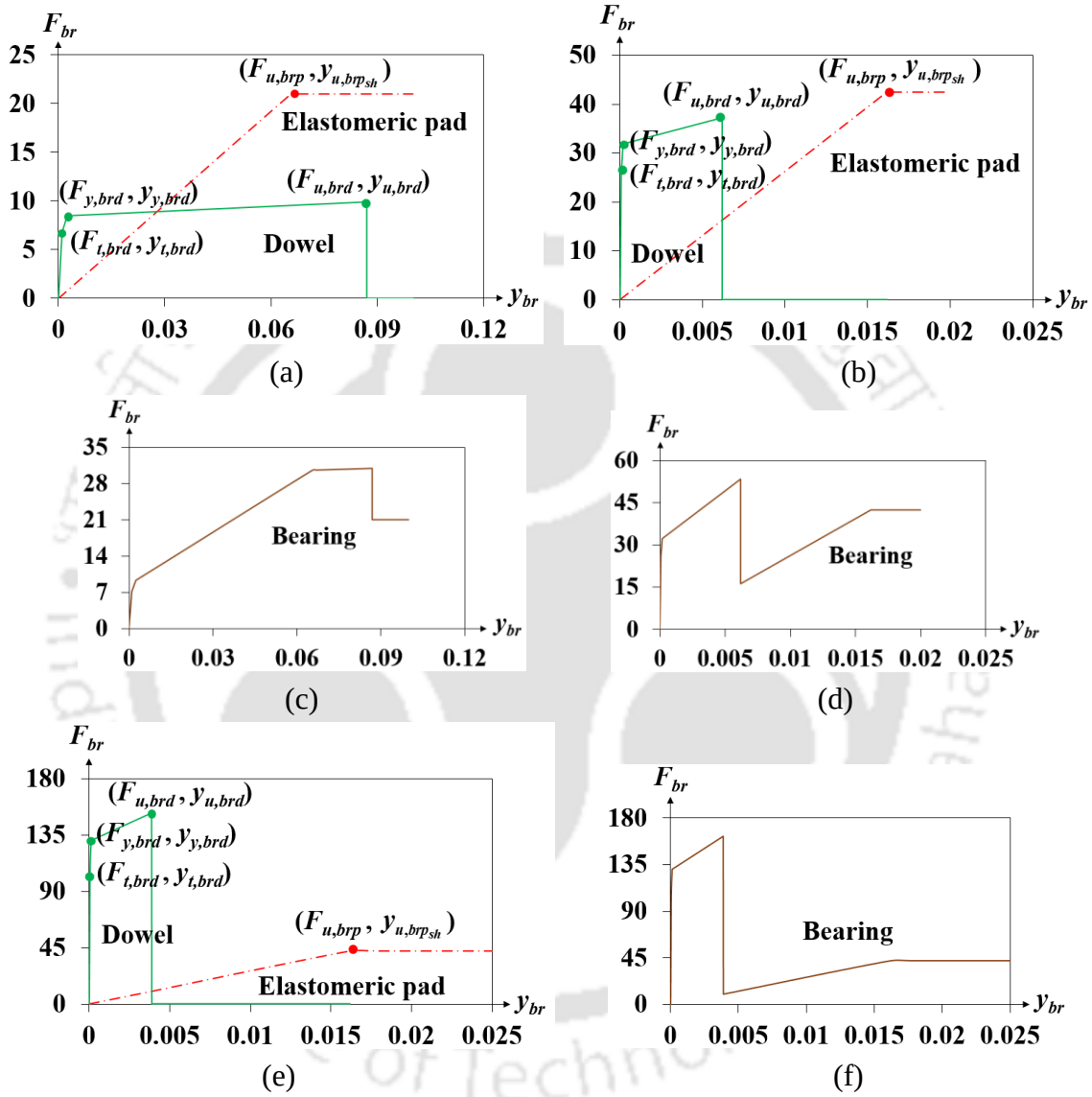

Figure 3.9 Lateral force deformation capacity curves for the individual bearing constituents in samples (a) *A*, (b) *B* and (c) *C*, and the bearing assembly of samples (d) *A*, (e) *B* and (f) *C*.

Table 3.1 Deck widths for two and four lane road and highway bridges

Nos. of lane	W_d (m) (DRTH, 2009)	
	Road bridge	Highway bridge
2	$2\times3.5+2\times(0.25+0.45+1.50+0.20)=11.80$	$2\times5+2\times(0.25+0.45+1.50+0.20)=14.80$
4	$4\times3.5+2\times(0.25+0.45+1.50+0.20)=18.80$	$4\times5+2\times(0.25+0.45+1.50+0.20)=24.80$

Table 3.2 Attributes of the column bent type

n_{pr}	W_d (m)	D_{pr} (m)
1	$11 \leq W_d < 14$	$1.8 \leq D_{pr} < 2$
2	$14 \leq W_d < 18$	$1.4 \leq D_{pr} < 1.8$
3	$18 \leq W_d < 22$	$1.0 \leq D_{pr} < 1.4$
4	$22 \leq W_d \leq 26$	$0.8 \leq D_{pr} \leq 1.0$

The cap beam width should be dimensioned so that a projection of 200 mm exists beyond the edge of the top of the pier on either side. In this study, the cap beam width is taken as D_{pr} plus twice of T_d and the depth of the cap beam is kept 1.5 times its width as observed in the bridge inventory adopted in Ramanathan (2012). Pier used in the study, is assumed to be fixed against rotation at both ends owing to its rigid connections with the cap beam and pile cap at the top and bottom respectively, and thereby bends in double curvature under seismic load F_{pr} at its top in the transverse direction of the bridge (Figure 3.10(a)). Thus, proper detailing of moment connections are assumed to be provided at the joints. Piers with circular cross sections are considered in the study (Figure 3.10(b)).

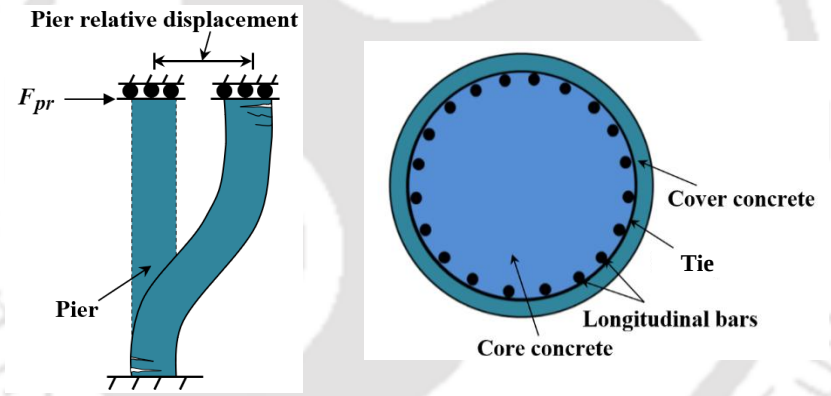

Figure 3.10 (a) Seismic deformation pattern of pier in the transverse direction of the bridge and (b) typical pier cross section.

3.2.4 Pile Foundation

Integral abutments founded on single row of steel H piles are the most prevalent design type in USA as well as the countries with expertise in IABs. However, in countries where integral abutments are seldom used, e.g., Portugal, India etc., there is a tendency for the use of reinforced concrete piles in IABs following their traditional use in non-integral bridges (Yen and Kuo). Hence, the study adopts reinforced concrete pile foundations for abutments as well as bents, as a case in India, as were also employed by countries like Germany, Ireland, England and Finland (White, 2007) for IABs. Like Aygun et al. (2011), Brandenberg et al. (2011), Choine et al. (2014) etc., this study too considers single row of

reinforced concrete piles below the backwall. The present study adopts loose sands as the foundation soil. Deep foundations for bridges in soft or medium soil often rely on the use of reinforced concrete piles that are restrained from rotation at the pile head (Song et al., 2004), following which the study considers fixed-headed piles, as a group and a single row below each pier and backwall respectively. Square and octagonal cross sections, being most commonly used (Pile Foundation Design as per IS 2911-2010), the study considers square piles (Figure 3.11(a)).

To ensure rigid behaviour with respect to fixed head for the piles in groups below piers (Figure 3.11(b)), the cap thickness is taken as 1.5 times D_{pl}, as per Cl. 709.5.4 of IRC (2014a), as well as sufficient embedment lengths at the connections. To avoid any soil passive wedge interference among the piles, the pile spacing is kept as four times the pile width D_{pl} in the study, as per Cl. 709.1.5 of IRC (2014a) (for friction piles). A minimum offset of 150 mm is provided beyond the outer faces of the outer-most piles in the group as per Cl 709.5.1 of IRC (2014a). Number of piles n_{pl} under the pile cap is determined based on the pile settlement (due to the gravity load transferred from the pier), which is limited to be within 20mm to 30mm in the study. The criterion is based on BIS (1986), Skempton and MacDonald (1956) and RDSO (2013); the first two recommend the permissible limits for isolated foundations in sand to be 50mm and 40 mm respectively, while the last one considers it to be 25 mm for simply supported bridges with somewhat larger value allowed for the continuous bridges. Pile cap plan dimensions are adopted based on n_{pl}, pile spacing and the overhang length beyond the outermost piles.

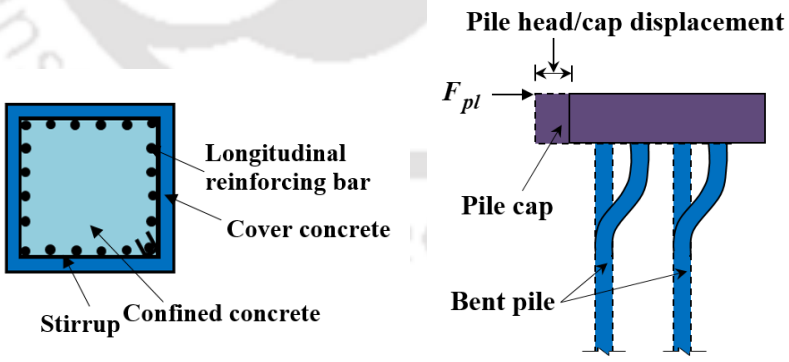

(a) (b)

Figure 3.11 (a) Pile cross section and (b) seismic deformation pattern of bent-pile foundation.

The present study deals with long flexible piles. Hence, only a certain portion of the length L_{pl} near the pile cap participates during the seismic excitation in the form of pile head load F_{pl}, whereas pile lateral deflections in the regions below the first zero deflection point are

negligible (Figure 3.11(b)). Flexible category criterion is checked, as per Equation (3.5), where, E_s is the concrete Young's modulus, $K_{pl\text{-}s}$ is the pile-soil stiffness factor, I_{pl} is the moment of inertia, η is the coefficient of subgrade reaction. The expressions are given as,

$$K_{pl\text{-}s} = (E_c I_{pl}/\eta)^{0.2} \; ; \; L_{pl}/K_{pl\text{-}s} \geq 4 \tag{3.5}$$

3.2.5 Abutment-Backfill System

Abutment-Backfill System (ABS) in this study consists of a RC backwall of height H_{ab} connected integrally with the superstructure and two cantilevered RC wing walls (Figure 3.12(a)), with compacted dense sandy soil as backfill. To make the rigid connection assumption valid, sufficient embedment lengths are provided at the deck slab-abutment, abutment-girder and abutment-pile connections to avoid the otherwise flexibility in the system (Itani and Peckan, 2011). The corresponding deformation pattern of the ABS and the underlying fixed head flexible piles under seismic loading in the form of the lateral load F_{ab} are shown in Figure 3.12(b).

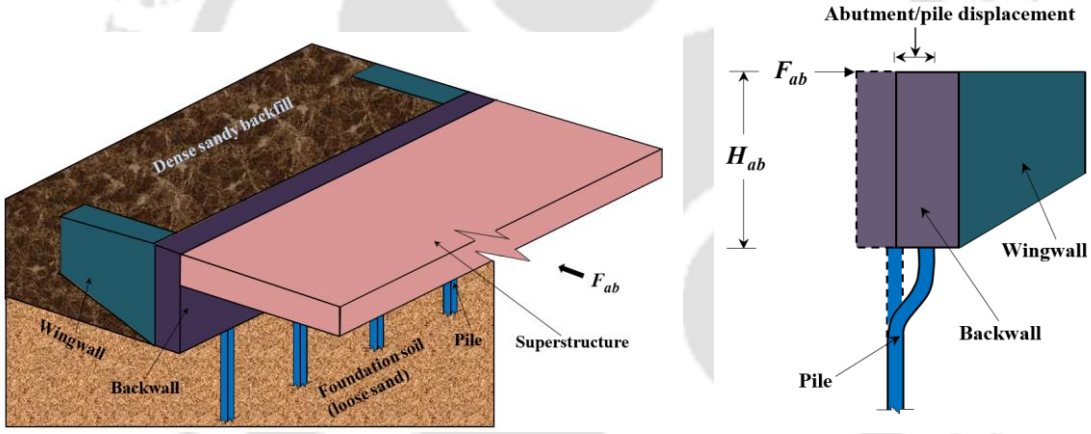

(a) (b)

Figure 3.12 (a) Integral abutment configuration used in the study and (b) abutment backfill-pile-soil system seismic deformation pattern.

3.3 NUMERICAL MODELING OF THE BRIDGE COMPONENTS

Proper idealisation of seismic behaviour of the structural components (as investigated in Section 3.3) is crucial for obtaining realistic estimates of the desired goal. Appropriate analytical models for the components are developed using the open source code software OpenSees (Open System for Earthquake Engineering Simulation), Version 2.4.5 (McKenna and Feneves, 2005).

3.3.1 Bridge Superstructure

Compared to the detailed modeling of the deck stiffness in assessing the effects of vertical loads (Kappos et al., 2012), significantly simpler models suffice for the seismic analysis,

provided they represent effective stiffness characteristics and mass distribution (Priestley et al., 1996). In this study, the superstructure is modeled by spline of *elasticBeamColumn* elements following the center of gravity of the cross section along the length, with tributary masses lumped at the discretised nodes at the deck centre, the bent and the abutment locations. The deck and the girders' geometries and location are used to evaluate the equivalent sectional frame-element properties, like the cross sectional area, moment of inertias, modulus of elasticity, shear modulus which are to be given as input in OpenSees.

3.3.2 Bent Elements

The cap beam is modeled as *elasticBeamColumn* elements in OpenSees and is discretised at the pier locations. The lateral force deformation capacity curves of underlying foundation (parallel combination of the PSS curves, for a given number of piles in the foundation) and pier, as derived in succeeding Sections 3.3.6.1 and 4.3.1 respectively, are incorporated within the *Zero-Length* elements in OpenSees. This two-noded elements have six independent springs defined by UniaxialMaterial objects to represent the force-deformation relationship for the element in each of the six directions. The lateral capacity curve is assigned to the *ElasticMultilinear uniaxial material* in the lateral spring, while *Elastic uniaxial materials* with very high stiffness are assigned in the remaining five unidirectional springs to reflect the lateral response only, each for the pier and the foundation. The top node of a pier spring element is interconnected with overlying capbeam node, while its bottom node is interconnected with the top node of the underlying foundation spring element. The bottom node of the foundation spring element is kept fixed.

3.3.3 Abutment Elements

Backwall and the cantilevering wingwalls are assumed to translate rigidly under seismic loading and hence are modeled as *RigidLink* elements in OpenSees. The respective backfill pressures on the backwall and wingwall are represented with *Zero-Length* elements in OpenSees. The ABS lateral capacity curve with respect to each of the backwall and wingwall (Section 3.3.6.2) is assigned to the *ElasticMultilinear uniaxial material* in the lateral spring, while *Elastic uniaxial materials* with very high stiffness are assigned in the remaining five unidirectional springs to reflect the lateral response only.

3.3.4 Bearings

Bearing in the study, resists the seismic force through shear and is considered to be axially rigid. It is modeled using *Zero-Length* elements in OpenSees, wherein *Elastic uniaxial materials* with very high and zero stiffness, and *ElasticMultilinear uniaxial materials*

representing the bearing lateral force deformation capacity curve (as depicted in Figure 3.8(b)) are assigned in the vertical and the three rotational, and the shear directions respectively.

3.3.5 Pier and Pile

Pier model is built, as *nonlinearBeamColumn* elements in OpenSees, with the two end nodes kept fixed against rotation to ensure the double curvature bending. Pile is modeled with *dispBeamColumn* element as pile tends to form plastic hinges at multiple locations along its length and the rotational degrees of freedom of the top node are restrained to model the fixed head of the pile. Material nonlinearity is incorporated through fibre sections distributed along the length of the elements. Each fibre section comprises of core and cover concrete patches and layer of reinforcing bars (Figures 3.13(a) and 3.13(b)) for pier circular and pile square sections respectively) and the representative stress-strain curves (with the parameters designated as '*pr*' and '*pl*' after a comma in the subscripts with respect to pier and pile respectively) are shown in Figures 3.13(c) and 3.13(d).

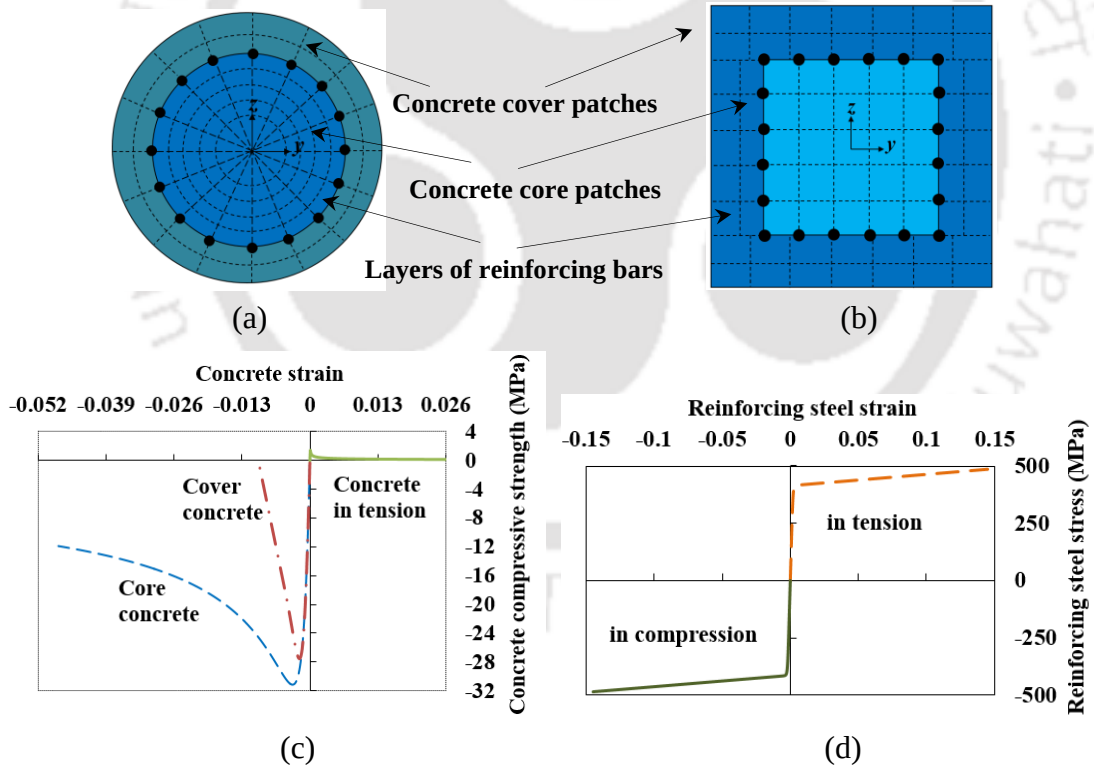

Figure 3.13 RC fiber section for (a) pier and (b) pile, and sample stress strain curves for (c) concrete and (d) reinforcing steel.

Bars with yield stress f_y, ultimate stress f_u and ultimate strain ε_{su} in the study are modeled with Steel02. Core concrete is modeled with Concrete06, which requires the peak compressive stress f_{cc} and the corresponding strain of confined concrete (evaluated based

on the respective longitudinal ρ_l and transverse ρ_t reinforcement ratios in pier and pile using Mander et al., 1988) and the descending branch parameter of the concrete stress strain path (evaluated using Popovics, 1973). Cover concrete is modeled with Concrete07, which requires E_c, the peak compressive stress of the unconfined concrete and the corresponding strain, the descending branch as well as the concrete spalling strain (both evaluated using Waugh, 2009). The concrete peak tensile stress and the corresponding strain are considered the same for confined and unconfined concretes and adopted as per Belarbi and Hsu (1994).

3.3.6 Soil-Structure Interaction

Free field motion is apparently unaffected by the presence of the structures founded on bedrock. However, it gets significantly modified along the motions of the structure founded on soft soils resulting in a feedback loop which involves the structure responding to the motion of the soil which in turn responds to the motion of the structure (Tabatabaiefar and Clifton, 2016). This phenomenon is known as soil-structure interaction which causes shifts in structural performance levels (Somali et al., 2011) and thus forms an integral part of structural analysis when performance estimate is the basic aim. A BS generally encounters two types of soil-structure interaction, namely (a) pile with the surrounding soil, i.e., the pile-soil interaction and (b) abutment with the backfill, i.e., the abutment-backfill interaction. DSs and the respective LSTs of the ABS and PSS are thus inherently dependent on abutment-backfill interaction and pile-soil interaction respectively. Since, the present study considers pile foundation on loose sand and dense sandy soil as the backfill, the imminent pile-soil and abutment-backfill interactions are idealised and incorporated through appropriate models to arrive at the precise fragility estimates.

Continuum based methods for analysing pile-soil interaction (pioneered by Poulos, 1971) which basically consider pile as a strip applying pressure on the soil mass (treated as a continuum) are the most realistic and conceptually more appealing ones. Several researchers have used different forms of finite element methods; however, these are less popular, as these involve either complicated mathematics or do not provide simple and practical steps for obtaining the pile deflection (Basu et al., 2008). Many practicing engineers therefore opted for a simpler beam on Winkler foundation approach through *p*–*y* curves (*p* is the soil pressure/pile length and *y* is the lateral pile deflection) closely spaced along the pile length. The traditional formulations like Matlock (1970), Reese et al. (1974) etc. do not incorporate all the influential PSS parameters as well as the soil continuity and due to the influence of the specific test conditions, these cannot be considered universally

applicable. Strain Wedge Model (SWM), initially developed by Norris (1986) and improved by Ashour et al. (1998), (2000), and Ashour and Norris (2000a), is a theoretical formulation and incorporates any soil type and profile, along with the pile structural properties. Kampitsis et al. (2015) carried out the inelastic analysis of Euler–Bernoulli beam resting on elastoplastic foundation for the free headed aluminium pile in their study, but was not extended to RC pile. Though pile structural characteristics were considered by Limkatanyua et al. (2009), Reese et al. (1974) was used to model the soil response; hence it ignored the influence of the deflection profile of pile (associated with the given properties) on the development of *p–y* curve. Strain wedge formulation provides good agreement with the previous experimental results, as observed by Hajialilue-Bonab et al. (2011) and Xu et al. (2017). Because of efficient handling of pile-soil interaction, SWM has been implemented by Ashour and Norris (2000b), Ashour et al. (2002), Ashour et al. (2004), Piling et al. (2001), Ashour and Ardalan (2011), (2012) and Yang et al. (2018) in different applications and so is adopted in the study to analyse pile-soil interaction.

In case of IABs, the backfill compressive passive resistance gets immediately mobilised due to the transfer of seismic force from the superstructure through the monolithic abutment. For a typical highway bridge, length of the backwall L_{bw} is much greater than its height. Thus, abutment-backfill interaction is essentially a plane-strain problem and any bridge abutment lateral capacity curve should be designed to reproduce this condition (Shamsabadi et al., 2010). However, none of the previous passive earth pressure theories (Coulomb, 1776; Rankine, 1857 and Terzaghi, 1943) (based on plain strain conditions) could correctly assesses the passive earth pressure resistance or the size and shape of the rupture wedge. This leads to the recognition of the essence of the knowledge of soil's stress-strain properties for the complete analysis of earth pressure problem. At increasing levels of abutment displacement, intermediately mobilised logarithmic spiral Soil Passive Wedge (SPWs) are formed with intermediate levels of passive resistance until backfill reaches its full shear strength (observed for both wall rotation and translation). The SPW geometry is governed by H_{ab} and the backfill shear strength and strain in backfill get mobilised in proportion to its movement. Such a mechanism is simulated by Shamsabadi et al. (2005) through logarithmic-spiral failure surface model, which is adopted herein.

3.3.6.1 Pile-Soil Interaction in the Study

(a) Description of SWM

The present study simulates pile-soil interaction through SWM which characterises a SPW (Figure 3.14(a), mobilising in front of the pile) with depth H_{spw}, base angle β_{spw}, fan angle

α_{ss} and soil-pile friction angle ϕ; it results in horizontal stress change $\Delta\sigma_h$, pile side shear stress τ and p (with subscript 'm' against the mobilised values (Figure 3.14(a))). For a given horizontal soil strain (ε_{ss}) developing within SPW and at a discretised wedge sublayer, E_s (Figure 3.14(b), with subscript 'j' against the j^{th} sublayer) is derived by relating p with $\Delta\sigma_h$ and τ, and y (denoted with y_{pl} hereafter) (with pile deflection pattern angle δ_{pl}, leading to pile head deflection $y_{0,pl}$) with ε_{ss}. Proper value of H_{spw} (initially unknown) is achieved through the convergence of SWM with the beam on Winkler foundation problem of PSS (Figure 3.14(b)) for given lateral F_{pl}, and axial P_{pl} loads and pile head boundary conditions.

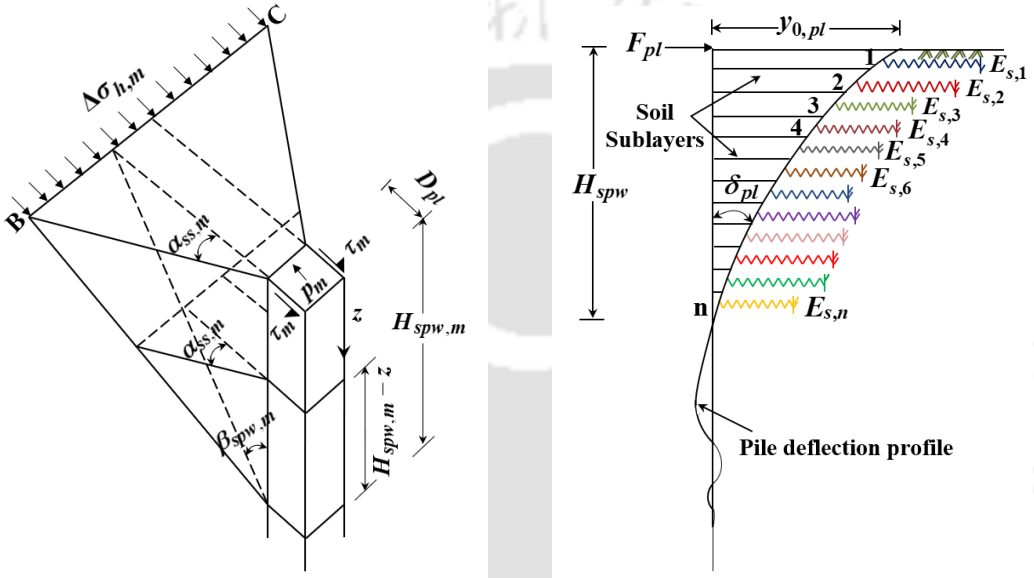

Figure 3.14 (a) Basic SPW and (b) beam on Winkler foundation approach in SWM (Ashour et al., 1998).

For an assumed value for H_{spw}, p is computed using the initial expression, as in Eq. (3.6a), which is followed by the expressions required for computing its constituent parameters, namely the horizontal stress change at failure $\Delta\sigma_{hf}$, horizontal stress level SL_s in soil (having friction angle φ_s and unit weight γ_s), α_{ss}, β_{spw}, ϕ, overburden pressure $\overline{\sigma_{ov}}$ (at soil depth z). These, in turn, requires φ_s, SL_s–ε_{ss} relationships (Ashour et al., 1998), $\varepsilon_{ss,50}$ (ε_{ss} at SL_s of 50%) employing $(\varepsilon_{ss,50})_{42.5}$ (ε_{ss} at $\overline{\sigma_{ov}}$ of 42.5 kPa, for a given uniformity coefficient and void ratio of sand), as the inputs with expressions in Equation (3.6a). The values are obtained at the middle of each of the soil sublayers; thus, the symbols are denoted with subscript 'ij' corresponding to the j^{th} sublayer at depth z_j and against the i^{th} value ($\varepsilon_{ss,i}$) of the ε_{ss} range. Similarly, y is computed using the initial expression, as in Equation (3.6b), followed by the expressions required for computing the constituent parameters, namely δ_{pl} and the sandy soil Poisson's ratio v_s. In SWM, S_1 and S_2 are adjustment factors, both take

the value 1 for square pile. Accumulation of y_{ij}s (from the wedge base till the pile head) leads to $y_{0,i}$, as in Equation (3.6c). Finally, E_s is obtained using the simplified expression, as in Equation (3.6c).

$$\begin{aligned}
&p = \Delta\sigma_h \overline{BC} S_1 + 2\tau D_{pl} S_2 \;\leftarrow \Delta\sigma_h = SL_s \Delta\sigma_{hf},\ \tau = \overline{\sigma_{ov}} \tan\phi, \\
&\overline{BC} = D_{pl} + 2(H_{spw} - z)\tan\beta_{spw}\tan\alpha_{ss} \;\leftarrow \varepsilon_{ss,50} = (\varepsilon_{ss,50})_{42.5}(\overline{\sigma_{ov}} / 42.5)^{0.2}, \\
&\alpha_{ss} = 2\tan^{-1}\sqrt{SL_s(\tan^2(45^o + \varphi_s/2) - 1) + 1} - 90^o,\ \alpha_{ss} \le \varphi_s,\ \beta_{spw} = 45^o + \alpha_{ss}/2, \\
&\tan\phi = 2\tan\alpha_{ss} \le \tan\varphi_s,\ \Delta\sigma_{hf} = \overline{\sigma_{ov}}\left[\tan^2(45 + \varphi_s/2) - 1\right]
\end{aligned} \tag{3.6a}$$

$$y = (H_{spw} - z)\delta_{pl} \;\leftarrow \delta_{pl} = 0.5\varepsilon_{ss}(1+\nu)\sin(90^\circ - \alpha_{ss}),\ \nu_s = 0.1 + 0.4SL_s, y_{0,i} = \sum y_{ij} \tag{3.6b}$$

$$E_s = p / y = \frac{\Delta\sigma_h D_{pl}}{\delta_{pl}}\left[\frac{S_1 G}{D_{pl}} + \frac{S_1 + 2S_2 R}{H_{spw} - z}\right],\ G = \tan^2\beta_{spw} - 1,\ R = \tan\phi / G \tag{3.6c}$$

(b) Evaluation of PSS Responses in the Study

In this study, SWM is linked with the finite element analysis of the modeled PSS to achieve the required convergence in SWM and thus obtain the appropriate values for the PSS response parameters. SWM parameters are computed in spreadsheets and the PSS finite element model is built in OpenSees.

Pile is modeled as per Section 3.4.3 and its length is discretised at the same locations as done for the soil wedge (Figure 3.15(b)) during SWM computations, to have compatible outputs from beam on Winkler foundation problem. The pile segments and the soil sublayers are of equal and constant thickness (of the order of half of pile diameter (Meyer and Reese, 1979)) throughout the pile length. The sandy soil is modeled with *ZeroLength* elements distributed along the pile length and at the pile tip (Figure 3.15(a)); the responses are assigned to the *uniaxial materials* in the unidirectional springs of the elements, with one node of each spring connected to the adjacent pile node and the other kept fixed.

Soil lateral response is represented by $E_{s,ij}$s against $\varepsilon_{s,i}$ at j^{th} sublayers at depth z_js along the pile length. E_s values to be inputted below H_{spw} are calculated assuming these to be increasing linearly with depth based on η (Xu et al., 2013). Soil axial responses are modeled by *t*–*z* (pile skin friction versus pile deflection) and *q*–*z* (pile tip resistance versus pile deflection) curves using API (2000); typical curves evaluated for a pile with D_{pl}, L_{pl}, φ_s and γ_s of 0.733m, 14.50m, 32.2° and 18.58kN/m^3 respectively are shown in Figures 3.15(b) and 3.15(c) respectively. $E_{s,ij}$ and *t*–*z*, and *q*–*z* values are inputted within *Elastic* and *ElasticPP*, and *ElasticMultilinear uniaxialMaterials* which are assigned to lateral and vertical springs

along the pile length, and the vertical spring at pile tip node respectively of the *ZeroLength* elements. Implementation of the procedure is depicted in a flowchart, as in Figure 3.16.

The present study focuses on the lateral response of long flexible pile with D_{pl} < 0.9 m, thus the effect of vertical side shear resistance is eliminated as per Ashour and Helal (2013).

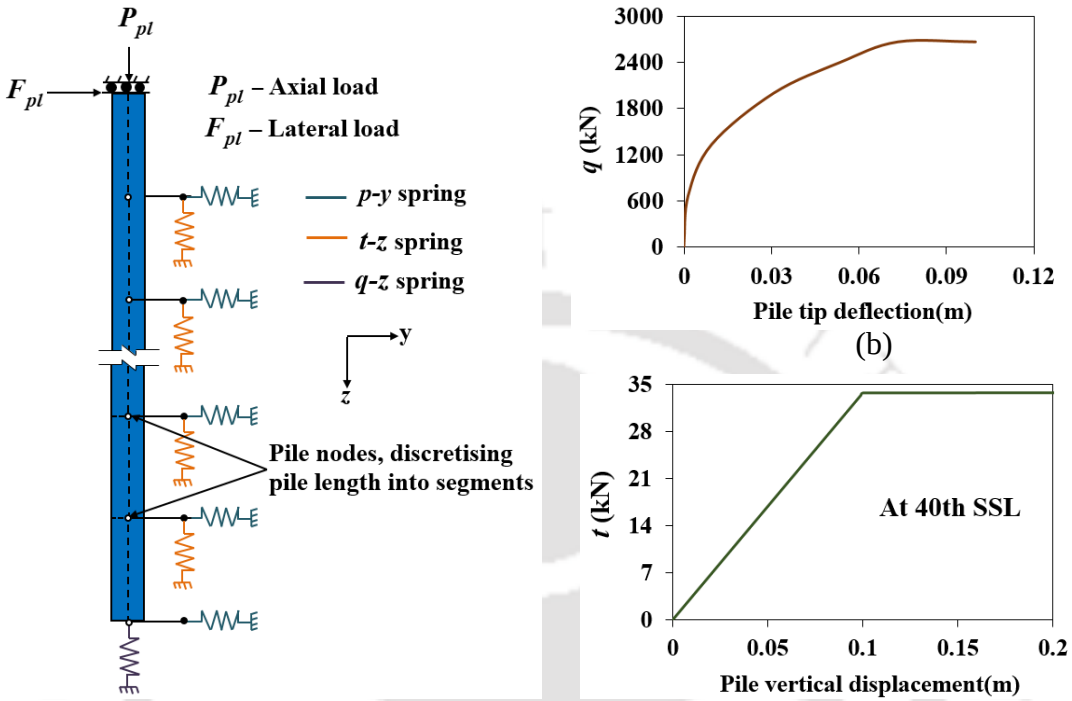

Figure 3.15 (a) Beam on Winkler foundation model of PSS, (b) *t*–*z* and (c) *q*–*z* curves.

(c) Validation of the procedure of evaluating the PSS responses

For validating the procedure for simulating the PSS responses in absence of SWM based software package, the evaluated F_{pl} versus $y_{0,pl}$ and F_{pl} versus maximum moment $M_{\max,pl}$ responses, for the set of pile and sandy soil properties as in the static load test of Reese et al. (1974), are compared with those observed from the test (details in Cox et al., 1974). Since, the loading was continued upto the maximum allowable strain in the test steel pile, its behaviour can be assumed to be within elastic limit. Hence, it is modeled in OpenSees as an elastic element requiring properties like L_{pl}, modulus of elasticity and moment of inertias, and is discretised such that pile nodes also exist at the (a) ground line for applying the control displacement as y_{0,pl_i} and (b) loading point (some distance below the pile free head, as in the test), for the simulation to obtain $F_{pl,i}$ ((y_{0,pl_i} and $F_{pl,i}$ being evaluated at $\varepsilon_{s,i}$). $E_{s,ij}$s are evaluated for the sublayers of the discretised SPW mobilising in front of the embedded length of the pile, and are inputted to the modeled soil springs attached to the adjacent pile nodes. Displacement controlled pushover analysis of the PSS is carried out

and iterations are continued till the convergence in SWM is achieved. $M_{\max,pl_i}$ (at $\varepsilon_{ss,i}$) is noted by monitoring the moment profile in pile along its length. The procedure is repeated at increasing ε_{ss} values, till the ultimate $y_{0,pl}$ (as in the test) is achieved. The generated $F_{pl} - y_{0,pl}$ and $F_{pl} - M_{\max,pl}$ curves are shown in Figures 3.17(a) and 3.17(b) respectively.

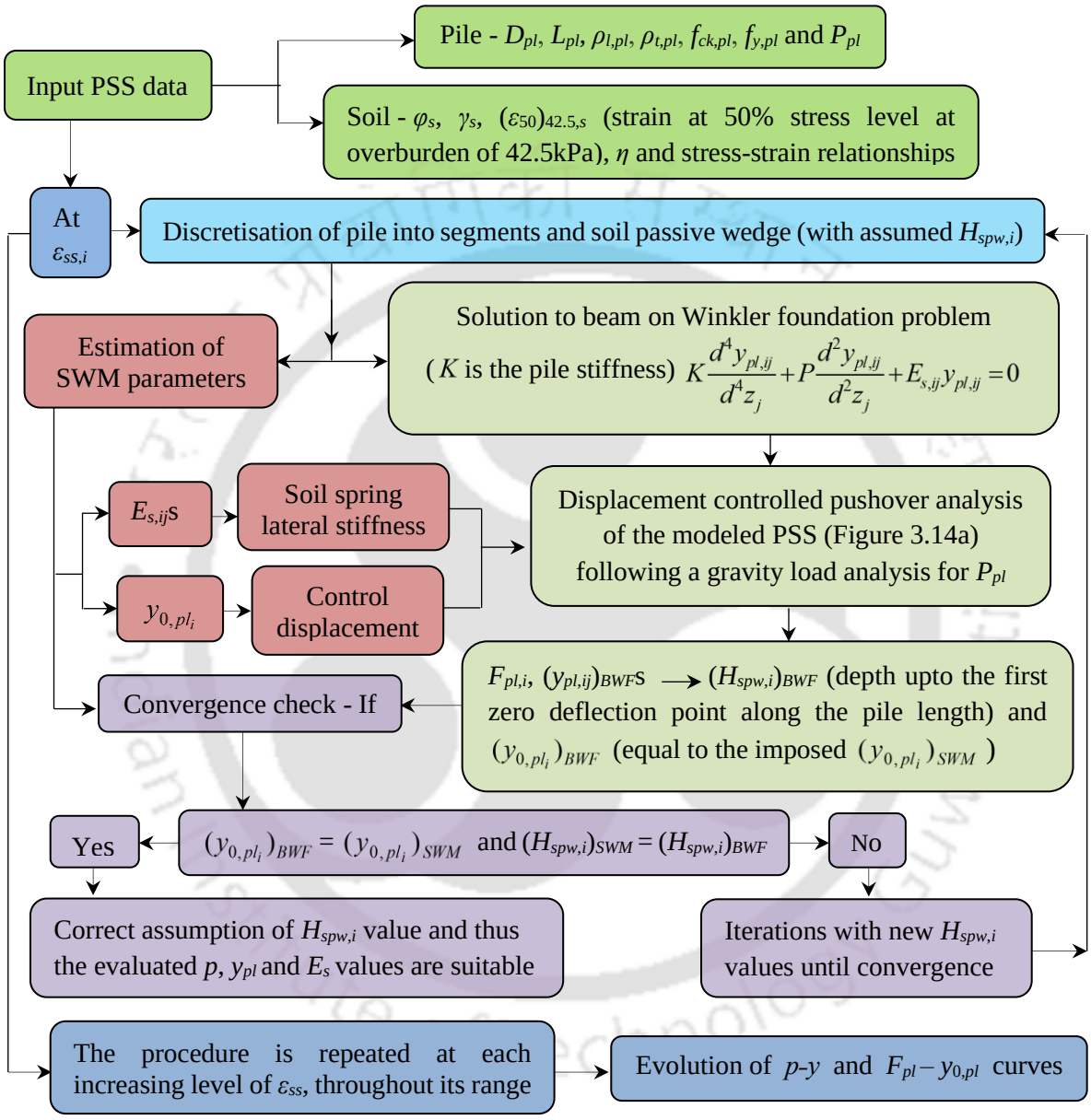

Figure 3.16 Flowchart describing the procedure to evaluate PSS responses in the study.

It is observed that for the initial portions of the curves in Figures 3.17(a) and 3.17(b), SWM values match well with those of the test. As $y_{0,pl}$ increases, SWM shows deviations within 6.5% (Figure 3.17(a)) and 9% (Figure 3.17(b)) from the test. Deviations might have been lesser if the actual η value for the site was utilised; however, in its absence (both in Reese et al., 1974) and Cox et al., 1974), the η value for dense sand (from Reese et al.

(1974) was adopted below the wedge. Intermediate seams of clays at the site (rather than the uniform sand profile, as assumed in SWM simulation) added to the deviations. Thus, the structural response outputs can be considered reasonable, to further examine the PSS damages or failures and assess the respective LSTs.

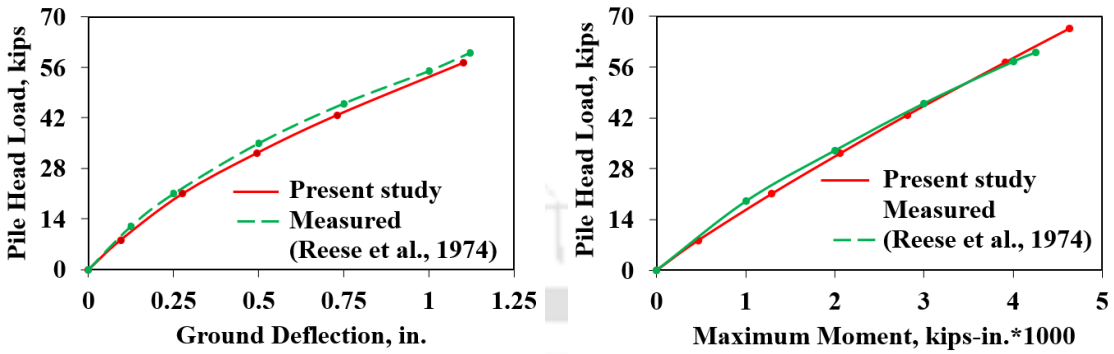

(a) (b)

Figure 3.17 Comparisons of the evaluated (a) $F_{pl} - y_{0,pl}$ and (b) $F_{pl} - M_{\max,pl}$ curves with those in Reese et al. (1974).

(d) Influence of Pile Structural Nonlinearity on PSS Response

With the ability of SWM to incorporate the pile structural properties, the influence of the corresponding nonlinear behaviour in pile on the PSS response can be captured. To depict the consequences, two piles - one to behave linearly and the other nonlinearly under lateral response, are considered in loose sandy soil. Parameters required for modeling the linear pile are L_{pl} = 12m, E_c and the moments of inertia of the pile section and those for the nonlinear pile are D_{pl} = 0.520m, $f_{ck,pl}$ (concrete characteristic compressive strength) = 40MPa, $f_{y,pl}$ = 415MPa, $\rho_{l,pl}$ = 4.290%, $\rho_{t,pl}$ =0.300%,, with both the piles subjected to υ_{pl} of 0.1. Sand properties include $\varphi_s = 30^{\circ}$, γ_s = 16.5 kN/m^3, $(\varepsilon_{50})_{42.5,s}$ = 0.005, η = 12487kN/m^3 and A_u = 14.64 (A_u being the ultimate value of the parameter A controlling sand Flow Around Failure (FAF)), as discussed in Section 3.4.3). F_{pl}–$y_{0,pl}$ curves evaluated using SWM for both the PSSs are depicted in Figure 3.18(a) and as expected, difference in the very initial portion of the curves is negligible, when neither FAF nor pile nonlinearity has initiated. Nonlinearity in pile causes mobilisation of soil passive wedge of comparatively smaller depth at $\varepsilon_{s,i}$; deeper wedge causes A_u (at the top soil sublayer) to attain faster (discussed later) and thus the flow to initiate earlier, i.e., at a lesser ε_s value (= 0.0044 at H_{spw} =5.77m) in linear pile, as compared to the pile with nonlinear behaviour (H_{spw} =5.48m and ε_s = 0.0055) at that instant. At $\varepsilon_{s,i}$, y_{0,pl_i} is larger in linear pile, due to accumulation of $y_{pl,ij}$s from more numbers of soil sublayers within a deeper SPW; however, mobilisation of higher ε_s value until the FAF initiation, in case of PSS with nonlinear pile, leads to larger

$y_{0,pl}$ at that instant (Figure 3.18(a)). Magnitude of $F_{pl,i}$ is lower for the PSS with nonlinear pile due to mobilisation of capacity from a lesser number of sublayers within a shallower SPW at $\varepsilon_{s,i}$; nonlinearity in pile structural capacity, owing to the initiation and propagation of pile damages with increasing ε_s (and thus $y_{0,pl}$) values, further reduces the growth of F_{pl} (Figure 3.18(a)). PSS with linear pile fails only when FAF progresses to sufficiently large numbers of soil sublayers, while the PSS with nonlinear pile fails mostly through structural damages before the FAF could propagate to a considerable number of sublayers. Hence, any formulation must include the possible structural nonlinearity in pile or rather should incorporate the pile material and detailing properties to avoid the likely over or under estimation in the outputs and bring pile structural damages into the picture.

(e) Comparison of SWM p–y Curves with those from Previous Formulations

Formulations like Reese et al. (1974) and API (2000) incorporated only D_{pl}, φ_s, γ_s and η,, and assumed linear E_s profile with soil depth. Pile structural properties like L_{pl}, $f_{c,pl}$, $f_{y,pl}$, $\rho_{l,pl}$ and $\rho_{t,pl}$ as well as υ_{pl} and the pile head condition influence the pile-soil interaction and thus determining the precise PSS responses. For instance, for given values of D_{pl}, φ_s, γ_s and η, only a single *p–y* curve is obtained. However, for the same set, a family of curves can be obtained based on the variation in L_{pl}, $f_{ck,pl}$, $f_{y,pl}$, $\rho_{l,pl}$ and $\rho_{t,pl}$ as well as υ_{pl} and a different pile head condition. Hence, any pile-soil interaction formulation must include their affects. SWM is able to incorporate these parameters and derives $E_{s,ij}$s s as factors, with which the respective soil's Young's modulus values along the pile length are modified to reflect the extent of pile-soil interaction. *p–y* Curves are generated using Reese et al. (1970) and API (2000) corresponding to D_{pl} = 0.520m, φ_s = 30°, γ_s = 16.5 kN/m^3, η = 12487kN/m^3. With additional parameters as L_{pl} = 12m, $f_{ck,pl}$ = 35MPa, $f_{y,pl}$ = 415MPa, $\rho_{l,pl}$ = 4.290%, $\rho_{l,pl}$ =0.300%, P_{pl} = 0kN and 850 kN, and considering the pile head to be fixed, SWM *p–y* curves are also developed. It is expected that at any depth, the SWM curves will differ from those obtained from Reese et al. (1970) and API (2000), as is evident from Figure 3.18(b) (shown for the depth of 0.80 m below the pile top), owing to the effects of the additional parameters. One such influence is reflected through the differences in the two SWM *p–y* curves generated for two different P_{pl} values. Also, these curves are evolved accounting for the effects of the FAF and pile damages, and are generated upto the ultimate point of PSS failure; these are not possible with the previous formulations. For this set of values of the parameters, the ultimate *p* and the corresponding *y* values are the highest in case of SWM. While, iterating through ranges of values of the additional parameters, SWM curves might

coincide with those from Reese et al. (1970) and API (2000) for some particular sets.

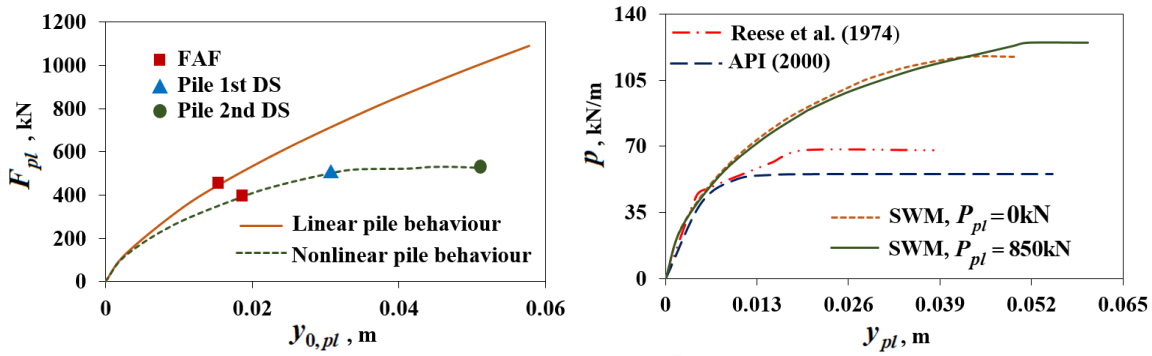

(a) (b)

Figure 3.18 (a) influence of pile structural nonlinearity and (b) comparative $p-y$ curves.

(f) Parametric Influence on pile-soil interaction

To investigate the parametric influences, the 'one factor at a time' approach is employed herein (described in Section 4.3). A reference PSS model is created with the base values (usually the average or near-average values of the ranges (adopted from literature or assumed based on the usual practice, as in Table 3.3) of the parameters (sorted out based on their tentative influences on PSS lateral responses and thus on LSTs). Other models are created by changing one parameter to a second value (usually the lower limit of its range) and then to a third value (usually the upper limit of its range), one at a time while keeping the other parameters at their base values, and repeating the process for all the parameters.

The study considers high strength deformed bars, basically comprising Fe 415, Fe 500 and Fe 550 (IRC, 2011); Fe415 has been most commonly used in construction, attributed to the highest ductility. Increase in υ_{pl} beyond 0.1 (which is near normal range) leads to significant decrease in $y_{0,pl}$. Thus, to observe the usual ranges of PSS responses in practice and the near maximum bounds of LST, models are created and analysed, with the lowest values (as in Table 3.3) of $f_{y,pl}$ and υ_{pl} as the respective base values. Effects of $f_{y,pl}$ and υ_{pl} are then examined through additional models generated with the higher values for these.

$K_{pl\text{-}s}$ and thus $L_{pl}/K_{pl\text{-}s}$ values for all the generated PSS models are computed and found to be within the range (Equation (3.5)), so that the piles can be analysed as flexible piles. Properties of the loose and dense sands have been adopted from Ashour and Norris (2000a).

As already mentioned, formulations in Reese et al. (1970) and API (2002) included only D_{pl} as pile parameter; hence, out of the results with respect to the parametric variations, the for the varying D_{pl} can be compared with those evaluated using Reese et al. (1970), as in Figure 3.19(a)) and API (2002) (Figure 3.19(b)) with respect to the soil depth of 0.8m.

Table 3.3 List of parameter values used for generating the PSS models

Parameter	base value		second value		third value
$f_{y,pl}$ (MPa)	415		500		550
$f_{ck,pl}$ (MPa)	40		35		45
$\rho_{l,pl}$ (%)	4.290		2.140		5.360
$\rho_{t,pl}$ (%)	0.300		0.160		0.590
D_{pl} (m)	0.520		0.395		0.734
L_{pl} (m)	12		10		15
υ_{pl}	0.1		0.2		0.3
Sand type	φ_s°	γ_s (kN/m^3)	$(\varepsilon_{ss,50})_{42.5}$	η (kN/m^3)	A_u (calculate in the present study)
Loose	30	16.5	0.0050	12487	14.64
Dense	40	19.6	0.0025	74648	28.74

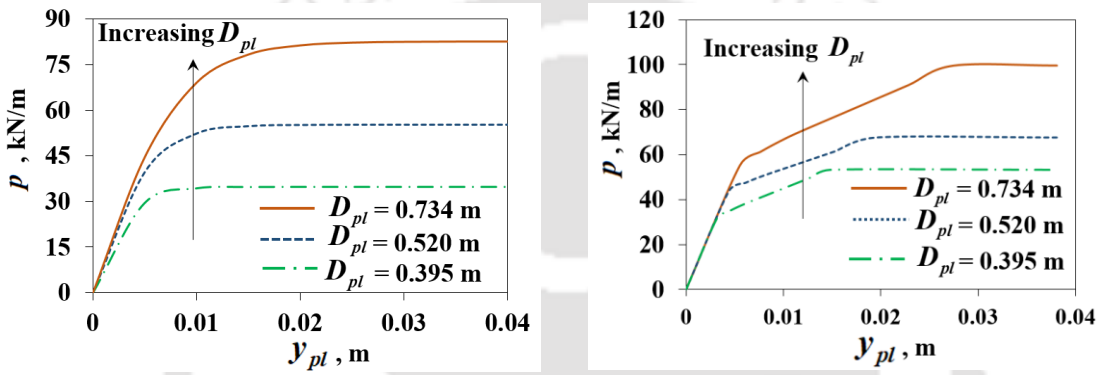

Figure 3.19 *p–y* curves using (a) Reese et al. (1970) and (b) API (2002).

- *Effect of Soil Friction Angle*

Influence of φ_s is illustrated through the transition in properties from loose to dense state variants of sand (Table 3.3). Pile acts stiffer with respect to loose sand, leading to a deeper SPW (consistent with Ashour and Norris (2000a)) and thus yielding larger y_{0,pl_i} at $\varepsilon_{ss,i}$, as compared to that in dense sand. For instance, at ε_{ss} of 0.01, (H_{spw}, $y_{0,pl}$) corresponds to (5.48m, 0.034m) in loose sand and (4.03m, 0.023m) in dense sand. Though a larger number of mobilised soil sublayers within a deeper SPW in loose sand contribute to $F_{pl,i}$, $F_{pl,i}$ value is higher in dense sand owing to its higher shear strength. Sand FAF and pile DSs commence (Figure 3.20(a), marked as in Figure 3.18(a)), as ε_{ss} increases. Owing to deeper SPW, A_u and thus FAF initiation (even if SL_s in the top sublayer is much less than unity) are attained earlier in loose sand; FAF has already had progressed to a few sublayers before any pile DS could occur. In dense sand, at least one or both the pile DSs and thus the pile ultimate load capacity (marked by grey shape in Figure 3.20(a)) might reach earlier (leading to fixed H_{spw} thereafter) before FAF could occur (due to higher A_u value (Table 3.3)) or SL_s could reach unity. Observation that the plastic hinge may develop

in pile before the FAF initiation in dense sand, as in Figure 3.20(a), tallies with that in Ashour and Norris (2008). Pile LSTs are achieved at higher ε_{ss} and thus larger $y_{0,pl}$ values in loose sand (Figure 3.20(a)). $F_{\max,pl}$ (maximum F_{pl}) and ultimate $y_{0,pl}$ are observed as about 55% more and 43% less respectively in dense sand compared to loose sand.

- *Variation in Width of Pile Cross Section*

  As D_{pl} increases, pile acts stiffer relative to sand leading to a deeper SPW and thus higher $F_{pl,i}$ and y_{0,pl_i} values at $\varepsilon_{ss,i}$; for instance, at ε_{ss} of 0.007, (H_{spw}, $y_{0,pl}$) corresponds to (5.48m, 0.024m) for D_{pl} of 0.520m and (7.47m, 0.032m) for D_{pl} of 0.734m. As D_{pl} decreases, H_{spw} decreases; the rate of decrease of H_{spw} with respect to the decrease in D_{pl} being slower, A_u is attained earlier leading to FAF initiation at a lower ε_{ss} and thus smaller $y_{0,pl}$ values (Figure 3.20(b)). At that instant, (ε_{ss} , H_{spw}, $y_{0,pl}$) corresponds to (0.0055, 5.48m, 0.019m) for D_{pl} of 0.520m and (0.0063, 7.47m, 0.029m) for D_{pl} of 0.734m. Pile LSTs are attained at higher ε_{ss} values in case of pile with smaller D_{pl}; however, for the case with larger D_{pl}, accumulation of $y_{pl,j}$ s over more sublayers within a deeper H_{spw} leads to larger $y_{0,pl}$ values (Figure 3.20(b)) at those instants. Increments in $F_{\max,pl}$ and ultimate $y_{0,pl}$ are observed to be 110.19% and 7.60%, and 417.70% and 28.66% when D_{pl} is increased from 0.395m to 0.520m (i.e., 31.65%), and to 0.734m (i.e., 85.82%) respectively.

- *Variation of Longitudinal Reinforcement Ratio in Pile*

  With increasing $\rho_{l,pl}$ in pile, pile acts stiffer relative to sand, leading to a deeper SPW and thus higher $F_{pl,i}$ and y_{0,pl_i} values and earlier initiation of FAF. In case of a lower $\rho_{l,pl}$, FAF initiation at a higher ε_{ss} leads to a larger $y_{0,pl}$, even with a shallower SPW (Figure 3.20(c)); (ε_{ss}, H_{spw}, $y_{0,pl}$) corresponds to (0.0055, 5.48m, 0.019m) for $\rho_{l,pl}$ of 4.288% and (0.0064m, 5.30m, 0.021m) for $\rho_{l,pl}$ of 2.144% at that instant. With higher $\rho_{l,pl}$, pile LSTs are attained at higher ε_{ss} and thus larger $y_{0,pl}$ values; with very small $\rho_{l,pl}$, delay in the FAF initiation can cause pile first DS to occur very closely or even before it (Figure 3.20(c)). $F_{\max,pl}$ and ultimate $y_{0,pl}$ are observed to increase by 26.22% and 6.21%, and 38.13% and 9.58% when $\rho_{l,pl}$ is increased from 2.14% to 4.29% (i.e., 100%), and to 5.36% (i.e., 150%) respectively.

- *Variation of Transverse Reinforcement Ratio in Pile*

  For varying $\rho_{t,pl}$, F_{pl}–$y_{0,pl}$ response follows the same path through the FAF initiation till the pile first DS is achieved (Figure 3.20(d)). Thus, PSS LSTs are attained at similar ε_{ss}, $y_{0,pl}$ and $F_{pl,i}$ values irrespective of the $\rho_{t,pl}$ values. Pile ultimate DS occurs at larger ε_{ss}, $y_{0,pl}$ and $F_{pl,i}$ values (Figure 3.20(d)) with increasing $\rho_{t,pl}$. $F_{\max,pl}$ and ultimate $y_{0,pl}$ are

observed to increase by about 2.25% and 21%, and 34% and 257% with increase in $\rho_{t,pl}$ from 0.16% to 0.30% (i.e., 91%), and to 0.59% (i.e., 274%) respectively.

- *Variation of Grade of Reinforcement in Pile*

  $F_{pl} - y_{0,pl}$ response follows the same path until the FAF is initiated, at similar ε_{ss}, $y_{0,pl}$ and F_{pl} values irrespective of the $f_{y,pl}$ values (Figure 3.20(e)). Pile DSs occur at higher ε_{ss} and $F_{pl} - y_{0,pl}$ response follows the same path until the FAF is initiated, at similar ε_{ss}, $y_{0,pl}$ and F_{pl} values irrespective of the $f_{y,pl}$ values (Figure 3.20(e)). Pile DSs occur at higher ε_{ss} and thus larger $y_{0,pl}$ and higher F_{pl} values with increasing $f_{y,pl}$. Increments in $F_{\max,pl}$ and ultimate $y_{0,pl}$ are observed to be about 9.5% and 8.5%, and 15% and 13% when $f_{y,pl}$ is increased from 415 to 500 MPa (i.e., 20%), and to 550 MPa (i.e., 33%) respectively.

- *Variation of Grade of Concrete in Pile*

  With increase in $f_{ck,pl}$ in pile, deeper SPW is formed, leading to higher $F_{pl,i}$ and y_{0,pl_i} values and earlier initiation of FAF. With lower $f_{ck,pl}$, pile DSs are attained at higher ε_{ss} and thus larger $y_{0,pl}$ and lower F_{pl} (due to smaller pile capacity and soil capacity contribution from lesser number of soil sublayers from a shallower H_{spw}) values (Figure 3.20(f)). Increments and decrements in $F_{\max,pl}$ and ultimate $y_{0,pl}$ are observed to be 1.27% and 2.1%, and 3% and 2.4% when $f_{ck,pl}$ is increased from 35 to 40 MPa (14%) and to 45 MPa (29%) respectively.

- *Variation of Axial Load Ratio on Pile*

  With increase in υ_{pl}, deeper SPW is formed, leading to higher $F_{pl,i}$ and y_{0,pl_i} values, upto a certain level beyond which its influence is less pronounced; sand FAF and pile DSs are attained at lower ε_{ss} and thus lesser $y_{0,pl}$ values (Figure 3.20 (g)). Nominal increase of 2.3% in $F_{\max,pl}$, and decrements of 16% and 23% in ultimate $y_{0,pl}$ are observed when υ_{pl} is increased from 0.1 to 0.2, and 0.1 to 0.3 respectively; effects are negligible thereafter.

- *Variation in Length of Pile*

  L_{pl} ('flexible pile' category) has no effect on the features of pile-soil interaction and thus on the FAF and the pile LSTs.

With respect to D_{pl} , the result from the present study (Figure 3.20(b)) is compared with those evaluated using Reese et al. (1970) (Figure 3.19(a)) and API (2002) (Figure 3.19(b)). All of these show the same trend, i.e., pile with larger D_{pl} leads to higher p and y values before p gets constant.

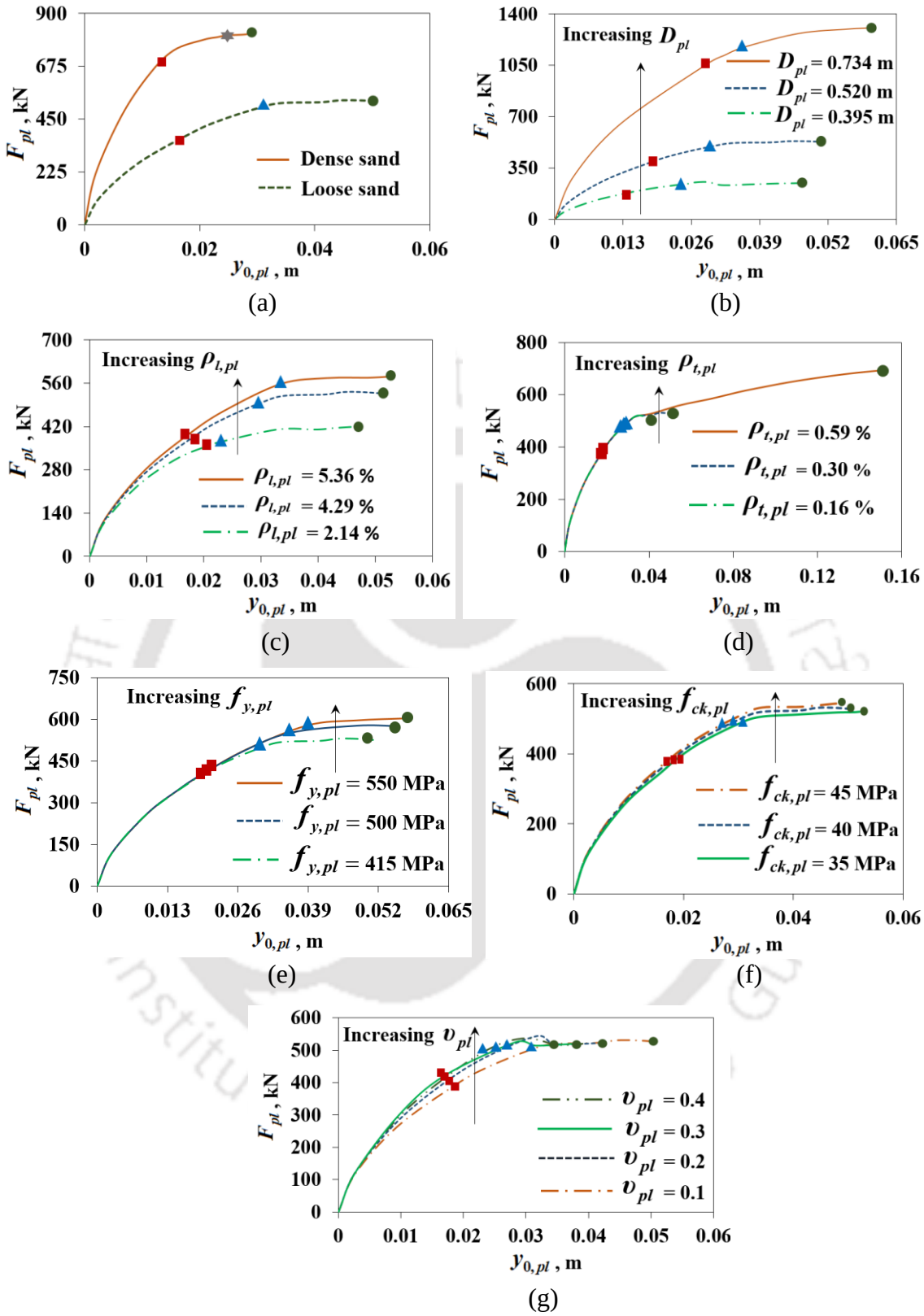

Figure 3.20 Effects of (a) φ_s , (b) D_{pl} , (c) $\rho_{l,pl}$, (d) $\rho_{t,pl}$, (e) $f_{y,pl}$, (f) $f_{c,pl}$ and (g) υ_{pl}.

3.3.6.2 Abutment-Backfill Interaction in the Study

The study adopts the abutment-backfill interaction by Shamsabadi et al. (2005) which considers a failure surface having a logarithmic spiral and a straight portion behind the

abutment, as depicted in Figure 3.21. Triangle CDE represents the ultimate Rankine SPW with inclination angle α_{bfr} and the logarithmic spiral arc $\overline{BC}$ must leave the abutment bottom at the takeoff angle α_{bft}. At the k^{th} value of the backfill (of unit weight γ_{bf} and Poisson's ratio v_{bf}) stress level SL_{bf} i.e., $SL_{bf,k}$, the failure surface geometry is characterised by the mobilised values (denoted with subscript 'k'), as in the Figure 3.21, of the backfill friction angle φ_{bf}, H_{ab} , α_{bfr} , α_{bft} and abutment-backfill interface friction angle δ_{abf}, which changes with level of loading up to the ultimate state with SL_{bf} =1; $\varphi_{bf,k} = SL_{bf,k} \cdot \varphi_{bf}$, and $H_{ab,k} = SL_{bf,k} \cdot H_{ab}$, $\alpha_{bfr,k} = SL_{bf,k} \cdot \alpha_{bfr}$, $\alpha_{bft,k} = SL_{bf,k} \cdot \alpha_{bft}$ and $\delta_{abf,k} = SL_{bf,k} \cdot \delta_{abf}$.

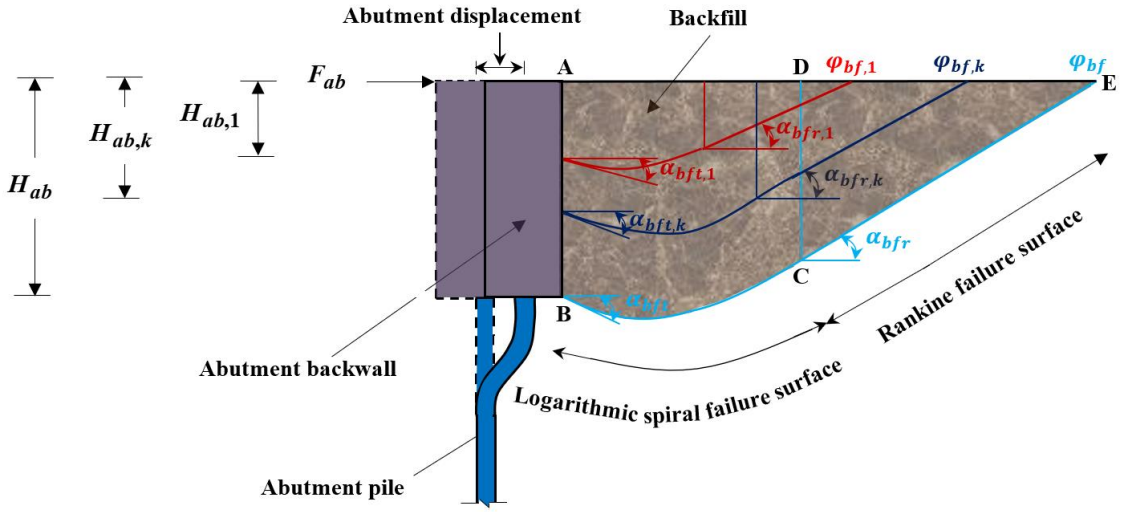

Figure 3.21 Geometries of the intermediate failure surfaces mobilised in the backfill and the seismic deformation of the abutment and the underlying pile.

Each k^{th} surface (with horizontal extent $X_{bf,k}$ from the backwall face) is divided into n numbers of vertical slices (all parameters denoted with subscript 'ik' corresponding to the i^{th} slice), as shown in Figure 3.22(a). i^{th} slice (of weight $W_{bf,ik}$ and base angle $\alpha_{bf,i}$) is in equilibrium under the interslice forces $E_{bf,ik}$ (horizontal) and $T_{bf,ik}$ (vertical) (Figure 3.22(b)), leading to the evaluation of $F_{ab,k}$ (horizontal component of the resultant passive force $P_{ab,k}$, with $F_{abf,k}$ being the vertical one). Employing some stress-strain relationships, e.g., as by Ashour et al. (1998) based on triaxial test data of sand, Duncan and Chang (1970) etc., the displacements of the soil slices $\Delta y_{bf,ik}$s (converting the shear strains $\gamma_{bf,ik}$s to horizontal strain $\varepsilon_{bf,ik}$s (as by Ashour et al., 1998) with $\varepsilon_{bf,50}$ as the ε_{bf} at 50% SL_{bf}) are computed (Figure 3.22(c)). Parameters with respect to a intermediately mobilised failure surface are computed in spreadsheets employing the expressions, as in Equation (3.7) and the repetition over increasing values of SL_{bf} till unity leads to the lateral force deformation capacity curve; a typical curve generated for an ABS with H_{ab} = 3.5m, φ_{bf} = 40°, D_w = 18.5m, γ_{bf} = 20.1kN/m^3 and δ_{abf} = 28° is shown in Figure 3.22(d).

In the transverse direction, the abutment stiffness and strength obtained for longitudinal direction were modified corresponding to wingwall effectiveness and participation, with with factors of 2/3 and 4/3, respectively (Maroney and Chai, 1994).

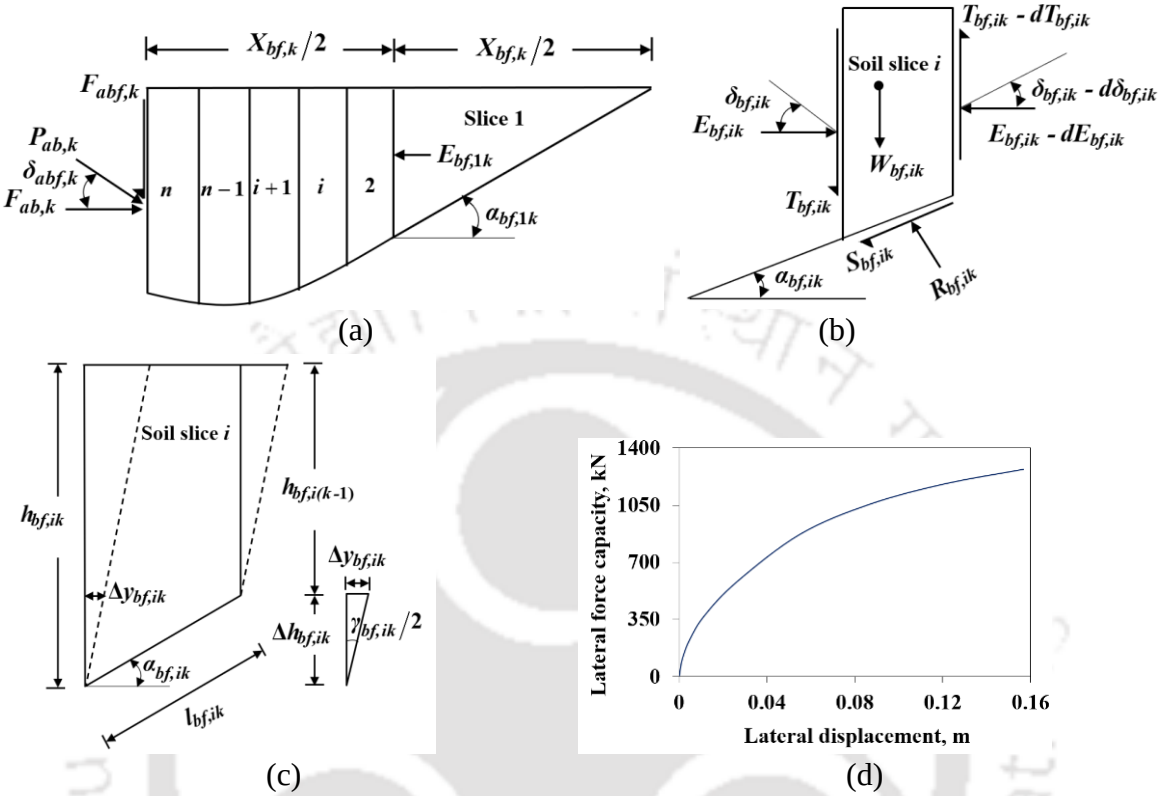

Figure 3.22 (a) Division of the failure surface into slices; (b) slice equilibrium under a set of forces; (c) deformed configuration of a slice (Shamsabadi et al., 2005); (d) an ABS lateral force deformation capacity curve evaluated in the study.

$$\alpha_{bfr} = (45^{\circ} - \varphi_{bf}/2);\ \sum_{i=1}^{n} dE_i = \frac{W_{bf,i}\tan(\alpha_{bf,i+}\varphi_{bf,i})}{1-\tan\delta_{abf,i}\tan(\alpha_{bf,i+}\varphi_{bf,i})};$$

$$\delta_{abf,i} = \tan^{-1}\left[\frac{(\sin(2(\alpha_{abr}-\alpha_{bf,i})))\sin\varphi_{bf,i}}{1+\sin\varphi_{bf,i}\cdot\cos(2(\alpha_{abr}-\alpha_{bf,i}))}\right];\ F_{ab} = \frac{\sum_{i=1}^{n} dE_i}{1-\tan\delta_{abf}\tan(\alpha_{bft}+\varphi_{bf})}; \quad (3.7)$$

$$y_{ab} = \sum \Delta h_{bf,i}\cdot 0.5\varepsilon_{bf,ik}(1+\nu_{bf})\sin(2\alpha_{bf,i});\ \nu_{bf} = 0.1+0.4SL_{bf};$$

$$\varepsilon_{bf,i} = \frac{SL_{bf}\cdot\varepsilon_{bff}\cdot\varepsilon_{bf,50}}{(\varepsilon_{bff}-\varepsilon_{bf,50})-SL_{bf}(\varepsilon_{bff}-2\varepsilon_{bf,50})}\ \text{(Duncan and Chang, 1970)}$$

3.4 DAMAGE MODELS FOR THE IAB COMPONENTS

This study generates its own damage models for the IAB components for yielding the LSTs corresponding to the respective properties in the study, which are employed while computing the respective fragilities. Although plenty of literature providing the LSTs exists

and which has been adopted in many subsequent studies (Section 2.4.3), the above necessity arises due to the peculiarity of LSTs being specific to the particular component properties, as the former would vary with the variation of the latter. The earlier prescriptions, were based on particular structural system characteristics in the respective studies. Besides, most of the previous damage models for pier did not incorporate all the possible failure modes and/or were evaluated for fewer DSs. Bearing LSTs corresponded to particular dimensions and material properties; LSTs in Hwang et al. (2001) were evaluated considering the capacity of the dowel bar only while ignoring that of the pad. Many past prescriptions for the ABS LSTs corresponding to the backfill mobilisation were obtained through extrapolation of the Caltrans guidelines (Caltrans, 1999) for the sets of H_{ab}s and φ_{bf}s in their studies. This might not give precise LST estimates for the sets quite different from the tested ones, as in Caltrans, (1999). In some studies, LSTs were taken in terms of backfill maximum displacement capacity $y_{\max,bf}$ like Zakeri et al. (2014); Choine et al. (2014); Nielson (2005). The latter two studies adopted $y_{\max,bf}$ as a fraction of H_{ab} based on a particular soil type, following Choi (2002); Martin and Yan (1995) respectively. LSTs will vary with other ABI parameters also like φ_{bf} and δ_{abf}s and not just H_{ab}. Similarly, pile-soil interaction characteristics and thus the LSTs of PSS change with its properties; the available LSTs are specific to the pile structural properties and soil profiles in their studies.

Thus, those prescriptions should not be adopted in other studies with different structural properties to avoid incorrect estimation of the desired results. Hence, in order to arrive at the reliable estimation of FCs specific to the IAB attributes in the study, the employed LST values should be specific to the IAB properties. Hence, the present study constructs its own damage models to yield the LSTs, instead of adopting from the literature. Those models are developed by considering bearing and pier as primary (govern the vertical stability and load carrying capacity; failure leads to bridge closure) and ABS and PSS as secondary (do not affect the vertical stability; failure leads to restriction on traffic conditions) components, so as to achieve similar consequences in terms of functionality and repair at the BS level as that at component level. This is done by defining four DSs for pier and bearing in such a way that those can be mapped directly onto BS DSs and those defined for ABS and PSS will be mapped onto the initial BS DSs, following Ramanathan (2012).

3.4.1 Pier

Pier damage model is based on flexural damages, definitions of which as discussed below. As the lateral force deformation capacity curve progresses, evaluated through the

displacement-controlled pushover analysis of pier (control node at the pier head) following the analysis for the axial load P_{pr}, the possibility of shear failure, P–δ collapse and longitudinal bar buckling are monitored.

As the pier undergo flexural deformation under lateral loading, four DSs are identified based on the acceptable criteria for compressive $\varepsilon_{c,\,pr}$ and tensile $\varepsilon_{s,\,pr}$ strains of the extreme concrete and steel fibres respectively, monitored at the critical sections (pier fixed ends), as done in many past studies (Section 2.4.3). LSs are set in terms of the lateral displacement of the pier top relative to the bottom, i.e., y_{pr}, as $y_{pr,\,fi}$ s with respect to flexure and i^{th} DS rank where, i = 1to 4 (for pier) (Table 3.4). These are converted to displacement ductility μ_{pr} (ratio of the instantaneous value of y_{pr} to that at yielding of the extreme longitudinal bar in pier), set as $\mu_{pr,\,fi}$ s for i^{th} flexural DSs.

(i) Slight Damage/Serviceability Limit State – Below this LS, the seismic response of the pier is within the linear elastic range. The bridge is in full operation with minor damage. To avoid remedial action after earthquake, residual crack width should not exceed 1mm nor should cover concrete spall so as to impair the functionality (Priestley et al., 1996).

(ii) Moderate Damage/Damage Control Limit State – Certain amount of repairable damage may be permissible like spalling of cover concrete requiring replacement and formation of wide cracks requiring injection grouting to avoid corrosion problems. Only limited service may be allowed for emergency vehicles. The required repair should be essentially superficial with no fracture of transverse reinforcement or buckling of the longitudinal reinforcement and the core concrete should not require replacement in the plastic hinge zones (Priestley et al., 1996).

(iii) Extensive Damage Limit State – Significant damage is expected. It is possible to repair the structure, however this may not be economically feasible and reconstruction might be necessary (Ger et al., 2012). Life safety is of prime concern with some margin against collapse of pier owing to reserved capacity beyond the damage control LS.

(iv) Complete Damage Limit State – Avoiding structural collapse is the main goal. Large permanent lateral deformation could occur and gravity load capacity is reduced significantly and replacement is required due to higher repair costs (Ger et al., 2012).

The study monitors the possibility of shear failure by checking if the shear capacity $V_{pr,s}$ the pier plastic hinge is reached before the flexural capacity $V_{pr,f}$ (i.e., F_{pr} from the pushover analysis) leading to a premature failure in a brittle mode. It is done by estimating $V_{pr,s}$ against μ_{pr} and comparing the $V_{pr,s} - \mu_{pr}$ and $V_{pr,f} - \mu_{pr}$ curves. If $V_{pr,s}$ is less than $V_{pr,f}$ at any

instant, shear failure occurs, located by the intersection of these curves, at the ductility designated as $\mu_{pr,s}$, as portrayed in Figure 3.23(a). $V_{pr,s}$ as function of μ_{pr}, i.e., $V_{pr,s}$ (μ_{pr}) is evaluated using the shear capacity model by Priestley et al. (1994) (Equation (3.8)) contributed by $V_{pr,s}^{c}$, $V_{pr,s}^{t}$, and $V_{pr,s}^{p}$, as the shear capacities contributed by concrete (evaluated as function of ductility) and transverse reinforcement, and axial compression resulting from a diagonal compressive strut respectively.

$$V_{pr,s}(\mu_{pr}) = V_{pr,s}^{c} + V_{pr,s}^{t} + V_{pr,s}^{p} \tag{3.8}$$

The Priestley's model incorporates the influence of axial load and ductility, which provides greatly improved predictions, as compared to the Codal recommendations like ASCE-ACI 426 (1974), ACI 318-89 (1989) etc., whereby those influences are either ignored or is at best treated in a simplistic fashion. ASCE-ACI 426 (1974) approach does not provide particularly good estimates for shear strength of columns and shows tentative excessively conservative estimates for low ductility levels. Adoption of Priestley's model is justified by the small scatter from experimental results. It is to be noted that, onset of shear failure is considered to be the ultimate LS. Hence, any additional element in the pier model to detect the failure and subsequently model the post failure degradation path and the axial failure (as by Elwood, 2004) is not required. Also, most codified equations determine the shear failure based on only the shear strength. However, for reliable prediction of the detection, complete force-deformation path should be involved. Priestley's model provides shear strength with relation to displacement ductility, hence allowing the comparison in the same frame and thus it is expected to determine the shear failure point precisely.

P–δ collapse, due to vertical instability, arises when the *P–δ* moment (i.e., product of P_{pr} and y_{pr}) exceeds the pier moment (M_{pr}) capacity and thus, the axial capacity is reduced below the existing gravity load owing to the plastic hinge disintegration. It is located as the intersection (if occurs) of the *P–δ* moment and the bending resistance versus y_{pr} (obtained from the pushover analysis) curves, as depicted in Figure 3.23(b), at the μ_{pr} value of $\mu_{pr,\delta}$.

Buckling of longitudinal bar, leading to untimely core concrete crushing at a lower $\varepsilon_{c,\,pr}$ compared to its ultimate value $\varepsilon_{cu,\,pr}$ (at fracture of tie with ultimate value $\varepsilon_{su,\,pr}$ of $\varepsilon_{s,\,pr}$), is monitored through the development of the critical tensile strain in the bar prior to it, at the μ_{pr} value of $\mu_{pr,b}$. The criteria (Feng et al., 2014) are shown in Table 3.4, where s_t is the tie spacing and d_b is the bar diameter

P–δ collapse and buckling are incorporated in the model in the same manner as done in case of shear failure (illustrated in Table 3.4). The value of LST against each DS of pier, in

terms of μ_{pr}, are standardised as $d_{i,pr}$ for the i^{th} DS.

Table 3.4 Limit state thresholds adopted for pier

Damage State	LSTs (from flexural analysis)
Slight	$d_{1,pr} \mid \mu_{pr}: y_{pr}: \varepsilon_{s,pr} = \varepsilon_{y,pr}$ (yield value of $\varepsilon_{s,pr}$)
Moderate	$d_{2,pr} \mid \mu_{pr} : \min \begin{pmatrix} y_{pr} : \varepsilon_{c,pr} = 0.004 \\ y_{pr} : \varepsilon_{s,pr} = 0.015 \end{pmatrix}$ (Priestley et al., 1996)
Extensive	$d_{3,pr} \mid \mu_{pr} : y_{pr} : \varepsilon_{cu,pr} = 0.004 + \frac{1.4\rho_{t.pr}\varepsilon_{su,pr} f_{y,pr}}{f_{cc,pr}}$ (Mander et al., 1988)
Collapse Prevention	$d_{4,pr} \mid \mu_{pr} : \min \begin{pmatrix} y_{pr} : M_{pr} \le 0.85 M_{\max,pr} \\ y_{pr} : \varepsilon_{s,pr} = 0.75\varepsilon_{su,pr} \end{pmatrix}$ (Stefanidou and Kappos, 2017) $M_{\max,pr}$ (= maximum M_{pr})
Shear Failure at $\mu_{pr,s}$	Bar buckling (Feng et al., 2014) $\mu_{pr,b} : y_{pr} : \varepsilon_{s,pr} = \begin{matrix} 0.06 : s_t / d_b > 4 \\ 0.09 : s_t / d_b \le 3 \end{matrix}$
Final value to be adopted	$d_{i,pr}$:min(μ_{pr,f_i} , $\mu_{pr,f}$, $\mu_{pr,b}$, $\mu_{pr,\delta}$)

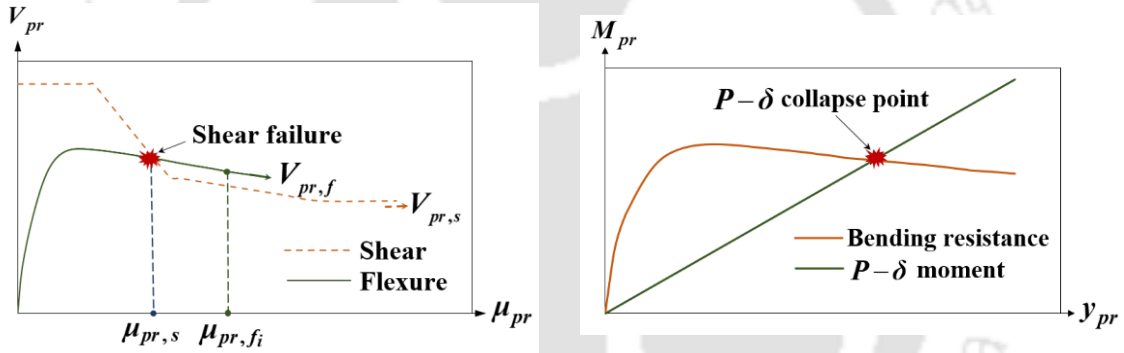

(a) (b)

Figure 3.23 (a) Check for shear/flexure failure and (b) Illustration of P–δ collapse.

3.4.2 Bearing

Since the bridge deck is continuous over the bearing supports, the possibility of pounding is eliminated. Being continuous and having rigid connections with the abutments, deck collapse in the longitudinal/transverse direction is due to the vertical instability resulting from loss of supports underneath, as the bearings slip and topple about the capbeam edge.

Under lateral loading, the bearing rubber pad remains elastic until about 100% shear strain, thereafter it experiences significant damages and finally tearing over the range of 300 to 350% shear strain. Hence, the pad strain magnitude is monitored to check the possible damage due to shear deformation as the deck moves horizontally and found to be within elastic limit. Four DSs and the respective LSTs set as $d_{1,br}$, $d_{2,br}$, $d_{3,br}$ and $d_{4,br}$ in terms of bearing displacement are described in Table 3.5. The last two LSs are based on the bearing seat width W_{seat}, which being dependent on cap beam width and L_{oh} in the the

longitudinal and transverse directions respectively are different in these directions.

(i) Slight Damage Limit State – This LS begins at the onset of the fracture of dowel bars, requiring some degree of repair (girder retention) in addition to deck realignment (Nielson, 2005). Only temporary loss of access occurs at this DS which can be restored (Avsar, 2009).

(ii) Moderate Damage Limit State – This LS begins on the verge of bearing sliding, leading to 50% service disruption. Depending on the variation in characteristics of the bearing constituents (Chapter 4), there can be two cases leading to this LS. One case involves the dowel fracture followed by the pad reaching $F_{u,brp}$, resulting in instant sliding, while in other case, sliding is restricted by the dowels in place, with its fracture occurring much after $F_{u,brp}$ is reached. As such, LST with respect to the latter case is taken as that at the fracture.

(iii) Extensive Damage Limit State – This DS corresponds to usability of the bridge for emergency traffic only, when the sliding displacement exceeds half of W_{seat}.

(iv) Complete Damage Limit State – For this LS to occur, the bearing sliding displacement is to be limited not to exceed beyond W_{seat} to avoid toppling of the bearing about the cap beam, or else the superstructure loses its support to carry the imposed gravity load.

Table 3.5 Limit state thresholds adopted for bearing

Damage State	Limit State Thresholds
Slight	$d_{1,br} : y_{u,brd}$
Moderate	$d_{2,br} : \text{either} \begin{pmatrix} y_{u,brp_{sh}} (\text{if} > y_{u,brd}) \\ y_{u,brd} (\text{if} > y_{u,brp_{sh}}) \end{pmatrix}$
Extensive	$d_{3,br} : y_{brp,sl} = W_{seat} / 2$
Collapse Prevention	$d_{4,br} : y_{u,brp_{sl}} = W_{seat}$

3.4.3 Pile-Soil System

With the procedure, as discussed in Section 3.3.6.1, the stress-strain behaviour of the pile sectional constituent material fibres (from the pushover analysis output) and the detection of the sand FAF initiation as well as the progression (from the SWM calculations) can be assessed simultaneously and at any instant. The PSS damages are discussed as below:

(a) Failure in loose sandy soil

Failure in loose sand (as in the present study) is assumed to be initiated when FAF in a soil sublayer occurs, causing sand at that depth to flow around pile in a local bearing capacity failure than for any additional sand to be brought to failure and added to the already developed SPW (Ashour et al., 1998). It is controlled by the ultimate value A_u of A, with

expression given in Equation (3.9) as,

$$A = (p / D_{pl}) / \Delta\sigma_h \ , \ A_u = \frac{k_a[(k_p)^4 - 1] + k_0 (k_p)^2 \tan\varphi_s}{k_p - 1}; \quad (3.9)$$

where, $k_0 = 1 - \sin\varphi_s$, $k_a = (1 - \sin\varphi_s)/(1 + \sin\varphi_s)$, $k_p = (1 + \sin\varphi_s)/(1 - \sin\varphi_s)$

As FAF is initiated at the top sublayer, its p and H_{spw} become constant. F_{pl} is thereafter contributed by the increasing p values in the sublayers below until the occurrence of FAF.

(b) Structural damages in pile

Damage states in reinforced concrete pile are identified based on the material strains at its most critical section, as done for reinforced concrete pier in studies like Hose et al. (2000) and Kowalsky (2000) etc. As stated in Budek et al. (2010), the section just below the fixed-head of the concrete pile is expected to be the first potential plastic hinge zone along its length from the top (as also reported by Song and Chai (2018)), along with the damages arising from the second highest bending moment) or as a result of the lack of detailing in reinforcement curtailment. This study, while observing the same, defines the DSs in pile based on the flexural damages just below its fixed head. Foundation is considered to be a secondary component (Ramanathan, 2012), as its damages do not have noticeable effects on bridge vertical stability (Pahlavan et al. (2016)) Hence, two DSs are considered, so as to map with the initial two DSs at the BS level, as discussed below:

(i) Serviceability DS – Repairable minor functional damage occurs following the end of essentially elastic behaviour in pile. Traffic may be required to be stopped, or restricted after an earthquake, while remedial measures are undertaken (Priestley et al., 1996).

(ii) Ultimate DS – Significant damage, following the fracture of the transverse reinforcement in pile is expected such that replacement is necessary, since major repairs at the pile location below the soil might not be feasible practically.

As the F_{pl}–$y_{0,pl}$ curve gets evovled, PSS damages and failure are monitored and the respective LSTs are obtained in terms of $y_{0,pl}$ (following Bradley et al., 2010) and set as $d_{1,pl}$ and $d_{2,pl}$ for the pile structural DSs and d_{FAF} for the FAF initiation. PSS LSTs are listed in Table 3.6, where, $\varepsilon_{y,pl}$, $\varepsilon_{su,pl}$, $\varepsilon_{c,pl}$ and $\varepsilon_{cu,pl}$ hold the same notations for pile as for pier.

Analysis of the damage model for the PSS samples (Chapter 4) reveal that there is no fixed sequence between d_{FAF} , and $d_{1,pl}$ and $d_{2,pl}$. In some samples, d_{FAF} precedes $d_{1,pl}$, while in some, d_{FAF} lies between $d_{1,pl}$ and $d_{2,pl}$. Hence, DSs corresponding to the PSS type in the study are based on pile LSs only. Although FAF is not considered as a DS, its initiation and progression (hence monitored) do affect the pile DSs by restricting the SPW depth and

thereby interfering with the y_{pl} profile and thus influencing the $y_{0,pl}$ values.

Table 3.6 Limit state thresholds adopted for PSS

Limit State	Limit State Thresholds
Serviceability (pile)	$d_{1,pl} \mid y_{0,pl} : \varepsilon_{s,pl} = \varepsilon_{y,pl}$
Ultimate (pile)	$d_{pl,2} \mid y_{0,pl} : \varepsilon_{cu,pl} = 0.004 + \frac{1.4\rho_{t.pl}\varepsilon_{su,pl} f_{y,pl}}{f_{cc,pl}}$
Sand FAF	$d_{FAF} \mid y_{0,pl} : A = A_u$

3.4.4 Abutment-Backfill System

In many studies, ABS LSs are set in terms of $y_{max,bf}$, as a fraction of H_{ab}, proposed, e.g., as $0.06H_{ab}$ for cohesionless soil by Martin and Yan (1995) and $0.05H_{ab}$ by Choi (2002). From the analyses of the ABS damage model for the samples (Chapter 4), mean $y_{max,bf}$ is found as 0.046 H_{ab}, with coefficient of variation of 0.082. Dispersion as well as difference with the previous prescriptions is due to parameter contributions other than H_{ab}, like φ_{bf} and δ_{abf} (taken as factor $\delta_{abf,f}$, being independent of φ_{bf}). Analyses reveal $0.1y_{max,bf}$ and $0.35y_{max,bf}$ to be approximately equal to y_{ab} values at $0.72SL_{bf}$ and $0.90SL_{bf}$ respectively, attaining $y_{max,bf}$ at$1.0SL_{bf}$. Hence, for the generalisation, SL_{bf} is taken as basis for DS (as discussed below) identification and LSs are set in terms of y_{ab} (Table 3.7) (LSTs set as $d_{1,ab}$, $d_{2,ab}$ and $d_{3,ab}$).

(i) Slight Damage Limit State– This LS is reached as the backfill soil shear modulus starts degrading. Repairable minor functional damage occurs in this DS.

(ii) Extensive Damage Limit State – In this LS, there is a significant reduction in the backfill shear modulus. Repairable major functional damage occurs in this DS.

(iii) Complete Damage Limit State – This LS is reached which the lateral stiffness becomes zero requiring component replacement.

Table 3.7 Limit state thresholds adopted for ABS

ABS damage states	BS-level damage state	Component-level damage states		Limit State Thresholds
		Zakeri et al. (2014)	Choine et al. (2014)	
Slight	Slight	0.1 $y_{max,bf}$ (moderate)	0.35 $y_{max,bf}$ (extensive)	$d_{1,ab} \mid y_{ab} : SL_{bf} = 80\%$
Extensive	Moderate	0.35 $y_{max,bf}$ (extensive)	$y_{max,bf}$ (ultimate)	$d_{2,ab} \mid y_{ab} : SL_{bf} = 95\%$
Ultimate	Extensive	$y_{max,bf}$ (ultimate)	-	$d_{3,ab} \mid y_{ab} : SL_{bf} = 100\%$

3.5 MODELING OF DAPA AND COMPARATIVE ASSESSMENT WITH CONVENTIONAL PUSHOVER ANALYSIS

Since, the study intends to adopt adaptive capacity spectrum method for the generation of FCs of the IAB class in the study, the employed DAPA within the method is performed on a typical 3-column bent to understand its algorithm. The conventional pushover analysis is also carried out on the bent. The differences in the lateral force deformation capacity curves of the 3-column bent as well as the lateral path profiles of the components, obtained from both the types of analyses, are observed. DAPA performs eigenvalue analysis at the beginning of an analysis step based on the instantaneous stiffness of the individual components at the end of the previous step and requires the inertia masses (lumped masses of the individual components at the respective levels) of the structure to be modeled in updating the shape and the magnitude of the load vector.

3-column bent consists of three piers with height, diameter, longitudinal and transverse reinforcement ratios of 6m, 1.4m, 2.185% and 0.30% respectively. Each pier is supported on eight reinforced concrete square-shaped piles of length, plan dimensions, longitudinal and transverse reinforcement ratios of 12m, 0.52m, 4.290% and 0.587% respectively. There are 12 bearings, each consisting of a 25 mm rubber pad with plan dimensions of 0.61 m × 0.56 m and two 25mm diameter steel dowel bars embedded within. Individual lateral force deformation capacity curves (a resultant one for all the bearings at the bearing level, one for each pier at the pier level and a resultant one for all the PSSs at the foundation level) are generated and incorporated in ZeroLength spring elements in OpenSees. Thus, the 3-coulmn bent is treated as an integrated system of these springs at the respective locations.

DAPA is first of all carried out on the assembly of a pier and the underlying foundation, referred to as pier-foundation system. The calculated tributary weight from the capbeam and its self-weight are lumped at the top node of the pier. Weight of the pile cap and those of the piles at the level of the pile cap, for its length upto the SPW are lumped at the interconnecting pier bottom node-top node of the foundation. The nominal displacement load vector to be applied on the two mass system is computed from the initial eigen value analysis using the initial stiffness of the components and the lumped mass in the excel spreadsheet and is normalised with respect to the top node. With a step size of 0.001 and the pier top node as the control node, the 1st step of the analysis is carried out in OpenSees. The computations of the stiffness states of the components and thus the instantaneous eigen value analysis are carried out in the spreadsheets at the end of each step to obtain the load

vector to be inputted in OpenSees for the next analysis step. With the updated load vector at each step, analysis is continued for as many steps, as required, till the DSs are attained.

The resulting base shear-top displacement curve for the pier-foundation system (upto the instant of ultimate damage in pile) is shown in Figure 3.24(a) where, the curves generated using both conventional pushover analysis and DAPA are compared. It is seen that for the initial few displacement increments, both the curves follow the same path, however the curves start diverging with increasing level of nonlinearity in the components. The conventional pushover analysis overestimates the ultimate displacement capacity of pier-foundation system. It is observed that the adaptive load pattern changes the relative magnitudes of loads in the members, as in Figure 3.24(b), wherein, the pier in a pier-foundation system attains larger deformation during the conventional pushover analysis compared to the DAPA case at the instant of ultimate damage in pile. As the pile is more flexible than the pier, DAPA updates the load pattern in a way such that pile undergoes larger displacement resulting in lesser displacement in pier for the same control node displacement as that in the conventional pushover analysis. This results in more damage accumulation in the relatively flexible component, i.e., pile, as get reflected by DAPA.

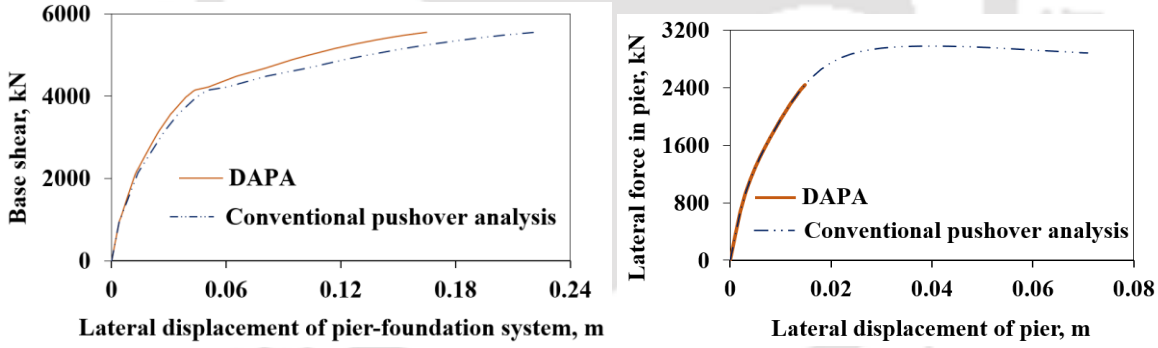

Figure 3.24 (a) Pushover curves for the pier-foundation system and (b) force-deformation of the pier.

Having evaluated the curve for each pier-foundation system, the resultant curve for all three such systems in the bent, which represents the entire bent, is obtained by combining them in parallel configuration. Thus, for the two mass system obtained by integrating the bearing spring with the bent spring, i.e., the bearing-bent system, the conventional pushover analysis and the DAPA are carried out. Figure 3.25(a) shows the comparison between the curves obtained. Here also the same trend is observed, as in the case of pier-foundation system (Figure 3.24(a)), where the curves start diverging as nonlinearity progresses in bearings and the conventional pushover analysis shows larger capacities compared to that

obtained by the DAPA till the attainment of the ultimate force capacity of the bearings. As the stiffness of the bearings start degrading by larger amount (after yielding of the dowel bars), a large proportion of the control node displacement gets concentrated as the internal deformation of the bearings, resulting in lesser deformation in the bent compared to the conventional pushover analysis, as can be observed in Figure 3.25(b). Thus, updating the load vector, as in DAPA algorithm, will lead to the actual distributions of the deformations among the components and thus the propagation of the corresponding damages.

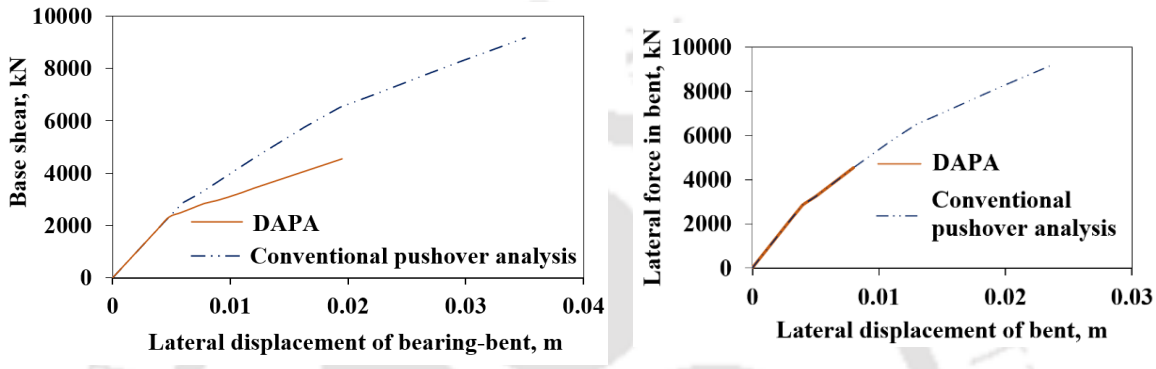

(a) (b)

Figure 3.25 (a) Pushover curves of bearing-bent system and (b) bent force-displacement.

3.6 SUMMARY

This chapter discusses the structural attributes of the adopted Integral Abutment Bridge (IAB) class. The identified seismic characteristics of those components are narrated and the modeling aspects to approximately simulate the behaviour of the components are discussed. Analytical models are generated (a) in OpenSees for pier and Pile-Soil System (PSS), (b) adopting the logarithmic spiral failure surface model to simulate the abutment-backfill interaction with respect to Abutment-Backfill System (ABS) and (c) in the study for bearing, and the corresponding numerical models for the respective samples are generated. Pile-soil interaction is modeled by linking the finite element model of the PSS with the Strain Wedge Model (SWM) computations for the PSS carried out herein in spreadsheets. Convergence between SWM and the beam on Winkler foundation problem of the pile is carried out herein through the displacement-control pushover analysis of the PSS while iterating with the updated modulus of subgrade reaction profile throughout the pile length computed from SWM each time. The implemented technique is validated through good agreement with the results of a past field test. Thus, the lateral force deformation capacity curves of the components are generated through pushover analysis and the mathematical expressions relevantly. The study has developed individual component damage models to

identify the Damage States (DSs) and yield the Limit State Threshold values (LSTs) values for the components. ABS LSTs are prescribed based on the backfill stress level, which can correlate with the DSs more realistically than just the abutment height, as it involve the other abutment-backfill interaction parameters as well such as the backfill friction angle and the abutment backfill interface friction angle; pier LSTs are based on the possible failure modes apart from flexure. The damage models yield the LSTs specific to the component properties in the study, which would lead to more precise fragility estimates for the adopted IAB class, instead of adopting prescriptions from literature to avoid error propagation. A preliminary modeling of Displacement based Adaptive Pushover Analysis (DAPA) is carried out to understand its algorithm, as it will be employed subsequently in the adaptive capacity spectrum method of analysis of the bridge system for the seismic demand assessment. Its ability to simulate the actual deformation profiles and the propagation of damages in the components as nonlinearity progresses within the various components of the bridge system are observed, while investigating the consequences of the DAPA on a typical three column bent and comparing the results with those from the conventional pushover analysis are made.

Chapter 4
UNCERTAINTY TREATMENT IN FRAGILITY FORMULATION

CONTENTS

4.1 INTRODUCTION

The study follows the recent trend of taking up the probabilistic framework of assessing the seismic vulnerability through the generation of FC. Since none of the capacities (LSTs) and demands (EDPs) corresponding to a DS of a given component in a structural system is deterministic, precise evaluation of the expected values of the assessment output in the form of FCs is required. Because the analytical fragility method uses bridge models and suites of real or synthetic GMs instead of the actual damage data, the associated uncertainties have to be considered and mitigated throughout the entire process (Dukes and Padgett, 2008). Hence, in fragility formulation, the different types of uncertainties which exist in engineering systems (Haldar and Mahadevan, 2000) can be dealt with by performing uncertainty analysis and sensitivity analysis when evaluating the models (Pathmanathan et al., 2019). Reliability of the computational predictions very much depend on (a) uncertainty analysis which involves uncertainty characterisation and propagation (Pathmanathan et al., 2019) and (b) sensitivity analysis which reflects how uncertainty in the model outputs can be apportioned to uncertainties in the inputs (Saltelli et al., 2008). This chapter deals with uncertainty and sensitivity analyses, conducted in tandem to arrive at the probabilistic seismic capacity models and PSDMs, required in formulating the fragility. Uncertainty treatment in the present study is shown as a flowchart in Figure 4.1.

4.2 UNCERTAINTY CHARACTERISATION

The first step of uncertainty analysis involves characterising the input parameters, treated as the random variables in the fragility formulation. The respective practical probable ranges are gathered through a literature survey and modeled with certain probability distributions, either assumed or referred to the literature. The distribution properties ascertained include mean μ, standard deviation σ, coefficient of variation λ, median θ, logarithmic standard deviation ζ, lower l and upper u limits, as in Table 4.1.

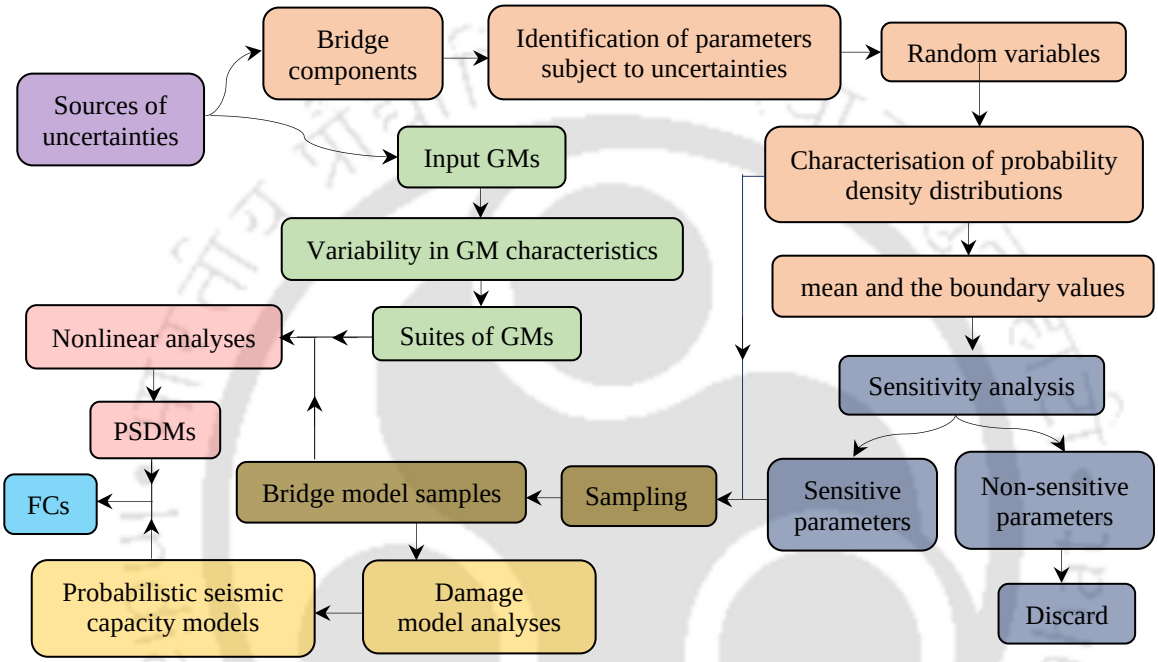

Figure 4.1 Flowchart summarising the uncertainty treatment in fragility formulation.

4.2.1 Uncertainty in Structural Geometric Parameters

The geometric parameters which are varied include H_{pr}, D_{pr}, D_{pl}, L_{pl}, L_{br}, B_{br}, h_{br}, d_{brd}, W_d, T_d, L_{sp}, D_{ss}/L_{sp}, H_{ab}, T_{ab} (abutment thickness), L_{ww} (length of wingwall), I-girder section dimensions such as web thickness T_w, top flange thickness T_{tf}, bottom flange thickness T_{bf}, bottom flange width W_{bf} and top flange width W_{tf} (obtained through a multiplier $W_{tf\text{-}m}$ applied to D_g). The ranges of the uniform distribution assumed for them are displayed in Table 4.1, along with the referred literature.

Bearing pad dimensions are adopted following Cl. 916.3.3 of IRC (1987) which implies $1 \leq L_{br}/B_{br} \leq 2$ and $0.1 \leq h_{br}/B_{br} \leq 0.2$. Starting with a minimum value of 0.4 (for L_{sp} above 15 m (Ramanathan, 2012)), varying L_{br} (as in Table 4.1) yields B_{br} and h_{br} sample values based on L_{br}/B_{br} and h_{br}/B_{br} variations. With the decided n_g (Section 3.2.1), the number of bearings and thus the tributary load P_{br} on each bearing in a BS sample are fixed. L_{br} and B_{br} values are iteratively paired up such that the condition $2\text{MPa} \leq \sigma_m \leq 10\text{MPa}$ (Cl. 916.3.6

of IRC, 1987) is obliged for all the samples. I-girder web thickness T_w is fixed providing a minimum of 0.2 m plus the duct hole diameter, and minimum thickness of both the top T_{tf} and bottom T_{bf} flanges is kept as 200mm, following Cls. 9.3.1.1, and 9.3.1.3 respectively of IRC (2000b).

n_{pl} at each bent as well as the abutment is fixed while satisfying the allowable settlement criterion for the pile foundation (adopted as 20mm to 30mm (Subsection 3.2.4)) in loose sand for the superimposed dead load. Thus, n_{pl} is also uncertain, owing to the variations in the BS geometric parameters and thus the superimposed load.

Table 4.1 Probability distribution properties of IAB geometric parameters in the study

Parameter	l	u	Remarks
L_{sp} (m)	20	50	Priestley et al. (1996); Avsar (2009); White (2007); Kumar and Babu (2016)
W_d (m)	11	26	DRTH (2009)
T_d (m)	0.20	0.30	IRC (2000b)(l), Assumed(u)
D_{ss}/L_{sp}	0.04	0.05	Ramanathan (2012); Kumar and Babu (2016)
T_w	0.20	0.30	IRC (2000b)(l), Naik and Yashavantha (2016); Peera et al. (2014)(u)
T_{tf} / T_{bf}	0.20	0.40	IRC (2000b)(l), Peera et al. (2014); Bhawar et al. (2015); Naik and Yashavantha (2016)(u)
W_{bf}	0.50	0.80	Peera et al. (2014); Bhawar et al. (2015); Naik and Yashavantha (2016)
$W_{tf\text{-}m}$	0.60	0.80	
D_{pr} (m)	0.80	2.00	Ramanathan (2012) (slightly relaxed)
H_{pr} (m)	5.0	15.0	Based on adopted H_{pr}/D_{pr} range of 2.5-18.75
D_{pl} (m)	0.350	0.800	Hwang et al. (2001)(l), Assumed(u)
L_{pl} (m)	10.0	15.0	Based on the flexible pile category criteria
L_{br} (m)	0.40	0.75	Ramanathan (2012)(l), Fusion of Technology(u)
B_{br} (m)	0.20	0.75	Based on L_{br}/B_{br}, as per IRC (1987)
h_{br} (m)	0.02	0.15	Based on h_{br}/B_{br}, as per IRC (1987)
d_{brd} (m)	0.025	0.040	IRC (2014b)(l), Maximum value used in practice(u)
H_{ab} (m)	2.0	5.0	Paraschos (2016)
L_{ww} (m)	2.0	4.0	Paraschos (2016)(l), White (2007)(u)
T_{ab} (m)	1.0	1.5	Paraschos (2016); Article 11.6.1.3 (2008)(l), Assumed(u)

4.2.2 Uncertainty in Material and Sectional Detailing Parameters

Structural and geotechnical material properties which are varied include f_{ck}, f_y, E_{st}, E_c , G, φ_s (thus, γ_s, η and $(\varepsilon_{ss,50})_{42.5}$), φ_{bf} (thus γ_{bf} and $(\varepsilon_{bf,50})_{42.5}$, i.e., $\varepsilon_{bf,50}$ at overburden pressure of 42.5kPa) and δ_{abf}, as in Table 4.2. The bridge class is assumed to be built in grade of concrete varying from 25 MPa to 45 MPa with the respective strengths assumed to follow certain distribution parameters to achieve the expected degree of quality control to be

exercised at the site. Reinforcing bars employed are of grade Fe 415. Variations are assumed for f_y and f_u (based on a statistical analysis of the strength test results of about 500 samples by Basu et al., 2004) and ε_{su} (as evaluated by Firat, 2016 for different diameter bars, though of a different grade) with the respective distribution parameters listed in Table 4.2. Those uncertainties are mainly associated with the strength of material itself, cross-sectional area, rate of the test loading, combined usage of reinforcing steels belonging to different groups and batches, effect of bar diameter on its mechanical properties, the nature and source of the data etc. (Firat, 2016). Uncertainties inherently associated with the empirical expressions used for determining E_c and μ_{br} are accounted for by applying multiplicative factors $E_{c,MF}$ and $\mu_{br,MF}$ respectively to the expressions, following distribution parameters, as in Table 4.2. ρ_l and ρ_t are based on the allowable minimum and maximum total area of longitudinal reinforcement A_l and transverse reinforcement spacing s_t respectively. Size and number of longitudinal bars are configured based on bar spacing satisfying the specifications of Cl. 15.2.1 of IRC (2011). Relevant parameters in Table 4.2 are designated with '*pr*', '*pl*' and '*brd*' in subscripts of the corresponding symbols for pier, pile and dowel bar respectively.

4.2.3 Uncertainty in Other Miscellaneous Parameters

Apart from the above parameters, superstructure mass is also considered a random variable, due to uncertainties from various incidental sources like the presence of parapets and barrier rails, electric poles and other equipment, re-pavement procedures, material densities etc. (Ramanathan, 2012). This is accounted for by applying a multiplicative factor $S_{m,MF}$ with distribution properties adopted from Ramanathan (2012) (as in Table 4.2) where the bounds are established by estimating the additional mass observed from the review of bridge plans.

Modeling uncertainty is another variant of uncertainty. System analysis models are only approximate representations of actual behaviour. Past experience on the difference between computational model and actual behaviour can be used to develop a statistical description of modelling error and include as an additional variable in the reliability analysis. Haldar and Mahadevan (2000) suggested variability associated with modeling to be taken as 0.25.

4.2.4 Uncertainty in Ground Motion Characteristics

GMs involve uncertainties and differences in severity, frequency and duration due to various fault rupture mechanisms causing the GMs and source-to-site distances, which when subjected to a structure cause variations in its responses. GMs for structural analyses should reflect all the characteristic variations, thus requiring appropriate selection.

Table 4.2 Probability distribution properties of IAB material, section detailing and miscellaneous parameters in the study

Parameter	Probability distribution			Remarks
	Type	Parameters		
Grade of concrete	Uniform	l = M25	u = M45	BIS (2010)(l), BIS (2000)(u)
f_{ck} (MPa) M25	Normal	μ = 33.75	σ = 5.30	BIS (2009)
f_{ck} (MPa) M45		μ = 56.55	σ = 7.00	BIS (2009)
f_y (MPa)		μ = 509.81	σ = 43.00	Basu et al. (2004)
f_u (MPa)		μ = 620.68	σ = 43.61	Basu et al. (2004)
ε_{su}		μ and l = 0.145	λ = 0.173	Firat (2016)
E_{st} (GPa)		μ = 201	λ = 0.033	Mirza and McGregor (1979)
G (MPa)	Uniform	l = 0.80	u = 1.20	IRC (1987)
φ_s °		l = 27	u = 35	Laboratory 8
γ_s (kN/m^3)		l = 16.5	u = 19.70	Appendix C
η (kN/m^3)		l = 4800	u = 16000	Appendix C
φ_{bf} °		l = 35	u = 45	Laboratory 8
γ_{bf} (kN/m^3)		l = 18.50	u = 21.70	Appendix C
δ_{abf}		l = 0.60	u = 0.80	Shamsabadi et al. (2007)
A_l (%)		l = 0.80	u = 4.00	BIS (2000)
s_t (m)		l = 0.08	u = 0.30	BIS (2000)
$E_{c,MF}$		l = 0.80	u = 1.20	BIS (2000)
$S_{m,MF}$		l = 0.80	u = 1.20	Ramanathan (2012)
$\mu_{br,MF}$	Lognormal	θ = 1.0	ζ = 0.10	Mander et al. (1996); Dutta (1999)

The simplest criterion for GM selection involves identifying the characteristic magnitude and the site to source distance pairs for the site of the structure and selecting bins of records with the target earthquake magnitude and source-to-site distance pairs, permitting a limited variation (Shome et al., 1998). Influence of the site soil profile on the seismic GMs forms an additional selection criterion. Dhakal et al. (2006) proposed criteria based on magnitude, distance, seismotectonic and local soil characteristics. GM duration also forms a criterion (Malhotra, 2003), particularly for energy-based indices while being insignificant for displacement-based demand indices (Iervolino et al., 2006). Selection of site-specific GMs involves matching the GM response spectra with a site-specific target response spectrum. Scaling in time domain or spectral matching in frequency domain over a range of time period is usually considered as a second-level selection criterion.

Increase in number of parameters in the selection criteria drastically reduces the number of eligible GM records when compared to the simpler magnitude-distance set. This significant reduction and the refinement may be ineffective because the impact of the seismotectonic environment on the structural response quantities is still not well understood

(Katsanos et al., 2010). Damage potential of the GMs is contributed by several factors which should reflect the influences of the basic excitation and the system characteristics contributing to the seismic responses of the structural systems (Sucuoglu and Nurtug, 1995). Frequency contents of the strong GMs are a key parameter for explaining and understanding the structural damages experienced during strong seismic events (Pavel and Lungu, 2012). PGA/PGV ratios for strong GMs have been found to be related to magnitude, distance plus frequency content of accelerograms (Tso et al., 1992) and being a damage indicator to cause severity of the structure under seismic excitation (Pawirodikromo, 2017), have been proposed as a complementary measure for the selection process. Thus, selection of accelerograms based on PGA/PGV ratios and grouping as 'low frequency contents', 'intermediate frequency contents' and 'high frequency contents' with ranges as < 0.8g/m/s, 0.8-1.2g/m/s and > 1.2g/m/s respectively, is believed to cover a wide range of earthquakes (Kwon and Elnashai, 2006). These groups thus will affect different sets of structures, according to their fundamental frequencies (Elassaly, 2015).

As stated by Krawinkler and Seviratna (1998), the possible structural response bounds can be predicted by incorporating broad range of values for the chosen IM. Thus, as the study intends to predict the means and the variabilities of the seismic demand responses of the IAB components, GMs with wide ranges of variations in amplitude, frequency and duration can be employed. For instance, Choine et al. (2015) for analysing the bridges in their study, adopted suites of GMs having the maximum S_a at T_Ns of the bridges. Since, T_N of the bridge samples are known in the study, GMs are selected encompassing wide ranges of frequency contents based on PGA/PGV criterion. Following Codal prescriptions like those of EN 1998-2 (2005); ASCE (2010); GB (2010) and NZS 1170.5 (2004) (the first three recommend a minimum of three while the last one suggests seven GMs (only actual records)), nine GMs are selected in the study. Since, the site of the structure is of no interest here, GMs are chosen over a broad range of PGA/PGV ratios, irrespective of the sites generating them, keeping in mind that wide ranges of frequency contents are covered. These GMs along with the corresponding PGA/PGV ratios, PGA and S_a (0.7s) (i.e., S_a at T_N fixed at 0.7*s* being the near average value in the regime of 0.45 to 1.3 secs, from damage initiation till collapse for the bridge samples) are listed in Table 4.3. Figure 4.2 displays the S_a - T_N spectra for the GMs. The input GMs in the study have been downloaded from PEER Ground Motion Database (http://peer.berkeley.edu) and COSMOS Virtual Data Center (https://www.strongmotioncenter.org/vdc/scripts/earthquakes.plx).

Table 4.3 Natural GMs employed for the analytical fragility formulation in the study

Frequency Contents	Earthquake/Station/Date/Magnitude	PGA/PGV (gs/m)	PGA (g)	S_a (0.7s) (g)
Low	Loma Prieta/ Emeryville/1989/7.0	0.490	0.307	0.763
	Loma Prieta/ Emeryville/1989/7.0	0.592	0.253	0.697
	Northridge/Newhall/1989/6.7	0.779	0.583	0.825
	Petrolia/Petrolia/1992/7.1	0.740	0.662	1.834
Medium	Loma Prieta/ Emeryville/1989/7.0	0.995	0.214	0.534
High	Chi-Chi/Taiwan/1999/7.7	1.839	0.618	0.689
	Northridge/Santa Monica/1994/6.7	2.112	0.880	0.528
	Northridge/Tarzana/1994/6.7	1.616	1.778	1.850
	Petrolia/Cape Mendocino/1992/7.1	2.565	1.039	0.275

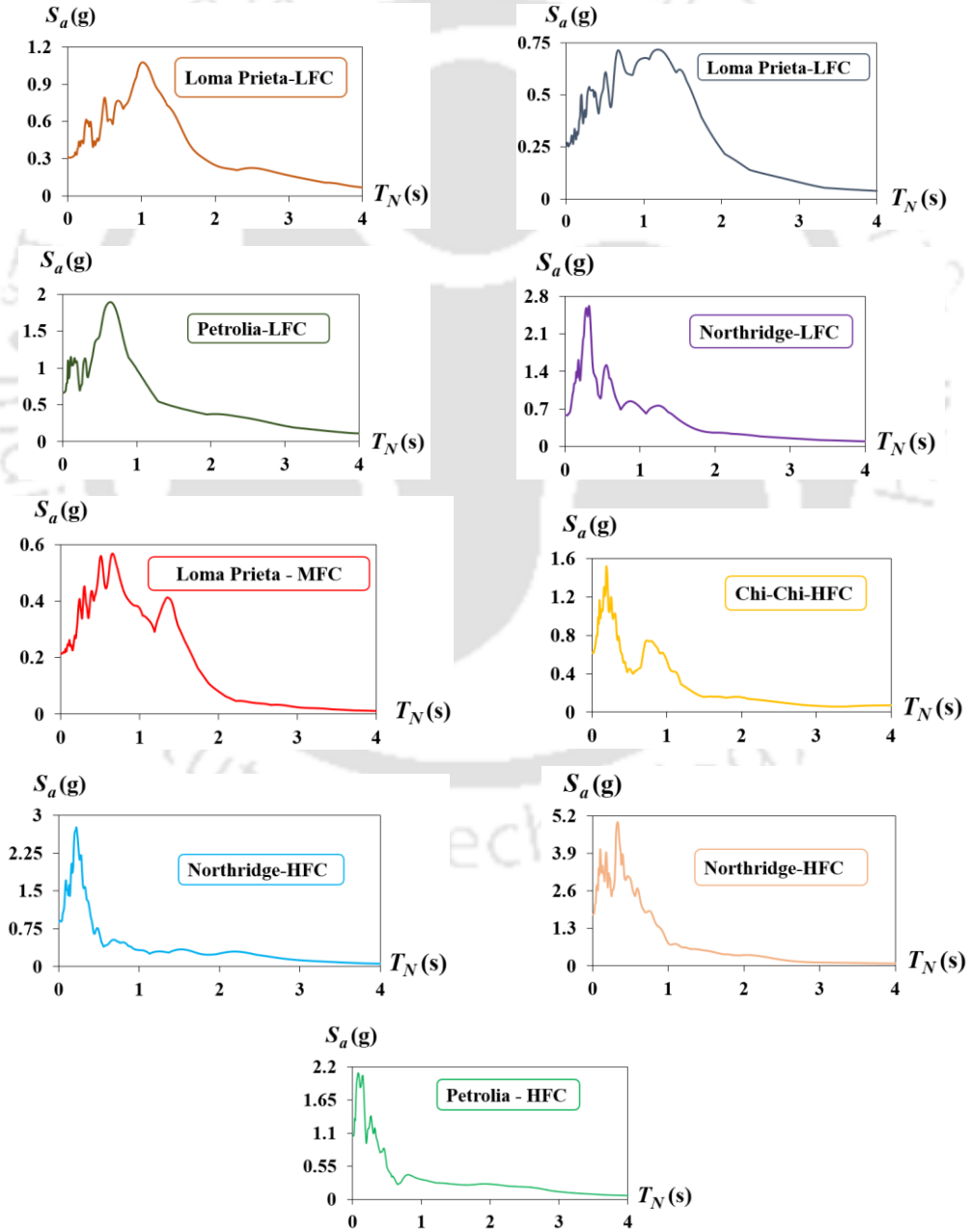

Figure 4.2 5% damped GM acceleration-time period response spectra.

4.3 SENSITIVITY ANALYSIS

Sensitivity analysis investigates the sensitivity of the output parameter to the variation of individual input parameters. A primary sensitivity test can ease the model calibrations by focusing on only the sensitive model parameters, not knowing which can result in time and efforts being uselessly spent on the non-sensitive ones (Bahremand and De Smedt., 2008).

Sensitivity analysis involves running the models (designed based on a set of parameter combinations) and thereby calculating the sensitivity measures of interest using the resulting outputs. The simplest form is 'one factor at a time' approach which varies each parameter independently using upper and lower bounds, one at a time, holding other parameters constant, to assess how the output is sensitive to parameter values. It requires $2M$ experiments, with M being the number of parameters studied; however, it is impossible to study the interactions among the parameters (Van Schepdael et al., 2016). The factorial design approach with the ability to examine the individual effects on the outputs as well as the interactions, involves simultaneous variations of all parameters, for instance, a two-level design requires 2^M models. However, it becomes very computationally expensive when a large number of parameters must be considered (Nielson, 2005).

The study carries out the Sensitivity analysis to examine the parametric influences on the LSTs, as they form the basis of FCs, derivation of which is the ultimate goal herein. As the aim is only to come out with the significant parameters, with no concern for the interaction, 'one factor at a time' approach is employed. It will allow fast exploration of the model and evaluation of the influential parameters (Iooss and Lemaitre, 2015), for the large number of parameters in this study. For each component, a reference 'one factor at a time' model is created using the base value of each of the ranges of its parameters. By changing each parameter to its second and third values (as in Table 4.4, based on the Tables 4.1 and 4.2), one at a time, the other models are created.

Damage model analysis of each of the three 'one factor at a time approach' models created for the variation of each parameter (corresponding to the base, second and third values, as in Table 4.4) yield three LST values against a damage state. Parametric sensitivity is assessed through the sensitivity index (Equation (4.1) (Mouida and Alaa, 2011)), where, I_1 and I_2 are two different input values and O_1 and O_2 are the corresponding output values. Two sensitivity indices are evaluated, firstly, while holding I_1 and O_1, and I_2 and O_2 with respect to the base, and the second value; and then I_1 and O_1, and I_2 and O_2 with respect to the base, and the third value. Average sensitivity indices (as calculated in

Appendix B) are shown as horizontal bars in increasing order from bottom to top yielding the tornado diagrams, as in Figures 4.3(a) to 4.3(i). Positive sensitivity index implies parameter role along the direction of response and vice versa.

Table 4.4 Description of the parameters selected for the sensitivity analysis

Parameter		base value	second value	third value
Bearing pad	A_{br} (m^2)	0.184	0.07	0.49
	h_{br} (mm)	80	20	150
	G (kPa)	1000	800	1200
	σ_m (kPa)	5000	2000	10000
Dowel bar	d_{brd} (mm)	32	25	40
	$f_{y,brd}$ (MPa)	490	415	564
	$f_{u,brd}$ (MPa)	601	573	629
	$\varepsilon_{u,brd}$	0.161	0.145	0.177
Pier and pile	D_{pr} (m)	1.4	0.846	1.730
	H_{pr} (m)	8	6	12
	$f_{y,pr}$ (MPa) / $f_{y,pl}$ (MPa)	415	500	550
	$f_{ck,pr}$ (MPa)	30	25	40
	$f_{ck,pl}$ (MPa)	40	35	45
	$\rho_{l,pr}$ (%)	2.185	1.165	3.241
	$\rho_{l,pl}$ (%)	4.290	2.140	5.360
	$\rho_{t,pr}$ (%)	0.240	0.133	0.300
	$\rho_{t,pl}$ (%)	0.300	0.160	0.590
	D_{pl} (m)	0.395	0.52	0.734
	L_{pl}(m)	10	12	15
	υ_{pr} / υ_{pl}	0.1	0.2	0.3
ABS	H_{ab} (m)	3.5	2	5
	φ_{bf} (º)	40	35	45
	γ_{bf} (kN/m^3)	20.10	18.50	21.70
	$(\varepsilon_{bf,50})_{42.5}$	0.0027	0.0025	0.0029
	$\delta_{abf,f}$	0.7	0.6	0.8
Foundation soil	Sand type	φ_s (º)	γ_s (kN/m^3)	$(\varepsilon_{ss,50})_{42.5}$	η (kN/m^3)
	Loose	30	16.5	0.0050	12487
	Dense	40	19.6	0.0025	74648

$$\text{Sensitivity Index} = \frac{(O_2 - O_1) / \text{Average}(O_1, O_2)}{(I_2 - I_1) / \text{Average}(I_1, I_2)} \tag{4.1}$$

Sensitivity analysis implies $d_{1,pl}$ and $d_{2,pl}$ to be more or less effected by the PSS parameters except for L_{pl}, along with $\rho_{t,pl}$ for $d_{1,pl}$, as depicted in Figures 4.3(a) and 4.3(b), whereas those affecting d_{FAF} are displayed in Figure 4.3(c). $d_{1,ab}$ and $d_{3,ab}$ are found to be highly sensitive to H_{ab}, followed by φ_{bf} and $\delta_{abf,f}$ interchanging their influence sequence for them

(Figures 4.3(d) and 4.3(e)). All the examined pier parameters are found influential, as in Figures 4.3(f) and 4.3(g) against $d_{1,pr}$ and $d_{4,pr}$ respectively. Similarly, while LST with respect to dowel fracture is found insensitive to $f_{y,brd}$ and $f_{u,brd}$, so is LST with respect to pad sliding to A_{br}. $d_{1,br}$ and $d_{2,br}$ are highly sensitive to h_{br} followed by the remaining parameters investigated, as in Figures 4.3(h) and 4.3(i).

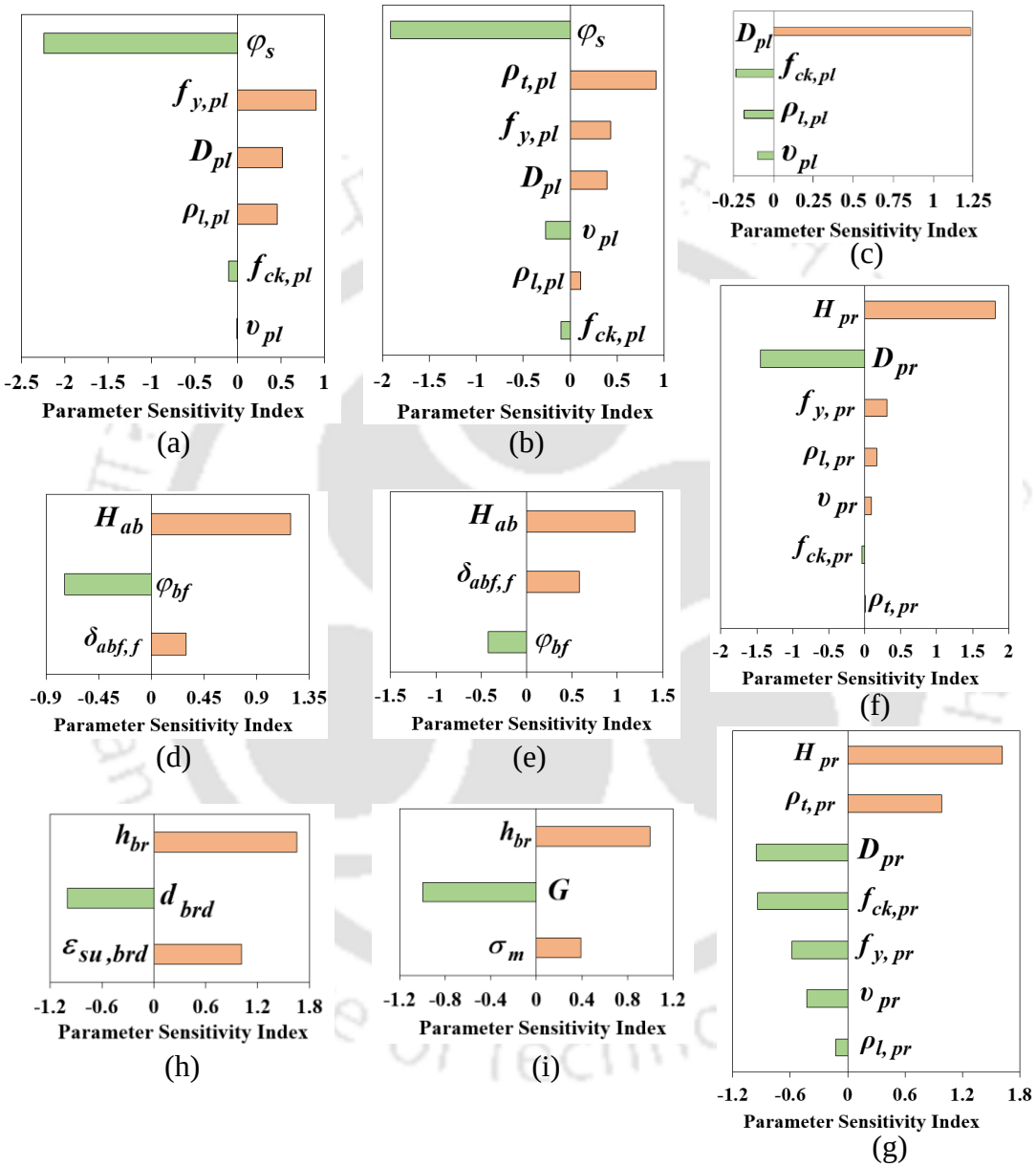

Figure 4.3 Sensitivity tornado diagrams with respect to (a) $d_{1,pl}$, (b) $d_{2,pl}$, (c) d_{FAF}, (d) $d_{1,ab}$, (e) $d_{3,ab}$, (f) $d_{1,pr}$, (g) $d_{4,pr}$, (h) dowel fracture and (i) pad sliding.

4.4 UNCERTAINTY PROPAGATION

The variability associated with an input parameter, when propagated to the output, can result in a large correlation between the parameter and significant variation in the output (Hamby, 1994). In this study, LSTs are observed to be sensitive to different degrees to

various parameters (Section 4.3) of the respective components. Hence, the second step of uncertainty analysis which involves propagation of the input uncertainty through the model to derive the resultant uncertainty in the outputs (Pathmanathan et al., 2019), is carried out herein through the creation of a large number of BS samples over the parameter ranges (Tables 4.1 and 4.2). Analyses of the damage and demand model of all those samples result in the probabilistic characterisations of the structural capacities and demands.

4.4.1 Generation of Bridge System Samples

BS samples are generated employing Latin Hypercube Sampling Technique (Wyss and Jorgensen, 1998); it produces similar and stable results with smaller sample size than the basic Monte Carlo simulation (Imam and Conover, 1980). As smaller sample size as 100 might be sufficient; Helton et al. (2005) investigated and found 100 samples generated using latin hypercube sampling technique to be adequate for the uncertainty and sensitivity analyses for the waste isolation plant in their study.

The study incorporates the variation in P_{pl} (owing to varying dimensions of the bridge components) and sand properties (resulting in variation in its axial load capacity). Hence, though L_{pl} is found insensitive, it is varied so that adequate axial load capacity of PSS is mobilised throughout to sustain P_{pl} and the associated pile settlement is within the allowable criterion. Thus, the L_{pl} sample values and the numbers of pile n_{pl} are iteratively paired up, such that the above two conditions are satisfied for all the BS samples.

Employing the sampling technique, each of the parameter ranges (Tables 4.1 and 4.2) is divided into 10 equivalent intervals and the median value of each of the intervals (following Zhang, 2006) is picked along with the lower and the upper boundary values to give 12 values. Although, in this technique all the parameters can be sampled together, a two-step approach from a global to local level is adopted, as is done in studies like Nielson and DesRoches (2007) and Abbasi and Moustafa (2017). This is expected to bring out better and more widespread propagation of uncertainties throughout the samples. At level 1, 12 values created for each of the geometric parameters are paired up randomy with 12 values of each such remaining parameters randomly to form 12 different geometric samples (Table 4.5, numbered ‘1’ to ‘12’). At level 2, 12 sub-samples are generated by pairing randomly the 12 values obtained from each of the ranges of the structural material and section detailing, geotechnical material, and the miscellaneous parameters, as in Tables 4.6, 4.7 and 4.8 respectively and named alphabetically from ‘a’ to ‘l’. All the sub-samples are linked with each of the samples, resulting in 144 BS samples, named 1a,..,1l;2a,..,2l;...;12a,..,12l.

The sample values for D_{pl} are paired up with the proportional sample values for D_{pr} which in turn are paired up with W_d sample values so as to conform with Table 3.2. Employment of the sampling technique for the purpose herein is depicted in Figure 4.4.

Table 4.5 Sampling on the IAB geometric parameters

Sample No.	L_{sp} (m)	W_d (m)	n_{pr}	D_{pr} (m)	L_{pr} (m)	D_{pl} (m)	L_{pl} (m)
1	24.50	13.25	1	1.82	9.50	0.733	14.75
2	39.50	23.75	4	0.98	14.50	0.418	13.75
3	33.50	25.25	4	0.86	11.50	0.373	11.25
4	27.50	26.00	4	0.80	15.00	0.350	10.00
5	50.00	11.75	1	2.00	5.00	0.800	12.25
6	30.50	16.25	2	1.46	13.50	0.598	13.25
7	21.50	20.75	3	1.10	12.50	0.463	12.50
8	45.50	19.25	3	1.34	5.50	0.553	15.00
9	42.50	17.75	2	1.70	10.50	0.688	11.75
10	20.00	22.00	3	1.22	7.50	0.508	10.75
11	48.50	11.00	1	1.94	8.50	0.778	12.75
12	36.50	14.75	2	1.58	6.50	0.643	14.25
Sample No.	L_{br} (mm)	B_{br} (mm)	h_{br} (mm)	H_{ab} (m)	L_{ww} (m)	T_{ab} (m)	
1	523	283	30	3.05	2.73	1.425	
2	628	465	86	3.35	3.78	1.075	
3	453	362	42	4.85	3.93	1.025	
4	400	200	20	5.00	4.00	1.000	
5	698	423	74	4.55	2.58	1.500	
6	418	398	66	2.75	3.03	1.275	
7	558	360	49	2.45	3.48	1.125	
8	593	304	38	3.65	3.33	1.225	
9	750	750	150	4.25	3.18	1.375	
10	488	337	52	2.15	3.63	1.175	
11	663	577	112	2.00	2.50	1.475	
12	733	419	61	3.95	2.88	1.325	

Table 4.6 Sampling on the IAB structural section detailing and material parameters

Sub-sample no.	A_l %	s_t (m)	f_c (MPa)	f_y (MPa)	f_u (MPa)	E_c (MPa)	E_{st} (MPa)	ε_{su}	G (MPa)
a	1.92	0.179	53.73	541.08	640.77	37383.38	208033.09	0.1674	860
b	2.88	0.091	27.55	555.39	652.40	27818.69	190369.26	0.1758	1060
c	0.80	0.300	40.27	529.61	630.43	36171.43	209500.53	0.1632	1200
d	4.00	0.080	65.52	564.91	676.57	44519.43	204055.95	0.1716	900
e	3.84	0.223	37.99	415.00	485.00	36981.62	200991.69	0.1450	800
f	2.24	0.289	31.61	464.02	574.25	24175.79	205824.64	0.1771	1180
g	1.28	0.201	48.37	500.07	620.62	27819.42	196153.67	0.1744	1100
h	0.96	0.267	40.53	519.42	666.92	31194.96	185569.33	0.1599	980
i	3.52	0.113	57.72	478.38	588.82	44824.47	202483.72	0.1566	1140
j	1.60	0.245	21.41	489.87	600.47	21747.34	199499.22	0.1536	1020
k	2.56	0.157	62.16	440.88	550.79	35478.73	197925.55	0.1478	940
l	3.20	0.135	34.62	509.75	610.81	24123.89	193937.67	0.1506	820

Table 4.7 Sampling on the IAB geotechnical material parameters

Sub-sample No.	φ_s (°)	γ_s (kN/m^3)	η (kN/m^3)	φ_{bf} (°)	γ_{bf} (kN/m^3)	$\delta_{abf,f}$
a	32.20	18.58	12080	37.5	19.30	0.750
b	29.80	17.62	8720	39.5	19.94	0.710
c	31.40	18.26	10960	42.5	20.90	0.600
d	33.00	18.90	13200	44.5	21.54	0.650
e	30.60	17.94	9840	45.0	21.70	0.770
f	27.00	16.50	4800	35.0	18.50	0.670
g	28.20	16.98	6480	43.5	21.22	0.790
h	35.00	19.70	16000	35.5	18.66	0.690
i	34.60	19.54	15440	36.5	18.98	0.630
j	27.40	16.66	5360	40.5	20.26	0.800
k	33.80	19.22	14320	38.5	19.62	0.610
l	29.00	17.30	7600	41.5	20.58	0.730

Table 4.8 Sampling on miscellaneous parameters

Sub-sample	$E_{c,MF}$	$S_{m,MF}$	$\mu_{br,MF}$	Sub-sample	$E_{c,MF}$	$S_{m,MF}$	$\mu_{br,MF}$
a	1.02	1.385	1.02	g	0.80	1.145	0.93
b	1.06	1.355	1.08	h	0.98	1.4	0.79
c	1.14	1.205	0.95	i	1.18	1.115	0.85
d	1.10	1.175	1.14	j	0.94	1.265	0.90
e	1.20	1.295	1.00	k	0.90	1.235	1.05
f	0.86	1.1	1.11	l	0.82	1.325	0.98

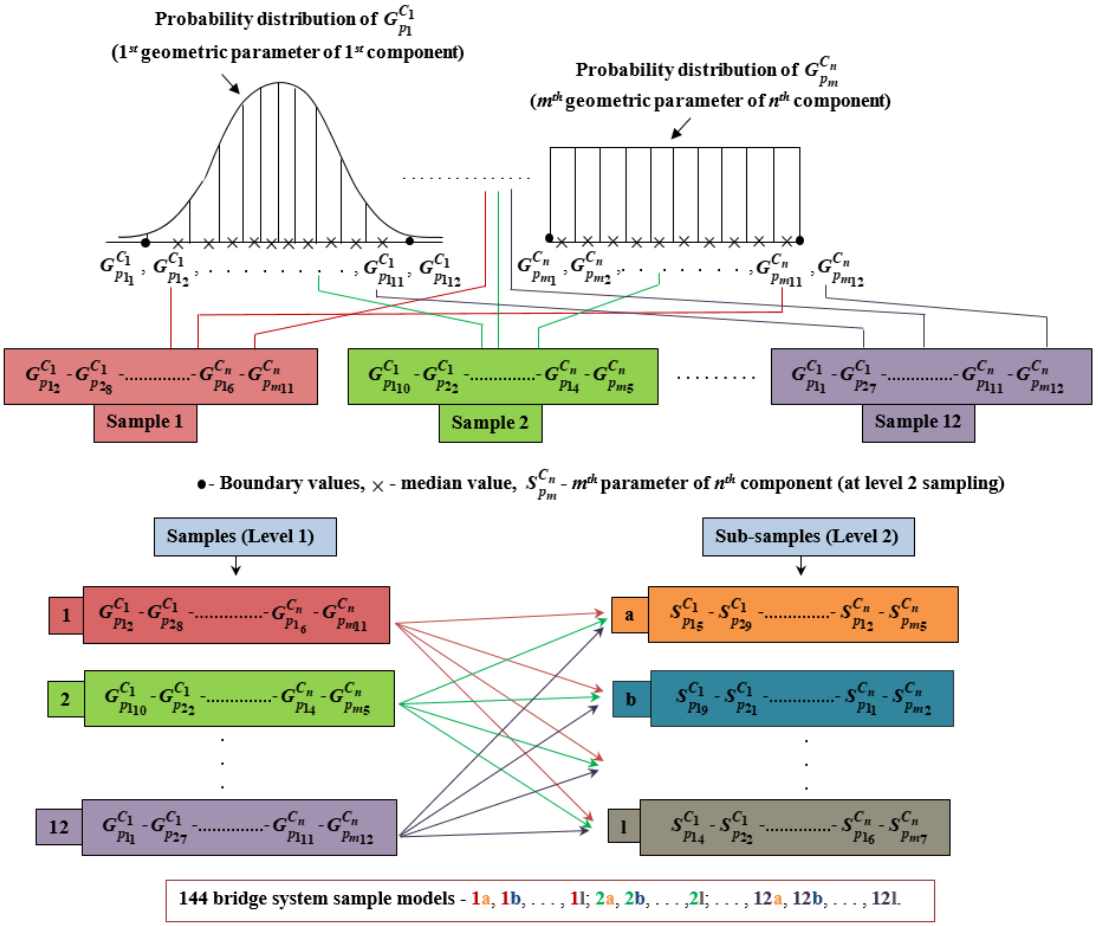

Figure 4.4 Bridge sample generation using Latin hypercube sampling technique.

4.4.2 Probabilistic Seismic Capacity Model

With respect to fragility formulation, modeling capacity in probabilistic terms constitutes the first half of the problem. For each of the components, analyses of the damage model (Section 3.4) for the samples (Section 4.4.1) result in dispersed data (144 values) for the LST against each of the DSs. LST (denoted by LST1, LST2, LST3 and LST4 with respect to 1st, 2nd, 3rd and 4th DSs) data corresponding to each of the DSs (denoted by DS1, DS2, DS3, DS4 with respect to increasing DS ranks) with respect to PSS, pier and bearing follow lognormal distribution roughly. Exceptions are the bearing LST3 and LST4 being based on W_{seat}, which are of different values for all the 12 geometric samples while being the same for all the 12 sub-samples linked to each of the samples. LST data of the ABS DSs approximately follow uniform distribution. These are depicted in Figures 4.5(a) and 4.5(b) for PSS, Figures 4.6(a), 4.6(b) and 4.6(c) for ABS, Figures 4.6(a), 4.6(b), 4.6(c) 4.6(d), 4.6(e) 4.6(f) and 4.6(g) for bearing and Figures 4.7(a), 4.7(b), 4.7(c) and 4.7(d) for pier.

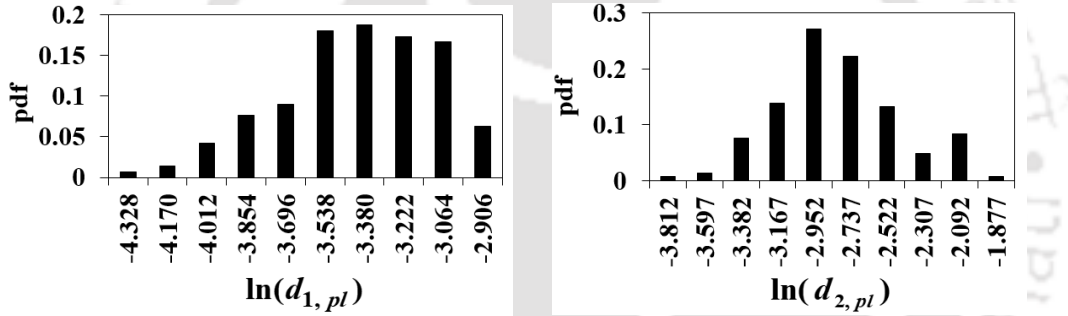

Figure 4.5 Data distributions for PSS **(a)** LST1 and **(b)** LST2.

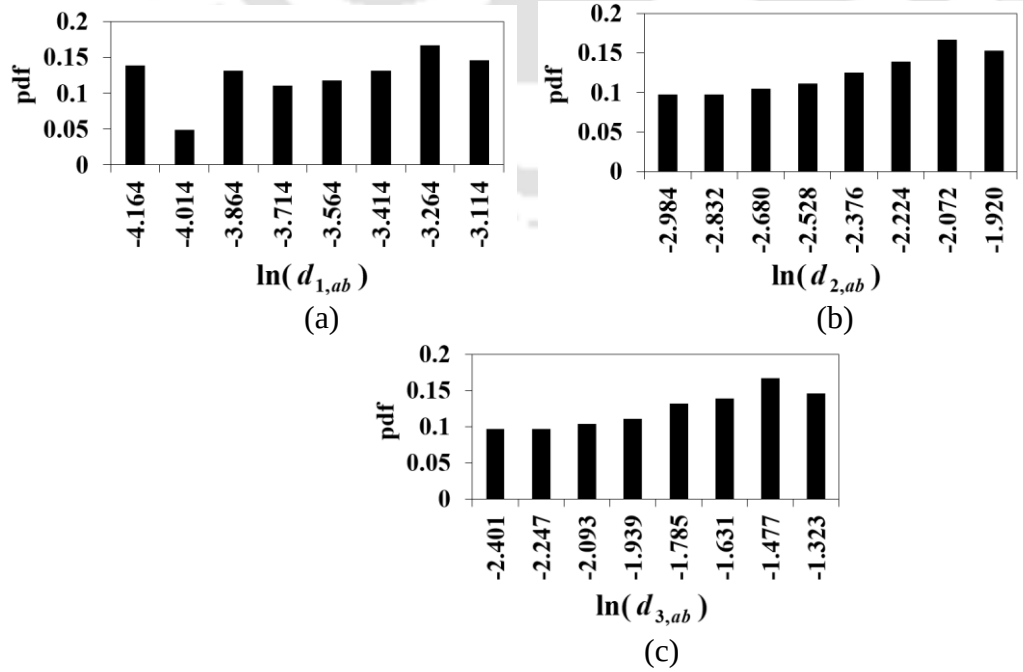

Figure 4.6 Data distributions for ABS (a) LST1, (b) LST2 and (c) LST3.

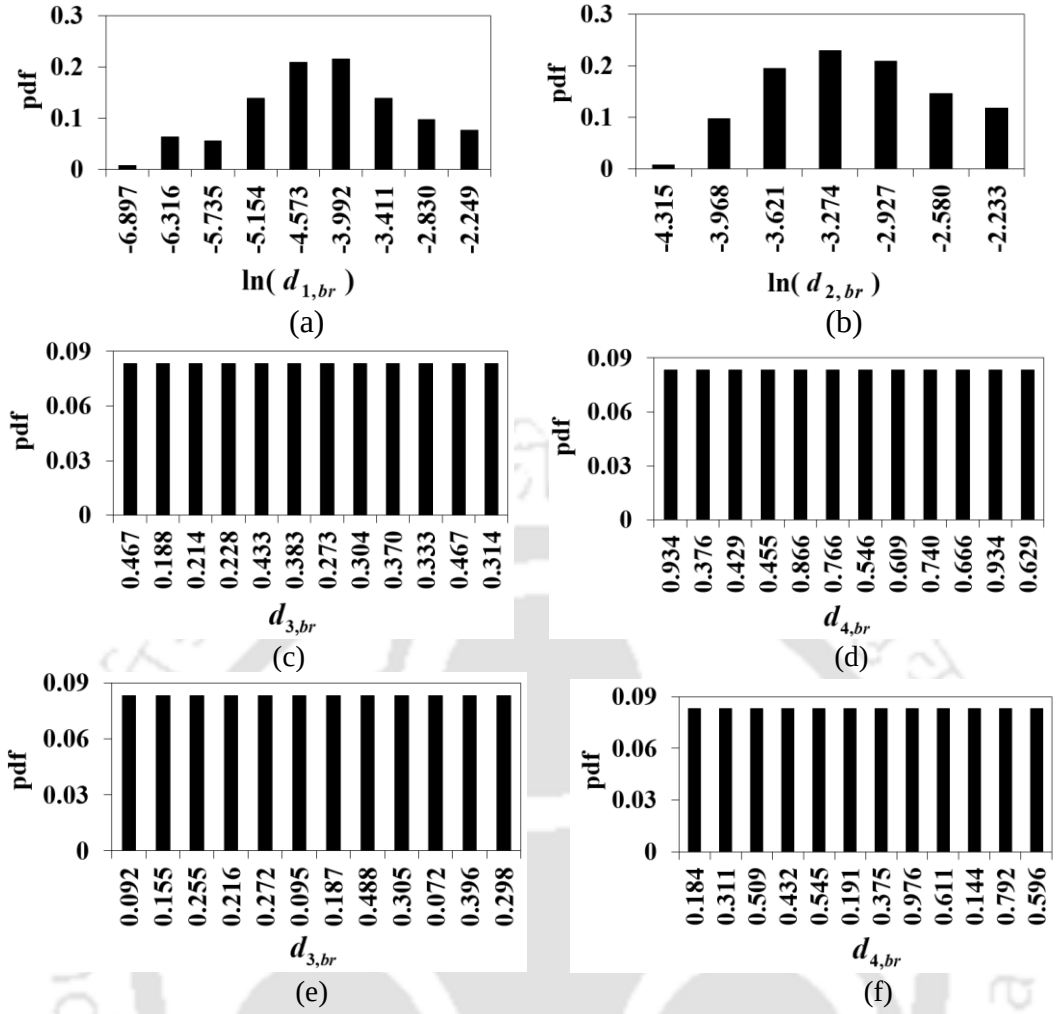

Figure 4.7 Data distributions for bearing (a) LST1, (b) LST2, (c) LST3 (*L*), (d) LST4 (*L*), (e) LST3 (*T*) and (f) LST4 (*T*).

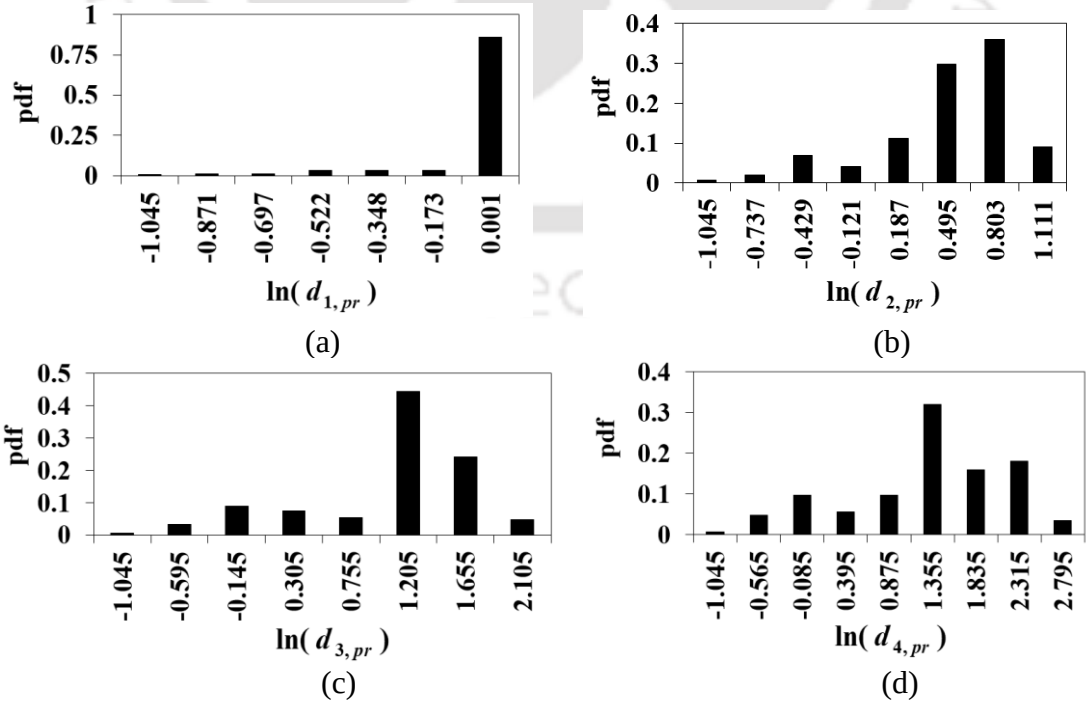

Figure 4.8 Data distributions for pier (a) LST1, (b) LST2, (c) LST3 and (d) LST4.

The distribution properties in terms of μ and λ of the original LST data as well as θ and ζ of the transformed data are listed in Table 4.9. It is to be noted that for most of the bearing samples, dowel fracture (defining DS1) occurs much earlier before the pad reaches its ultimate friction capacity leading to bearing sliding (defining DS2). For a few samples, the fracture is preceded by the ultimate friction capacity and as such bearing slides only after the fracture at a relatively higher displacement. For such a sample, LSTs with respect to DS1 and DS2 are considered to be the same and is kept equal to that corresponding to dowel fracture. This anomaly might be the cause of the reverse trend in v in case of bearing

Table 4.9 Probability distribution properties of LSTs corresponding to the DSs of pier, PSS, bearing and ABS respectively

LSTs of the components			μ	λ	θ	ζ
Pier (ductility)	$d_{1,pr}$		0.941	0.159	0.924	0.210
	$d_{2,pr}$		1.551	0.358	1.427	0.446
	$d_{3,pr}$		2.785	0.526	2.311	0.690
	$d_{4,pr}$		4.081	0.761	2.945	0.887
PSS (mm)	$d_{1,pl}$		32	0.289	31	0.306
	$d_{2,pl}$		57	0.397	54	0.364
Bearing (m)	$d_{1,br}$		0.019	1.152	0.011	1.094
	$d_{2,br}$		0.043	0.565	0.0370	0.541
	$d_{3,br}$	L	0.331	0.278	0.318	0.292
		T	0.236	0.515	0.203	0.581
	$d_{4,br}$	L	0.662	0.278	0.636	0.292
		T	0.472	0.515	0.406	0.581
ABS (mm)	$d_{1,ab}$		27	0.331	26	0.352
	$d_{2,ab}$		90	0.329	85	0.352
	$d_{3,ab}$		163	0.333	153	0.355

4.4.3 Probabilistic Seismic Demand Model

PSDM, relating the GM IM with D placed on each bridge component in terms of the its EDP, constitutes the second half of the fragility formulation problem. Development of PSDMs in the study involves the following stepwise tasks undertaken:

- Pairing up of each of the analytical models created for all of the 144 nos. of BS samples (Subsection 4.4.1) with each of the 9 nos. of chosen GMs to obtain 1296 BS-GM pairs.
- Selection of range of m nos. of values of each of PGA and S_a (0.7s) upto 1.8g and thus, scaling up and down the PGA and S_a (0.7s) values of each GM to the m^{th} values. Corresponding to the m^{th} value (IM_m) of each of PGA and S_a (0.7s), at a given DS of a particular component, following steps are carried out:
  - IACSM analysis of each of the BS-GM pairs, results in 1296 values in terms of S_a

demand for the BS conditioned on IM_m.

- 1296 values for the EDP (form a stripe) are extracted from the S_d demands corresponding to the S_a demands based on the weighted contribution of the component to the BS mode shape.

- Repetition of these steps at increasing IM values results in dispersed data, regression analysis against IM results in the required PSDM, as in Equation (2.1) (Chapter 2).

4.5 SUMMARY

This chapter deals with the uncertainties in the structural and geotechnical parameters to be incorporated in the fragility formulation. Parameters of the IAB components subject to variations are treated as random variables and the respective practical probable ranges and the probability distribution properties are fixed based on literature survey and with some assumptions. Sensitivity analysis is carried out using a simple one factor at a time approach to examine the influences of those random variables on the component Limit State Threshold (LSTs) and their respective sensitivities are quantified in terms of sensitivity indices. Further steps to fragility evaluations are to be proceeded while propagating the uncertainties associated with those sensitive parameters. This is done by generating 144 sets of the Bridge System (BS) samples by employing Latin Hypercube Sampling technique on these probability distributions through a two-step approach from a global (using geometric parameters) to local (using material and structural detailing parameters) level. Analyses of the damage models for component samples yield LST data, which roughly follow lognormal distribution for pier, pile-soil system and bearing and a uniform one for abutment-backfill system. Computations of the LST distribution properties in probabilistic terms lead to probabilistic seismic capacity models for the components. To account for the uncertainties in demand side, other those arising from variations in bridge properties, nine GMs with wide ranges of variations in frequency contents are selected. By pairing the analytical models of all of the 144 BS samples with each of the 9 GMs, 1296 BS analytical model-GM pairs are created. The study considers two GM Intensity Measures (IMs) in the form of Peak Ground Acceleration (PGA) and spectral acceleration at the time period of 0.7s (which is the near average value of the time period range obtained through the nonlinear analyses of the BS samples) S_a (0.7s). At each of the specified IM values upto 1.8g to which the respective PGAs and S_a (0.7s)s of all the selected GMs are scaled, the 1296 BS model-GM pairs are to be analysed, thus paving the way to generation of probabilistic seismic demand models, as discussed in the Chapter 5.

This page has been left intentionally blank

Chapter 5

GENERATION OF PROBABILISTIC SEISMIC DEMAND MODEL AND FRAGILITY CURVES

CONTENTS

5.1 INTRODUCTION

Generation of the PSDMs constitute the second half of the fragility formulation; the procedure in the present study is shown in Figure 5.1. Consequently, the FCs are generated.

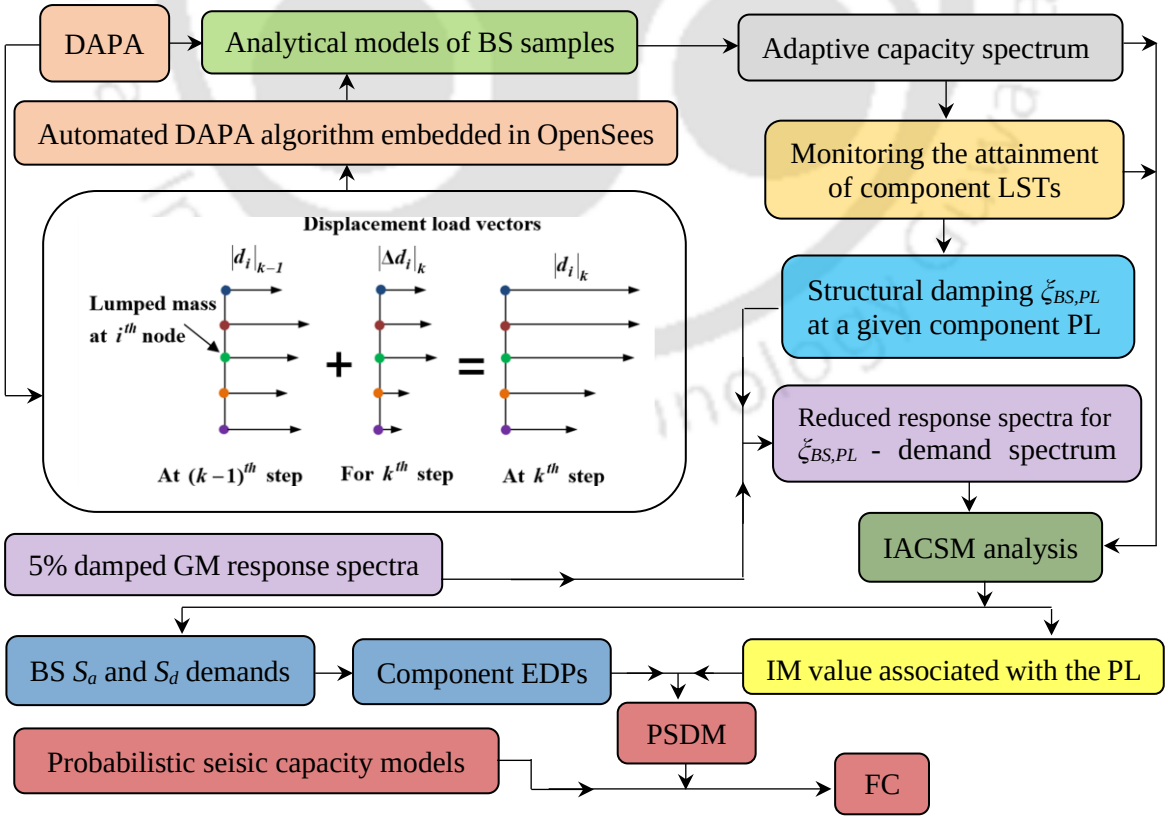

Figure 5.1 Flowchart describing the generation of PSDM in the present study.

5.2 GENERATION OF BRIDGE SYSTEM MODEL

To estimate the seismic demands on the bridge components, these are coalesced into a single unit that represents the BS, using the 'structural components modeling' analogy (Priestley et al. 1996). Herein, the superstructure is substituted by a spline and supported on a series of springs representing the bridge components, as depicted in Figure 5.2 for the BS in the study. The equivalent properties are computed from the material properties, dimensions, and locations of the girders and deck (Seo and Rogers, 2017). Hence, in OpenSees, the spline is modeled with *elasticBeamColumn* elements, following the centre of gravity of the cross section along the deck length, with the computed properties as input. Masses of the tributary weights are lumped at the nodes at the bearing and the abutment locations, as in Figure 5.2. Lateral force deformation capacity curves generated for pier, bearing, PSS and ABS (as in Chapter 3) are incorporated in the *Multilinear ZeroLength* element springs. At the abutment, the underlying piles being rigidly connected to the backwall, both ABS and PSS springs are arranged in parallel to the end node of the spline element, with masses of the backwall, wingwalls, backfill and the underlying PSS lumped at that node. At the bent, the top node of the spring representing the resultant lateral force deformation capacity curves of all the bearing is connected to the overlying spline node and the end node is connected to the cap beam central node. Tributary weight from the cap beam and self-weight of the pier are lumped at its top node interconnected with the overlying cap beam node. PSS mass is lumped at the interconnecting bottom node of the pier and the top node of the PSS spring, while keeping the end node of the PSS spring fixed. Such an arrangement for a 2-column bent IAB sample in the study is shown in Figure 5.2.

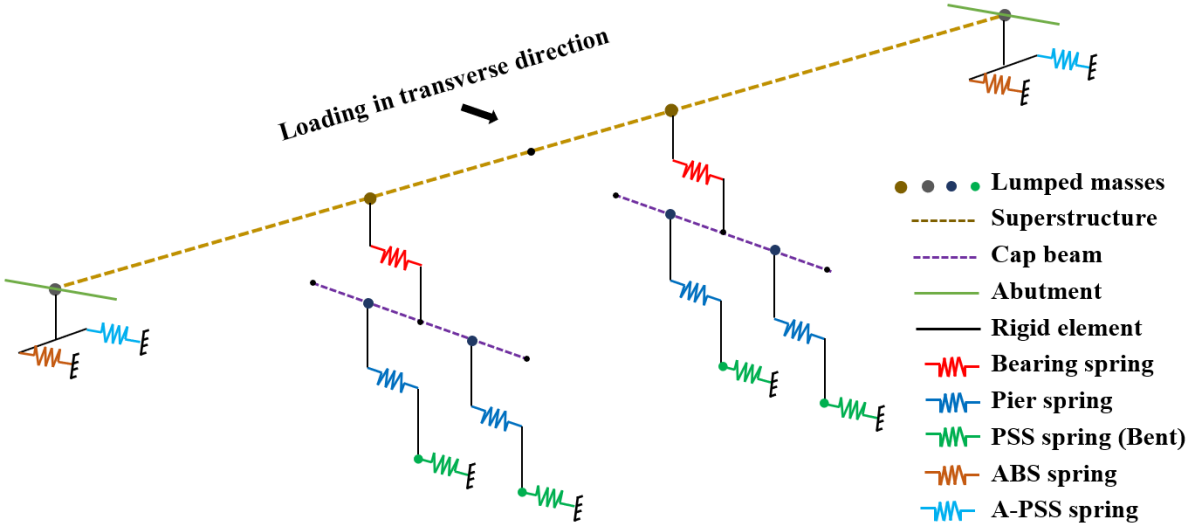

Figure 5.2 Bridge system representation – Structural Components Modeling analogy.

5.3 SEISMIC DEMAND ANALYSIS OF THE ADOPTED IAB CLASS

In this study, seismic demand analysis of the BS is carried out employing IACSM. Nonlinear dynamic analysis has been the preferred choice, as it directly employs the GM time histories as the input to the BS analysis and hence is more reliable. However, the nonlinear dynamic analysis being computationally demanding and time consuming, a more practice oriented method in the form of the capacity spectrum method has emerged. The capacity spectrum method, when utilises DAPA, has been validated by Casarotti et al. (2007) to give reasonable estimates of inelastic deformation demands at par with those obtained employing the nonlinear dynamic analysis, but with less efforts and time. Steps involved in IACSM leading to the PSDMs are discussed in the subsections below:

5.3.1 Generation of Adaptive Capacity Spectra

As an initial step, modal analyses of the analytical models of all the 144 BS samples (as in Chapter 4) are carried out to determine the fundamental vibration properties. T_N s of the samples are found to lie within 0.28 – 0.39s, predominantly vibrating in the transverse direction with 94% to 98% modal participation. The adaptive capacity spectra for the samples are generated by implementing the following steps:

- The nominal load vector for the DAPA is defined, based on the initial deformed configuration of the BS. It comprises of the displacements at the top nodes of the bearing, pier, PSS springs and the abutment nodes (where the masses are lumped), normalised with respect to the maximum one.
- With the analysis step size decided, first step of the analysis is carried out with the nominal load vector. The current state of thecstiffness of the components are computed and Eigen value analysis is performed, to obtain the load vector for the next step.
- DAPA algorithm is automated through a built-in code, embedded in the BS analytical model. It is repeated for as many steps as long as the BS is exhausted of the DSs of the components. Step size is adjusted at intermediate steps so as to coincide with the attainments of the DSs.
- With the deformed configuration of the BS assessed through DAPA, at each analysis step k, the equivalent Single degree-of-freedom displacement in terms of $S_{d,k}$ is obtained by combining the displacements $y_{br,k}$, $y_{pr,k}$, $y_{pl,k}$ and $y_{ab,k}$ of the bearing, pier, PSS and ABS along with the associated lumped masses in a similar way, as in Equation (2.13) and thereby $M_{BS,k}$ and $S_{a,k}$ are calculated. Computations are carried out in spreadsheets, leading to generation of the adaptive capacity spectra.

Figures 5.3(a), 5.3(b), 5.3(c) and 5.3(d) display the capacity spectra of BS samples 5e , 2l, 3l and 3i, along with damage sequence for the components. Instances of occurrence of *DSs* are marked and denoted as B_1 and B_2 for bearing LST1 and LST2; P_1, P_2, P_3 and P_4 for pier LST1, LST2, LST3 and LST4; A_{b1}, A_{b2} and A_{b3} for ABS LST1, LST2 and LST3; and A_{p1} and A_{p2} for A-PSS (PSS at the abutment) LST1 and LST2 respectively.

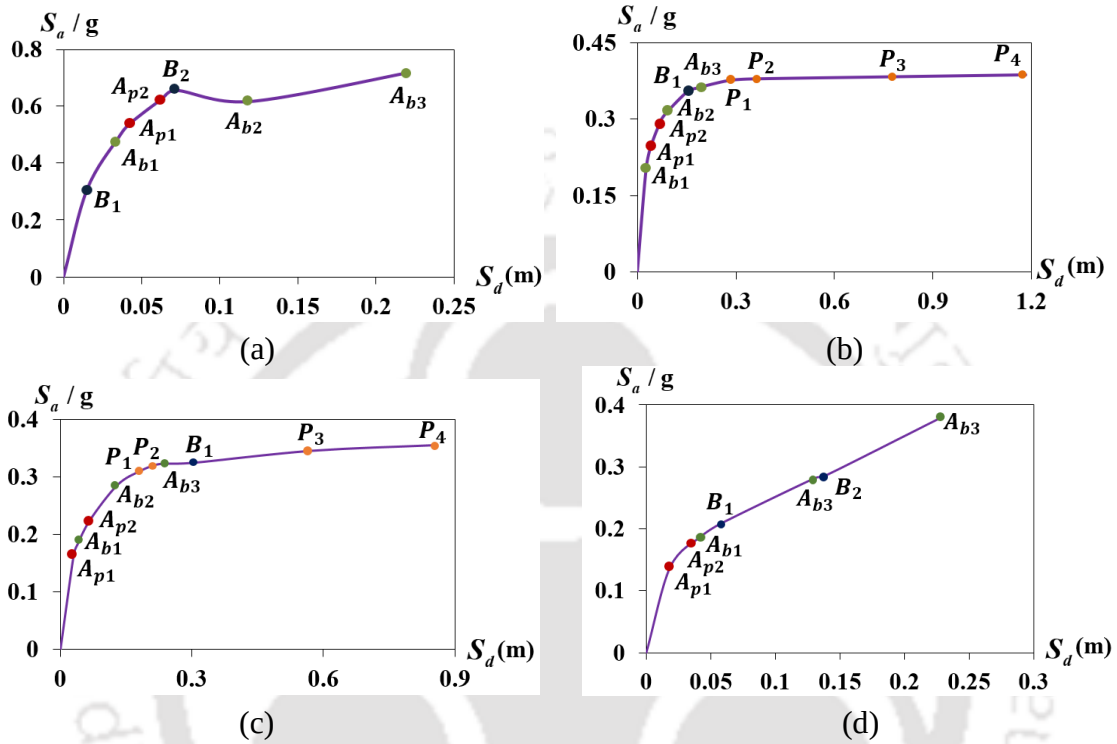

Figure 5.3 Adaptive capacity spectra generated for BS sample no. (a) 5e, (b) 2l, (c) 3l and (d) 3i.

As can be observed, the BS sample 5e (Figure 5.3(a)), which is a 1-column bent type model, is governed by the bearing sliding, depicted by the instant of drop-down in the capacity, thereafter which it rises due to contributions from the ABSs. Samples 2l and 3l belonging to 4-column bent type are governed by pier DSs before bearing sliding occurs. It is to be noted that at the instant of sliding, BS gets isolated from the bent, resulting in no further base shear contribution as well as no further damages to the bent components. Though all samples of 4-column bent types should have been governed by pier DSs, as is also followed by the sample no. 3l (Figure 5.3(c)), sample no. 3i (Figure 5.3(d)) shows an exception to this, as bearing sliding (corresponding to LST2) precedes any pier DS. This is because the sample 3i is built with bearing parameters with such a set of values that it exhibits low stiffness while pier shows relatively higher stiffness with the set of parameter values in that sample. Similarly, most of the 2-column bent type models show bearing sliding preceding some or all the pier DSs, whereas most of the 3-column bent type models show some or all

the pier DSs preceding the sliding, with a few exceptions in both the cases.

5.3.2 Evaluation of Bridge System Damping in the Study

5% damped acceleration-displacement response spectra generated from input GMs have to be reduced to account for the damping that occurs during the BS inelastic behaviour to obtain the seismic demand spectra. A proportion of the maximum strain energy stored during a loading cycle gets dissipated through damping and is based on the area enclosed by the hysteretic loop at the peak displacement response and peak acceleration response. With the known BS inelastic deformed shape at each step of the DAPA, damping of a component when a DS of concern is attained, is computed from its displacement at that instant. Subsequently, the BS damping $\xi_{BS,PL}$ is evaluated by properly combining all the individual contributions at all PLs of every components and for all the 144 BS samples.

(a) Bearing

Since yielding and fracture of dowel bars occur at very small displacements, the damping contributions are negligible. Damping is mainly contributed by friction in rubber pad, as shown in Figure 5.4 where, AB, OB and BD represent $F_{u,brp}$, $y_{u,brp_{sh}}$ and $y_{brp,sl_{PL}}$ ($y_{brp,sl}$ value at a given DS/PL), and is computed by Equation (5.1). The grey (OACDO) and the rectangular lined (ACDEFGHA) portions represent the stored energy $E_{s,br_{PL}}$ at a given PL and the energy loss $E_{fr,br_{PL}}$ due to friction in one cycle of amplitude $y_{brp,sl_{PL}}$ respectively. Equivalent viscous damping $\xi_{br,PL}$ is obtained as the sum of friction damping $\xi_{fr,br_{PL}}$ (based on Chopra (2007) and inherent elastic damping of 5% (Irvine, 2004), in as Equation (5.1).

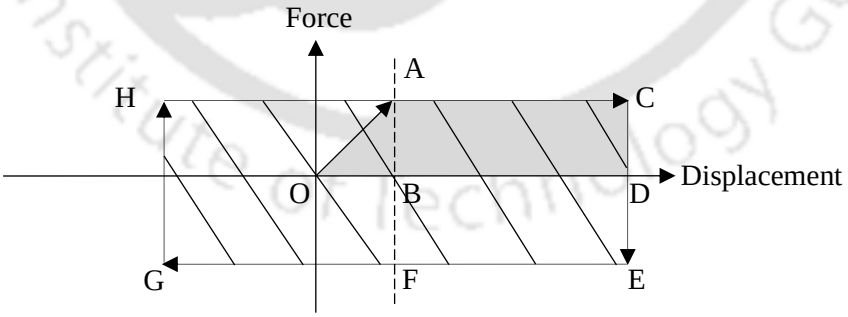

Figure 5.4 Energy dissipation from friction damping in bearing at a given DS/PL.

$$\xi_{fr,br_{PL}} = \frac{E_{fr,br_{PL}}}{4\pi \cdot E_{s,br_{PL}}} = \frac{4F_{u,brp} \cdot y_{br,sl_{PL}}}{4\pi(0.5F_{u,brp} \cdot y_{u,br_{sh}} + F_{u,brp} \cdot y_{br,sl_{PL}})} = \frac{2y_{br,sl_{PL}}}{\pi(y_{u,br_{sh}} + 2y_{br,sl_{PL}})};$$
$$\xi_{br,PL} = 0.05 + \xi_{fr,br_{PL}} = 0.05 + \frac{2y_{br,sl_{PL}}}{\pi(y_{u,br_{sh}} + 2y_{br,sl_{PL}})} \quad (5.1)$$

(b) Pier

For pier, damping is mainly contributed by the hysteresis loop developing during its post-yielding phase. The equivalent viscous damping $\xi_{pr,PL}$ is calculated, accounting for an inherent elastic damping of 5% and hysteretic damping $\xi_{hyst,pr_{PL}}$ (expression adopted from Calvi et al., 2013), at a given DS/PL in Equation (5.2) as,

$$\xi_{hyst,pr_{PL}} = 0.444\left(\frac{\mu_{pr,PL}-1}{\pi\mu_{pr,PL}}\right); \quad \xi_{pr,PL} = 0.05 + 0.444\left(\frac{\mu_{pr,PL}-1}{\pi\mu_{pr,PL}}\right) \tag{5.2}$$

(c) PSS

For PSS, damping is jointly contributed by pile and soil. Pile damping is calculated, as is done for pier (as per Equation (5.3a), where the notations hold the same meanings as for pier). Damping of sandy soil $\xi_{s,PL}$ at a given PL is calculated (Equation (5.3b)) as a function of $G_s/G_{max,s}$ (Equation (5.3c)) and the minimum damping ratio $\xi_{min,s}$ (taken as 0.8%), where, G_{max} and G_s are the shear moduli of the sandy soil at a very low shear strain amplitude ($\leq 10^{-4}$) (Zhang and Aggour, 1996) and at an instantaneous value of shear strain respectively. The equivalent viscous damping $\xi_{PSS,PL}$ is given by Equation (5.3c).

$$\xi_{hyst,pl_{PL}} = 0.444\left(\frac{\mu_{pl,PL}-1}{\pi\mu_{pl,PL}}\right); \quad \xi_{pl,PL} = 0.05 + \xi_{hyst,pl_{PL}} \tag{5.3a}$$

$$\xi_{s,PL} = f(G_s/G_{max,s}) + \xi_{min,s} \tag{5.3b}$$

$$f(G_s/G_{max,s}) = 10.6(G_s/G_{max,s})^2 - 31.6(G_s/G_{max,s}) + 21 \tag{5.3b}$$

$$\xi_{PSS,PL} = \xi_{pl,PL} + \xi_{s,PL} \tag{5.3c}$$

(d) Abutment

Abutment damping is contributed by the abutment (inherent elastic damping of 5%), backfill and A-PSS. At a given PL, the dampings $\xi_{bf,PL}$ (in the backfill) and $\xi_{A\text{-}PSS,PL}$ (at the underlying PSS) are calculated in the similar ways, as are done for sand (Equation (5.3b)) and the PSS at the bent (Equation (5.3c)) respectively. Thus, the equivalent viscous damping $\xi_{ab,PL}$ is calculated in Equation (5.4) as,

$$\xi_{ab,PL} = 0.05 + \xi_{bf,PL} + \xi_{A\text{-}PSS,PL} \tag{5.4}$$

(e) Bent

Equivalent damping at bent $\xi_{bent,PL}$ at a given *DS* is computed by combining the damping contributions of bearing, pier and PSS in proportion to the individual displacements $y_{br,PL}$, $y_{pr,PL}$ and $y_{pl,PL}$ respectively in Equation (5.5) as,

$$\xi_{bent,PL} = \frac{\xi_{br,PL} \cdot y_{br,PL} + \xi_{pr,PL} \cdot y_{pr,PL} + \xi_{PSS,PL} \cdot y_{pl,PL}}{y_{br,PL} + y_{pr,PL} + y_{pl,PL}} \tag{5.5}$$

(f) Overall BS

Finally, $\xi_{BS,PL}$ is obtained by weighing the damping contributions of each j^{th} bent and the abutments, in proportion to the corresponding base shear levels $F_{bent,PL}$ and $F_{ab,PL}$ with respect to the total base shear $F_{BS,PL}$ in Equation (5.6). Table 5.1 displays the damping values evaluated for the components as well as for the BS for some of the BS samples.

$$\xi_{BS,PL} = \frac{\sum_{j=1}^{j} \xi_{bent,PL} F_{bent,PL} + 2\xi_{ab,PL} F_{ab,PL}}{\sum_{j=1}^{j} F_{bent,PL} + 2F_{ab,PL} (= F_{BS,PL})} \tag{5.6}$$

5.3.3 Generation of Seismic Demand Spectra

Once $\xi_{BS,PL}$ is calculated, the corresponding overdamped GM response spectrum i.e., the seismic demand spectrum is obtained by reducing each of the generated 5% damped GM elastic spectra (Section 4.2.4) for $\xi_{BS,PL}$, using the software SeismoSignal herein. One such demand spectrum obtained from the elastic spectrum corresponding to Chi-Chi earthquake 1999 (Figure 5.5(a)) for $\xi_{BS,PL}$ of approximately 13% is shown in Figure 5.5(b).

Table 5.1 List of evaluated component and BS dampings for some of the BS samples

Components		BS no.	Damping (%)	Components		BS no.	Damping (%)
Pier	DS1	4(e)	5	Bearing	DS1	1(b)	5
	DS2		9.60		DS2		5
	DS3		13.47		DS3		7.86
	DS4		14.01		DS4		7.99
A-PSS	Pile	11(c)	Pile	ABS	DS1	10(e)	15.57
	DS1		5		DS2		18.32
	DS2		12.21		DS3		19.45
	Sand		Sand	BS@ABS DS2		3(a)	13.26
	DS1		17.67	BS@Bearing DS1		7(e)	11.70
	DS2		18.92				

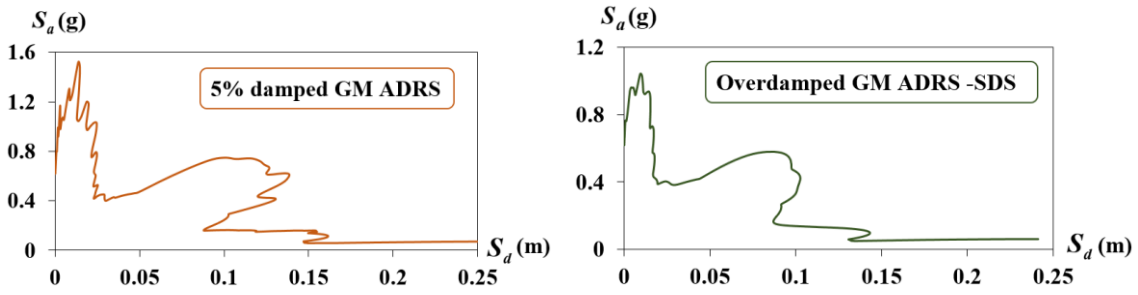

(a) (b)

Figure 5.5 (a) An elastic spectrum and (b) a demand spectrum in the present study.

5.3.4 Evaluation of IM and Seismic Demands Corresponding to a Given DS

PSDM, which involves evaluating the seismic demands and relating these to the IM, is obtained herein while evolving a few steps beyond the present usage of IACSM. It traditionally involves evaluating the IM value causing a component DS or PL (i.e., IM_{PL}), and using it as the median value to derive the FC using LF. IACSM is extended herein for extracting the BS S_a demand at that DS and arriving at the EDP values of the components.

At a given component DS, IM_{PL} is determined by translating the corresponding demand spectrum (generated) onto the capacity spectrum at that DS (the instant of occurrence, as marked on the capacity spectrum). Analytically, it is obtained, as in Equation (5.7), where, $S_{a,C}$ and $S_{a,D}$ respectively are the S_a values from the capacity and demand spectra (against the T_N at that PL), IM_{GM} is the IM (both PGA and S_a (0.7s))) value of the GM associated with the demand spectrum, and $S_{d,C}$ is the S_d value against $S_{a,C}$. Since, the GMs are scaled up or down from their respective IMs to specified values within the range of 0−1.8g, IACSM analyses of the i(=144)×j(=9) BS sample-GM pairs yield 1296 values, each for IM_{PL} and $S_{a,D}$ at the m^{th} value (IM_m) of the IM range (denoted with subscript 'ij' corresponding to the i^{th} BS sample − j^{th} GM pair), as in Equation (5.7).

$$IM_{PL,ij} = \frac{S_{a,C_{ij}}}{S_{a,D_{ij}} / IM_{GM,j}}; \quad T_{N_i} = 2\pi\sqrt{\frac{S_{d,C_i}}{g \cdot S_{a,C_i}}}; \quad {}^{m}S_{a,D_{ij}} = S_{a,D_{ij}} \cdot IM_m / IM_{GM} \tag{5.7}$$

The S_d value with respect to the ${}^{m}S_{a,D_{ij}}$, i.e., ${}^{m}S_{d,D_{ij}}$, is evaluated. EDP values of individual components are assessed as proportions of ${}^{m}S_{d,D_{ij}}$, based on the respective weighted contributions to BS mode shape at the instant of attainment of the PL; computations are carried out in spreadsheets. EDP distributions obtained for A-PSS, ABS, bearing and pier, denoted by $D_{i,pl}$, $D_{i,ab}$, $D_{i,br}$ and $D_{i,pr}$ (where, i = 1 to 4 corresponds to DS rank), are shown in Figures 5.6, 5.7, 5.8 and 5.9 respectively against the value of 0.1g for both the IMs.

5.3.5 Generation of the Component EDP-IM relationships.

As seen in Section 5.3.5, a stripe of 1296 component-level demand data values is obtained at an IM value. Repetition of IACSM analysis over the IM range results in multiple stripes, as shown in Figure 5.10(a) with respect to A-PSS demand at DS2. Regressing the mean (at each IM value) values of the demands ($\overline{D}$s), denoted by $\overline{D_{i,pl}}$, $\overline{D_{i,ab}}$, $\overline{D_{i,br}}$ and $\overline{D_{i,pr}}$ for A-PSS, ABS, bearing and pier respectively, against IM in log space results in the D-IM relationships. One such regression fit is shown in Figure 5.10(b), with respect to PSS DS1.

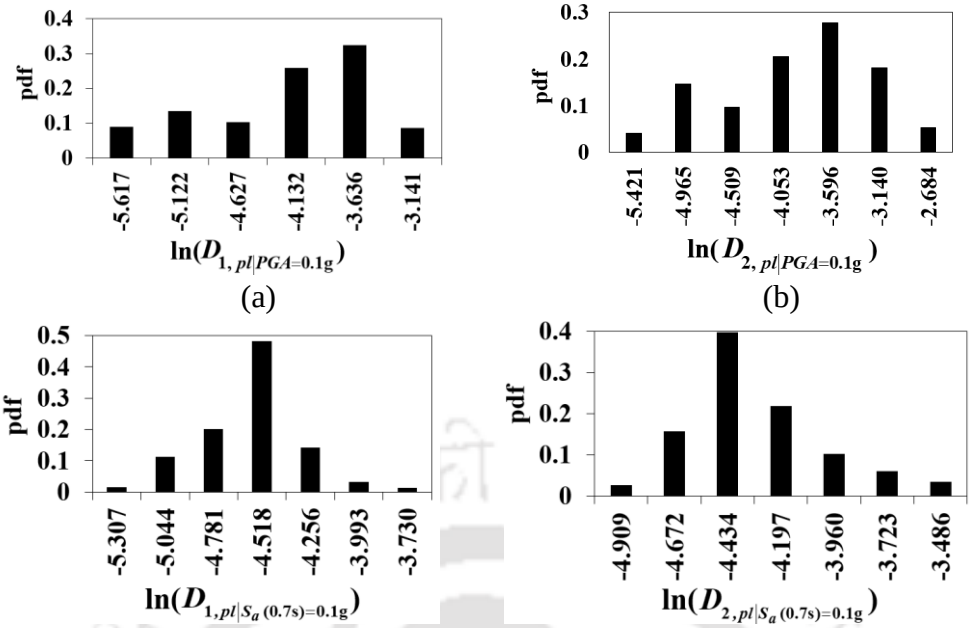

Figure 5.6 A-PSS EDP distributions at (a) DS1 and (b) DS2 with respect to PGA, and (c) DS1 and (d) DS2 with respect to S_a (0.7s).

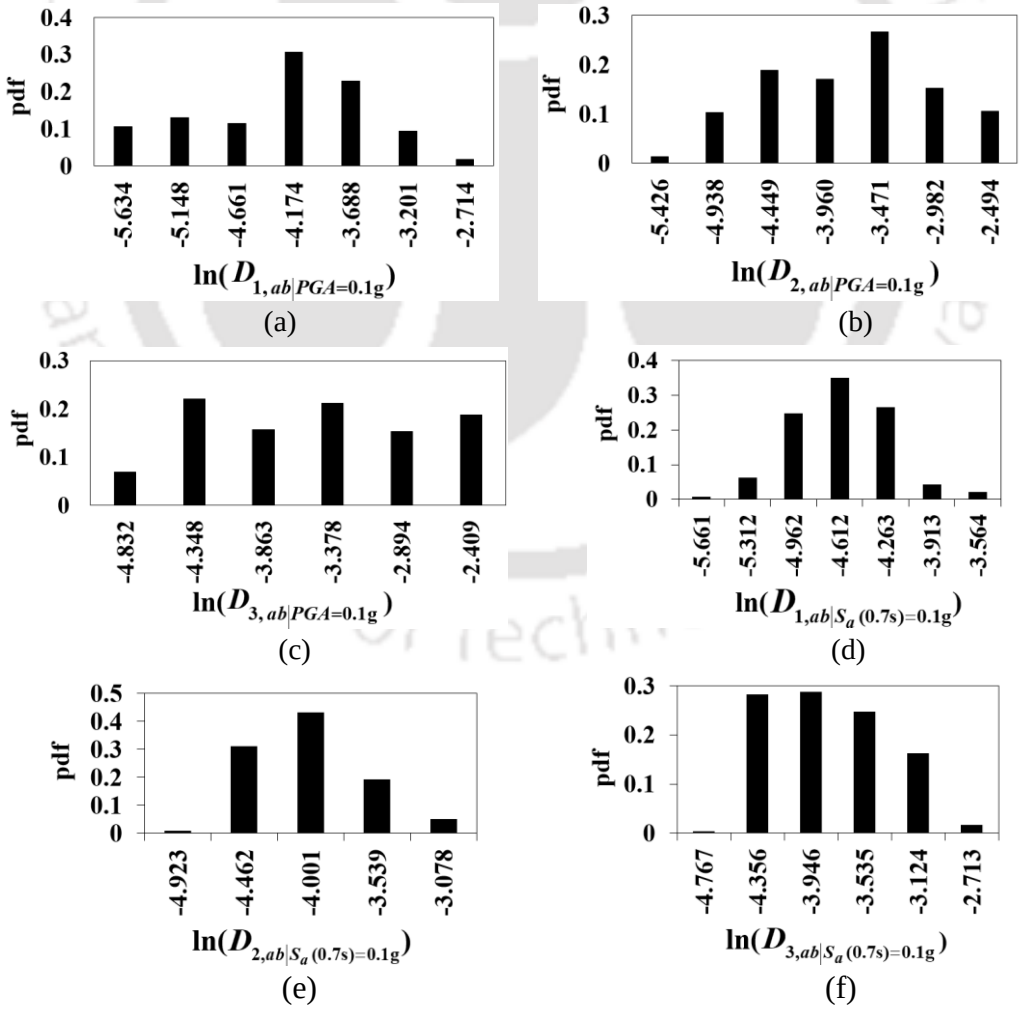

Figure 5.7 ABS EDP distributions at (a) DS1, (b) DS2 and (c) DS3 with respect to PGA, and (d) DS1, (e) DS2 and (f) DS3 with respect to S_a (0.7s).

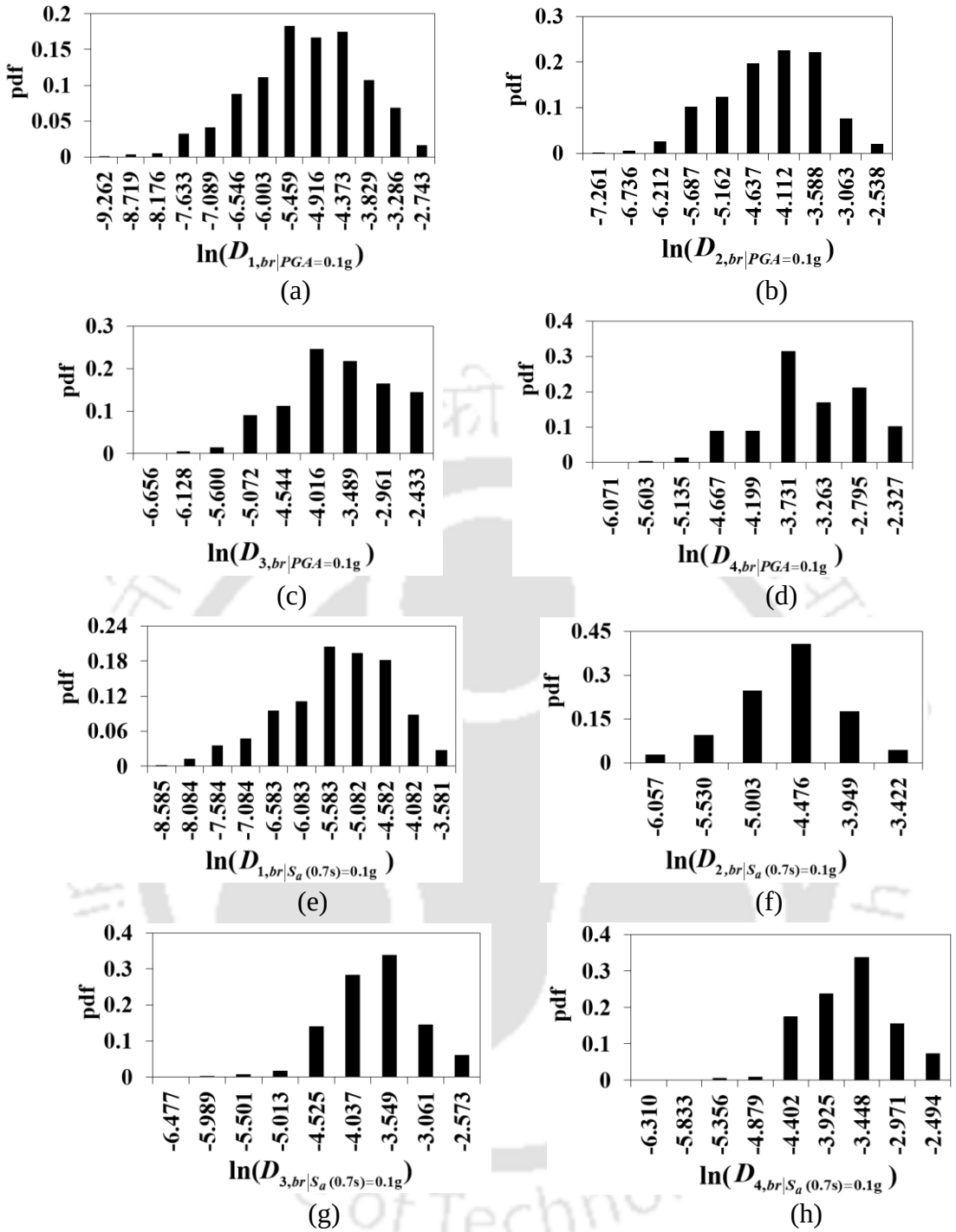

Figure 5.8 Bearing EDP distributions at (a) DS1, (b) DS2, (c) DS3 and (d) DS4 against PGA, and (e) DS1, (f) DS2, (g) DS3 and (h) DS4 against S_a (0.7s).

5.3.6 Investigation of Optimality of the IMs

Optimality of the IMs adopted herein are decided based on the efficiency criterion, which implies reduction of the amount of variation in the estimated demand for a given IM value (Mackie and Stojadinovic, 2004) and quantified through less dispersion about the estimated median in the data resulting from the seismic demand analysis. Thus, the study examines the extent of the respective dispersions $\beta_{D|PGA}$ and $\beta_{D|S_a(0.7s)}$ of the demands when each of

PGA and S_a (0.7s) is considered as the IM while evaluating the demands, as listed in Table 5.2. Employment of $S_a(0.7s)$ significantly reduces the demand dispersion for both A-PSS and ABS as compared to PGA, while the effect is moderate to small for bearing DSs and moderate for pier initial DSs. In case of higher DSs of pier, IM type has no effect at all.

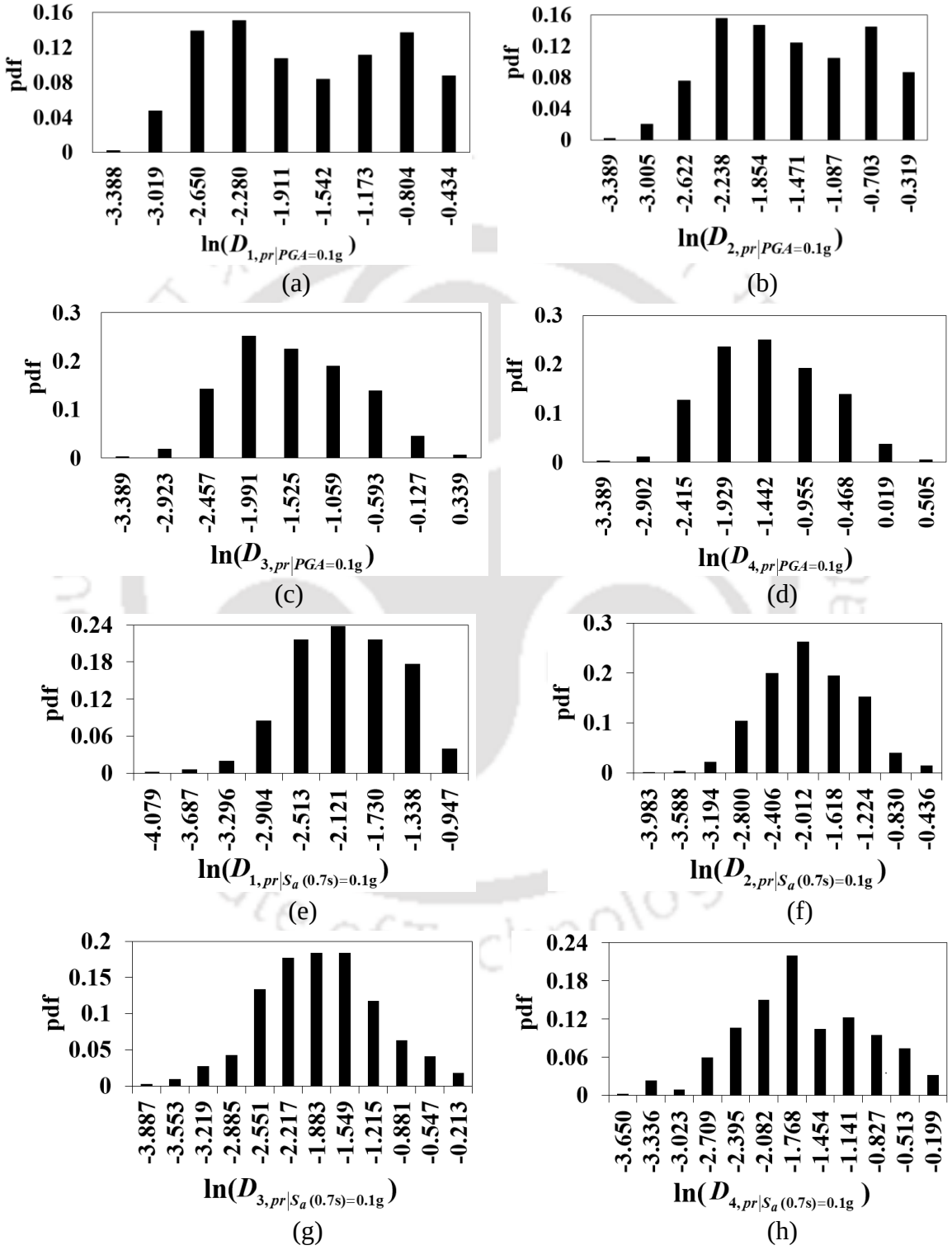

Figure 5.9 Pier EDP distributions at (a) DS1, (b) DS2, (c) DS3 and (d) DS4 with respect to PGA, and (e) DS1, (f) DS2, (g) DS3 and (h) DS4 with respect to S_a (0.7s).

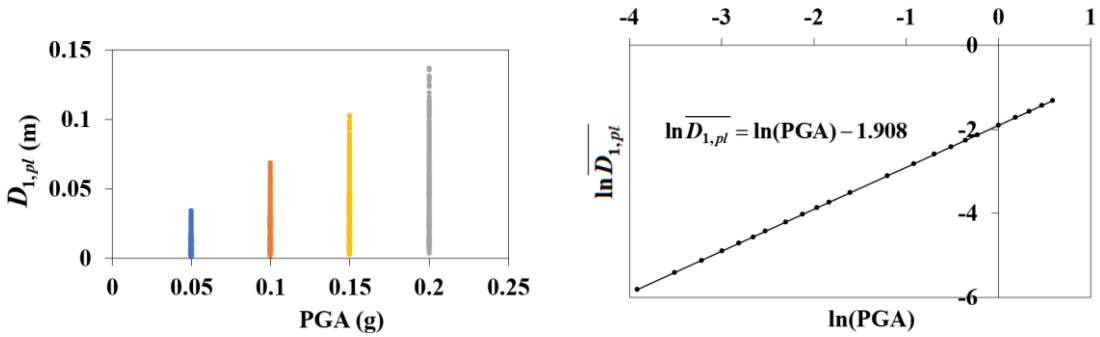

(a) (b)

Figure 5.10 (a) *D*-IM stripe data and (b) Regression fit to ln($\overline{D}$)-ln(IM) data.

Table 5.2 Dispersions of seismic demands with respect to PGA and S_a (0.7s)

Components	DSs	$\beta_{D\|PGA}$	$\beta_{D\|S_a(0.7s)}$	Components	DSs	$\beta_{D\|PGA}$	$\beta_{D\|S_a(0.7s)}$
A-PSS	DS1	0.719	0.275	ABS	DS1	0.737	0.374
	DS2	0.707	0.304		DS2	0.750	0.380
					DS3	0.778	0.430
Bearing	DS1	1.148	0.990	Pier	DS1	0.798	0.558
	DS2	0.853	0.553		DS2	0.732	0.597
	DS3	0.831	0.669		DS3	0.683	0.677
	DS4	0.715	0.639		DS4	0.682	0.671

IM effectiveness criterion, determined by the ability to fit a mathematical form to the median trend of *D*, is achieved by the median *D* ($\overline{D}$)-IM relationships in the forms of linear equations in log space, of the format as in Equation (5.8) where, *a* and *b* are the regression coefficients for the demand data versus IM, as listed in Table 5.3. The practicality criterion of the *D*-IM pair, which involves some direct correlation with known engineering quantities and measured by the '*b*' value in the probabilistic seismic demand model, is considered to be moderately fulfilled through the achievement of moderate quantity magnitude of '*b*' of 1 for all the component PSDMs with respect to both the IMs, as in Table 5.3.

$$\ln(\overline{D}) = \ln(a) + b\ln(IM) \tag{5.8}$$

Sufficiency criterion is also examined; the cut-off for an insufficient IM is assumed to be a *p*-value of 0.10, as by Padgett et al. (2008), for the regression upon the residuals from the PSDMs against the earthquake magnitude. Investigated for the case of A-PSS DS2, *p*-values of the regression models, corresponding to the PSDM with respect to PGA is found to be 0.03 and that with respect to S_a (0.7s) is found to be 0.12. For the cases of ABS DS2, bearing DS2, and pier DS2, these values are 0.04 and 0.27, 0.59 and 0.43, 0.47 and 0.05, with respect to PGA and S_a (0.7s). Thus, for ABS and A-PSS, S_a (0.7s) is a more sufficient IM than PGA, whereas PGA is slightly found to more sufficient than S_a (0.7s) in case of bearing. PGA is a quite sufficient IM in case of pier while S_a (0.7s) is found to insufficient.

Table 5.3 *D*-IM relationships for the Bridge Components

DS		PGA	S_a (0.7s)
A-PSS	DS1	$\ln \overline{D_{1,pl}} = \ln(\text{PGA}) - 1.908$	$\ln \overline{D_{1,pl}} = \ln(S_a(0.7s)) - 2.367$
	DS2	$\ln \overline{D_{2,pl}} = \ln(\text{PGA}) - 1.627$	$\ln \overline{D_{2,pl}} = \ln(S_a(0.7s)) - 2.078$
ABS	DS1	$\ln \overline{D_{1,ab}} = \ln(\text{PGA}) - 1.966$	$\ln \overline{D_{1,ab}} = \ln(S_a(0.7s)) - 2.410$
	DS2	$\ln \overline{D_{2,ab}} = \ln(\text{PGA}) - 1.397$	$\ln \overline{D_{2,ab}} = \ln(S_a(0.7s)) - 1.864$
	DS3	$\ln \overline{D_{3,ab}} = \ln(\text{PGA}) - 1.152$	$\ln \overline{D_{3,ab}} = \ln(S_a(0.7s)) - 1.623$
Bearing	DS1	$\ln \overline{D_{1,br}} = \ln(\text{PGA}) - 2.541$	$\ln \overline{D_{1,br}} = \ln(S_a(0.7s)) - 2.972$
	DS2	$\ln \overline{D_{2,br}} = \ln(\text{PGA}) - 1.977$	$\ln \overline{D_{2,br}} = \ln(S_a(0.7s)) - 2.434$
	DS3	$\ln \overline{D_{3,br}} = \ln(\text{PGA}) - 1.360$	$\ln \overline{D_{3,br}} = \ln(S_a(0.7s)) - 1.725$
	DS4	$\ln \overline{D_{4,br}} = \ln(\text{PGA}) - 1.158$	$\ln \overline{D_{4,br}} = \ln(S_a(0.7s)) - 1.466$
Pier	DS1	$\ln \overline{D_{1,pr}} = \ln(\text{PGA}) + 0.658$	$\ln \overline{D_{1,pr}} = \ln(S_a(0.7s)) + 0.214$
	DS2	$\ln \overline{D_{2,pr}} = \ln(\text{PGA}) + 0.712$	$\ln \overline{D_{2,pr}} = \ln(S_a(0.7s)) + 0.344$
	DS3	$\ln \overline{D_{3,pr}} = \ln(\text{PGA}) + 0.816$	$\ln \overline{D_{3,pr}} = \ln(S_a(0.7s)) + 0.527$
	DS4	$\ln \overline{D_{4,pr}} = \ln(\text{PGA}) + 0.899$	$\ln \overline{D_{4,pr}} = \ln(S_a(0.7s)) + 0.749$

5.4 GENERATION OF COMPONENT-LEVEL FRAGILITY CURVES

FCs can be obtained using the traditional Lognormal Formulation (LF), as done in many previous studies (discussed in Section 2.5.2), which assumes lognormal distribution for both capacity *C* and demand *D*. The *C* and *D* distributions evaluated, as above, in the study are found to be very rough fit in many cases while misfit in a few cases, with those of the ABS having significant deviation to the lognormal form. Thus, the present study presents a new approach of obtaining the bridge component fragility through NC, which can be applied for any types of distributions, just as evaluated for the component-level *D*s and *C*s in a study. Thus, the possible under or over estimation is avoided, when the *C* and *D* data are actually very rough fit as well as misfit to the imposed lognormal distribution, so as to estimate the lognormal parameters required as inputs in the traditional LF. Nevertheless, following the traditional practice, FCs are also generated adopting LF. Subsequently, the extents of deviation of the FC-NCs from FC-LFs are examined.

A structure will reach a DS if the value of *D* (load) exceeds that of *C* (resistance) for that DS, with probability (*P*) equal to P_f, i.e., $P(D > c_i)$, where, c_i is any specific value of *C*. Since *C* is a random variable, there is a probability associated with the c_i value; therefore, P_f is composed of all possible combinations of $C = c_i$ and $D > c_i$, expressed in Equation (5.9) (Nowak and Collins, 2012) as

$$P_f = \sum P(C = c_i \bigcap D > c_i) = \sum P(D > C | C = c_i) \cdot P(C = c_i) \quad (5.9)$$

With the above concept, P_f is computed herein, from the probability density functions (pdf) for C and D (against a given IM value) at hand corresponding to each DS for a bridge component, as in Figures 5.11(a) and 5.11(b) respectively. Thus, the value for each bin of the C distribution (i.e., c_1, c_2,…., c_6, …, with respective probabilities per unit values as p_{C_1} , p_{C_2} ,…., p_{C_6} ,…, is compared with all the bin values of the D distribution (i.e., d_1, d_2,…, d_6,… with respective probabilities per unit values as p_{D_1} , p_{D_2} ,…, p_{D_6} ,…, and the events wherein a value of D exceeds that of C are summed up to obtain P_f .

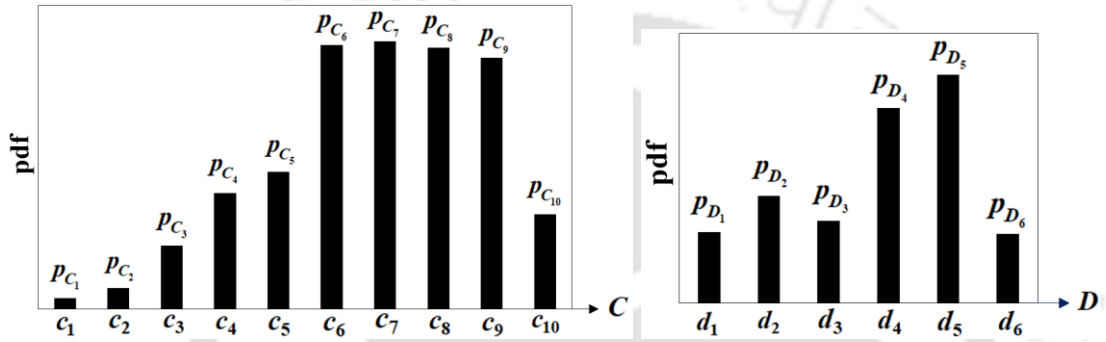

Figure 5.11 Typical probability distribution functions for (a) capacity and (b) demand.

Expression of P_f is simplified form of Eq. (3), as required in the study. The computation is repeated for the C and D distributions evaluated against each increasing value of IM to obtain the corresponding P_f values, resulting in the generation of the FC

$$P_f = \sum_{i=1} (p_{ci} \cdot \sum_j p_{dj}) | c_i < d_j ; \quad j = 1,2,3... \quad (5.10)$$

All the bearing DSs do not occur in all the BS samples, as in those cases, pier DS4 precedes all or a few bearing DSs leading to the BS collapse before all or the remaining DSs of bearing could occur. Also, there are cases where bearing sliding (DS2) occurs before any or a few pier DSs have reached, thus causing the BS-bent isolation, thereby preventing all or remaining pier DSs to occur. As such, the occurrence probability of a bearing (or pier) DS, i.e., OP_{br} (or OP_{pr}) is calculated as the ratio of the number of cases $n_{br\text{-}DS}$ (or $n_{pr\text{-}DS}$) wherein that bearing (or pier) DS occurs and the total number of simulations (=144). Probability of reaching a DS for a given IM, i.e., $P[DS|IM]$ for bearing (or pier) is obtained by multiplying OP_{br} (or OP_{pr}) with the probability of reaching the DS for $n_{br\text{-}DS}$ (or $n_{pr\text{-}DS}$) cases, i.e., $P[DS|IM]|n_{br\text{-}DS}$ (or $P[DS|IM]|n_{pr\text{-}DS}$) and is expressed in Equation (5.11) as,

$$P[DS|IM]|br = OP_{br} \cdot P[DS|IM]|n_{br\text{-}DS} \; ; \; P[DS|IM]|pr = OP_{pr} \cdot P[DS|IM]|n_{pr\text{-}DS} \qquad (5.11)$$

5.4.1 Different Forms of FCs Evaluated in the Study

Though, S_a (0.7s) is observed to be a better IM, FCs are generated with respect to both the IMs. FC-LFs corresponding to A-PSS, ABS, bearing and pier are shown in Figures 5.12(a), 5.12(b), 5.12(c) and 5.12(d) with respect to PGA, and Figures 5.13(a), 5.13(b), 5.13(c) and 5.13(d) with respect to S_a (0.7s). FC-NCs corresponding to A-PSS, ABS, bearing and pier are shown in Figures 5.14(a), 5.14(b), 5.14(c) and 5.14(d) with respect to PGA and Figures 5.15(a), 5.15(b), 5.15(c) and 5.15(d) with respect to S_a (0.7s).

It is to be noted that, for some of the FC-NCs, as in Figures 5.14(c); 5.14(d); 5.15(c); and 5.15(d) corresponding to bearing DS4; pier DS1; bearing DS3 and and DS4; and pier DS1 and DS2, smooth profiles (as those of FC-LFs) are not followed and consist of flat parts, one stepping up to the next one. Since, bearing DS3 and DS4 and almost all the pier DSs usually occur at large BS T_Ns for the IAB class, the respective D values are closer (as most GM response spectra show almost constant values at very large T_Ns). Subsequently, increase in D rate with IM is slow and for the next higher level of IM, most of the bin values of the D distributions might not be able to exceed the respective bin values of the C distributions causing the fragility values to be more or less of similar values. Magnitude of D builds up only after a considerable IM range, causing C to be exceeded, leading to a higher fragility value at the IM level beyond that range, causing step up in the FC profile.

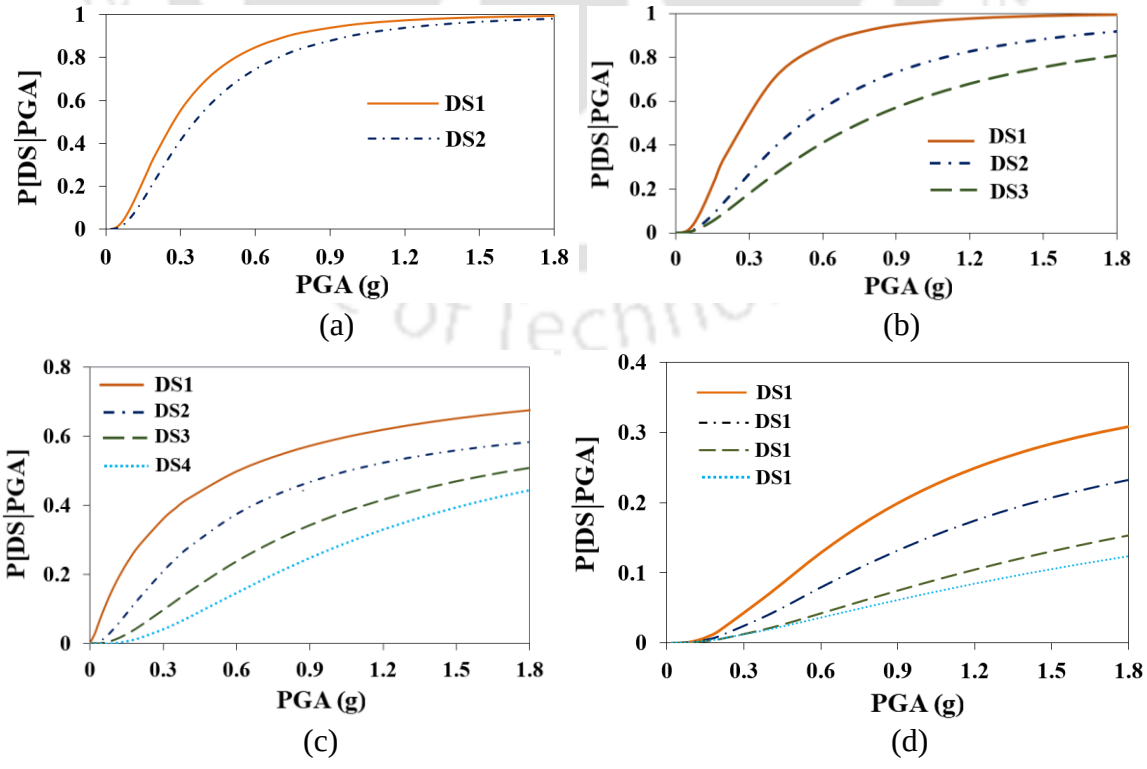

Figure 5.12 Component-level FCs generated for (a) A-PSS, (b) ABS, (c) bearing and (d) pier with respect to PGA and employing LF.

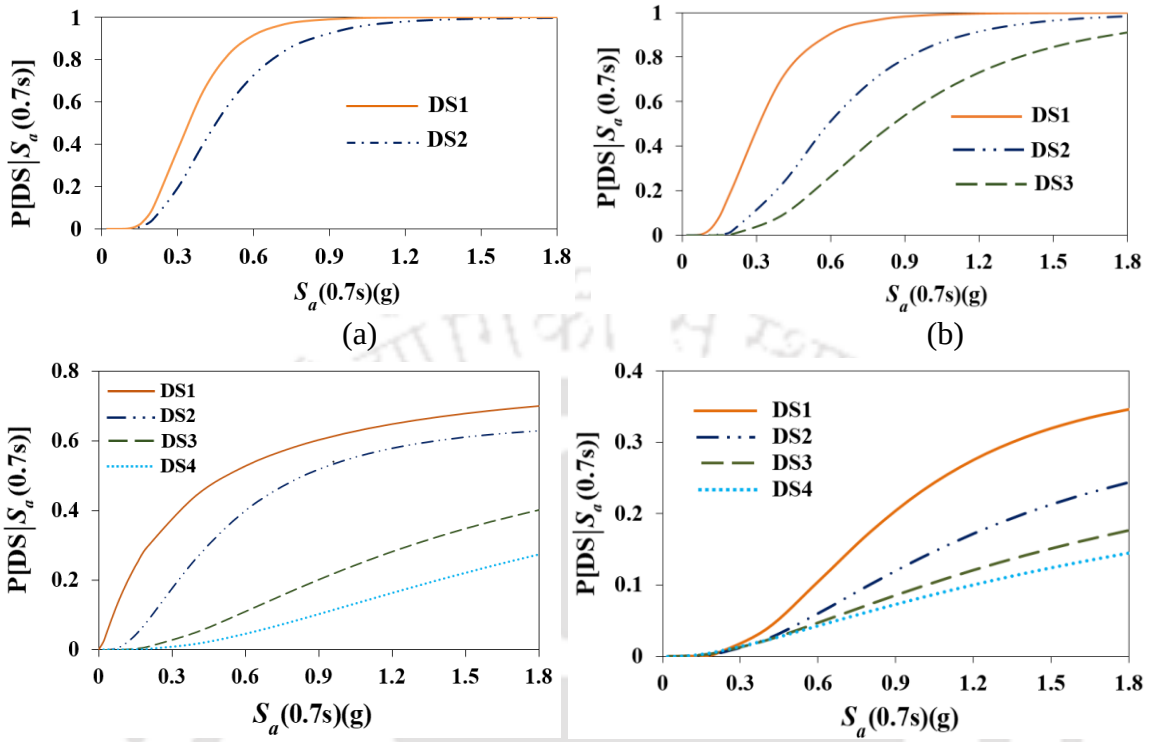

Figure 5.13 Component-level FCs generated for (a) A-PSS, (b) ABS, (c) bearing and (d) pier with respect to S_a (0.7s) and following LF.

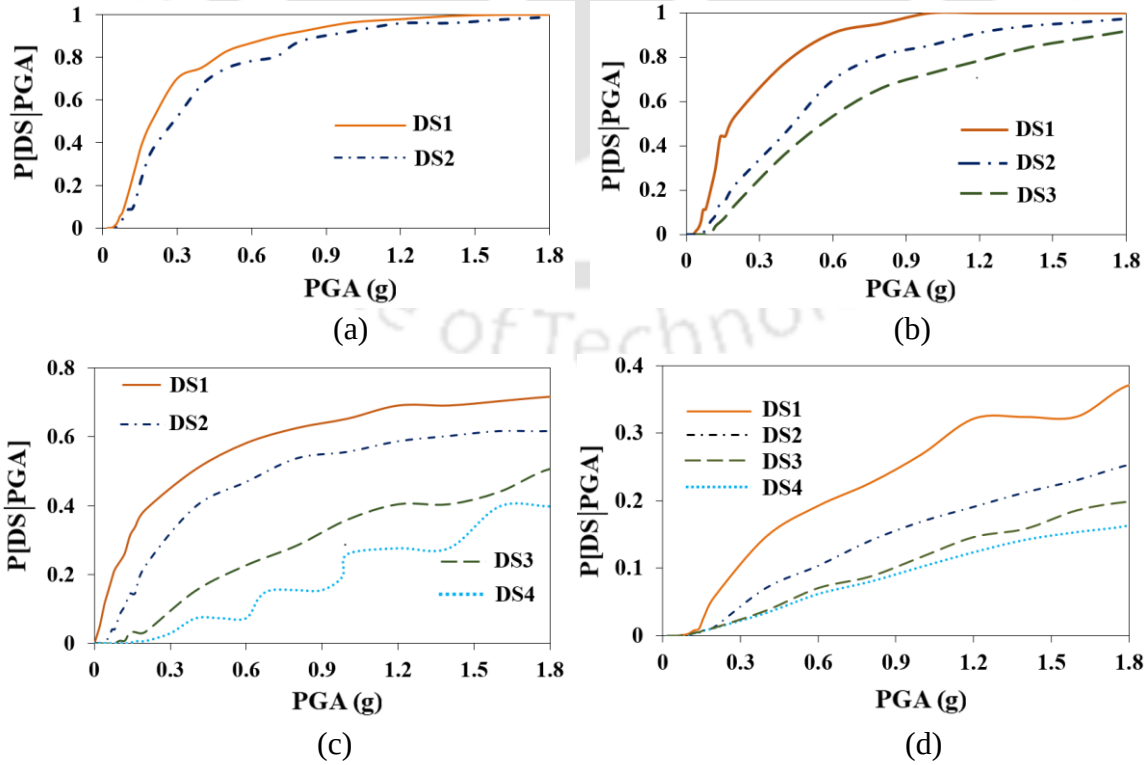

Figure 5.14 Component-level FCs for (a) A-PSS, (b) ABS, (c) bearing and (d) pier with respect to PGA and NC.

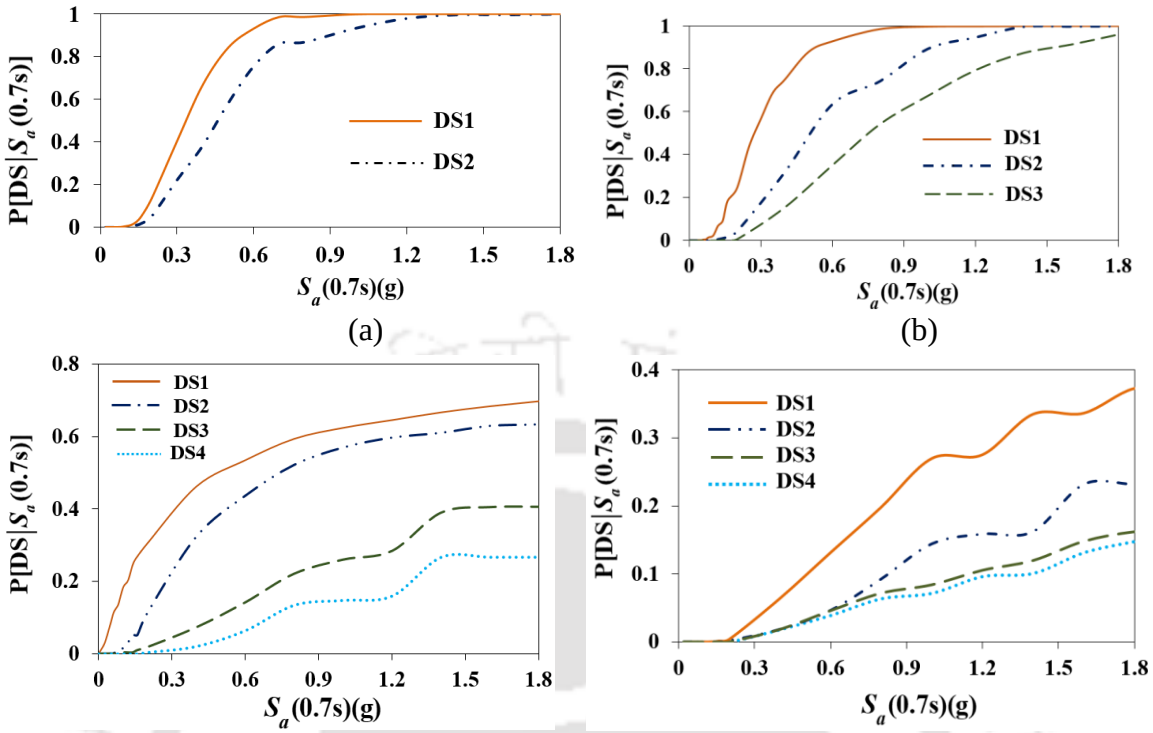

Figure 5.15 Component-level FCs for (a) A-PSS, (b) ABS, (c) bearing and (d) pier with respect to S_a (0.7s) and NC.

5.4.2 Influences of the IM Types and the Fragility Computation Approaches

Impact of IM type as well as fragility estimation approach on component-level vulnerabilities can be examined through comparisons among the FCs with respect to PGA-LF, PGA-NC, S_a (0.7s)-LF and S_a (0.7s)-NC pairs. Difference between any two FCs is not uniform along the curves and varies with respect to IM. Thus, comparison is based on the extent of variation between two FCs, measured as the percentage difference in fragility with respect to IM, i.e., δ_{FC}, and expressed in Equation (5.12), where $FC1_{v|IM_v}$ and $FC2_{v|IM_v}$ are the probability values at an IM value (IM_v) on the first and second FCs respectively.

$$\delta_{FC} = \left(\frac{FC1_{v|IM_v} - FC2_{v|IM_v}}{IM_v} \right) \times 100\% \tag{5.12}$$

5.4.2.1 Impacts of LF and NC Approaches on the Component-Level FCs

Figures 5.16(a) and 5.16(b) show the comparative FC-LFs and FC-NCs, with respect to PGA and S_a (0.7s) for A-PSS DSs; Figures 5.16(c) and 5.16(d) display the trends of δ_{FC} between FC-LFs and FC-NCs. Figures 5.17(a) and 5.17(b) show the comparative FC-LFs and FC-NCs, with respect to PGA and S_a (0.7s) for ABS DSs; Figures 5.17(c) and 5.17(d)

display the trends of δ_{FC} between FC-LFs and FC-NCs. Figures 5.18(a) and 5.18(b) show the comparative FC-LFs and FC-NCs, with respect to PGA and S_a (0.7s) for bearing DSs; Figures 5.18(c) and 5.18(d) display the trends of δ_{FC} between FC-LFs and FC-NCs. Figures 5.19 (a) and 5.19(b) show the comparative FC-LFs and FC-NCs, with respect to PGA and S_a (0.7s) for pier DSs; Figures 5.19(c) and 5.19(d) display the trends of δ_{FC} between FC-LFs and FC-NCs.

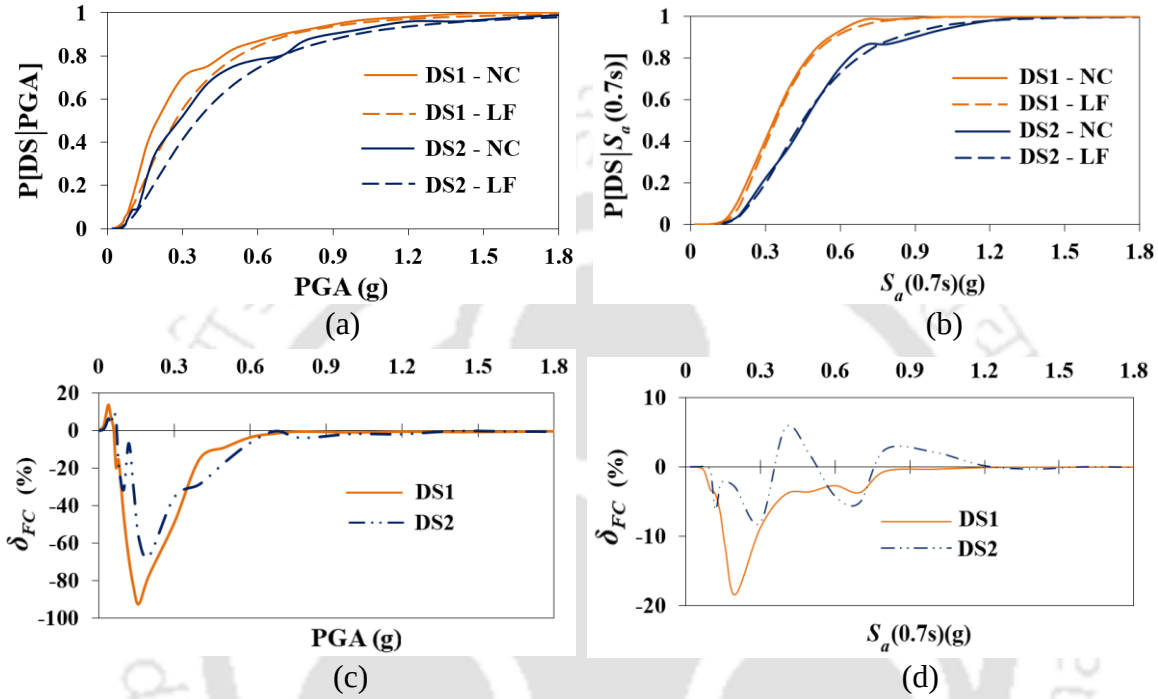

Figure 5.16 Comparative FC-LFs and FC-NCs with respect of (a) PGA and (b) S_a (0.7s); and trends of δ_{FC} with respect to (c) PGA and (d) S_a (0.7s) for A-PSS.

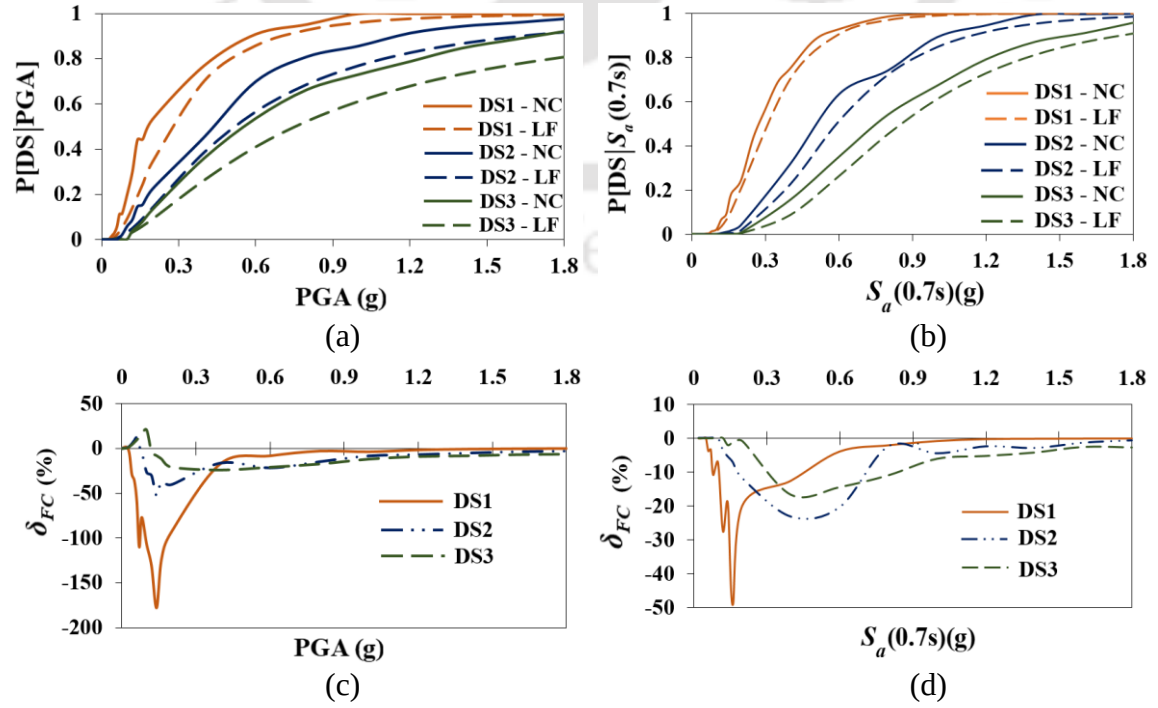

Figure 5.17 Comparative FC-LFs and FC-NCs with respect to (a) PGA and (b) S_a (0.7s); and trends of δ_{FC} with respect to (c) PGA and (d) S_a (0.7s) for ABS.

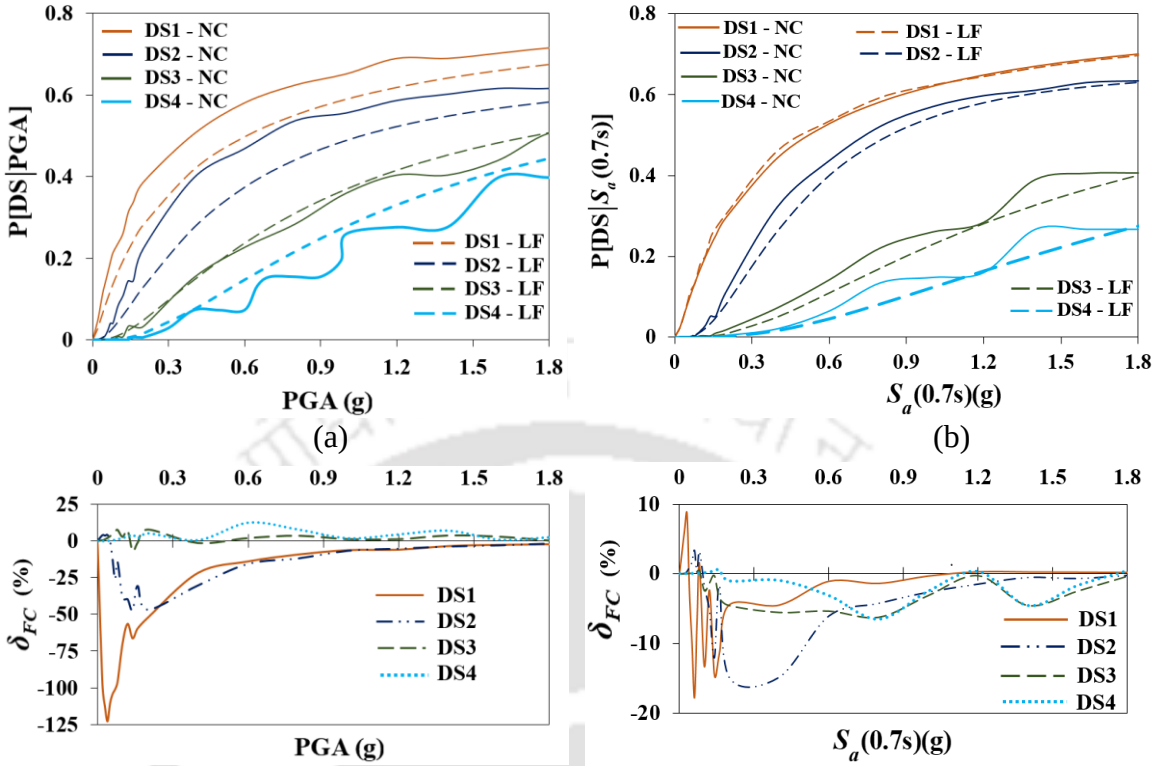

Figure 5.18 Comparative FC-LFs and FC-NCs with respect to (a) PGA and (b) S_a (0.7s); and trends of δ_{FC} with respect to (c) PGA and (d) S_a (0.7s) for bearing.

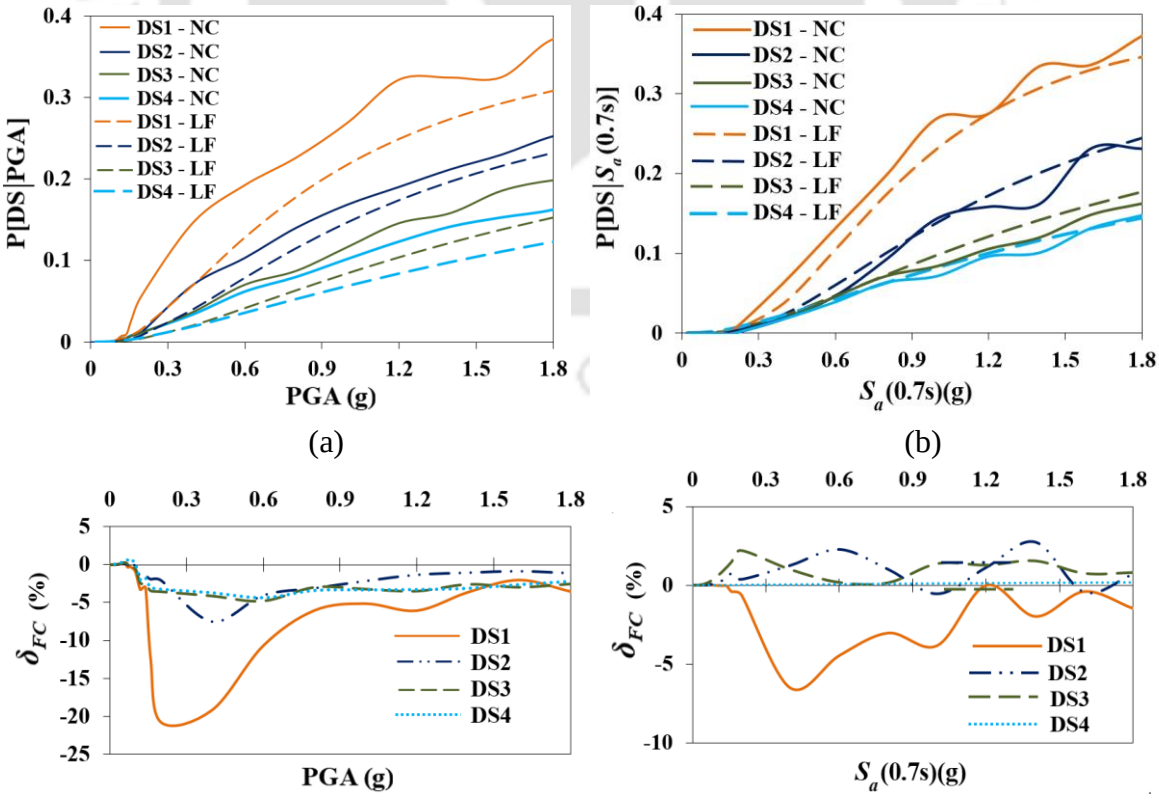

(c) (d)

Figure 5.19 Comparative FC-LF and FC-NC with respect to (a) PGA and (b) S_a (0.7s); and trends of δ_{FC} with respect to (c) PGA and (d) S_a (0.7s) for pier.

In all cases, LF is observed to generally give lower values of fragilities at all IM_vs in comparison to NC, irrespective of the IM type; however, for very initial and small IM_vs, NC gives slightly higher values. Exceptions are the cases of A-PSS DS2 (Figure 5.16(d)), bearing DS3 and DS4 with respect to PGA (Figure 5.18(c)) and pier DS2, DS3 and DS4 (Figure 5.19(d)) with respect to S_a (0.7s), and where, LF show higher values of fragilities, as compared to NC at some IM_vs and vice-versa at other IM_vs. Difference in the fragilities with respect LF and NC is the greatest at DS1 in case of all the components and the point where the peak difference occurs tends to shift to a higher IM_v, with the increasing DS rank, irrespective of the IM type. Table 5.4 lists the $\delta_{FC,\max}$s (maximum δ_{FC}) between FC-LF and FC-NC, with respect to both the IMs and throughout the IM range.

Differences between FC-LFs and FC-NCs are much lesser with respect to S_a (0.7s) compared to PGA, as the *D* distributions for all the components show more refinement towards the lognormal form in case of S_a (0.7s) compared to PGA. Thus, the fragility estimated through NC tends to be closer to those through LF, with respect to S_a (0.7s). δ_{FC} values with respect to S_a (0.7s) between FC-LFs and FC-NCs are much lesser, and FC-NCs almost merge onto FC-LFs compared to PGA (Figures 3.16(c) and 3.16(d)). This is because, apart from the *C* distributions following the lognormal form with fair approximation, *D* data of A-PSS with respect to S_a (0.7s) fit pretty well to lognormal distribution than those with respect to PGA. Thus, NC yields similar fragility magnitudes as those through LF. In case of ABS, FC-NCs considerably differ from FC-LFs, in fact, it shows the highest deviations between FC-LFs and FC-NCs among all the components. For instances, δ_{FC} values between FC-LF and FC-NC, obtained with respect to PGA and DS1 for ABS (Figure 3.17(c)) are observed to be much higher, almost twice, compared to those (Figure 3.16(c)) for A-PSS. δ_{FC} values with respect to S_a (0.7s) between FC-LF and FC-NC, as obtained for ABS (Figure 3.17(d)) are observed to be much higher, almost 2.5 times compared to those (Figure 3.16(d)) of A-PSS. This is because, the *C* distributions are misfit to the lognormal form and the *D* distributions show very rough lognormal profiles for ABS.

It is to be noted that the pier is the least vulnerable component at all its DSs as well the bearing at its higher DSs; thus, the fragility values with respect to both LF and NC are very low and hence $\delta_{FC,\max}$s are also very low. With respect to both the IMs, $\delta_{FC,\max}$s between FC-LFs and FC-NCs are similar, which again supports the observations that the

change in IM type has moderate to negligible effects on pier and moderate to small effects on bearing for the IAB class in the study.

Table 5.4 Comparative fragilities with respect to LF and NC

A-PSS		PGA		S_a (0.7s)	
		IM_v range	$\delta_{FC,\max}$ (IM_v)	IM_v range	$\delta_{FC,\max}$ (IM_v)
DS1	LF > NC	≤ 0.06g	14% (0.04g)	-----	
	LF < NC	> 0.06g	92% (0.16g)	0 ≤ -- ≤ 1.8g	19% (0.20g)
DS2	LF > NC	≤ 0.072g	10% (0.06g)	0.359g < -- ≤ 0.528g	6% (0.40g)
				> 0.768g	3% (0.80g)
	LF < NC	> 0.072g	67% (0.20g)	≤ 0.359g	8% (0.30g)
				0.528g < -- ≤ 0.768g	5% (0.7g)
ABS		**PGA**		**S_a (0.7s)**	
		IM_v range	$\delta_{FC,\max}$ (IM_v)	IM_v range	$\delta_{FC,\max}$ (IM_v)
DS1	LF > NC	≤ 0.022g	1.4% (0.02g)	≤ 0.05g	0.13% (0.05g)
	LF < NC	> 0.022g	178% (0.14g)	> 0.05g	50% (0.16g)
DS2	LF > NC	≤ 0.074g	12% (0.06g)	≤ 0.089g	0.063% (0.08g)
	LF < NC	> 0.074g	53% (0.14g)	> 0.089g	23% (0.40g)
DS3	LF > NC	≤ 0.117g	21% (0.10g)	≤ 0.121g	0.083% (0.12g)
	LF < NC	> 0.117g	24% (0.40g)	> 0.121g	17% (0.40g)
Bearing		**PGA**		**S_a (0.7s)**	
		IM_v range	$\delta_{FC,\max}$ (IM_v)	IM_v range	$\delta_{FC,\max}$ (IM_v)
DS1	LF > NC	-----	-----	≤ 0.037g	9% (0.03g)
				> 1.112g	0.27% (1.2g)
	LF < NC	≤ 0.04g	123% (0.04g)	0.037g < -- ≤ 1.112g	8% (0.20g)
DS2	LF > NC	≤ 0.05g	4% (0.04g)	≤ 0.093g	3% (0.06g)
	LF < NC	> 0.05g	48% (0.14g)	> 0.093g	15% (0.20g)
DS3	LF > NC	≤ 0.130g	4% (0.04g)	≤ 0.083g	0.50% (0.08g)
		0.166g < -- ≤ 0.366g	8% (0.20g)		
		> 0.493g	4% (1.4g)		
	LF < NC	0.130g < -- ≤ 0.166g	7% (0.14g)	> 0.083g	6% (0.80)
		0.366g < -- ≤ 0.493g	2% (0.40g)		
DS4	LF > NC	0 ≤ -- ≤ 1.8g	13% (0.60g)	≤ 0.173g	0.50% (0.16g)
	LF < NC	-----	-----	> 0.173g	7% (0.80g)
Pier		**PGA**		**S_a (0.7s)**	
		IM_v range	$\delta_{FC,\max}$ (IM_v)	IM_v range	$\delta_{FC,\max}$ (IM_v)
DS1	LF > NC	≤ 0.065g	0.30% (0.06g)	≤ 0.090g	0.02% (0.08g)
	LF < NC	> 0.065g	21% (0.20g)	> 0.090g	7% (0.40g)
DS2	LF > NC	≤ 0.070g	0.18% (0.05g)	0 ≤ -- ≤ 1.8g	1 % (0.40g)
	LF < NC	> 0.070g	8% (0.40g)	-----	-----
DS3	LF > NC	≤ 0.071g	0.15% (0.05g)	0 ≤ -- ≤ 1.8g	2% (0.20g)
	LF < NC	> 0.071g	5% (0.60g)	-----	-----
DS4	LF > NC	≤ 0.101g	0.74% (0.08g)	0 ≤ -- ≤ 1.8g	0.19% (1.8g)
	LF < NC	> 0.101g	4% (0.60g)	-----	-----

5.4.2.2 Impacts of the Adopted IM Types on the Component-Level FCs

Figures. 5.20(a) and 5.20(b) show the comparative FC-PGAs and FC-S_a(0.7s)s with respect to LF and NC for A-PSS DSs; Figures. 5.20(c) and 5.20(d) display the trends of δ_{FC}. Figures. 5.21(a) and 5.21(b) show the comparative FC-PGAs and FC-S_a(0.7s)s with respect to LF and NC for ABS DSs; Figures. 5.21(c) and 5.21(d) display the trends of δ_{FC}. Figures. 5.22(a) and 5.22(b) show the comparative FC-PGAs and FC-S_a(0.7s)s with respect to LF and NC for bearing DSs; Figures. 5.22(c) and 5.22(d) display the trends of δ_{FC}. Figures. 5.23(a) and 5.23(b) show the comparative FC-PGAs and FC-S_a(0.7s)s with respect to LF and NC, for pier DSs; Figures. 5.23(c) and 5.23(d) display the trends of δ_{FC}.

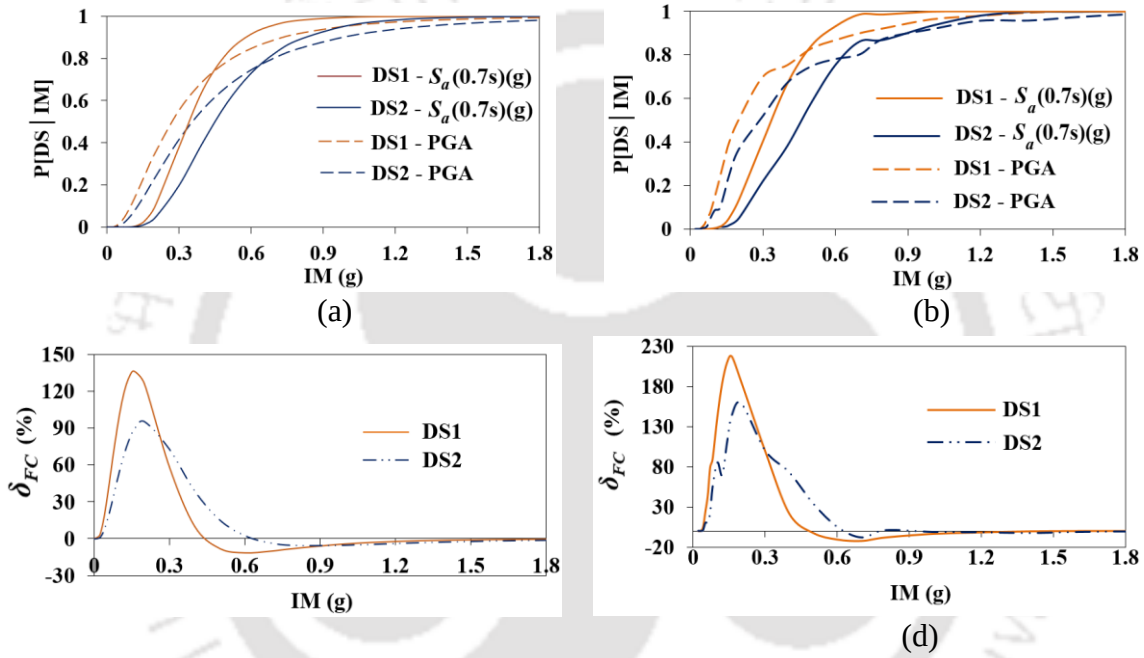

Figure 5.20 Comparative FC-PGAs and FC-S_a(0.7s)s with respect to (a) LF and (b) NC; and trends of δ_{FC} with respect to (c) LF and (d) NC for A-PSS.

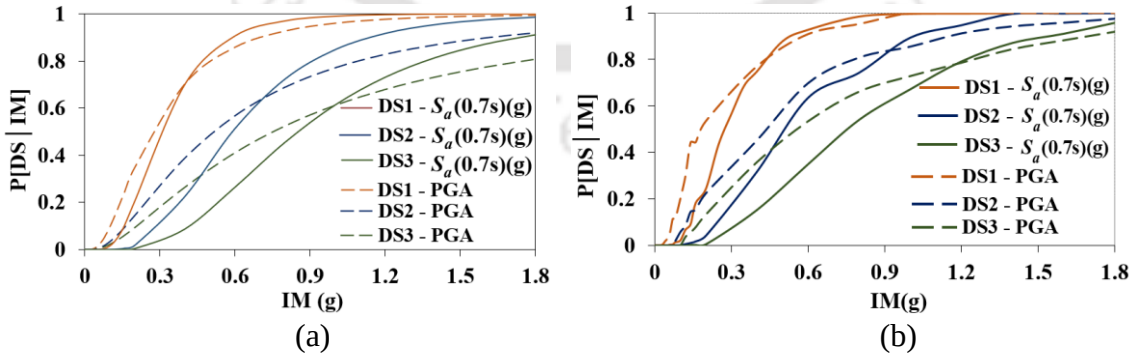

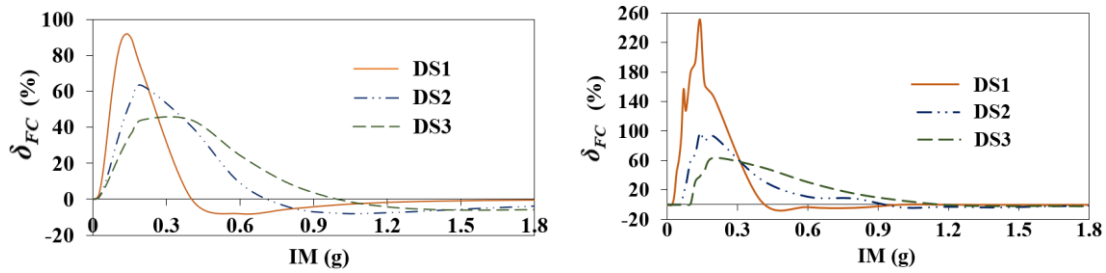

(c) (d)

Figure 5.21 Comparative FC- PGAs and FC-S_a (0.7s)s with respect to (a) LF and (b) NC; and trends of δ_{FC} with respect to (c) LF and (d) NC for ABS.

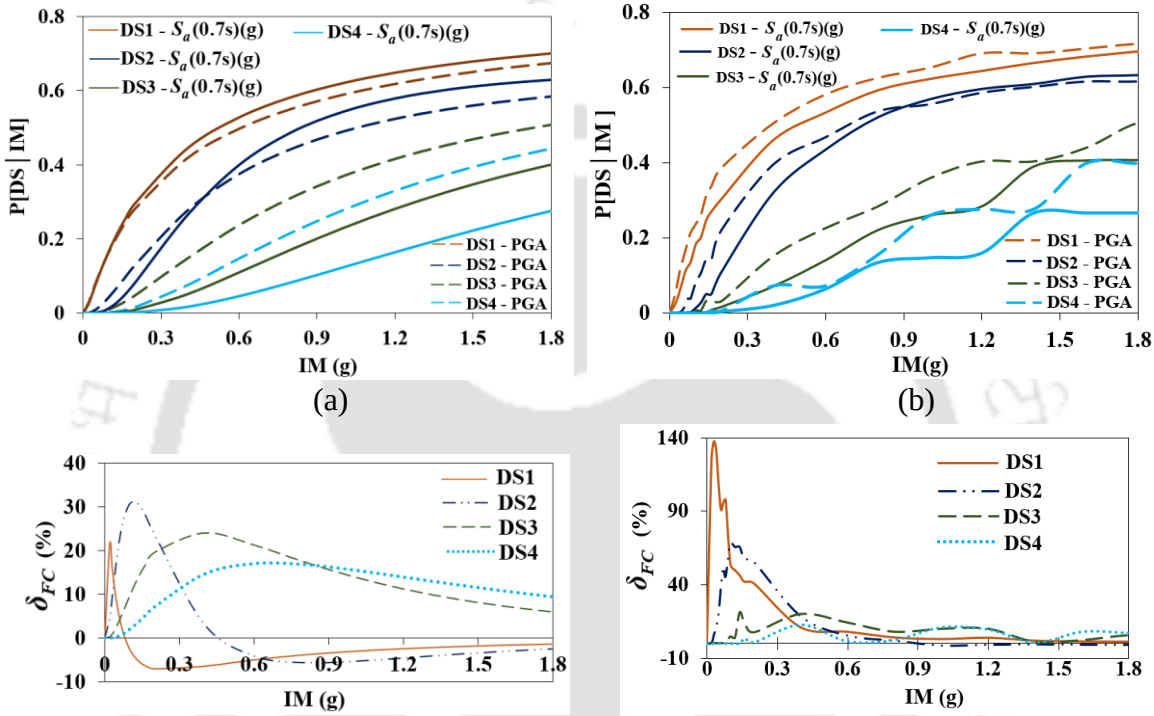

(a) (b)

(c) (d)

Figure 5.22 Comparative FC-PGAs and FC-S_a (0.7s)s with respect to (a) LF and (b) NC; and trends of δ_{FC} with respect to (c) LF and (d) NC for bearing.

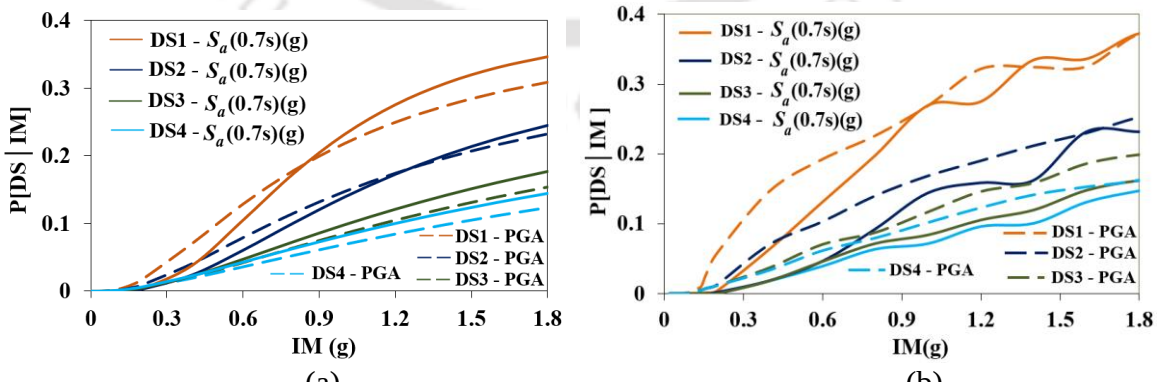

(a) (b)

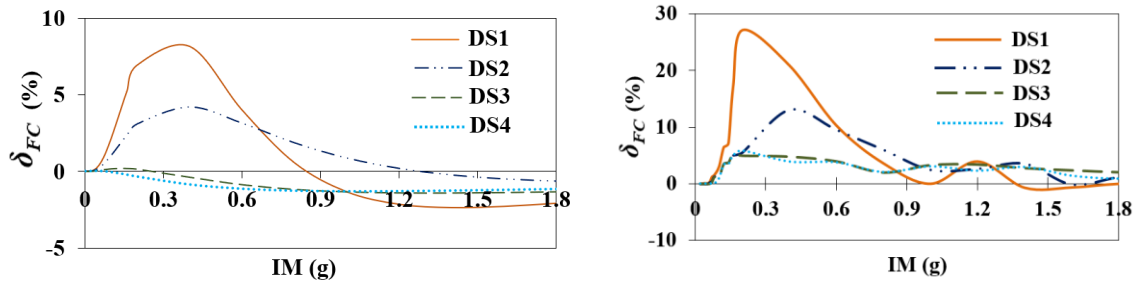

(c) (d)

Figure 5.23 Comparative FC-PGAs and FC-S_a (0.7s)s with respect to (a) LF and (b) NC; and trends of δ_{FC} with respect to (c) LF and (d) NC for pier.

Fragilities evaluated with respect to PGA is more upto a certain range of IM_vs than those with respect to S_a (0.7s), thereafter which FCs evaluated with respect to S_a (0.7s) show a little higher values, irrespective of the fragility computation approach. Exceptions to this trend, while employing LF, are bearing DS1 and DS2, and pier DS1, where, the fragilities evaluated with respect to S_a (0.7s) show moderately higher values compared to PGA, whereas in cases of pier DS3 and DS4, fragilities with respect to S_a (0.7s) are higher throughout the range of IM_vs. It is to noted that the differences between FC-PGA and FC-S_a (0.7s) are very high for A-PSS and ABS, while these differences are moderate and small in cases of bearing and pier respectively. This is because the IM types adopted in the study significantly affect the A-PSS and ABS demands compared to bearing, while pier is least affected by the change in IM type. Difference between FC-PGA and FC- S_a (0.7s) is found to be varying with respect to IM, as observed in case that between FC-PGA and FC- S_a (0.7s); similarly, the differences in fragilities with respect both the IMs is the greatest at DS1 for all the components and point where the peak difference occurs shift to higher IM_v, as the DS rank increases, irrespective of the computation approaches. Table 5.5 lists the $\delta_{FC,\max}$s between FC-PGA and FC-S_a(0.7s) throughout the IM range.

Table 5.5 Comparative fragilities with respect to PGA and S_a (0.7s)

A-PSS		LF		NC	
		IM_v range	$\delta_{FC,\max}$ (IM_v)	IM_v range	$\delta_{FC,\max}$ (IM_v)
DS1	PGA > S_a (0.7s)	≤ 0.456g	137% (0.16g)	≤ 0.489g	217% (0.16g)
	PGA < S_a (0.7s)	> 0.456g	12% (0.60g)	> 0.489g	12% (0.70g)
DS2	PGA > S_a (0.7s)	≤ 0.645g	95% (0.20g)	≤ 0.790g	159% (0.20g)
	PGA < S_a (0.7s)	> 0.645g	5% (0.80g)	> 0.790g	8% (0.70g)
ABS		LF		NC	
		IM_v range	$\delta_{FC,\max}$ (IM_v)	IM_v range	$\delta_{FC,\max}$ (IM_v)
DS1	PGA > S_a (0.7s)	≤ 0.416g	92% (0.14g)	≤ 0.523g	251% (0.14g)
	PGA < S_a (0.7s)	> 0.416g	8% (0.60g)	> 0.523g	4% (0.80g)

DS2	PGA > S_a (0.7s)	≤ 0.736g	63% (0.20g)	≤ 0.937g	97% (0.14g)
	PGA < S_a (0.7s)	> 0.736g	8% (1.0g)	> 0.937g	4% (1.4g)
DS3	PGA > S_a (0.7s)	≤ 1.0g	44% (0.40g)	≤ 1.183g	64% (0.20g)
	PGA < S_a (0.7s)	> 1.0g	6% (1.6g)	> 1.183g	2% (1.8g)
Bearing		LF		NC	
		IM_v range	$\delta_{FC,max}$ (IM_v)	IM_v range	$\delta_{FC,max}$ (IM_v)
DS1	PGA > S_a (0.7s)	≤ 0.081g	21% (0.02g)	throughout	137% (0.03g)
	PGA < S_a (0.7s)	> 0.081g	7% (0.20g)	-----	-----
DS2	PGA > S_a (0.7s)	≤ 0.483g	31% (0.12g)	≤ 0.918g	68% (0.10g)
	PGA < S_a (0.7s)	> 0.483g	6% (0.80g)	> 0.918g	1% (1.0g)
DS3	PGA > S_a (0.7s)	throughout	24% (0.40g)	throughout	21% (0.14g)
	PGA < S_a (0.7s)	-----	-----	-----	-----
DS4	PGA > S_a (0.7s)	throughout	17% (0.60g)	throughout	13% (0.40g)
	PGA < S_a (0.7s)	-----	-----	-----	-----
Pier		LF		NC	
		IM_v range	$\delta_{FC,max}$ (IM_v)	IM_v range	$\delta_{FC,max}$ (IM_v)
DS1	PGA > S_a (0.7s)	≤ 0.859g	8% (0.40g)	≤ 1.368g	27% (0.20g)
	PGA < S_a (0.7s)	> 0.859g	2% (1.4g)	> 1.368g	0.74% (1.4g)
DS2	PGA > S_a (0.7s)	≤ 1.287g	4% (0.40g)	throughout	10% (0.60g)
	PGA < S_a (0.7s)	> 1.287g	0.70% (1.8g)	-----	-----
DS3	PGA > S_a (0.7s)	≤ 0.259g	0.21% (0.14g)	throughout	5% (0.16g)
	PGA < S_a (0.7s)	> 0.259g	1.4% (1.4g)	-----	-----
DS4	PGA > S_a (0.7s)	≤ 0.066g	0.04% (0.021g)	throughout	6% (0.20g)
	PGA < S_a (0.7s)	> 0.066g	1.32% (1.0g)	-----	-----

5.5 COMPARATIVE VULNERABILITIES OF INDIVIDUAL BRIDGE COMPONENTS

The bridge components are vulnerable upto different degrees of damages under various levels of the seismic loading, as reported in Priestley et al. (1996) for various bridge typologies during the 1964 Alaska, 1971 San Fernando, 1985 Chile, 1990 Costa Rica, 1995 Kobe earthquakes etc. Thus, the comparative vulnerabilities of the damageable IAB components are assessed and thereby, the vulnerability sequence is established. Figures 5.24(a) and 5.24(b), Figures 5.24(c) and 5.24(d), Figures 5.24(e) and 5.24(f), and Figures 5.24(g) and 5.24(h) show the comparative component-level FCs at their respective DS1s, DS2s, DS3s and DS4s with respect to PGA and S_a (0.7s). Sequences of vulnerabilities with respect to both the IMs are presented in Table 5.6. Table 5.7 quantitatively displays the comparative vulnerabilities, through $\delta_{FC,max}$ occurring at particular IM_vs.

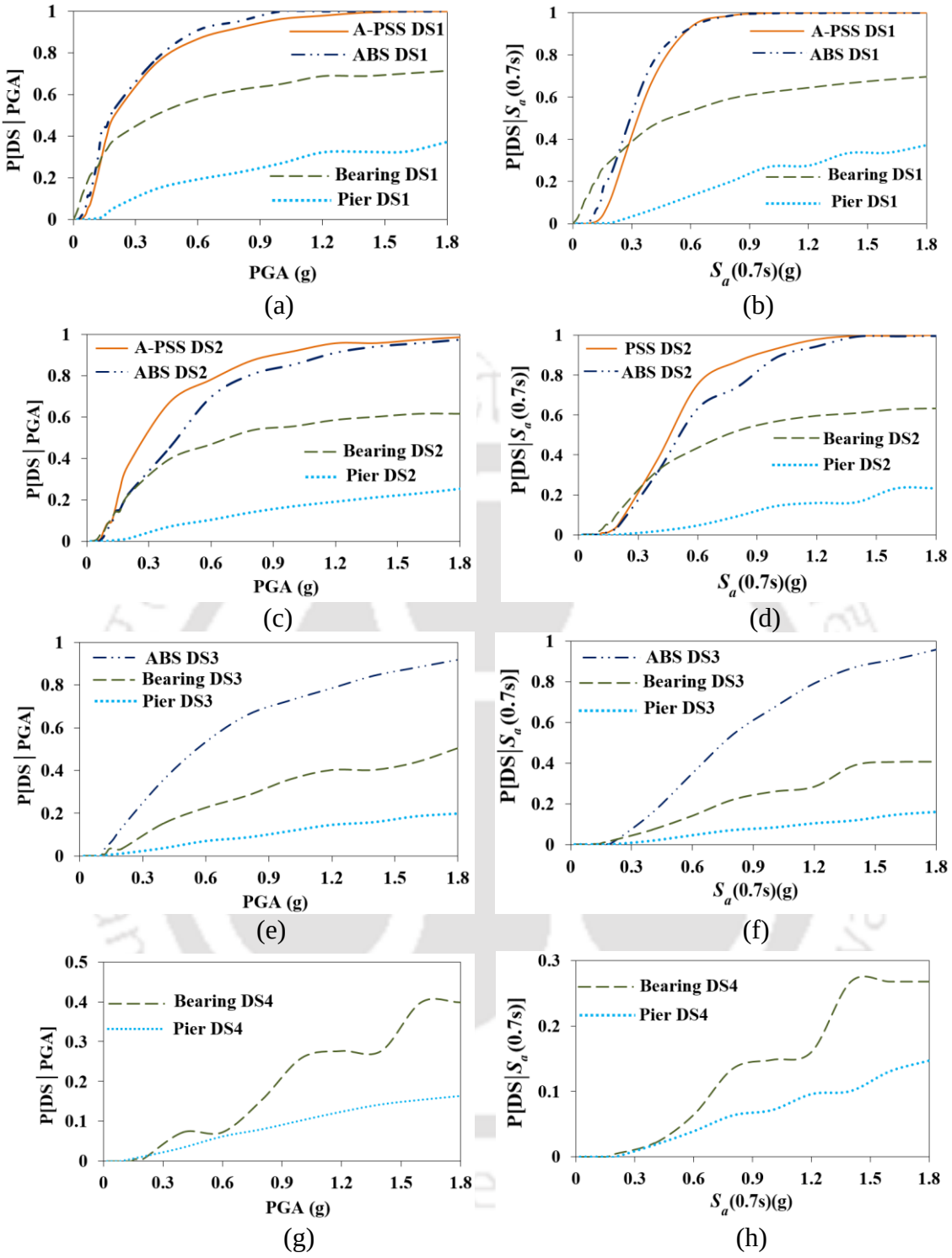

Figure 5.24 Comparative component-level FCs with respect to (a) PGA and (b) S_a (0.7s), at respective DS1s; (c) PGA and (d) S_a (0.7s), at respective DS2s; (e) PGA and (f) S_a (0.7s), at respective DS3s, and (g) PGA and (h) S_a (0.7s) at respective DS4s.

Table 5.6 Sequence of vulnerabilities of the individual IAB components

With respect to PGA at DS1, at IM_v of			With respect to S_a (0.7s) at DS1, at IM_v of			
≥ 0.11g	0.11< -- ≤ 0.14g	< 0.14g	≥ 0.26g	0.26 < -- ≤ 0.32g	0.32 < -- ≤ 0.60g	< 0.60g

Bearing ABS A-PSS Pier	ABS Bearing A-PSS Pier	ABS A-PSS Bearing Pier	Bearing ABS A-PSS Pier	ABS Bearing A-PSS Pier	ABS A-PSS Bearing Pier	A-PSS ABS Bearing Pier	
With respect to PGA at DS2, at IM_v of			With respect to S_a(0.7s) at DS2, at IM_v of				
≥ 0.08g	0.08 < -- ≤ 0.14g	< 0.14g	≥ 0.34g	0.34 < -- ≤ 0.41g	< 0.41g		
Bearing A-PSS ABS Pier	A-PSS Bearing ABS Pier	A-PSS ABS Bearing Pier	Bearing A-PSS ABS Pier	A-PSS Bearing ABS Pier	A-PSS ABS Bearing Pier		
With respect to PGA at DS3, at IM_v of			With respect to S_a(0.7s) at DS3, at IM_v of				
≥ 0.08g	0.08 < -- ≤ 0.1g	< 0.10g	≥ 0.24g		< 0.24g		
Pier Bearing ABS	Bearing Pier ABS	ABS Bearing Pier	Bearing ABS Pier		ABS Bearing Pier		
With respect to PGA at DS4, at IM_v of			With respect to S_a(0.7s) at DS4, at IM_v of				
≥ 0.25g		< 0.25g	0 ≤ -- ≤ 1.80g				
Pier Bearing		Bearing Pier	Bearing Pier				

Table 5.7 Quantitative comparisons of vulnerabilities of the individual components

Inequality at DS1	with respect to PGA		with respect to S_a(0.7s)	
	IM_v range	$\delta_{FC,\max}$ (IM_v)	IM_v range	$\delta_{FC,\max}$ (IM_v)
ABS > A-PSS	0 ≤ -- ≤ 1.80g	89% (0.14g)	≤ 0.596g	82% (0.16g)
ABS < A-PSS	----	------	> 0.596g	0.47% (0.60g)
Bearing > A-PSS	≤ 0.137g	285% (0.04g)	≤ 0.325g	186% (0.06g)
Bearing < A-PSS	> 0.137g	62% (0.40g)	> 0.325g	66% (0.60g)
Bearing > ABS	≤ 0.110g	259% (0.03g)	≤ 0.259g	181% (0.06g)
Bearing < ABS	> 0.110g	94% (0.14g)	> 0.259g	72% (0.40g)
Pier < A-PSS		231% (0.16g)		151% (0.40g)
Pier < ABS	0 ≤ -- ≤ 1.80g	309% (0.14g)	0 ≤ -- ≤ 1.80g	172% (0.40g)
Pier < Bearing		289% (0.04g)		186% (0.06g)
Inequality at DS2	with respect to PGA		with respect to S_a(0.7s)	
	IM_v range	$\delta_{FC,\max}$ (IM_v)	IM_v range	$\delta_{FC,\max}$ (IM_v)
A-PSS > ABS	0 ≤ -- ≤ 1.80g	71% (0.20g)	0 ≤ -- ≤ 1.80g	20% (0.60g)
Bearing > A-PSS	≤ 0.08g	35% (0.07g)	≤ 0.337g	31% (0.20g)
Bearing < A-PSS	> 0.08g	69% (0.40g)	> 0.337g	53% (0.60g)
Bearing > ABS	≤ 0.138g	42% (0.07g)	≤ 0.409g	35% (0.20g)
Bearing < ABS	> 0.138g	38% (0.60g)	> 0.409g	33% (0.60g)
Pier < A-PSS		178% (0.20g)		118% (0.60g)
Pier < ABS	0 ≤ -- ≤ 1.80g	106% (0.20g)	0 ≤ -- ≤ 1.80g	98% (0.60g)
Pier < Bearing		105% (0.20g)		76% (0.40g)
Inequality at DS3	with respect to PGA		with respect to S_a(0.7s)	
	IM_v range	$\delta_{FC,\max}$ (IM_v)	IM_v range	$\delta_{FC,\max}$ (IM_v)
Bearing > ABS	≤ 0.104g	7% (0.10g)	≤ 0.245g	6% (0.20g)
Bearing < ABS	> 0.104g	52% (0.40g)	> 0.245g	41% (1.0g)

Pier > ABS	≤ 0.099g	1% (0.08g)	---------	
Pier < ABS	> 0.099g	81% (0.40g)	0 ≤ -- ≤ 1.80g	59% (1g)
Pier > bearing	≤ 0.083g	1% (0.08g)	---------	
Pier < bearing	> 0.083g	29% (0.40g)	0 ≤ -- ≤ 1.80g	19% (1.4g)
Inequality at DS4	with respect to PGA		with respect to S_a (0.7s)	
	IM_v range	$\delta_{FC,max}$ (IM_v)	IM_v range	$\delta_{FC,max}$ (IM_v)
Pier > bearing	≤ 0.248g	4% (0.14g)	---------	
Pier < bearing	> 0.248g	16% (1.0g)	0 ≤ -- ≤ 1.80g	12% (1.40g)

5.6 GENERATION OF BRIDGE SYSTEM FRAGILITY CURVES

BS FCs in the present study are generated, in succession to the component-level FCs using the evaluated respective *C* and *D* distributions, as discussed in the following subsections:

5.6.1 Definition of the BS DSs

Four BS DSs are considered, based on the mapping at the system level, of the different component-level DSs (Ramanathan, 2012). DS descriptions and the mapping are elaborated in a flowchart in Figure 5.25. While developing the damage models for the components, DS of a component with the assigned rank is designed such that it has the same functionality consequences at the BS level with respect to the same DS rank. Hence, the BD DS1; DS2; DS3; and DS4 are defined by the mapped contributions of the DS1s of PSS, ABS, bearing and pier; DS2s of PSS, ABS, bearing and pier; DS3s of ABS, bearing and pier; and DS4s of bearing and pier respectively.

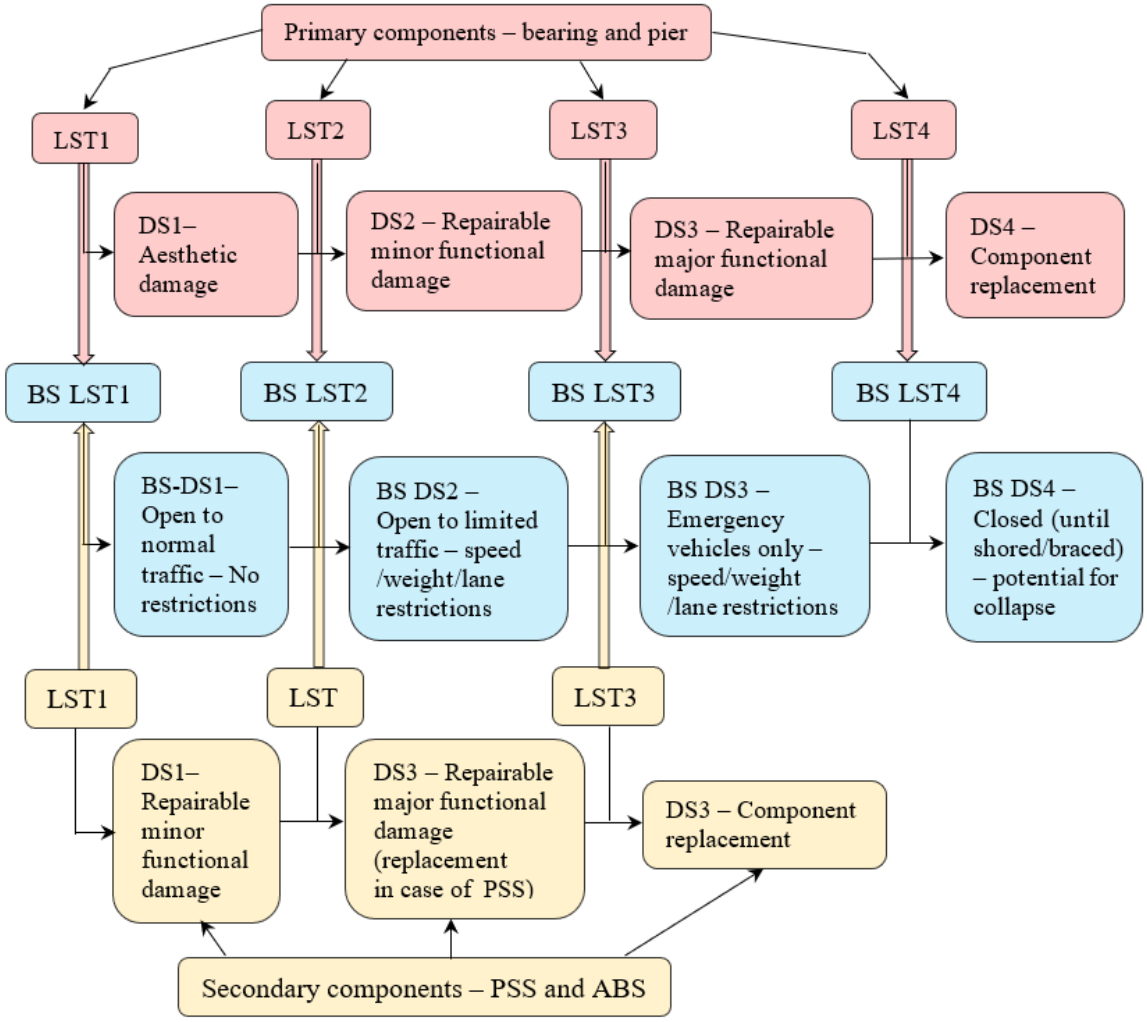

Figure 5.25 Descriptions of the DSs and mapping of the component-level DSs onto the BS DSs.

5.6.2 Evaluation of cumulative distribution surface for the joint demands of the IAB components

Seismic demands of the components being correlated, BS fragility evaluation requires derivation of the joint demand cumulative probability distribution surface. Thus, the correlation coefficient $\rho_{1,p\text{-}q}$ between every two (p^{th} and q^{th}) components (A-PSS, ABS, bearing and pier, denoted as '*pl*', '*ab*', '*br*' and '*pr*' respectively) at i^{th} DS rank is computed using respective ln(D) data (1296 values) (i.e., ln($D_{i,p}$) and ln($D_{i,q}$)), as in Equation (5.13), and listed in Table 5.8 for all the DSs. Using $\rho_{i,p\text{-}q}$s and standard deviations of ln($D_{i,p}$) and ln($D_{i,q}$) data (i.e., $\zeta_{D_{i,p}}$ and $\zeta_{D_{i,q}}$), the correlation matrix is evaluated. Joint demand surface against the i^{th} BS DS is then generated using MATLAB 8.6 (2015) with the correlation matrix and the individual component demand distributions at that DS as the input.

$$\rho_{i,p-q} = \frac{\sum_{1296}\{\ln(D_{i,p}) - \overline{\ln(D_{i,p})}\}\{\ln(D_{i,q}) - \overline{\ln(D_{i,q})}\}}{\sqrt{\sum_{1296}\{\ln(D_{i,p}) - \overline{\ln(D_{i,p})}\}^2 \sum_{1296}\{\ln(D_{i,q}) - \overline{\ln(D_{i,q})}\}^2}} \quad (5.13)$$

Table 5.8 Correlation coefficients among the bridge component demands

DS1	IM	value	DS2	IM	value	DS3	IM	value
$\rho_{1,pl\text{-}ab}$	PGA	0.938	$\rho_{2,pl\text{-}ab}$	PGA	0.914	$\rho_{3,ab\text{-}br}$	PGA	0.797
	S_a (0.7s)	0.738		S_a (0.7s)	0.614		S_a (0.7s)	0.493
$\rho_{1,pl\text{-}br}$	PGA	0.555	$\rho_{2,pl\text{-}br}$	PGA	0.781	$\rho_{3,ab\text{-}pr}$	PGA	0.697
	S_a (0.7s)	0.250		S_a (0.7s)	0.328		S_a (0.7s)	0.521
$\rho_{1,pl\text{-}pr}$	PGA	0.725	$\rho_{2,pl\text{-}pr}$	PGA	0.735	$\rho_{3,br\text{-}pr}$	PGA	0
	S_a (0.7s)	0.216		S_a (0.7s)	0.468		S_a (0.7s)	0
$\rho_{1,ab\text{-}br}$	PGA	0.544	$\rho_{2,ab\text{-}br}$	PGA	0.778	DS4	*PGA*	S_a (0.7s)
	S_a (0.7s)	0.243		S_a (0.7s)	0.339			
$\rho_{1,ab\text{-}pr}$	PGA	0.683	$\rho_{2,ab\text{-}pr}$	PGA	0.777	$\rho_{4,br\text{-}pr}$	0	0
	S_a (0.7s)	0.177		S_a (0.7s)	0.532			
$\rho_{1,pr\text{-}br}$	PGA	0.418	$\rho_{2,pr\text{-}br}$	PGA	0.786			
	S_a (0.7s)	0.487		S_a (0.7s)	0.916			

5.6.3 Computation of System-Level Fragilities

Probability of reaching the i^{th} BS DS is obtained by comparing the joint demands of the components with the mutually independent component capacities *C*s (denoted as $C_{i,pl}$, $C_{i,ab}$, $C_{i,br}$ and $C_{i,pr}$ respectively for PSS, ABS, bearing and pier) at their respective i^{th} DSs, while assuming system failure with the sequence in series. Employing the Latin hypercube sampling technique on the joint demand surface and the individual *C* distributions, 102 sample values for joint demands as well as individual *C*s are obtained, while dividing each of the distributions into 100 equal probability intervals and extracting the median values of the intervals along with the boundary values. Samples for the individual component *C*s are paired up randomly among them to have 102 quartets of *C*s. 102 joint demand sets are randomly paired with 102 capacity quartets. For a joint demand-capacity quartet pair, the BS DS is considered to have reached, if the *C* values are exceeded by the respective *D* values within the pair, at least for one component. The corresponding probability $P_{i,BS}$ is computed as the ratio of the number of pairs wherein the DS is reached to the total number of pairs (i.e., 102). Computation is repeated at each increasing value of both the IMs and for all the BS DSs to obtain the corresponding BS FCs. The BS FC generation procedure is depicted in a flowchart, as in Figure 5.26 and the generated BS FCs with respect to PGA and S_a (0.7s) are displayed in Figures 5.27(a) and 5.27(b) respectively. Figure 5.27(c) shows

the comparative BS FCs generated with respect to the IMs, at all the BS DSs. Figure 5.27(d) shows the trends of δ_{FC} between FC-PGAs and FC-S_a (0.7s)s, which show the similar patterns, as those for component-level FCs, with respect to the influence of adopted IMs. Table 5.9 lists the $\delta_{FC,\max}$s between FC-PGAs and FC- $S_a(0.7\,\mathrm{s})$ s, throughout the IM range.

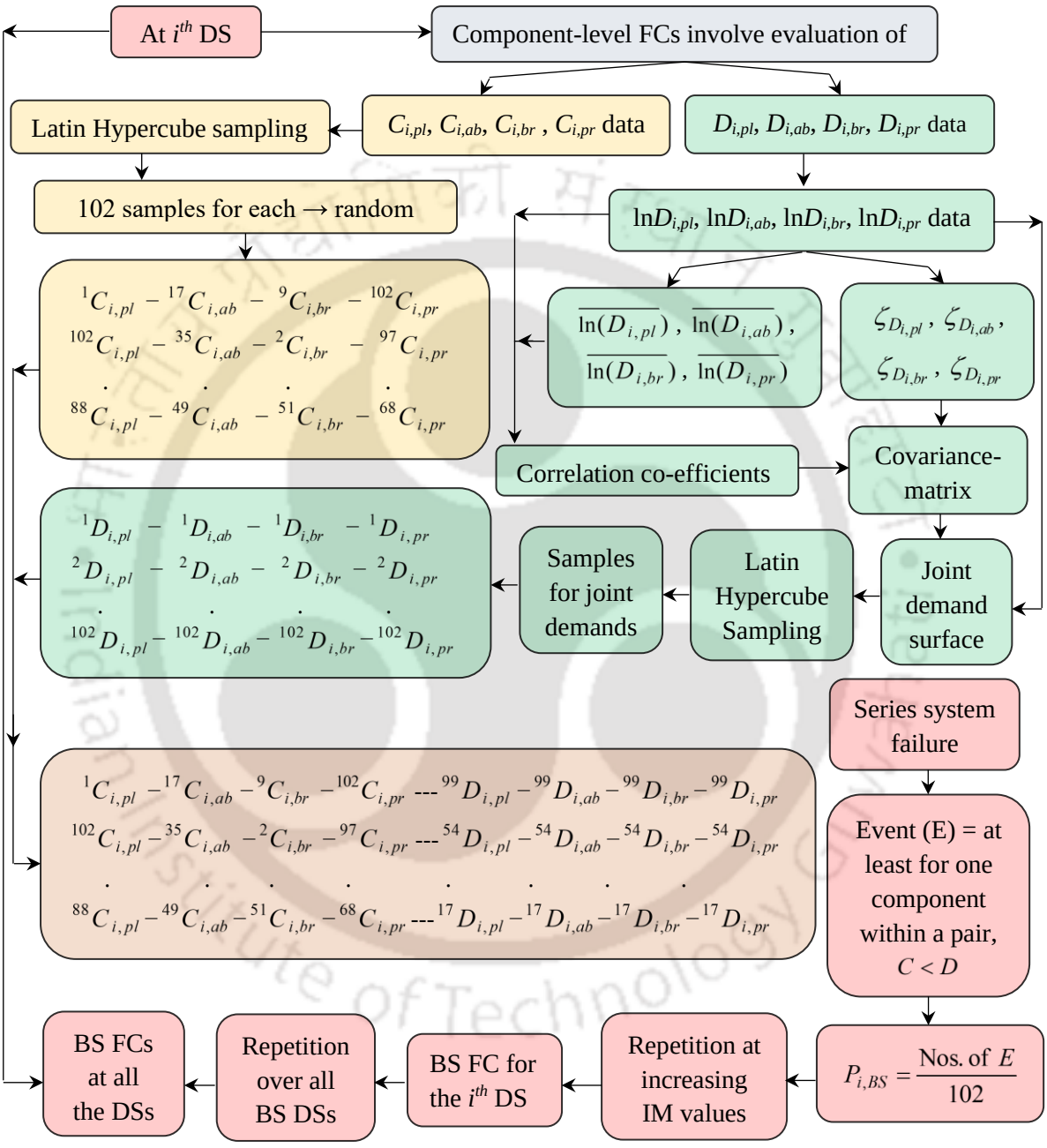

Figure 5.26 Flowchart describing the generation of the BS FCs.

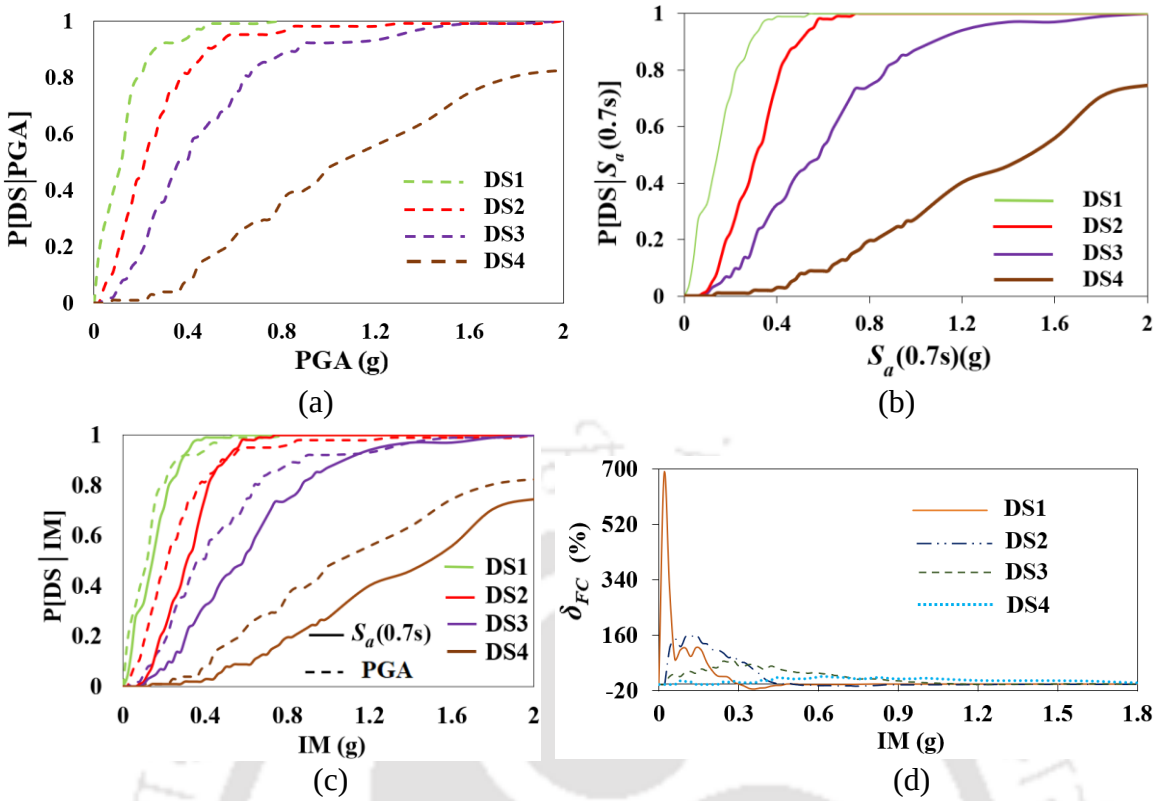

Figure 5.27 BS FCs with respect to (a) PGA and (b) S_a (0.7s); and (c) comparative BS FCs with respect to the IMs; and (d) trends of $\delta_{\max,FC}$ with respect to the IMs.

Table 5.9 Comparative BS fragilities with respect to PGA and S_a (0.7 s)

System-level FCs	DS1		DS2	
	IM_v	$\delta_{FC,\max}$ (IM_v)	IM_v	$\delta_{FC,\max}$ (IM_v)
PGA > S_a (0.7s)	≤ 0.30g	686% (0.02g)	≤ 0.500g	161% (0.14g)
PGA < S_a (0.7s)	> 0.30g	16% (0.36g)	≤ 0.500g	7% (0.74g)
System-level FCs	DS3		DS4	
	IM_v	$\delta_{FC,\max}$ (IM_v)	IM_v	$\delta_{FC,\max}$ (IM_v)
PGA > S_a (0.7s)	throughout	77% (0.28g)	throughout	27% (0.62g)

Many authors, while working on various bridge typologies have generated the BS FCs. Though, of different typologies, for bridges like those with monolithic bent-box girder-seat type abutment by Taskari and Sextos (2015), simply supported-I-girder- seat type abutment by Neilson and DesRoches (2007), simply supported-I-girder- seat type abutment and full integral configuration by Choine et al. (2014) and continuous-I-girder- seat type abutment by Ramanathan et al. (2012) – all with 3-spans and the 2-span continuous-box girder- seat type abutment by Zakeri et al. (2014), differences in the BS fragilities are observed with respect to those evaluated in the study, as shown in Tables 5.10, 5.11 and 5.12.

Though, direct comparisons cannot be made against different typologies nor conclusions can be drawn, yet, the present study shows very high fragilities. Specifically, the BS DS1

followed by DS2 show very fragility values; it might be due to the very high vulnerabilities of the A-PSS, ABS as well as the bearing (for the initial DSs).

Table 5.10 Comparative BS fragilities from past studies and the present study at DS1

PGA	Present study	Taskari and Sextos (2015)	Neilson and DesRoches (2007)	Choine et al. (2014) (jointed)	Choine et al. (2014) (full integral)	Ramanathan et al. (2012)
0	0	0	0	0	0	0
0.2	0.80	0.30	0.55	0.82	0.02	0.37
0.4	0.94	0.78	0.86	0.92	0.25	0.75
0.6	0.99	0.96	0.96	1	0.68	0.90
0.8	1	0.99	0.99	1	0.92	0.94
1.0	1	1	1	1	0.98	0.97

Table 5.11 Comparative BS fragilities from past studies and the present study at DS2

PGA	Present study	Taskari and Sextos (2015)	Neilson and DesRoches (2007)	Choine et al. (2014) (jointed)	Choine et al. (2014) (full integral)	Ramanathan et al. (2012)	Zakeri et al. (2014)
0	0	0	0	0	0	0	0
0.2	0.45	0.09	0.05	0.10	0	0	0.025
0.4	0.81	0.32	0.29	0.40	0	0.065	0.22
0.6	0.95	0.60	0.53	0.60	0.025	0.25	0.45
0.8	0.96	0.8	0.70	0.82	0.10	0.40	0.74
1.0	1	0.9	0.81	0.88	0.28	0.58	0.82

Table 5.12 Comparative BS fragilities from past studies and the present study at DS3 and DS4

DS3				DS4		
PGA	Present study	Taskari and Sextos (2015)	Ramanathan et al. (2012)	PGA	Present study	Ramanathan et al. (2012)
0	0	0	0	0	0	0
0.2	0.18	0.05	0	0.2	0.01	0
0.4	0.51	0.18	0.05	0.4	0	0
0.6	0.75	0.33	0.12	0.6	0	0
0.8	0.88	0.49	0.27	0.8	0	0
1.0	0.92	0.65	0.37	1.0	0	0

5.7 COMPARATIVE VULNERABILITIES OF THE BS AND THE INDIVIDUAL COMPONENTS

Relative vulnerabilities of the BS with respect to each of the individual components are assessed by drawing comparisons between the respective FCs, as in the Subsections below:

5.7.1 Comparison of the BS FCs at all its DSs with the individual component FCs at the respective DS1s

Figure 5.28(a) shows the comparative component-level and BS FCs, with respect to PGA. Figures 5.28(b); 5.28(c); 5.28(d); and 5.28(e) show the corresponding trends of δ_{FC} between

the FCs of BS and each of A-PSS, ABS, bearing and pier at respective DS1, at BS DS1; DS2; DS3; and DS4. Table 5.13 quantitatively displays the comparative vulnerability between the BS at each of its DSs and each of the individual components at respective DS1, in the form of $\delta_{FC,\max}$ occurring at particular IM_v.

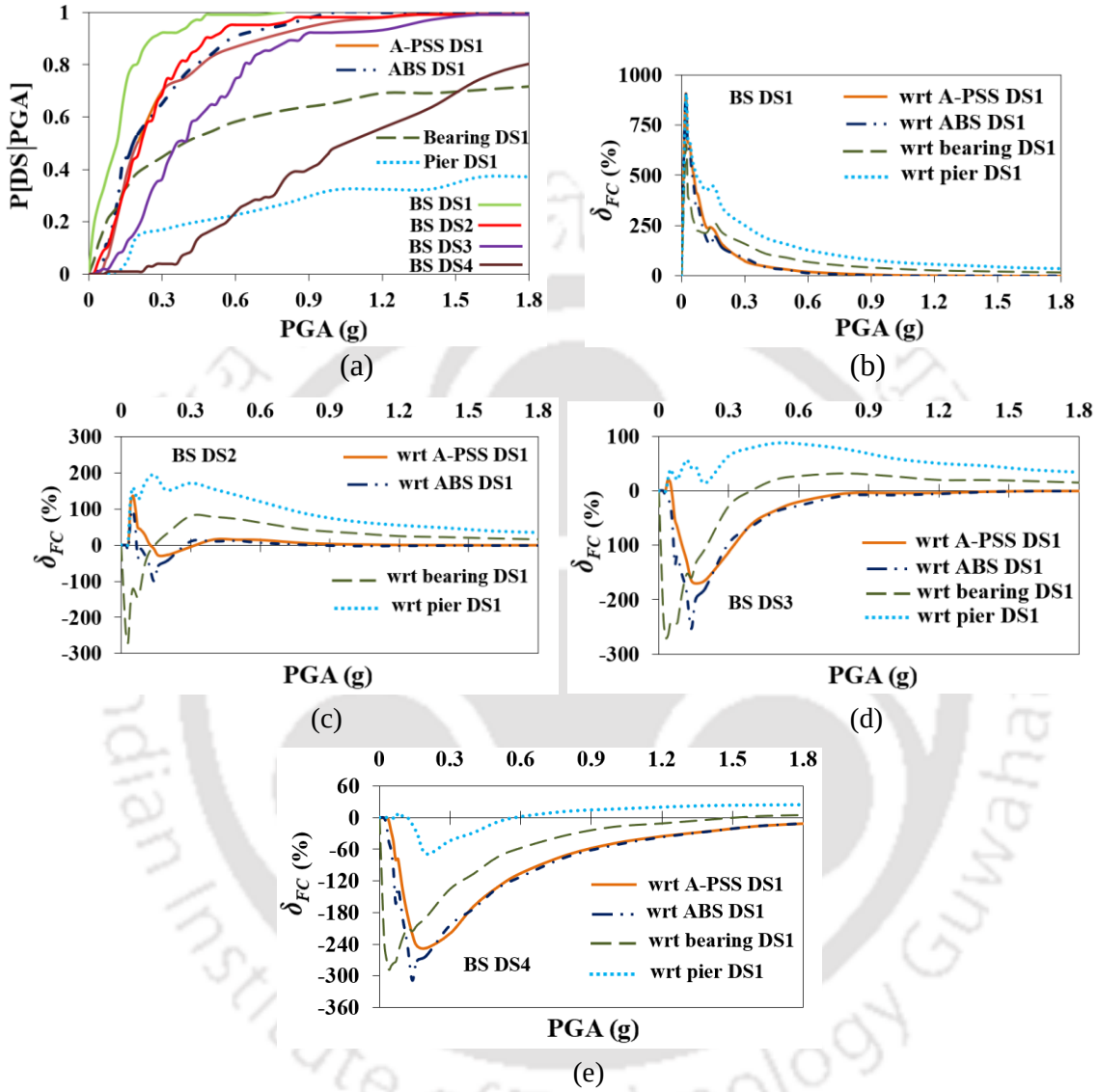

Figure 5.28 (a) Comparative component-level and BS FCs against PGA; trends of δ_{FC} between BS FC at (b) DS1, (c) DS2, (d) DS3 and (e) DS4 and FC of each component at respective DS1.

Figure 5.29(a) shows the comparative component-level and BS FCs, with respect to S_a (0.7s). Figures 5.29(b); 5.29(c); 5.29(d); and 5.29(e) show the corresponding trends of δ_{FC} between the FCs of BS and each of A-PSS, ABS, bearing and pier at respective DS1, at BS DS1; DS2; DS3; and DS4. Table 5.14 quantitatively displays the comparative vulnerability between BS at each of its DSs and each of the individual component at respective DS1, in the form of $\delta_{FC,\max}$ occurring at particular IM_v.

Table 5.13 Quantitative comparative vulnerabilities of BS and individual components at respective DS1s and with respect to PGA, at all the BS DSs

Vulnerability of BS at DS1 with respect to A-PSS at DS1				
Inequality IM_v $\delta_{FC,max}$ (IM_v)	more at all values 882% (0.02g)			
Vulnerability of BS at DS2 with respect to A-PSS at DS1				
Inequality IM_v $\delta_{FC,max}$ (IM_v)	more $\leq$ 0.12g 136% (0.05g)	less 0.12g < -- $\leq$ 0.32g 29% (0.16g)	more 0.32g < -- $\leq$ 1.26g 15% (0.40g)	less > 1.26g 0.60% (1.6g)
Vulnerability of BS at DS3 with respect to A-PSS at DS1				
Inequality IM_v $\delta_{FC,max}$ (IM_v)	more $\leq$ 0.06g 20% (0.04g)		less > 0.06g 170% (0.16g)	
Vulnerability of BS at DS4 with respect to A-PSS at DS1				
Inequality IM_v $\delta_{FC,max}$ (IM_v)	less at all values 247% (0.20g)			
Vulnerability of BS at DS1 with respect to ABS at DS1				
Inequality IM_v $\delta_{FC,max}$ (IM_v)	more at all values 882% (0.02g)			
Vulnerability of BS DS2 with respect to ABS DS1				
Inequality IM_v $\delta_{FC,max}$ (IM_v)	less $\leq$ 0.031g 12% (0.03g)	more 0.031g < -- $\leq$ 0.066g 99% (0.05g)	less 0.066g < -- $\leq$ 0.28g 99% (0.14g)	
Inequality IM_v $\delta_{FC,max}$ (IM_v)	more 0.28g < -- $\leq$ 0.87g 13% (0.50g)		less > 0.87g 2% (1.0g)	
Vulnerability with respect to ABS at DS1 of		BS at DS3	BS at DS4	
Inequality IM_v $\delta_{FC,max}$ (IM_v)		less at all values 253% (0.14g)	309% (0.14g)	
Vulnerability of BS at DS1 with respect to bearing at DS1				
Inequality IM_v $\delta_{FC,max}$ (IM_v)	more at all values 646% (0.02g)			
Vulnerability of BS at DS2 with respect to bearing at DS1				
Inequality IM_v $\delta_{FC,max}$ (IM_v)	less $\leq$ 0.147g 270% (0.03g)		more > 0.147g 80% (0.30g)	
Vulnerability of BS at DS3 with respect to bearing at DS1				
Inequality IM_v $\delta_{FC,max}$ (IM_v)	less $\leq$ 0.396g 270% (0.03g)		more > 0.396g 32% (0.80g)	

Vulnerability of BS at DS4 with respect to bearing at DS1				
Inequality	less		more	
IM_v	≤ 1.52g		> 1.52g	
$\delta_{FC,\max}$ (IM_v)	289% (0.04g)		5% (1.80g)	
Vulnerability with respect to pier at DS1 of	BS at DS1	BS at DS2	BS at DS3	
Inequality	more			
IM_v	at all values			
$\delta_{FC,\max}$ (IM_v)	882% (0.02g)	196% (0.14g)	88% (0.50g)	
Vulnerability of BS at DS4 with respect to pier at DS1				
Inequality	less	more	less	more
IM_v	≤ 0.072g	0.072g < -- ≤ 0.116g	0.116g < -- ≤ 0.585g	> 0.585g
$\delta_{FC,\max}$ (IM_v)	1.70% (0.07g)	9% (0.08g)	69% (0.20g)	23% (1.60g)

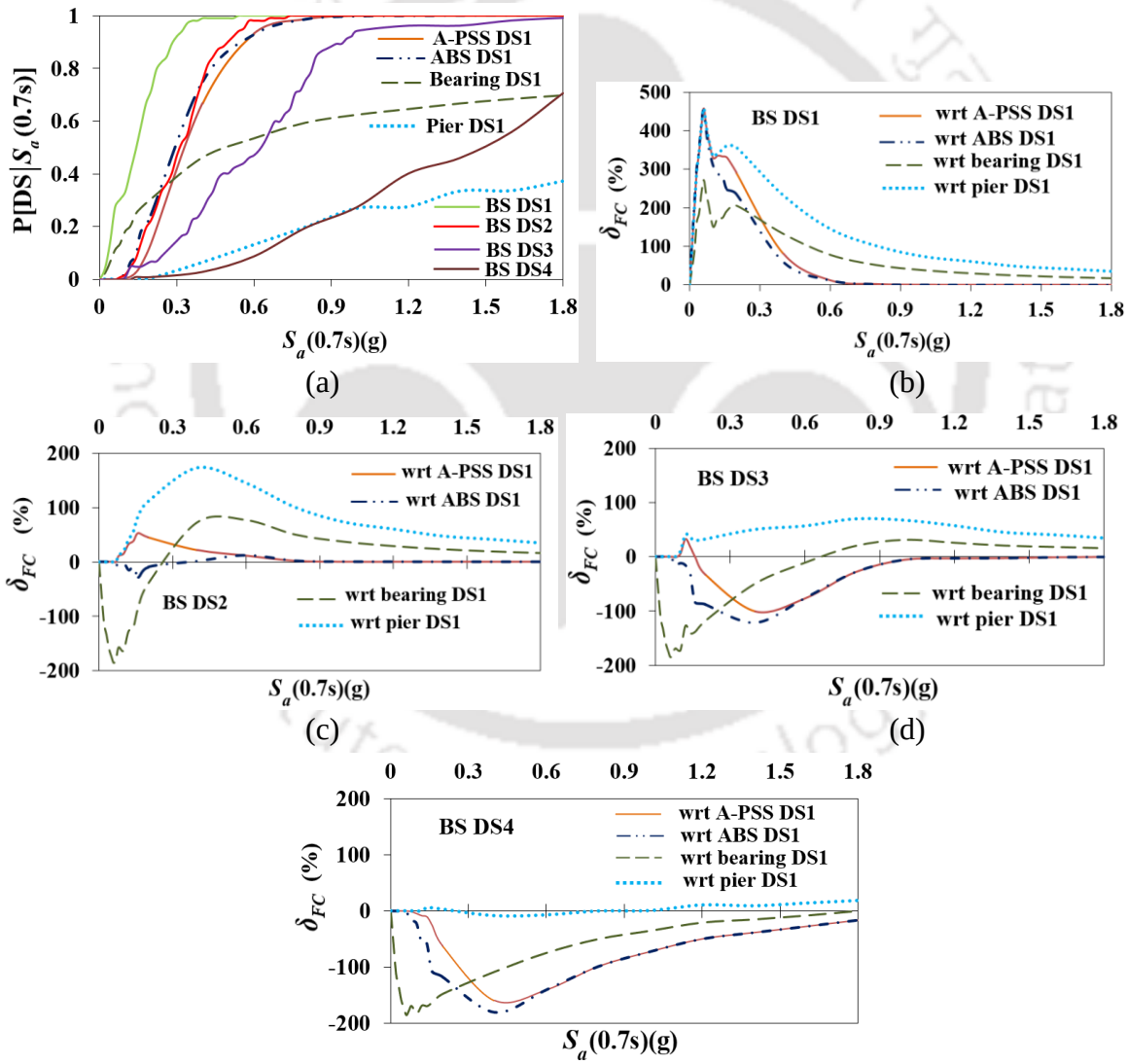

Figure 5.29 (a) Comparative component-level and BS FCs against S_a (0.7s); and trends of δ_{FC} between BS FC at (b) DS1, (c) DS2, (d) DS3 and (e) DS4 and FC of each component at respective DS1.

Table 5.14 Quantitative comparative vulnerabilities of BS and individual components at respective DS1s and with respect to S_a (0.7s), at all the BS DSs

Vulnerability of BS at DS1 with respect to A-PSS at DS1			
Inequality	more		
IM_v	at all values		
$\delta_{FC,max}$ (IM_v)	457% (0.06g)		
Vulnerability of BS at DS2 with respect to A-PSS at DS1			
Inequality	less		more
IM_v	≤ 0.07g		> 0.07g
$\delta_{FC,max}$ (IM_v)	0.37% (0.07g)		55% (0.16g)
Vulnerability of BS at DS3 with respect to A-PSS at DS1			
Inequality	less	more	less
IM_v	≤ 0.084g	0.084g < -- ≤ 0.158g	> 0.158g
$\delta_{FC,max}$ (IM_v)	1.25% (0.08g)	32% (1.20g)	101% (0.40g)
Vulnerability of BS at DS4 with respect to A-PSS at DS1			
Inequality	less		
IM_v	at all values		
$\delta_{FC,max}$ (IM_v)	159% (0.40g)		
Vulnerability of BS at DS1 with respect to ABS at DS1			
Inequality	more		
IM_v	at all values		
$\delta_{FC,max}$ (IM_v)	452% (0.06g)		
Vulnerability of BS DS2 with respect to ABS DS1			
Inequality	less		more
IM_v	≤ 0.38g		< 0.38g
$\delta_{FC,max}$ (IM_v)	29% (0.16g)		12% (0.60g)
Vulnerability with respect to ABS at DS1 of		BS at DS3	BS at DS4
Inequality		less	
IM_v		at all values	
$\delta_{FC,max}$ (IM_v)		121% (0.40g)	180% (0.40g)
Vulnerability of BS at DS1 with respect to bearing at DS1			
Inequality	more		
IM_v	at all values		
$\delta_{FC,max}$ (IM_v)	238% (0.05g)		
Vulnerability of BS at DS2 with respect to bearing at DS1			
Inequality	less		more
IM_v	≤ 0.270g		> 0.270g
$\delta_{FC,max}$ (IM_v)	186% (0.06g)		78% (0.60g)
Vulnerability of BS at DS3 with respect to bearing at DS1			
Inequality	less		more
IM_v	≤ 0.669g		> 0.669g
$\delta_{FC,max}$ (IM_v)	186% (0.06g)		32% (1.0g)
Vulnerability of BS at DS4 with respect to bearing at DS1			
Inequality	less		more
IM_v	≤ 1.788g		> 1.788g
$\delta_{FC,max}$ (IM_v)	186% (0.06g)		0.49% (1.80g)

Vulnerability with respect to pier at DS1 of	BS at DS1	BS at DS2	BS at DS3
Inequality		more	
IM_v		at all values	
$\delta_{FC,\max}$ (IM_v)	458% (0.06g)	173% (0.4g)	70% (0.80g)

Vulnerability of BS at DS4 with respect to pier at DS1				
Inequality	less	more	less	more
IM_v	$\leq$ 0.121g	0.121g < -- $\leq$ 0.251g	0.251g < -- $\leq$ 0.867g	> 0.867g
$\delta_{FC,\max}$ (IM_v)	0.17% (0.12g)	7% (0.14g)	9% (0.40g)	19% (1.80g)

5.7.2 Comparisons of the BS FCs at its DS2, DS3 and DS4 with the Individual Component FCs at respective DS2s

Figure 5.30(a) shows the comparative component-level and BS FCs, with respect to PGA. Figures 5.30(b); 5.30(c); and 5.30(d) show the corresponding trends of δ_{FC} between the FCs of BS and each of A-PSS, ABS, bearing and pier at respective DS2s, at the BS DS2; DS3; and DS4. Table 5.15 quantitatively displays the comparative vulnerability of the BS and each of the individual component at respective DS2s, in the form of $\delta_{FC,\max}$ occurring at particular IM_v, at the BS DS2, DS3 and DS4.

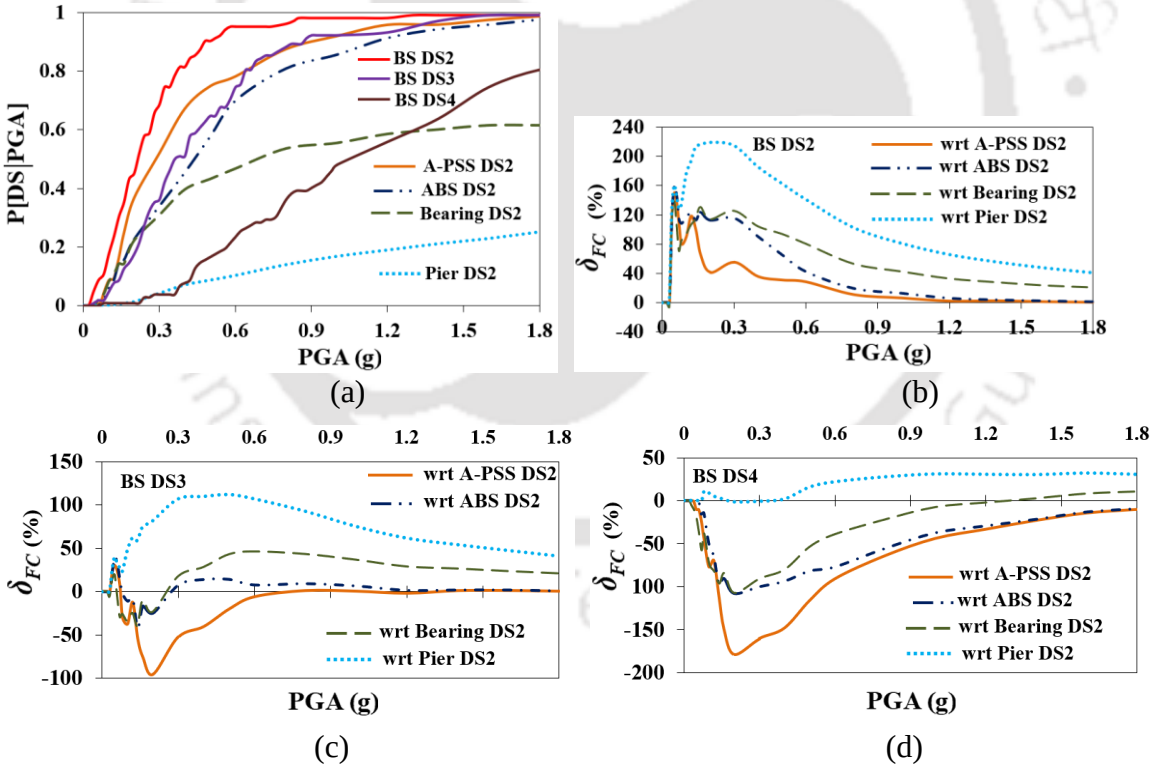

Figure 5.30 (a) Comparative component-level and BS FCs with respect to PGA; and trends of δ_{FC} between BS FC at (b) DS2, (c) DS3, (d) DS4 and FC of each component at respective DS2.

Figure 5.31(a) shows the comparative component-level and the BS FCs, with respect to S_a (0.7s). Figures 5.31(b); 5.31(c); and 5.31(d) show the corresponding trends of δ_{FC} between the FCs of the BS and each of A-PSS, ABS, bearing and pier at respective DS2, at the BS

DS2; DS3; and DS4. Table 5.16 quantitatively displays the comparative vulnerability of BS at each DS and each of the individual component at respective DS2, in the form of $\delta_{FC,\max}$ occurring at particular IM_v, at each of the BS DS2, DS3 and DS4.

Table 5.15 Quantitative comparative vulnerabilities of BS and individual components at respective DS2s and with respect to PGA, at BS DS2, DS3 and DS4

Vulnerability of BS at DS2 with respect to A-PSS at DS2				
Inequality	more			
IM_v	at all values			
$\delta_{FC,\max}$ (IM_v)	150% (0.05g)			
Vulnerability of BS at DS3 with respect to A-PSS at DS2				
Inequality	more	less	more	
IM_v	≤ 0.071g	0.071g < -- ≤ 0.776g	> 0.776g	
$\delta_{FC,\max}$ (IM_v)	30% (0.05g)	96% (0.20g)	0.95% (1.6g)	
Vulnerability of BS at DS4 with respect to A-PSS at DS2				
Inequality	less			
IM_v	at all values			
$\delta_{FC,\max}$ (IM_v)	179% (0.20g)			
Vulnerability of BS at DS2 with respect to ABS at DS2				
Inequality	more			
IM_v	at all values			
$\delta_{FC,\max}$ (IM_v)	146% (0.06g)			
Vulnerability of BS at DS3 with respect to ABS at DS2				
Inequality	more	less	more	
IM_v	≤ 0.079g	0.079g < -- ≤ 0.276g	> 0.276g	
$\delta_{FC,\max}$ (IM_v)	40% (0.05g)	42% (0.14g)	14% (0.50g)	
Vulnerability of BS at DS4 with respect to ABS at DS2				
Inequality	less			
IM_v	at all values			
$\delta_{FC,\max}$ (IM_v)	108% (0.20g)			
Vulnerability of BS at DS2 with respect to bearing at DS2				
Inequality	less		more	
IM_v	≤ 0.031g		> 0.031g	
$\delta_{FC,\max}$ (IM_v)	6% (0.03g)		139% (0.05g)	
Vulnerability of BS at DS3 with respect to bearing at DS2				
Inequality	less	more	less	more
IM_v	≤ 0.033g	0.033g < -- ≤ 0.058g	0.058g < -- ≤ 0.257g	> 0.257g
$\delta_{FC,\max}$ (IM_v)	6% (0.03g)	19% (0.05g)	40% (0.14g)	46% (0.60g)
Vulnerability of BS at DS4 with respect to bearing at DS2				
Inequality	less		more	
IM_v	≤ 1.296g		> 1.296g	
$\delta_{FC,\max}$ (IM_v)	107% (0.20g)		11% (1.80g)	
Vulnerability with respect to pier at DS2 of	BS at DS2		BS at DS3	
Inequality	more			
IM_v	at all values			
$\delta_{FC,\max}$ (IM_v)	219% (0.20g)		112% (0.50g)	

Vulnerability of BS at DS4 with respect to pier at DS2				
Inequality	less	more	less	more
IM_v	≤ 0.07g	0.07g < -- ≤ 0.176g	0.177g < -- ≤ 0.333g	> 0.276g
$\delta_{FC,max}$ (IM_v)	0.48% (0.07g)	11% (0.08g)	1.63% (0.20g)	32% (1.60g)

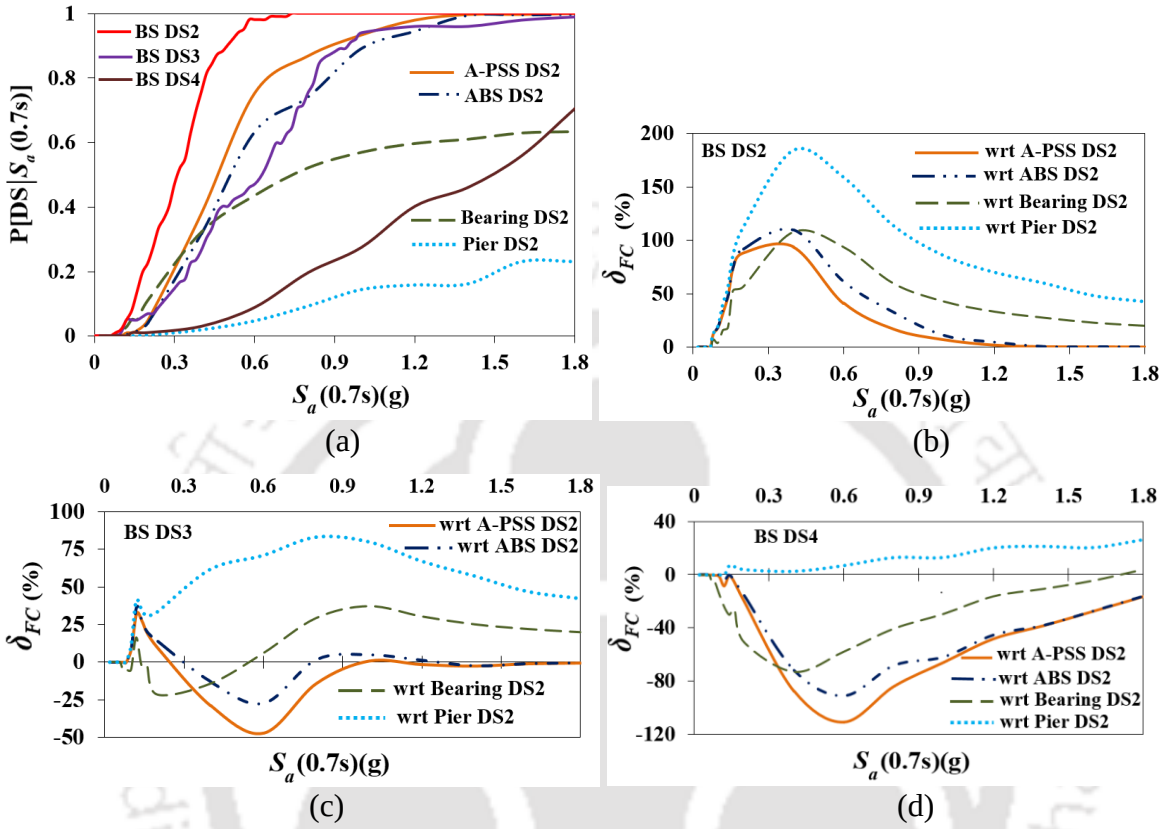

Figure 5.31 (a) Comparative component-level and BS FCs against S_a (0.7s); trends of δ_{FC} between BS FC at (b) DS2, (c) DS3, (d) DS4 and FC of each component at respective DS2.

Table 5.16 Quantitative comparative vulnerabilities of BS with individual components at respective DS2s and with respect to S_a (0.7s), at BS DS2, DS3 and BS4

Vulnerability of BS at DS2 with respect to A-PSS at DS2				
Inequality	more			
IM_v	at all values			
$\delta_{FC,max}$ (IM_v)	94% (0.40g)			
Vulnerability of BS at DS3 with respect to A-PSS at DS2				
Inequality	less	more	less	less
IM_v	≤ 0.081g	0.081g < -- ≤ 0.249g	0.249g < -- ≤ 0.989g	> 0.989g
$\delta_{FC,max}$ (IM_v)	0.31% (0.08g)	33% (0.12g)	47% (0.60g)	2.54% (1.4g)
Vulnerability of BS at DS4 with respect to A-PSS at DS2				
Inequality	less			
IM_v	at all values			
$\delta_{FC,max}$ (IM_v)	111% (0.60g)			

Vulnerability of BS at DS2 with respect to ABS at DS2				
Inequality	more			
IM_v	at all values			
$\delta_{FC,max}$ (IM_v)	110% (0.40g)			
Vulnerability of BS at DS3 with respect to ABS at DS2				
Inequality	more	less	more	less
IM_v	≤ 0.302g	0.302g < -- ≤ 0.789g	0.789g < -- ≤ 1.268g	> 1.268g
$\delta_{FC,max}$ (IM_v)	37% (0.12g)	27% (0.60g)	5% (1.0g)	3% (1.4g)
Vulnerability of BS at DS4 with respect to ABS at DS2				
Inequality	less			
IM_v	at all values			
$\delta_{FC,max}$ (IM_v)	100% (0.60g)			
Vulnerability of BS at DS2 with respect to bearing at DS2				
Inequality	less		more	
IM_v	≤ 0.074g		> 0.074g	
$\delta_{FC,max}$ (IM_v)	6% (0.07g)		108% (0.40g)	
Vulnerability of BS at DS3 with respect to bearing at DS2				
Inequality	less	more	less	more
IM_v	≤ 0.105g	0.105g < -- ≤ 0.138g	0.138g < -- ≤ 0.543g	> 0.543g
$\delta_{FC,max}$ (IM_v)	6% (0.07g)	16% (0.12g)	22% (0.20g)	37% (1.0g)
Vulnerability of BS at DS4 with respect to bearing at DS2				
Inequality	less			
IM_v	at all values			
$\delta_{FC,max}$ (IM_v)	73% (0.40g)			

Vulnerability with respect to pier at DS2 of	BS at DS2	BS at DS3	BS at DS4
Inequality	more		
IM_v	at all values		
$\delta_{FC,max}$ (IM_v)	184% (0.40g)	83% (0.80g)	26% (1.80g)

5.7.3 Comparisons of the BS FCs at its DS3 and DS4 with the Individual Component FCs at respective DS3s

Figure 5.32(a) shows the comparative component-level and BS FCs, generated against PGA. Figure 5.32(b); and 5.32(e) show the corresponding trends of δ_{FC} between the FCs of the BS and each of ABS, bearing and pier at respective DS3, at the BS DS3; and DS4. Table 5.17 quantitatively displays the comparative vulnerability of BS and each of the individual component at respective DS3, in the form of $\delta_{FC,max}$ occurring at particular IM_v, at each of the BS DS3 and BS DS4.

Figure 5.33(a) shows the comparative component-level and BS FCs, generated with respect to S_a (0.7s). Figures 5.33(b); and 5.33(c) show the corresponding trends of δ_{FC} between the FCs of the BS and each of ABS, bearing and pier at respective DS3, at the BS DS3; and DS4. Table 5.18 quantitatively displays the comparative vulnerability of BS and

each of the individual component at respective DS3, in the form of $\delta_{FC,\max}$ occurring at particular IM_v, at each the BS DS3 and DS4.

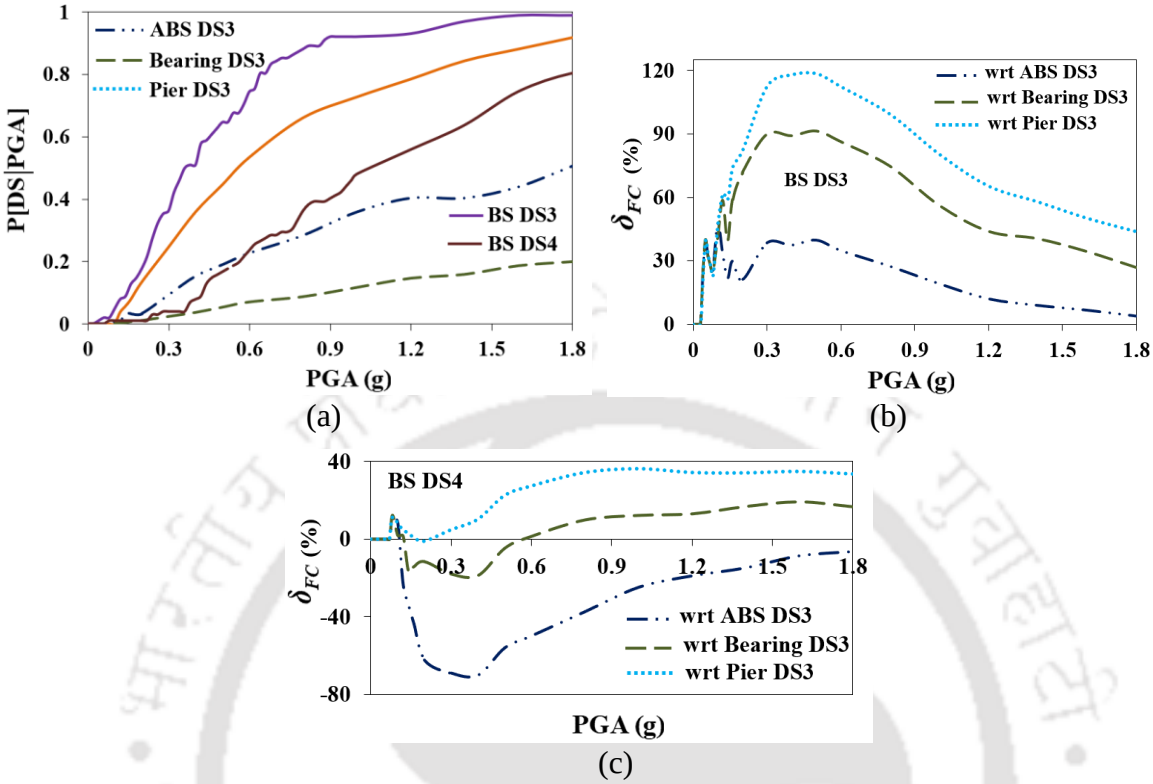

Figure 5.32 (a) Comparative component-level and BS FCs with respect to PGA; and trends of δ_{FC} between the BS FC at (b) DS3, and (c) DS4 and the FC of each component at respective DS3.

Table 5.17 Quantitative comparative vulnerabilities of BS and individual components at respective DS3s and with respect to PGA, at BS DS3 and DS4

Vulnerability of BS at DS3 with respect to ABS at DS3		
Inequality	more	
IM_v	at all values	
$\delta_{FC,\max}$ (IM_v)	48% (0.10g)	
Vulnerability of BS at DS4 with respect to ABS at DS3		
Inequality	more	less
IM_v	≤ 0.105g	> 0.105g
$\delta_{FC,\max}$ (IM_v)	12% (0.08g)	70% (0.40g)
Vulnerability of BS at DS3 with respect to bearing at DS3		
Inequality	more	
IM_v	at all values	
$\delta_{FC,\max}$ (IM_v)	91% (0.50g)	
Vulnerability of BS at DS4 with respect to bearing at DS3		
Inequality	more	less	more
IM_v	≤ 0.122g	0.122g < -- ≤ 0.576g	> 0.576g
$\delta_{FC,\max}$ (IM_v)	12% (0.08g)	19% (0.40g)	19% (1.60g)

Vulnerability of BS at DS3 with respect to pier at DS3				
Inequality	more			
IM_v	at all values			
$\delta_{FC,\max}$ (IM_v)	119% (0.50g)			
Vulnerability of BS at DS4 with respect to pier at DS3				
Inequality	less	more	less	more
IM_v	≤ 0.07g	0.07g < -- ≤ 0.179g	0.179g < -- ≤ 0.218g	> 0.218g
$\delta_{FC,\max}$ (IM_v)	0.30% (0.07g)	11% (0.08g)	1.04% (0.20g)	36% (1.0g)

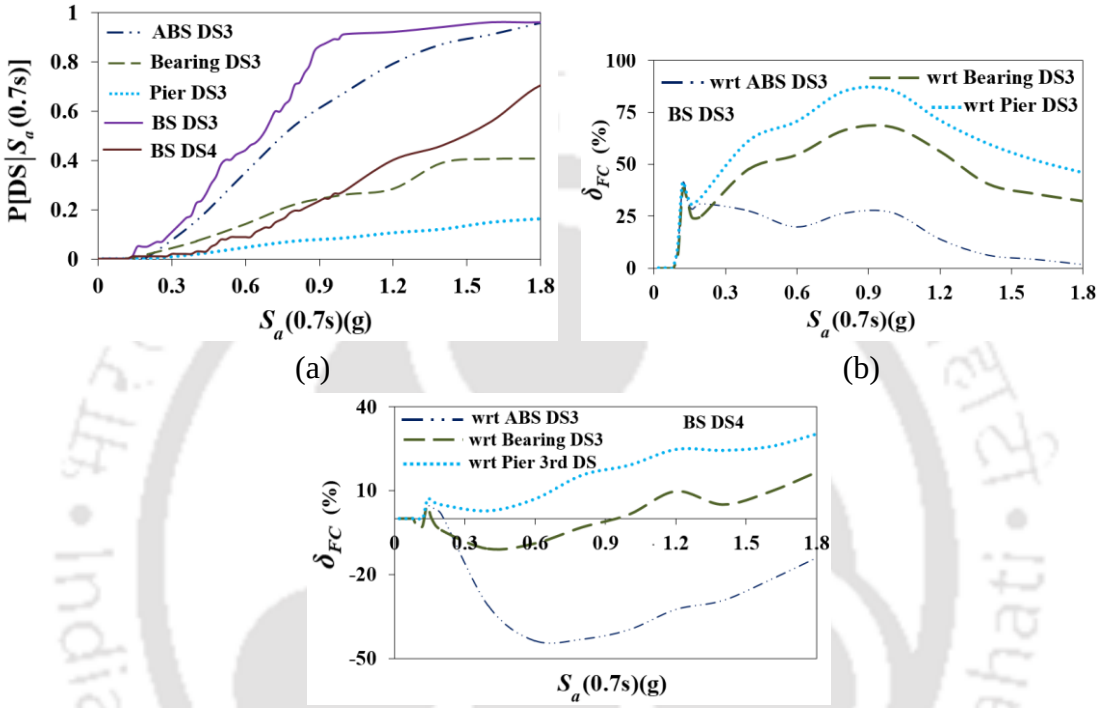

Figure 5.33 (a) Comparative component-level and BS FCs with respect to S_a (0.7s); trends of δ_{FC} between BS FC at (b) DS3 and (c) DS4 and FC of each component at respective DS3.

Table 5.18 Quantitative comparative vulnerabilities of BS and individual components at respective DS3s and with respect to $S_a(0.7\text{s})$, at BS DS3 and DS4

Vulnerability of BS at DS3 with respect to ABS at DS3			
Inequality	more		
IM_v	at all values		
$\delta_{FC,\max}$ (IM_v)	41% (0.12g)		
Vulnerability of BS at DS4 with respect to ABS at DS3			
Inequality	less	more	less
IM_v	≤ 0.12g	0.12g < -- ≤ 0.21g	> 0.21g
$\delta_{FC,\max}$ (IM_v)	0.10% (0.12g)	5% (0.14g)	44% (0.60g)
Vulnerability of BS at DS3 with respect to bearing at DS3			
Inequality	more		
IM_v	at all values		
$\delta_{FC,\max}$ (IM_v)	68% (1.0g)		

Vulnerability of BS at DS4 with respect to bearing at DS3				
Inequality	less	more	less	more
IM_v	≤ 0.128g	0.122g < -- ≤ 0.159g	0.159g < -- ≤ 0.938g	> 0.938g
$\delta_{FC,max}$ (IM_v)	3% (0.10g)	5% (0.14g)	11% (0.40g)	17% (1.80g)

Vulnerability with respect to pier at DS3 of	BS at DS3	BS at DS4
Inequality	more	
IM_v	At all values	
$\delta_{FC,max}$ (IM_v)	86% (1.0g)	30% (1.8g)

5.7.4 Comparisons of the BS FCs at its DS4 with the Individual Component FCs at respective DS4s

Figure 5.34(a) shows the comparative component-level and BS FCs, with respect to PGA. Figure 5.34(b) shows the trends of δ_{FC} between the BS FC at DS4 with the FC of each of bearing and pier at respective DS4. Table 5.19 quantitatively displays the comparative vulnerability of BS at DS4 and each of pier and bearing at respective DS4, in the form of $\delta_{FC,max}$ occurring at particular IM_v.

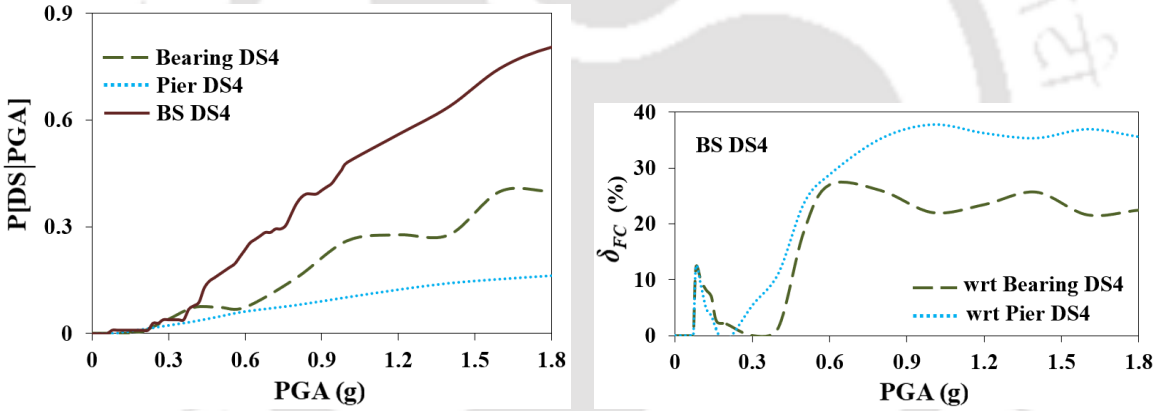

(a) (b)

Figure 5.34 (a) Comparative component-level and BS FC with respect to PGA, and (b) trends of δ_{FC} between the BS FC at DS4 and each of bearing and pier FCs at respective DS4.

Table 5.19 Quantitative comparative vulnerabilities of the BS at its DS4 and each of the bearing and pier at respective DS4s and with respect to PGA.

Comparison of vulnerability of BS at DS4 with respect to bearing at DS4	
Inequality	more
IM_v	at all values
$\delta_{FC,max}$ (IM_v)	27% (0.60g)

Comparison of vulnerability of BS at DS4 with respect to pier at DS4			
Inequality	more	less	more
IM_v	≤ 0.182g	0.182g < -- ≤ 0.215g	> 0.215g
$\delta_{FC,max}$ (IM_v)	12% (0.08g)	0.95% (0.20g)	38% (1.0g)

Figure 5.35(a) shows the comparative component-level and BS FCs, with respect to S_a (0.7s). Figure 5.35 (b) shows the trends of δ_{FC} between the BS FC at DS4 with the FC of each of bearing and pier at respective DS4. Table 5.20 quantitatively displays the comparative vulnerability of BS at DS4 and each of pier and bearing at respective DS4, in the form of $\delta_{FC,\max}$ occurring at particular IM_v.

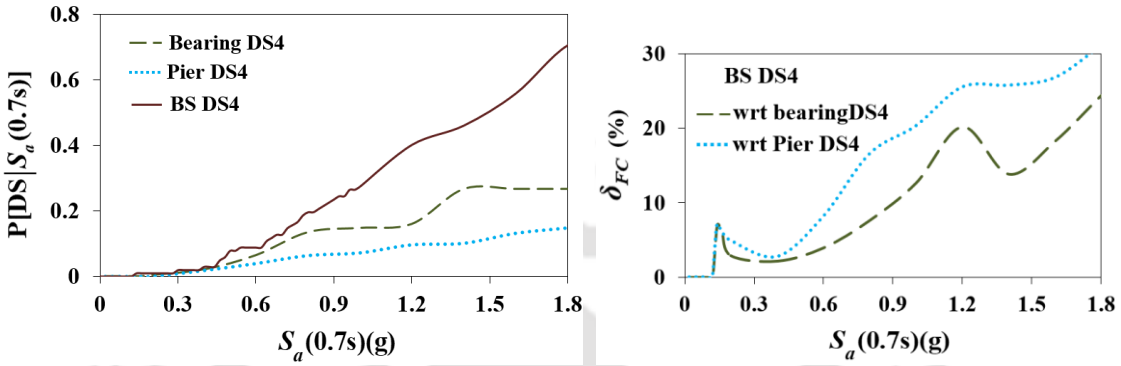

(a) (b)

Figure 5.35 (a) Comparative component-level and BS FCs with respect to S_a (0.7s), and (b) trends of δ_{FC} between BS FC at DS4 and each of bearing and pier FCs at respective DS4.

Table 5.20 Quantitative comparative vulnerabilities of the BS at its DS4 and each of bearing and pier at respective DS4 and with respect to S_a (0.7s).

Comparison of vulnerability at DS4 with respect to	bearing at DS4	Pier at DS4
Inequality	more	
IM_v	at all values	
$\delta_{FC,\max}$ (IM_v)	20% (1.2g)	31% (1.8g)

It is typical of all the generated FCs, that the stiffness of each curve keeps on rising and reach a maximum at a certain IM_v. For a more vulnerable component like A-PSS, i.e., a stiffer curve, the maximum stiffness point lies in a range of lower IM_vs, around 0.12-0.16g. For a less vulnerable component, that point shifts to a range of higher IM_vs, around 0.5-0.8g. This justifies the trend of obtaining the $\delta_{FC,\max}$ between two FCs, irrespective of the IM types as well as the fragility computation approach, at a higher IM_v, as the FCs gets less stiff with the increase in the DS rank.

5.8 SUMMARY

This chapter deals with the evaluation of the probabilistic seismic demand models (PSDMs) of the IAB components and subsequently generates the component-level and the system-level Fragility Curves (FCs). To this aim, probabilistic seismic demand analysis is carried out on each of the 1296 Bridge System (BS) analytical model sample - GM pairs through

the Inverse application of Adaptive Capacity Spectrum Method (IACSM) procedure. To implement IACSM, adaptive capacity spectra are generated employing the displacement based pushover technique, the algorithm of which is automated through a built in code within the BS analytical models in OpenSees. Seismic Demand Spectra corresponding to each of the Damage States (DSs) of all the components are generated employing the SeismoSignal software based on the evaluated BS dampings in the study. With the Peak Ground Acceleration (PGA) and S_a (0.7s) (spectral acceleration at time period of 0.7s) (adopted as the Intensity Measures (IMs) in the study) value of each of the adopted nine GMs scaled to specified values within the range 0-1.8g, component-level demands in terms of their respective Engineering Demand Parameters (EDPs) are assessed with respect to both the IMs. The resulting PSDMs, depicting the relationships of the EDPs with the IMs are developed. Optimality of the IMs are checked and S_a (0.7s) is found to the better IM for the Abutment-Backfill System (ABS) and Pile-Soil System at the abutment (A-PSS) owing to very low dispersions in EDPs. However, both the IMs are found to be of comparable suitability in case of pier and bearing. Owing to rough fit and complete misfit in case of some of the capacity and demand distributions, component-level FCs with respect to both the IMs are derived numerically utilising the actual capacity and demand distributions (FC-NCs). FCs are also derived adopting the traditional lognormal formulation (FC-LFs) as well. At system level, FCs are generated employing the correlations among the component demands. The joint probabiliity surface of the component demands is generated using the MATLAB software. The probability of reaching a BS DS is computed while comparing the set of joint demands with the set of the individual capacity values of the components. For the Integral Abutment Bridge (IAB) class in the study, FCs evaluated with respect to PGA as well as the FC-NCs show higher values as compared those with respect to S_a (0.7s) and FC-LFs respectively. For the three-span continuous IAB class, A-PSS and ABS are the most vulnerable components followed by bearing, pier and PSS at the bent in the order of decreasing level of vulnerability. The BS at a DS rank is found to be more vulnerable that the individual components at the respective same DS rank. BS DSs of higher ranks show more vulnerabilities upto certain IM ranges and vice versa beyond certain IM ranges with respect to the individual components.

Chapter 6
LIMIT STATES OF THE BRIDGE COMPONENTS

CONTENTS

6.1 INTRODUCTION

LSTs for the identified DSs of the bridge components form the basis of generation of the FCs. Hence, the precision of the LSTs values, directly influence the reliability of those FCs to be used as decision aid for mitigating the seismic hazard. LSTs are parameter specific and hence, though literature abounds in LST prescriptions, usage of those case-specific values would lead to error in the desired goal of a study with a set of different values of the structural parameters. Hence, the LST values to be employed for the generation of FCs should correspond to the properties of the BS to whom the FCs belong.

Plenty of literature is available, providing either the LSTs or the expressions for evaluating the expected values of LSTs of the bridge components, as discussed in Subsection 2.4.1. These are based on experimental and/or analytical results on the specimens in the respective studies and hence are case-specific. For instance, Hose et al. (2000) evaluated pier LSTs based on physical observations of damages of the test specimens in their study, yet not enough specimens were tested to encircle broad ranges of the pier parameters. The pier damage model by Panagiotakos and Fardis (2001) corresponded to test specimens controlled by flexure and anchorage slippage in particular; it didn't account for shear as well as buckling modes of failure. Moreover, the regression equations conforming to yielding and ultimate LSs were derived based on mixed data, resulting from the tests carried out on beams, columns as well as shear walls. Hence, those results were case dependent without considering all the possible failure modes and were evaluated for fewer DSs. Similarly, Berry and Eberhard (2003) proposed regression equations corresponding to two DSs (spalling and buckling) for flexure critical columns

bending in single curvature based on experimental results. Choi et al. (2004) presented LSTs based on the results of the tests on nonseismically designed columns accounting for lap splices at the column base in the study. Ramanathan (2012) provided different LST values for piers belonging to different design eras based on the damage assessment report by Sahs et al. (2008); however, each era was represented by a single model of pier properties. Likewise, LSTs estimated analytically by many studies belonged to specific values for pier properties. Existing LST prescriptions for different types of bearings corresponded to particular values of the bearing dimensions and material properties. In case of abutments, e.g., in most cases, LSTs with respect to the mobilisation of the backfill of particular soil type are based on extrapolation using Caltrans guidelines (Caltrans, 1999) for the respective values for H_{ab}s in those studies. This might not always give precise LST estimates for the sets of values for H_{ab}, φ_{bf} and δ_{abf} different from the tested ones, on which the guidelines are based. Some studies adopted LSTs in terms of the maximum displacement capacity $y_{max,bf}$ of the backfill, evaluated as a fraction of H_{ab} based on a particular soil type. However, LSTs vary with φ_{bf} and δ_{abf}, other than H_{ab} and no study prescribed any expressions reflecting such dependence. LSTs corresponding to superstructure-backwall impact are also based on Caltrans guidelines in many studies. In similar fashion, PSS LSTs evaluated by many studies corresponded to particular pile properties and soil types and profiles. The study by Wang et al. (2013) provided LST expressions in relation with only the imposed axial force; dependence on pile structural and soil constitutive properties was missing in the expressions.

Currently any structural performance assessment study either relies on the earlier prescriptions of LSTs or evaluates the LSTs based on structural analyses or test results of the models used in the studies. The estimated LST will change with variation in the structural characteristics. Thus, literature lacks in expressions, which can be generically applied to evaluate the probable LST values for the bridge components over wide ranges of structural and geotechnical properties. If the LSTs can be prescribed through generalised expressions (with proper validations), these can be readily used to obtain the expected values for large ranges of the component parameters, thereby avoiding repetitive analyses of the damage models every time. These would lead to more realistic assessment estimates, rather than using previous case-specific LSTs.

Research towards developing a generalised methodology was pioneered by Ghosh et al. (2012) while proposing a parameterised approach to PSDM generation. Dukes et al. (2012) extended the approach to develop a technique for evaluation of the fragility of bridge with

any given properties. Therein, the responses of the bridge components were regressed against the GM IMs as well as a number of bridge design parameters sensitive to earthquake shaking, thereby developing the fragility equation in parametric form. Stefanidou and Kappos (2017) did an endeavouring effort towards evaluation of the probable LSTs of structural components by developing some generalised expressions, applicable over wide ranges of the component parameters. The evaluation was carried out for RC piers (with cylindrical, hollow cylindrical, rectangular and hollow rectangular sections, with different boundary conditions as well as failure modes), seat-type abutments and different types of bearings (pot, elastomeric steel plate and lead rubber). For pier, LSTs are evaluated at cross section levels in terms of local EDPs by carrying out multiple section analyses over ranges of the pier sectional parameters which are then combined with different heights to obtain LSTs in global terms. Similarly, for other components too, multiple parametric analyses are performed to obtain the LSTs.

Hence, this study develops some numerical expressions (referred to as Parameterised Limit State Expressions (PLSEs) herein) in terms of the influential parameters, to be applicable over wide ranges of variation for future use. This approach is similar to that of Stefanidou and Kappos (2017); except that instead of multiple parametric analyses, Latin Hypercube sampling technique is employed to incorporate the parametric variations. The technique enables encompassing the variation of all the parameters simultaneously, thereby reducing the number of samples and the subsequent analyses without reducing efficiency, as compared to the multiple parametric analyses.

As the prescribed PLSEs are based on the damage models which incorporate all possible failure modes as well as soil-structure interaction of the relevant components, the chronology of occurrences of the DSs of the components for the IAB configuration in the study can be considered proper and realistic. As the LSTs of the respective components change with the parametric variations, the Sequence of Attainments (SoA) of the DSs of the components is liable to get altered. With the promptness of gauging the LSTs using those PLSEs, the trends in the SoAs of the DSs of the components can be easily assessed with changing geometrical and soil parameter values. These observations can be used as guidelines at the design stage itself to arrive at a set of parametric combination leading to the desired SoA such that the intended functional requirements are met.

6.2 DEVELOPMENT OF PLSES

Parameters to be incorporated in the PLSEs are the ones which are found to be influential

in sensitivity anaysis (Section 4.3). The PLSEs are obtained through regression analyses on the LST data (obtained in Chapter 4) and the regression model used is cross validated. These are thereafter attempted to be validated for providing accurate prediction of the expected LSTs for any set of parametric combination within the ranges, for direct usage in future studies. All the above steps are discussed in the Subsections below:

6.2.1 Regression on the Limit State Data

Regression forms can be derived employing artificial neural networking or genetic algorithm; the study employs the simpler multiple linear regression technique on the LST data against the parameters. The resulting PLSEs for PSS, ABS, bearing and pier are stated in Equations (6.1), (6.2), (6.3) and (6.4) respectively. To make the PLSEs dimensionless, parameters like $f_{y,pl}$, $f_{c,pl}$, φ_s, H_{ab}, φ_{bf}, G and σ_m are normalised by the minimum values of the respective ranges, denoted by $f_{y,pl}'$, $f_{c,pl}'$, φ_s', H_{ab}', φ_{bf}', G' and σ_m' respectively. ABS LSTs will be evaluated in terms of 'meters' while the parameters can be in any units.

Credibility of multiple linear regression technique for the purpose of the study is evident by the satisfactory values obtained for the goodness of fit parameters like the adjusted R squared ($adj\ R^2$), standard error (S_E), P -values, as listed in Table 6.1, associated with the regression equations. Also it leads to a more straightforward linear form of relationship rather than the complex expressions provided by the above mentioned techniques.

(a) Parameterised Limit State Expressions for PSS

The expressions for the two LSTs are given as,

$$d_{1,pl} = L_{pl}\exp\{0.7764\ln(D_{pl}/L_{pl}) - 1.0365(\upsilon_{pl}) + 0.6649(f_{y,pl}') - 0.0171\ln(f_{c,pl}') + 0.3207\ln(\rho_{l,pl}) + 0.0706\ln(\rho_{t,pl}) - 1.2636\ln(\varphi_s') - 1.1302\} \quad (6.1a)$$

$$d_{2,pl} = L_{pl}\exp\{1.0445\ln(D_{pl}/L_{pl}) - 1.2007(\upsilon_{pl}) + 0.0419(f_{y,pl}/f_{c,pl}) + 7.9709(\rho_{l,pl}) + 136.5951(\rho_{t,pl}) - 0.5116(\varphi_s')^2 + 5.1583\varepsilon_{su,pl} - 3.3924\} \quad (6.1b)$$

The above equations are applicable for D_{pl} = 0.350-0.800m, L_{pl} = 10-15m, υ_{pl} = 0.075-0.37, $f_{y,pl}$ = 415-565MPa, $f_{c,pl}$ = 21.41-65.52MPa, $\rho_{l,pl}$ = 0.01-0.07, $\rho_{t,pl}$ = 0.00095-0.0097, φ_s = 27-35° and $\varepsilon_{su,pl}$ = 0.145-0.177.

(b) Parameterised Limit State Expressions for ABS

The expressions for the three LSTs are given as,

$$d_{1,ab} = 0.0167H_{ab}' - 0.0061(\varphi_{bf}'/\delta_{abf,f}) + 0.0086 \quad (6.2a)$$

$$d_{2,ab} = 0.0546H_{ab}' - 0.0228(\varphi_{bf}'/\delta_{abf,f}) + 0.0346 \quad (6.2b)$$

$$d_{3,ab} = 0.0998H_{ab}' - 0.0440(\varphi_{bf}' / \delta_{abf,f}) + 0.0645 \quad (6.2c)$$

The above equations are applicable for H_{ab} = 2-5m, $\delta_{abf,f}$ = 0.6-0.8 and φ_{bf} = 35-45º.

(c) Parameterised Limit State Expressions for Bearing

The expressions for the two LSTs are given as,

$$d_{1,br} = d_{brd} \exp\{-1.9938\ln(d_{brd} / h_{br}) + 1.1016\ln(\varepsilon_{su,brd}) - 0.3803\} \quad (6.3a)$$

$$d_{2,br} = d_{brd} \exp\{-1.0101\ln(d_{brd} / h_{br}) - 1.3107\ln(G') + 0.3622\ln(\sigma_m') + 0.9003\ln(\varepsilon_{su,brd}) + 1.1793\} \quad (6.3b)$$

The above equations are applicable for G = 800-1200kPa, d_{brd} = 0.025-0.040m, σ_m = 2018-9970kPa, d_{brd} = 0.025-0.040m, h_{br} = 0.020-0.150m and $\varepsilon_{su,brd}$ = 0.145-0.177.

(d) Parameterised Limit State Expressions for Pier

The expressions for the four LSTs are given as,

$$d_{pr,1} = D_{pr}\exp\{-2.2271\ln(D_{pr}/H_{pr}) + 0.4191\ln(f_{y,pr}/f_{c,pr}) + 0.0848\ln(\rho_{l,pr}) + 0.1044\ln(\rho_{t,pr}) - 0.2293\ln(\upsilon_{pr}) - 8.1060\} \quad (6.4a)$$

$$d_{pr,2} = D_{pr}\exp\{-2.3518\ln(D_{pr}/H_{pr}) + 0.4206\ln(f_{y,pr}/f_{c,pr}) - 0.2196\ln(\rho_{l,pr}/\rho_{t,pr}) - 0.5838\ln(\upsilon_{pr}) - 9.1339\} \quad (6.4b)$$

$$d_{pr,3} = D_{pr}\exp\{-2.6703\ln(D_{pr}/H_{pr}) + 0.9377\ln(f_{y,pr}/f_{c,pr}) - 0.4282\ln(\rho_{l,pr}/\rho_{t,pr}) - 0.9041\ln(\upsilon_{pr}) - 10.7294\} \quad (6.4c)$$

$$d_{pr,4} = D_{pr}\exp\{-2.9366\ln(D_{pr}/H_{pr}) + 1.5508\ln(f_{y,pr}/f_{c,pr}) - 0.4526\ln(\rho_{l,pr}/\rho_{t,pr}) - 1.5027\ln(\upsilon_{pr}) - 13.8845\} \quad (6.4d)$$

The above equations are applicable for D_{pr} = 0.800-2.0m, H_{pr} = 5-15m, υ_{pr} = 0.042-0.31, $f_{y,pr}$ = 415-565MPa, $f_{c,pr}$= 21.41-65.52MPa, $\rho_{l,pr}$ = 0.0088-0.051, $\rho_{t,pr}$ = 0.00055-0.0055.

6.2.2 Cross Validation of the Proposed PLSEs

The PLSEs are cross validated by comparing the LST values predicted by Equations (6.1), (6.2), (6.3) and (6.4) with the observed values for a few sets of parameter values within the adopted ranges and different from those used for developing the PLSEs. With small S_Es of the regression models (Table 6.1), fair agreements between the observed (obtained directly from the analyses of the damage models of the component samples with those sets) and the predicted values are achieved, as in Tables 6.2, 6.3, 6.4 and 6.5 for PSS, ABS, bearing and

pier respectively. It is to noted, of all the PLSEs, those of piers show highest values for S_E, hence deviations of the predicted values from the observed values are the greatest in case of pier LSTs. However, the predicted values lie within $\pm 1.5S_E$ of the observed values.

Table 6.1 Goodness of fit test parameters for LSTs of pier, PSS, ABS and bearing

Regression parameters	Goodness of fit test parameters for pier						
	P - values				LST	adj R^2	S_E
	LST1	LST2	LST3	LST4			
$\ln(D_{pr}/H_{pr})$	3.4E-109	1.5E-84	3.54E-72	2.16E-60	LST1	0.99	0.17
$\ln(f_{y,pr}/f_{c,pr})$	1.76E-8	0.00068	1.82E-6	8.75E-10	LST2	0.96	0.29
$\ln(\rho_{l,pr}/\rho_{t,pr})$	-	9.01E-9	1.73E-13	1.48E-9			
$\ln(\upsilon_{pr})$	0.00014	5.68E-8	2.62E-8	4.21E-12	LST3	0.94	0.41
$\ln(\rho_{l,pr})$	0.00252	-	-	-			
$\ln(\rho_{t,pr})$	0.00072	-	-	-	LST4	0.90	0.56
Constant	8.53E-43	4.86E-31	2.21E-29	1.27E-22			

Goodness of fit test parameters for PSS						
Regression parameters (LST1)	*P* - values		RPs (LST2)	LST	adj R^2	S_E
	LST1	LST2				
$\ln(D_{pl}/L_{pl})$	2.12E-38	3.24E-51	$\ln(D_{pl}/L_{pl})$	LST1	0.92	0.08
υ_{pl}	0.0025	0.00017	υ_{pl}			
$f_{y,pl}'$	1.41E-16	6.49E-22	$f_{y,pl}/f_{c,pl}$			
$\ln(f_{c,pl}')$	0.00442	4.77E-31	$\rho_{l,pl}$	LST2	0.95	0.09
$\ln(\rho_{l,pl})$	3.05E-47	1.49E-48	$\rho_{t,pl}$			
$\ln(\rho_{t,pl})$	0.000172	4.9E-8	$(\varphi_s')^2$			
$\ln(\varphi_s')$	4.31E-7	4.77E-10	$\varepsilon_{su,pl}$			
constant	0.00416	1.2E-26	constant			

Regression parameters	Goodness of fit test parameters for ABS					
	LST1	LST2	LST3	LST	adj R^2	S_E
	P -value	*P* -value	*P* -value			
H_{ab}'	7.88E-77	1.03E-78	4.93E-78	LST1	0.92	0.0025
$\varphi_{bf}'/\delta_{abf,f}$	3.28E-7	1.14E-8	3.18E-9	LST2	0.92	0.0084
Constant	3.16E-5	6.79E-7	5.58E-7	LST3	0.92	0.0155

Goodness of fit test parameters for bearing					
Regression parameters	*P*-values		LST	adj R^2	S_E
	LST1	LST2			
$\ln(d_{brd}/h_{br})$	2.3E-302	1.6E-102	LST1	1	0.083
$\ln(\varepsilon_{su,brd})$	1.8E-313	1.27E-8			
$\ln G'$	-	2.25E-36			
$\ln\sigma_m'$	-	7.42E-41	LST2	0.96	0.103
Constant	5.32E-43	4.59E-5			

Table 6.2 Cross validation of the regression model for PSS PLSEs

Parameters	L_{pl} (m)	D_{pl} (m)	υ_{pl}	$f_{y,pl}$ (MPa)	$f_{c,pl}$ (MPa)	$\rho_{l,pl}$	$\rho_{t,pl}$	φ_s (°)	$\varepsilon_{su,brd}$
Base values	12.5	0.365	0.166	415	35	0.0324	0.0032	31	0.145

Set no.	Change in	value	Comparison	LST1	LST2
1	Base values		Observed	0.023	0.037
			Predicted	0.020	0.031
2	D_{pl}	0.592m	Observed	0.030	0.048
			Predicted	0.030	0.051
3	D_{pl}	0.740m	Observed	0.034	0.056
			Predicted	0.035	0.064

Table 6.3 Cross validation of the regression model for ABS PLSEs

Parameters (base values)	H_{ab} (2m)		φ_{bf} (35°)		$\delta_{abf,f}$ (0.6)	
Set no.	Change in	value	Comparison	LST1	LST2	LST3
1	Base values		Observed	0.014	0.046	0.082
			Predicted	0.015	0.051	0.091
2	H_{ab}	5m	Observed	0.044	0.138	0.245
			Predicted	0.040	0.133	0.241
3	φ_{bf}	45°	Observed	0.012	0.038	0.068
			Predicted	0.012	0.040	0.070

Table 6.4 Cross validation of the regression model for bearing PLSEs

Parameters (base values)	h_{br} (0.02m)	d_{brd} (0.025m)	$\varepsilon_{su,brd}$ (0.145)	G (800kPa)	σ_m (3120kPa)

Set no.	Change in	value	Comparison	LST1	LST2
1	Base values		Observed	0.0015	0.014
			Predicted	0.0013	0.013
2	h_{br}	0.150m	Observed	0.0858	0.107
			Predicted	0.0725	0.102
3	G	1200kPa	Observed	0.0015	0.010
			Predicted	0.0013	0.008

Table 6.5 Cross validation of the regression model for pier PLSEs

Parameters	H_{pr}	D_{pr}	υ_{pr}	$f_{y,pr}$	$f_{c,pr}$	$\rho_{l,pr}$	$\rho_{t,pr}$
Base values	8.0m	1.4m	0.046	415MPa	35MPa	0.0091	0.0008

Set	Change in	Parameter value	Comparison	LST1	LST2	LST3	LST4
1	Base values		Observed	0.030	0.087	0.166	0.338
			Predicted	0.037	0.091	0.188	0.346
2	D_{pr}	1.8m	Observed	0.022	0.064	0.118	0.155
			Predicted	0.027	0.065	0.123	0.213
3	$\rho_{t,pr}$	0.003	Observed	0.029	0.083	0.284	0.479
			Predicted	0.043	0.122	0.330	0.629

6.2.3 Numerical Plots with the PLSEs

With the LSTs obtained against the parametric variations while employing the PLSEs, the

trends in variations of the LSTs are observed. Reliability of the PLSEs is judged through the convergence of those numerical plots, as in Figures 6.1, 6.2, 6.3 and 6.4, with the sensitivity analysis results (Section 4.3).

In case of pier, although $d_{1,pr}$ is usually not influenced by $\rho_{t,pr}$ in flexural damage mode, moderate affect is observed (Figure 6.1(a)), owing to the detection and incorporation of shear failure in addition to flexural damages for the pier samples in the study. This is confirmed by the fact that pier sections with low values for $\rho_{t,pr}$ tend to fail in shear resulting in a decreased $d_{1,pr}$ value, compared to what would have been achieved when considering only flexural failure. Effect of $\rho_{t,pr}$ goes on increasing with pier DS rank, as is observed for $d_{4,pr}$ in Figure 6.1(a) and confirmed by the sensitivity analysis. However, for low values of $\rho_{t,pr}$, with most of the samples failing in shear, for such cases, LST values irrespective of the DS rank post the failure. is taken the same as the LS value at the instant of failure. Figure 6.1(a) shows a moderate increase in $d_{1,pr}$ due to increase in $\rho_{l,pr}$. Predominance of shear to flexure failure mode is more evident with increasing $\rho_{l,pr}$ (mostly at higher DS ranks) as this contributes to higher flexural capacity resulting in increasing tendency for shear failure, as is also observed by the comparable values of $d_{1,pr}$ and $d_{4,pr}$ in Figure 6.1(a), for higher values of $\rho_{l,pr}$. $d_{4,pr}$ decreases with $\rho_{l,pr}$, as found also in sensitivity analysis. Increase in $f_{y,pr}$ causes increase in $d_{1,pr}$ (Figure 6.1(b)). While in case of only flexural flexure, $d_{4,pr}$ decreases with increase in $f_{y,pr}$ due to decrease in the ultimate curvature capacity, while incorporating all the failure modes, decrease in $f_{y,pr}$ results in increasing tendency for shear failure as well as buckling, leading to the decrease in $d_{4,pr}$. $d_{4,pr}$ increases with increase in $f_{y,pr}$ (Figure 6.1(b)). With increase in both $f_{c,pr}$ and D_{pr}, yield as well as the ultimate curvature capacities decrease, leading to decreased values for all the LSTs, as shown for both $d_{1,pr}$ and $d_{4,pr}$ in Figures 6.1(b) and 6.1(c) respectively. For a given curvature, all the LSTs increase with H_{pr} (Figure 6.1(c)), as confirmed by the sensitivity analysis. Increase in υ_{pr} leads to increasing tendency for shear failure buckling as well as P-δ failure, thereby causing decrease in all the LSTs (Figure 6.1(d)). It is to be noted that sensitivity analysis carried out for pier is based on flexural failure only. An anomaly might be observed while evaluating the LSTs using the pier PLSEs, due to different degrees of goodness of fit for the PLSEs. For instance $d_{3,pr}$ (or even $d_{1,pr}$) might come out to be just higher than $d_{4,pr}$, for the sets of parametric combinations leading to shear or buckling or P-δ failure, if any of these failures occur close to the attainment of DS3 (or DS1), e.g., high values of υ_{pr} and small values of $\rho_{t,pr}$. For such cases, the LST values post the failure are to be taken the same, irrespective of the DS ranks.

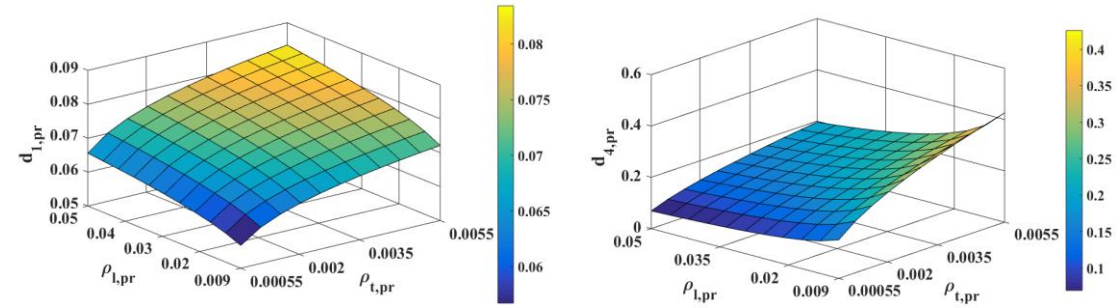

D_{pr} = 1.2m, H_{pr} = 10m, υ_{pr} = 0.15, $f_{y,pr}$ = 460MPa, $f_{c,pr}$ = 35MPa

(a)

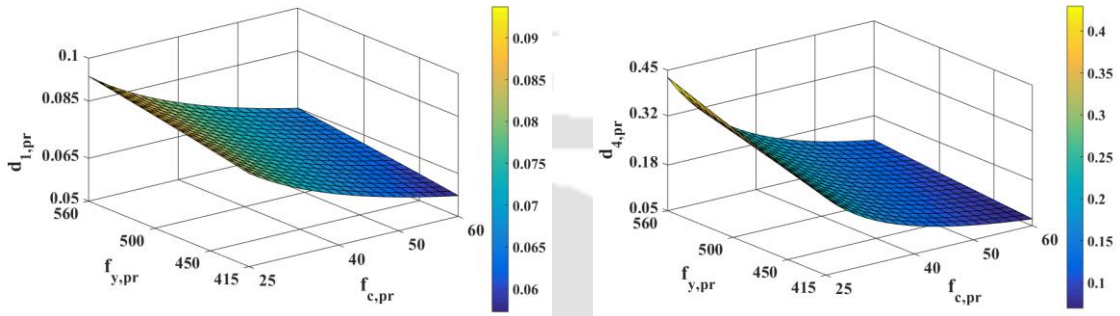

D_{pr} = 1.2m, H_{pr} = 10m, υ_{pr} = 0.15, $\rho_{l,pr}$ = 0.03, $\rho_{t,pr}$ = 0.003

(b)

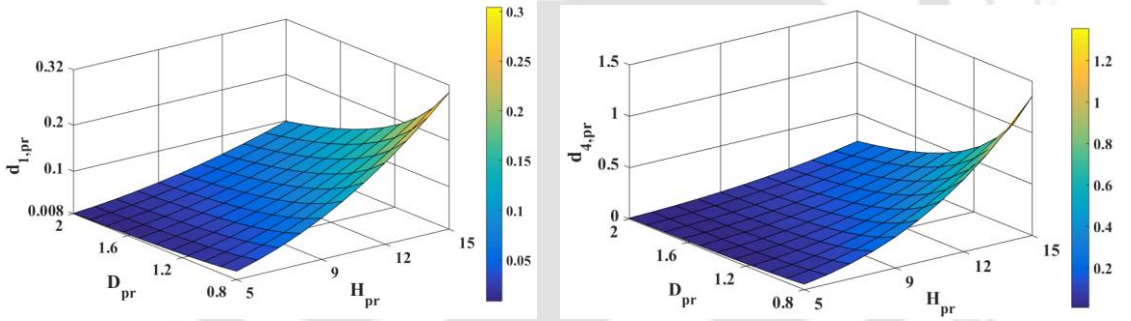

υ_{pr} = 0.15, $f_{y,pr}$ = 460MPa, $f_{c,pr}$ = 35MPa, $\rho_{l,pr}$ = 0.03, $\rho_{t,pr}$ = 0.003

(c)

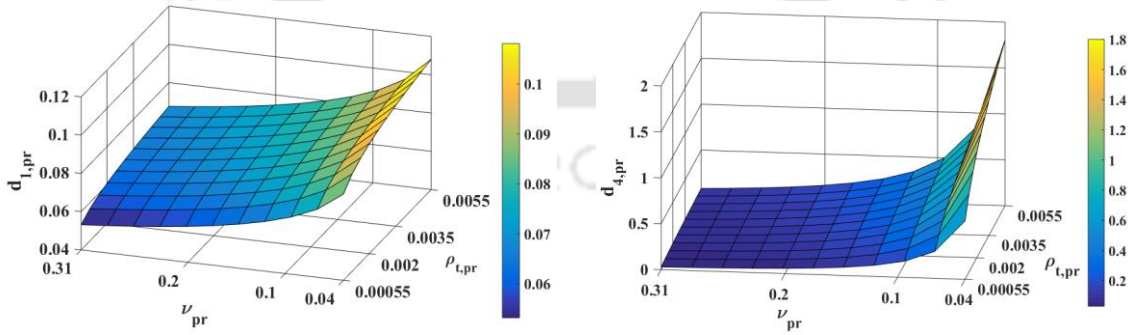

D_{pr} = 1.2m, H_{pr} = 10m, $f_{y,pr}$ = 460MPa, $f_{c,pr}$ = 35MPa, $\rho_{l,pr}$ = 0.03

(d)

Figure 6.1 Trends in variations of pier LSTs with (a) $\rho_{l,pr}$ and $\rho_{t,pr}$, (b) $f_{y,pr}$ and $f_{c,pr}$, (c) D_{pr} and H_{pr} and (d) υ_{pr} and $\rho_{t,pr}$.

In case of bearing, both $d_{1,br}$ and $d_{2,br}$ are significantly increased with increase in h_{br} due to

the decrease in the respective stiffness, and vice versa in case of $d_{1,br}$ with respect to d_{brd} (Figure 6.2(a)). Effect of d_{brd} is more at higher h_{br}. Both $d_{1,br}$ and $d_{2,br}$ are moderately increased with increase in $\varepsilon_{su,brd}$, while $d_{2,br}$ is not at all influenced by d_{brd} (Figure 6.2(b)). Increase in G significantly reduces $d_{2,br}$ due to reduction in the pad stiffness, while σ_m has the opposite effect on $d_{2,br}$ due to increase in both the force and displacement capacities of the pad at the constant stiffness (Figure 6.2(c)), as is confirmed by SA. It is to be noted that the DS2 of bearing is influenced by both the events of the pad attaining $F_{u,brp}$ as well the dowel fracture. Hence, the corresponding LST is obtained with respect to both the dowel and pad parameters. Nevertheless, $d_{2,br}$ is only influenced by $\varepsilon_{su,brd}$ and not at all by d_{brd}.

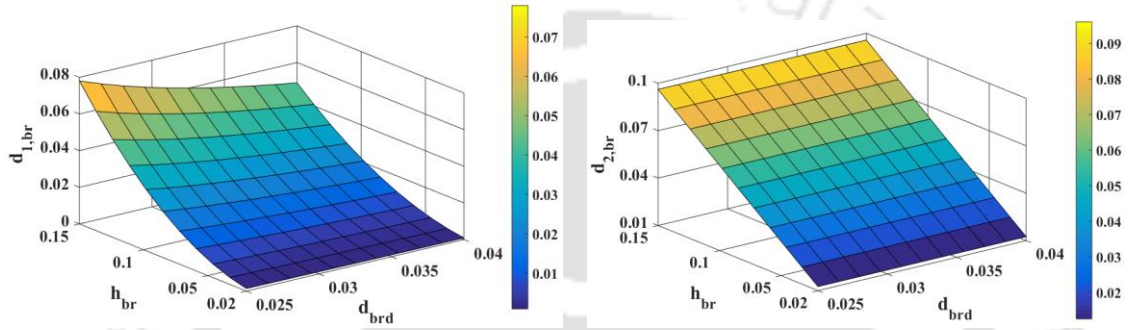

$\varepsilon_{su,brd}$ = 0.155, G =1000kPa, σ_m = 5000kPa

(a)

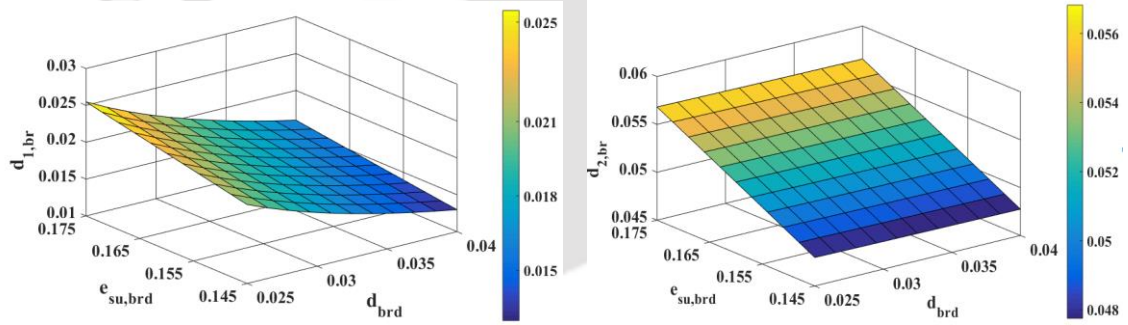

h_{br} = 0.08m, G =1000kPa, σ_m = 5000kPa

(b)

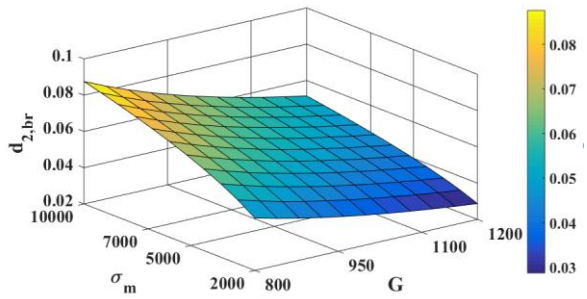

h_{br} = 0.08m, d_{brd} = 0.03m, $\varepsilon_{su,brd}$ = 0.155

(c)

Figure 6.2 Trends in variations of bearing LSTs with (a) h_{br} and d_{brd}, (b) $\varepsilon_{su,brd}$ and d_{brd} and (c) G and σ_m.

All the ABS LSTs increase significantly with increase in H_{ab}, as shown in Figure 6.3(a) for $d_{1,ab}$ and $d_{3,ab}$**.** As, H_{ab} increases, SPW dimensions increase resulting in increase in y_{ab} and thus the LSTs. The mobilised base angles of the soil slices increase with decrease in φ_{bf} and increase in $\delta_{abf,f}$, resulting in moderate increase in y_{ab} and thus the LSTs, as shown in Figures 6.3(a) and 6.3(b) respectively. The effects of both H_{ab} and φ_{bf} are more at lower values of $\delta_{abf,f}$. The effects of these parameters are in line with the sensitivity analysis results.

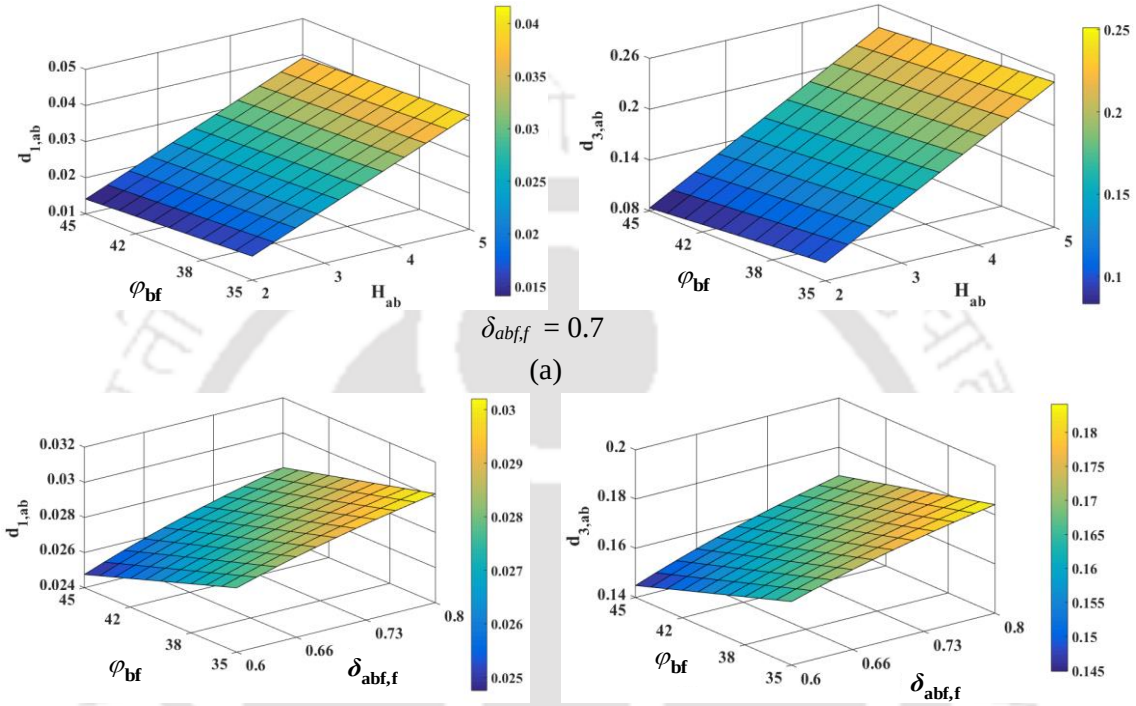

Figure 6.3 Trends in variations of ABS LSTs with φ_{bf} and (a) H_{ab} and (b) $\delta_{abf,f}$.

Both $d_{1,pl}$ and $d_{2,pl}$ increase significantly with D_{pl}, owing to the increasing dimensions of the SPW, while being uninfluenced by L_{pl} (Figure 6.4(a)). Figure 6.4 (b) shows moderate increases in the LSTs with $f_{y,pl}$ and vice versa with $f_{c,pl}$, as the DSs are delayed to higher ε_{ss} and thus larger $y_{0,pl}$ values with increase in $f_{y,pl}$ and decrease in $f_{c,pl}$. Figure 6.4(c) displays significant and small increases in $d_{1,pl}$ and $d_{2,pl}$ respectively with the increase in $\rho_{l,pl}$, as the DSs are delayed to larger ε_{ss} and thus larger $y_{0,pl}$ values, and the shift is more till the attainment of $d_{1,pl}$. While $d_{1,pl}$ is negligibly influenced by $\rho_{t,pl}$, $d_{2,pl}$ rises significantly with $\rho_{t,pl}$, as the ultimate DS occurs at a higher ε_{ss} and thus larger $y_{0,pl}$ with the increase in $\rho_{t,pl}$ (Figure 6.4(c)). Figure 6.4(d) shows the decrease in the LSTs with both φ_s and υ_{pl}, as the pile DSs are attained at lower ε_{ss} and thus lesser $y_{0,pl}$ values with increase in both φ_s and υ_{pl}. Increase in $\varepsilon_{su,pl}$ causes increase in $d_{2,pl}$ at moderate rate (Figure 6.4(e)). All these trends are confirmed by the sensitivity analysis.

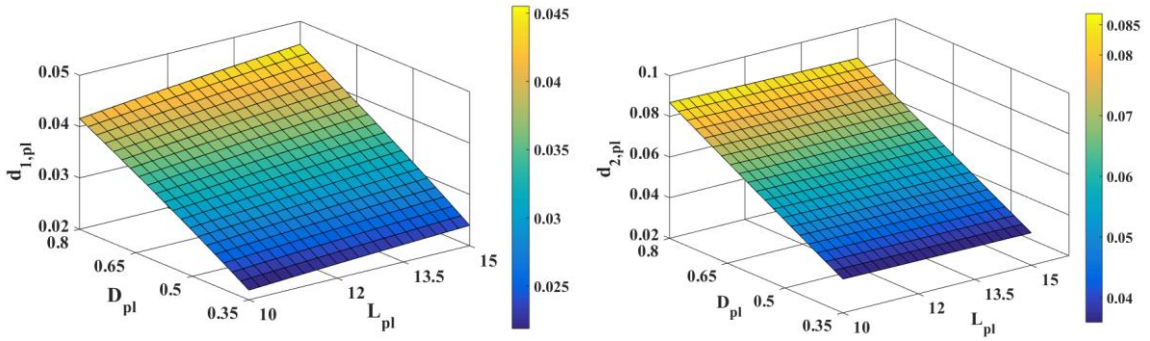

υ_{pl} = 0.15, $f_{y,pl}$ = 460MPa, $f_{c,pl}$ = 35MPa, $\rho_{l,pl}$ = 0.035, $\rho_{t,pl}$ = 0.003, $\varepsilon_{su,pl}$ = 0.166, φ_s = 30°

(a)

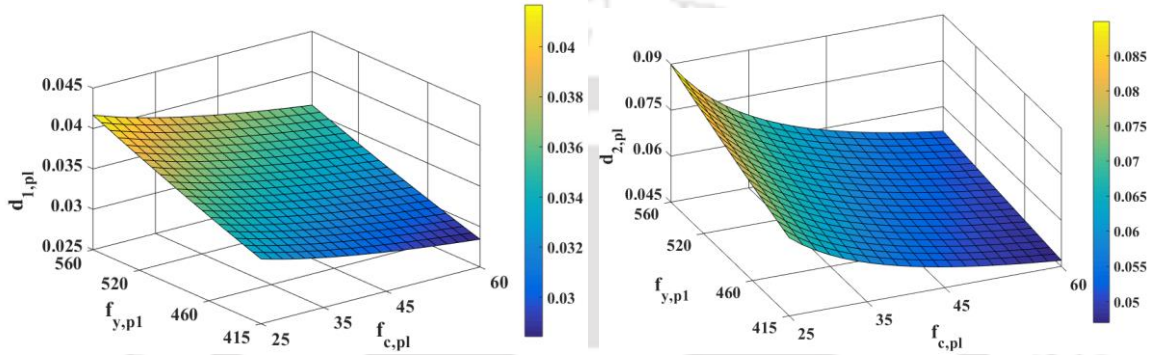

υ_{pl} = 0.15, D_{pl} = 0.575m, L_{pl} = 12m, $\rho_{l,pl}$ = 0.035, $\rho_{t,pl}$ = 0.003, $\varepsilon_{su,pl}$ = 0.166, φ_s = 30°

(b)

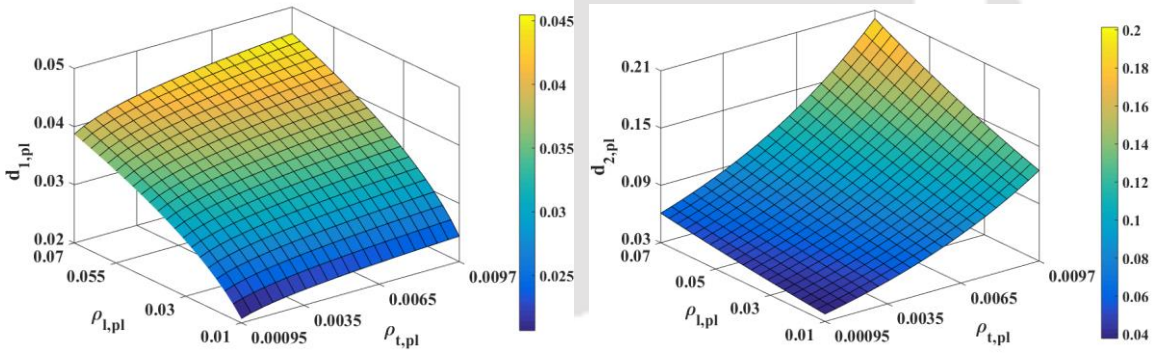

υ_{pl} = 0.15, D_{pl} = 0.575m, L_{pl} = 12m, $f_{y,pl}$ = 460MPa, $f_{c,pl}$ = 35MPa, $\varepsilon_{su,pl}$ = 0.166, φ_s = 30°

(c)

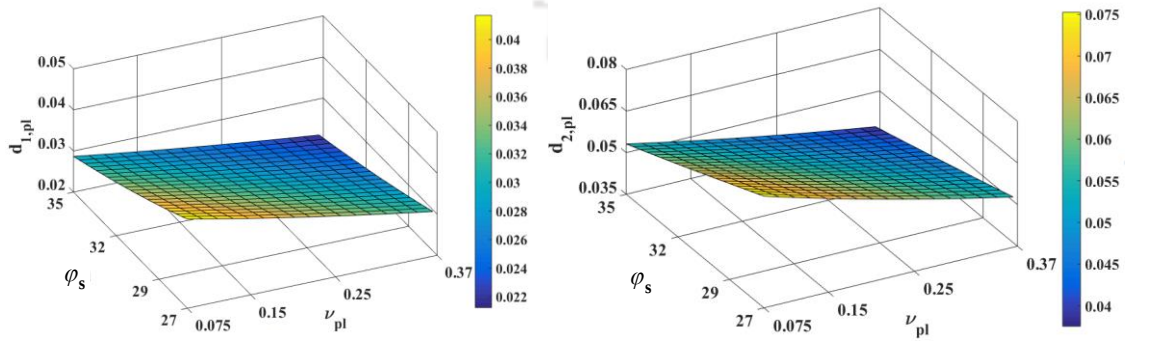

D_{pl} = 0.575m, L_{pl} = 12m, $f_{y,pl}$ = 460MPa, $f_{c,pl}$ = 35MPa, $\rho_{l,pl}$ = 0.035, $\rho_{t,pl}$ = 0.003, $\varepsilon_{su,pl}$ = 0.166

(d)

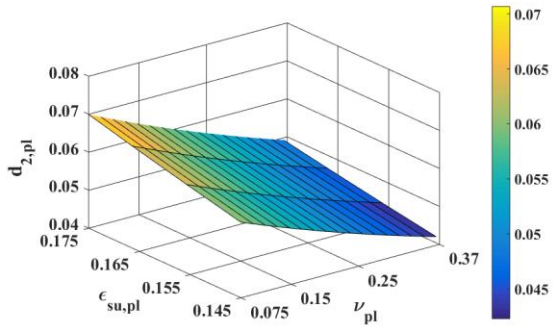

D_{pl} = 0.575m, L_{pl} = 12m, $f_{y,pl}$ = 460MPa, $f_{c,pl}$ = 35MPa, $\rho_{l,pl}$ = 0.035, $\rho_{t,pl}$ = 0.003, φ_s = 30°

(e)

Figure 6.4 Trends in variations of pile LSTs with (a) D_{pl} and L_{pl}, (b) $f_{y,pl}$ and $f_{c,pl}$, (c) $\rho_{l,pl}$ and $\rho_{t,pl}$, (d) υ_{pl} and φ_s and (e) $\varepsilon_{su,pl}$ and υ_{pl}.

6.2.4 Validation of PSS PLSEs with an Experimental Result

Lemnitzer et al. (2010) provided overview of many tests carried out on PSSs; tests of Lemnitzer et al. (2010), Chai and Hutchinson (2002), Hoit et al. (1996), Huang et al. (2001), Conte et al. (2013) on reinforced concrete piles are sorted out as relevant for validating the proposed PLSEs. Lemnitzer et al. (2010) tested fixed headed circular pile, with properties within the ranges as in the present study, however, the site was dominated by clayey soils. Though, the site soils were representatives of loose and dense sands, the test by Chai and Hutchinson (2002) was on free headed circular pile with the lateral load applied at a distance away from the ground level. Hoit et al. (1996) tested fixed headed square pile in loose sand with the parameter values within the ranges, except for the very high value of $f_{y,pl}$ and no mention of the provided $\rho_{t,pl}$. Thus, the only test which could be used, is that by Huang et al. (2001), which was on fixed headed reinforced concrete circular pile with the lateral load applied at the ground , though with some adjustments. The layered profile of silty sands and clayey silts of the site soil is assumed to coincide with the uniform profile (based on the subsoil data considered for simulating the test Huang et al. (2001), by Conte et al. (2013)) of sand with an average φ_s of 31°.

Thus, using the proposed PLSE (Equation (6.5)), with *adj* R^2 = 0.936 and S_E = 0.096, a form of Eq. (6.1b) excluding $\varepsilon_{su,pl}$), for the test values of Huang et al. (2001): L_{pl} = 34.9m, D_{pl} = 1.5m, υ_{pl} = 0, $f_{c,pl}$ = 27.5MPa, $f_{y,pl}$ = 471MPa, $\rho_{l,pl}$ = 0.025, $\rho_{t,pl}$ = 0.0042 and φ_s of 31°, $d_{2,pl}$ is computed as 0.114m against the test result of 0.124m from Huang et al. (2001) (Figure 6.5). The observed mismatch is probably because the test values for L_{pl}, D_{pl} and υ_{pl} are beyond the range of application of Equation (6.5) and the outcome would be a bit different for circular pile. Even so, Equation (6.5) is in good agreement with the field measurement which affirms its reliability to evaluate LST precisely. It is to be noted that

the validation could be done only for the PLSE with respect to pile LST2 and too with the assumption that the ultimate value of $y_{0,pl}$, as displayed in Huang et al. (2001) corresponded to transverse reinforcement fracture, as considered for the pile DS2 in the present study.

$$d_{2,pl} = L_{pl}\exp\{1.0353\ln(D_{pl}/L_{pl}) + 0.0454(f_{y,pl}/f_{c,pl}) + 7.1914(\rho_{l,pl}) + 146.03(\rho_{t,pl}) - 0.0899(\varphi_s')^6 - 3.8245\} \quad (6.5)$$

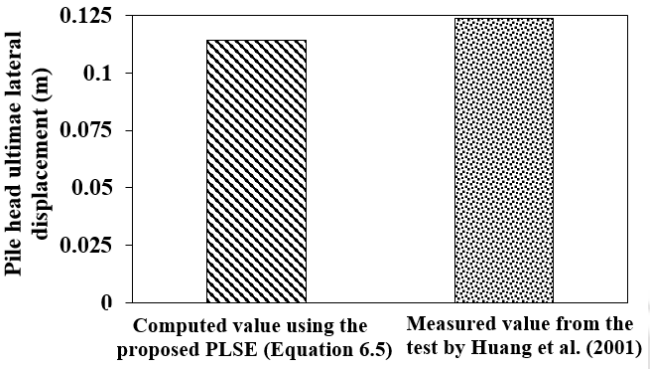

Figure 6.5 Validation of the PSS PLSE with the test result of Huang et al. (2001).

It is to be noted that the F_{pl}–$y_{0,pl}$ values computed from the LPILE analysis in Huang et al. (2001), using *p*–*y* curves from Reese et al. (1974) as input, initially did not coincide with the test values. The mismatch is possibly because the applied curves were not appropriate for the site and the construction conditions of Huang et al. (2001) and thereby had to be adjusted by some factor for the agreement. Thus, the traditional curves, as in Reese et al. (1974), are not appropriate for site conditions different from those tests based on which these had been formulated. SWM generates *p*–*y* curves based on pile and soil properties at the site in question and thus are more reliable and the same can be expected for the PLSEs derived while simulating pile-soil interaction through SWM.

6.3 SoAs of DSs of the Components with Parametric Variations

The present work investigates the SoA of the DSs of the components by monitoring the instances of attainments (in terms of BS displacements) of the respective LSTs on the BS capacity curve, as the BS is pushed laterally in a monotonic fashion. By observing the relative positions of the various LSTs of the components in the SoA corresponding to a given set of values of the parameters, the relative degrees of frailties of the components with respect to particular individual DSs can be assessed. As the LSTs of the respective components change with the parametric variations, SoA of the DSs of the components is liable to get altered, so does the relative frailties. With the promptness of gauging the LSTs using those PLSEs, the trends in the SoAs with geometrical and soil parametric variations

are examined, for the multispan continuous IAB and full integral bridge configurations, through the following sub-stages and the observations are represented as flowcharts.

6.3.1 Seismic Loading on the Bridge System

The bridge components are coalesced into a single unit that represents the BS (as in Chapter 5) and the full integral bridge configuration model is the modified version of Figure 5.2, corresponding to multispan continuous IAB model, with the bearing springs removed and the bent spring top nodes connected to the deck nodes directly. A built-in code is embedded within the OpenSees BS model which when run automates the DAPA, (as in Section 5.3.1), which is continued until the BS exhausts of all the DSs leading to its collapse.

6.3.2 Generation of BSs with the Variations in Geometric and Soil Parameters

Trends of SoAs of DSs with parameter values which fall under different column bent types cannot be compared, as these have different configurations for the superstructure, bearing and bent. Thus, the study observes SoAs with respect to the geometric and soil parameters, while confining to 2-coulmn bent type, followed by switching to 4-column bent type (with properties listed in Table 6.6). The BS base model is constituted by the base values of the parameters of the components (forming the base models of the respective components). The remaining models are generated by varying each component parameter, one at a time, from the respective *u* and *l* values. PSS and ABS, bearing, and pier models are listed in Tables 6.7, 6.8, and 6.9 respectively, (with Model 1 being the base model in each).

Table 6.6 2-column and 4-column bent type models for determining the SoAs

Model	D_w (m)	D_{pr} (m)	n_g	n_{pl}	Base values of parameters (common to 2-column and 4-column bent types)
2CBT	16	1.6	7	3, at both bent and abutment	L_{sp} = 35m, H_{pr} = 10m, H_{ab} = 3.5m, φ_{bf} = 40°, D_{pl} = 0.575m, L_{pl} = 15m, φ_s = 31° (both at bent and abutment)
4CBT	24	0.9	11	2 at pier and 4 at abutment	

Table 6.7 PSS and ABS models in the study for determining the SoAs

Model	PSS				ABS		
	D_{pl} (m)	φ_s °	Base values of other parameters	LSTs (mm) $d_{1,pl}$, $d_{2,pl}$	H_{ab} (m)	φ_{bf} °	LSTs (mm) $d_{1,ab}$, $d_{2,ab}$, $d_{3,ab}$
1	0.575	31	$f_{c,pl}$ = 35MPa, $f_{y,pl}$ = 415MPa, $\rho_{l,pl}$ = 0.0345, $\rho_{t,pl}$ = 0.003	30, 48	3.5	40	26, 87, 157
2	0.800	31		34, 60	5	40	41, 134, 241
3	0.350	31		22, 46	2	40	13, 44, 80
4	0.575	35		23, 39	3.5	45	24, 82, 149
5	0.575	27		38, 64	3.5	35	29, 93, 166

Table 6.8 Bearing models in the study for determining the SoAs

Model	h_{br} (m)	d_{brd} (m)	Base values of other parameters	LSTs ($d_{1,br}$, $d_{2,br}$) (mm)
1	0.058	0.032	G =1000kN/m^2, $\varepsilon_{su,brd}$ = 0.145	9.85, 35.90
2	0.136	0.032		55.10, 69.60
3	0.023	0.032		1.61, 21.42
4	0.058	0.040		7.90, 35.90
5	0.058	0.025		12.60, 35.90

Table 6.9 Pier models in the study for determining the SoAs

Model	D_{pr}	H_{pr}	Base values of other parameters	LSTs ($d_{1,pr}$, $d_{2,pr}$, $d_{3,pr}$, $d_{4,pr}$)(m)
1	1.6	10	$f_{c,pr}$ = 35MPa, $f_{y,pr}$ = 415MPa, $\rho_{l,pr}$ = 0.0272, $\rho_{t,pr}$ = 0.002	0.051, 0.100, 0.201, 0.257
2	1.8	10		0.047, 0.093, 0.183, 0.183
3	1.4	10		0.059, 0.112, 0.227, 0.612
4	1.6	15		0.115, 0.222, 0.447, 1.158
5	1.6	5		0.013, 0.013, 0.013, 0.013

6.3.3 Assessment of SoAs of DSs

Trends in variations of SoAs with parametric variations are assessed and registered as flowcharts. For the multispan continuous IAB base model with respect to 2-column bent type (Table 6.6), bearing DS1 followed by ABS DS1, DSs of A-PSS, bearing DS2, ABS DS2 and DS3, and bearing DS3 and DS4 form the SoA. For the full integral bridge base model (corresponding to the continuous configuration, as in Table 6.6), ABS DS1, followed by DSs of A-PSS, DSs of B-PSS (PSS at bent), ABS DS2 and DS3 and pier DSs form the SoA. Variations of trends in SoAs with parametric variations are observed with respect to the above established SoAs corresponding to the base models of the multispan continuous IAB and full integral bridge respectively. Figure 6.6 shows the impact of the column-bent type, with respect to change from 2-column to 4-column bent types. Flowcharts depicting the trends with respect to bearing, pier, PSS and ABS are shown in Figures 6.7, 6.8, 6.9, 6.10 and 6.11 in case of multispan continuous IAB and those with respect to pier, PSS and ABS are shown in Figures 6.12, 6.13 and 6.14 in case of full integral bridge.

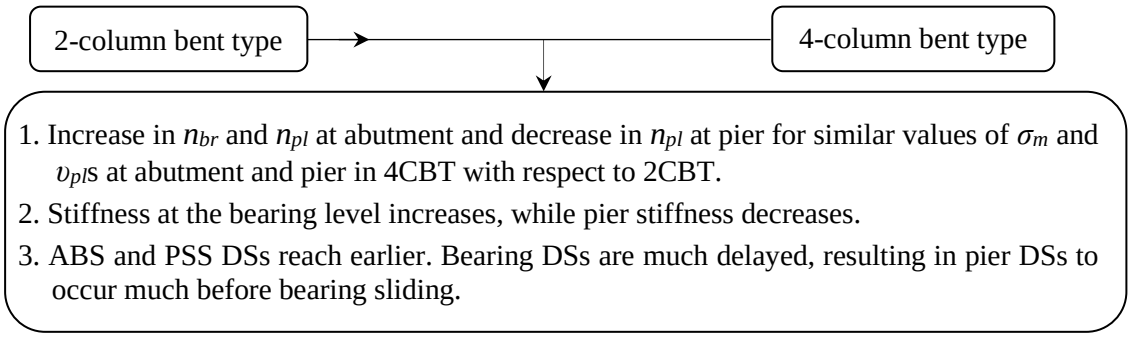

Figure 6.6 Trend in SoA with the change from 2- to 4-column bent types.

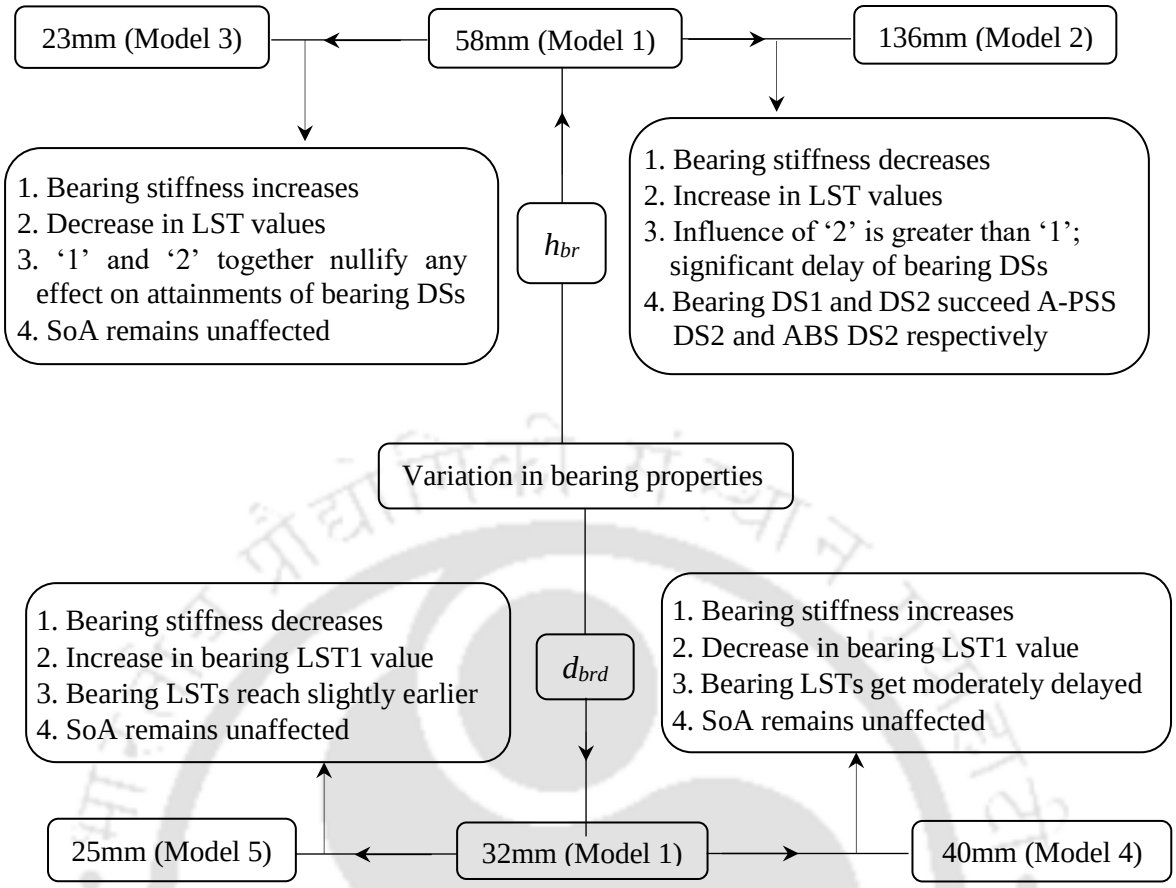

Figure 6.7 Trends of SoAs with bearing parameters in multispan continuous IAB.

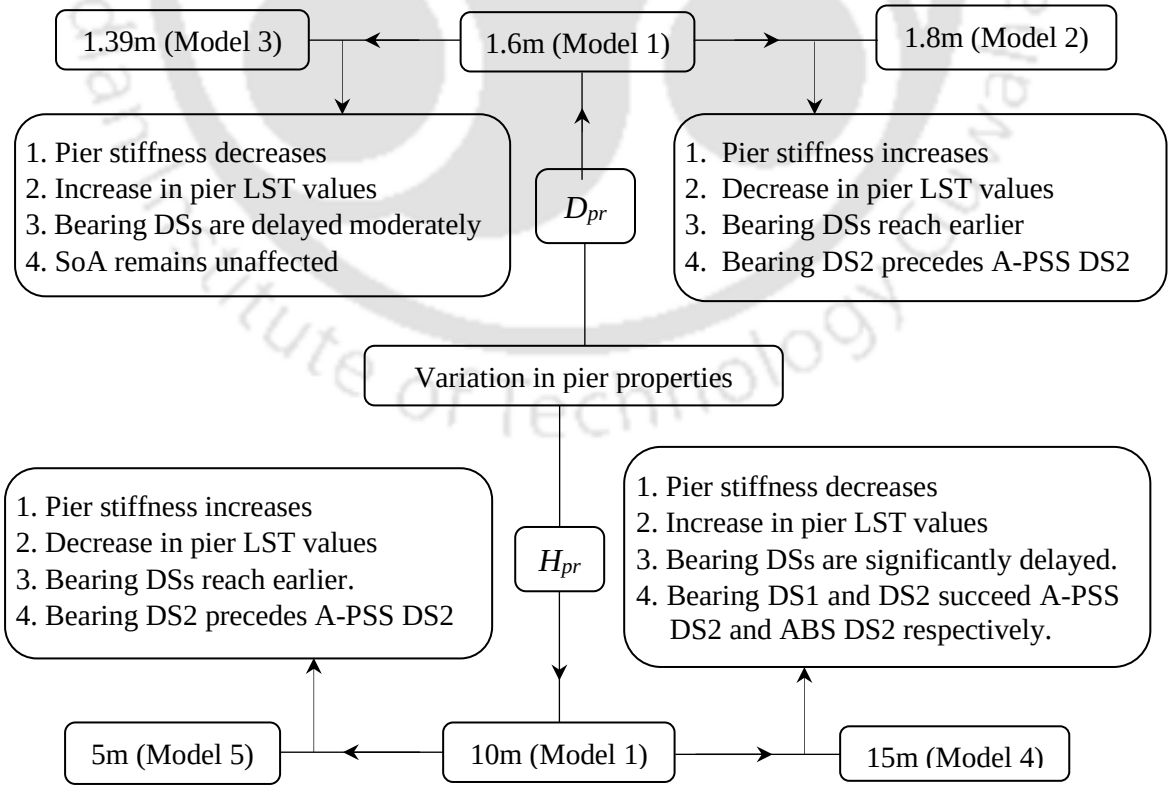

Figure 6.8 Trends of SoAs with pier parameters in multispan continuous IAB.

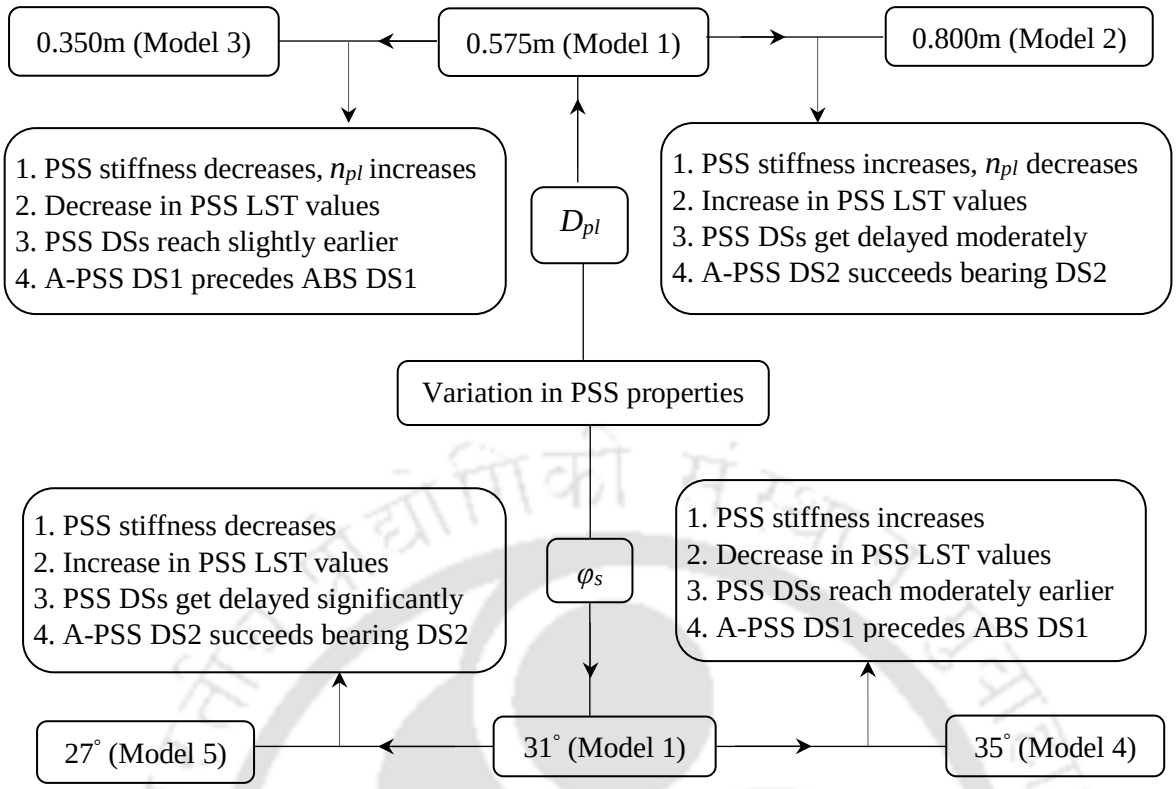

Figure 6.9 Trends of SoAs with variation in PSS parameters in multispan continuous IAB.

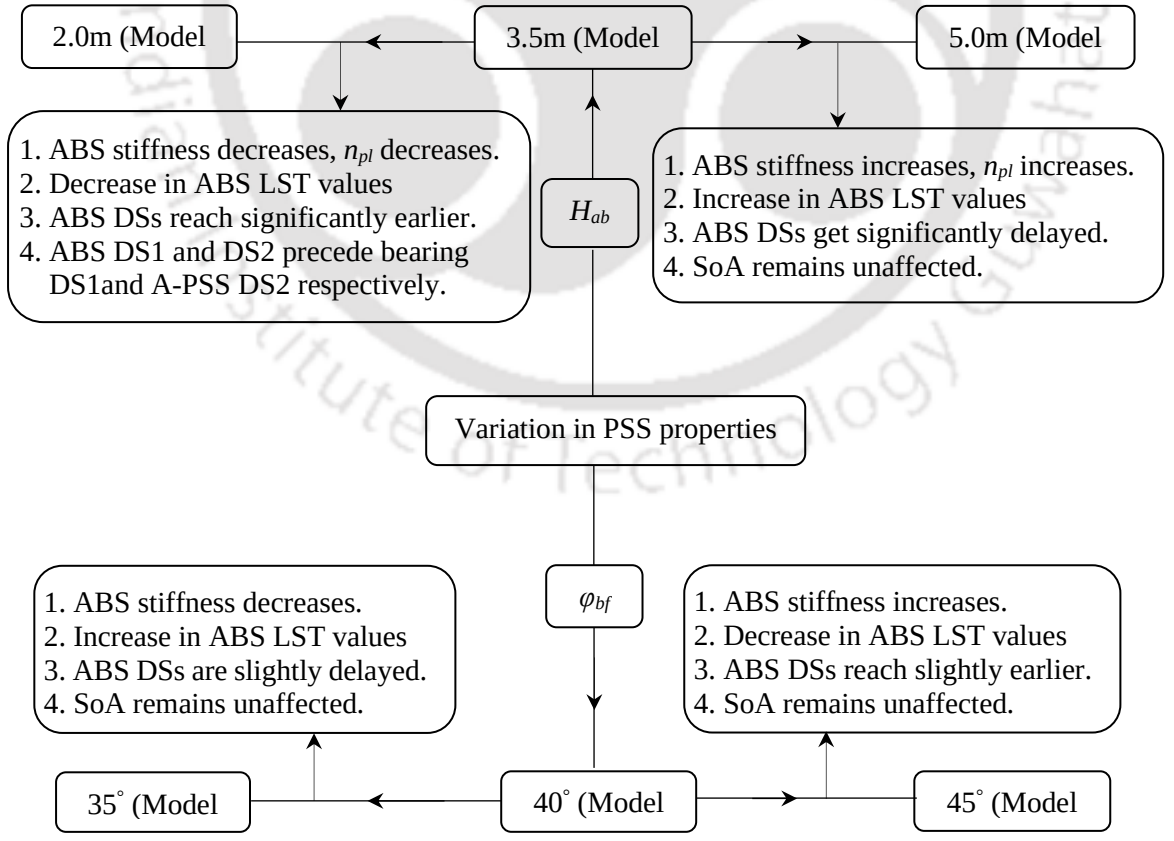

Figure 6.10 Trends of SoAs with ABS parameters in multispan continuous IAB.

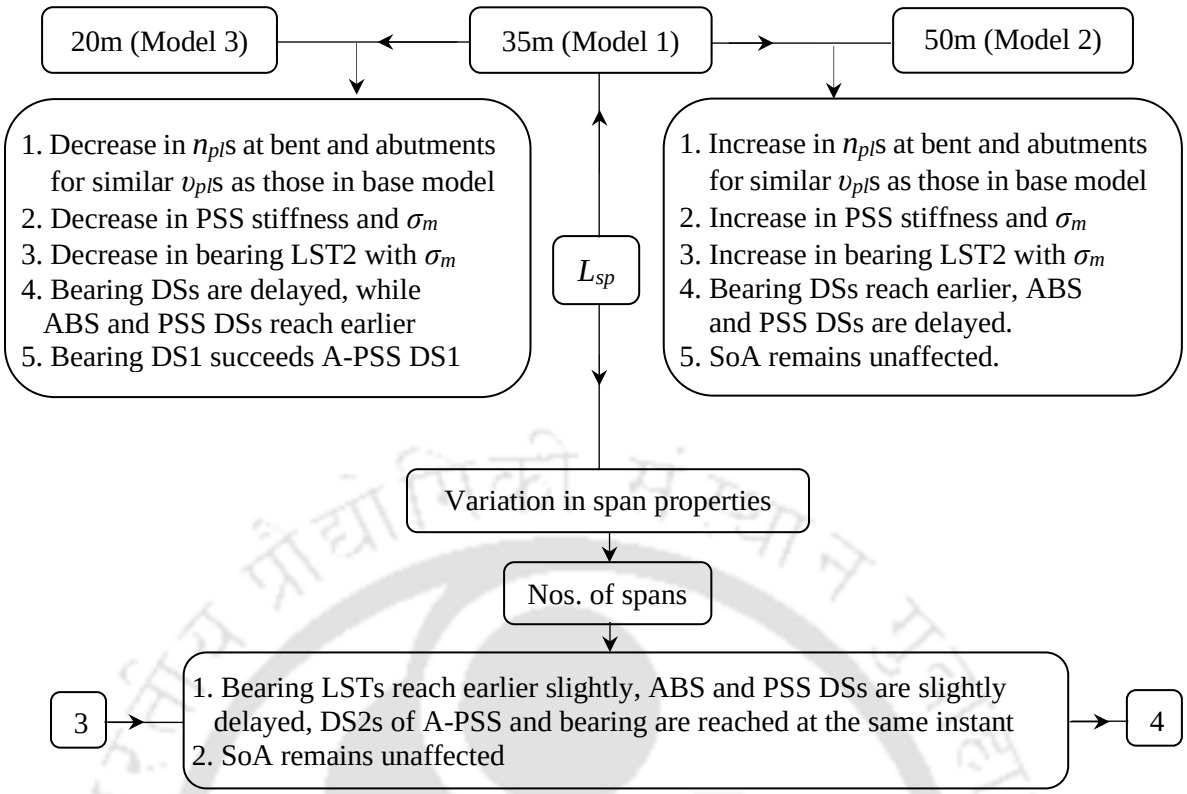

Figure 6.11 Trends of SoAs with span parameters in multispan continuous IAB.

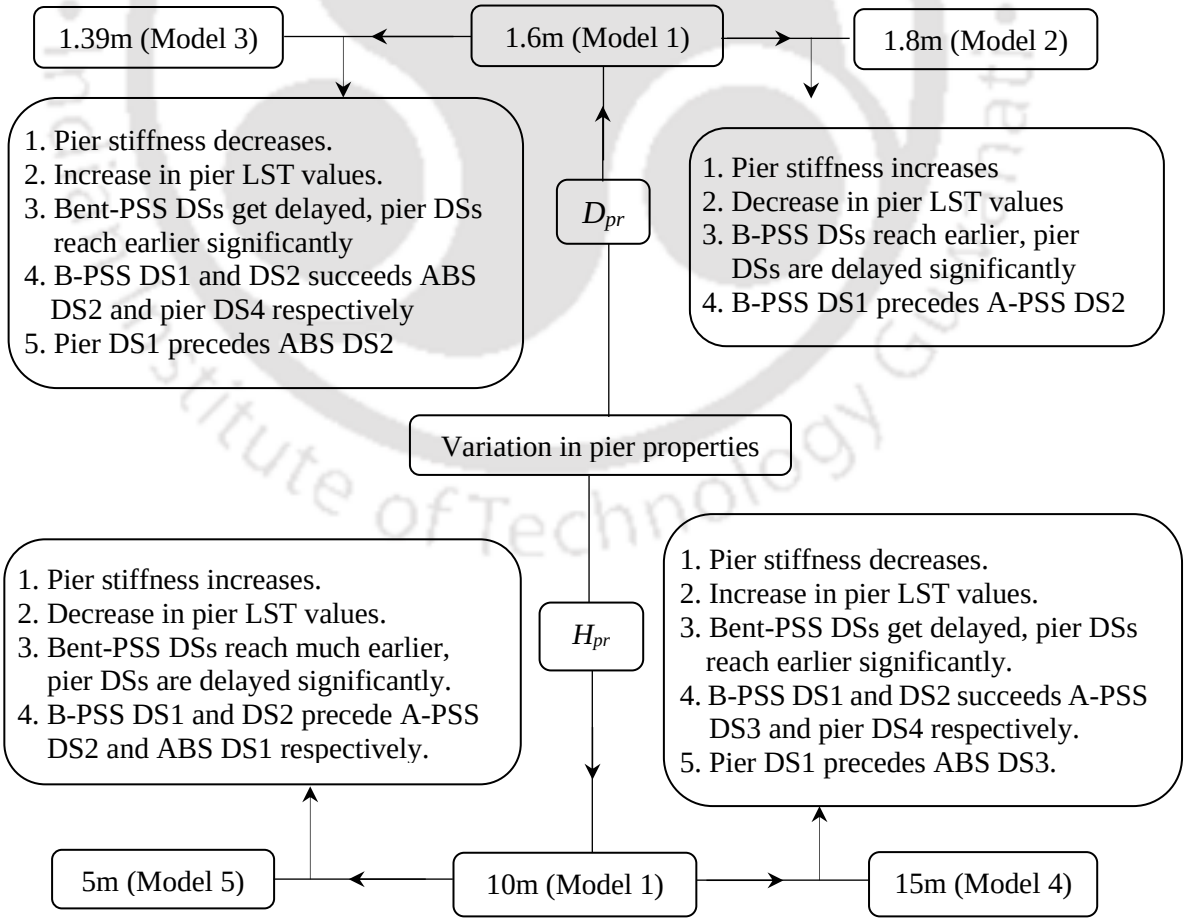

Figure 6.12 Trends of SoAs with pier parameters in full integral bridge.

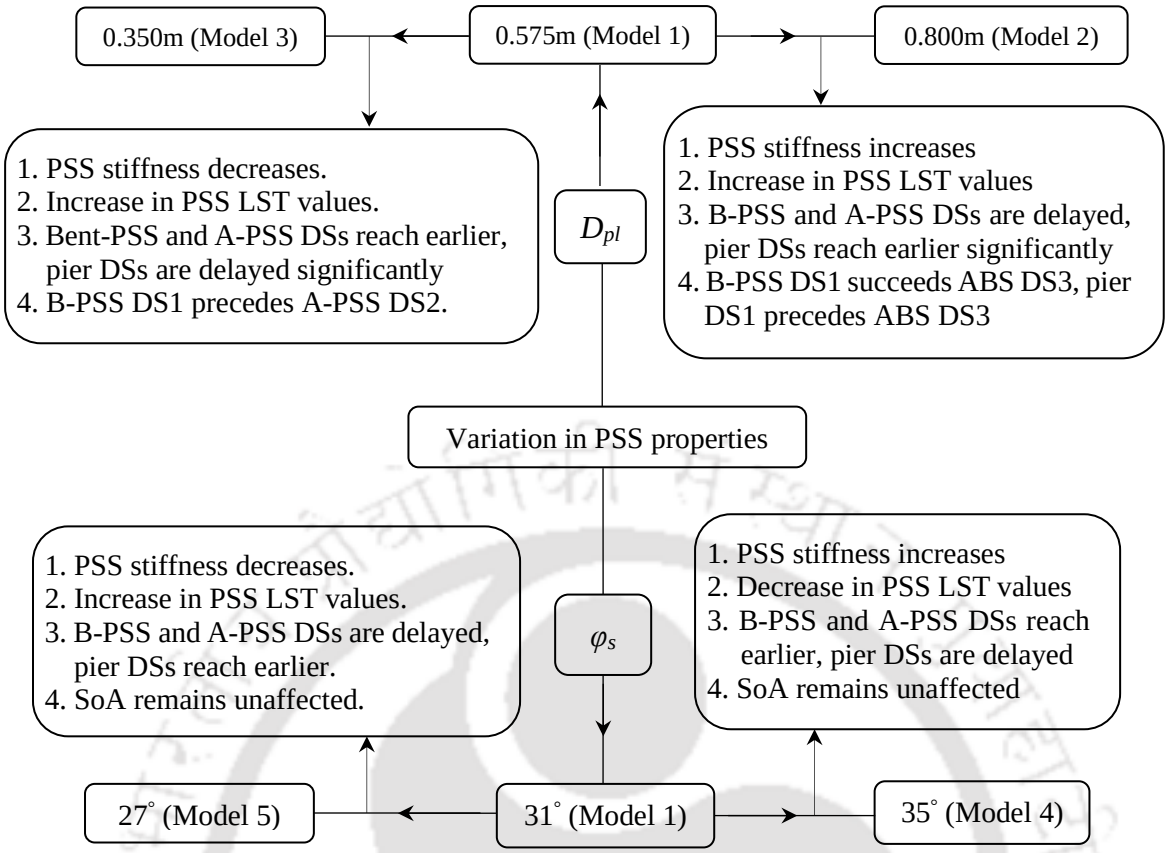

Figure 6.13 Trends of SoAs with PSS parameters in full integral bridge.

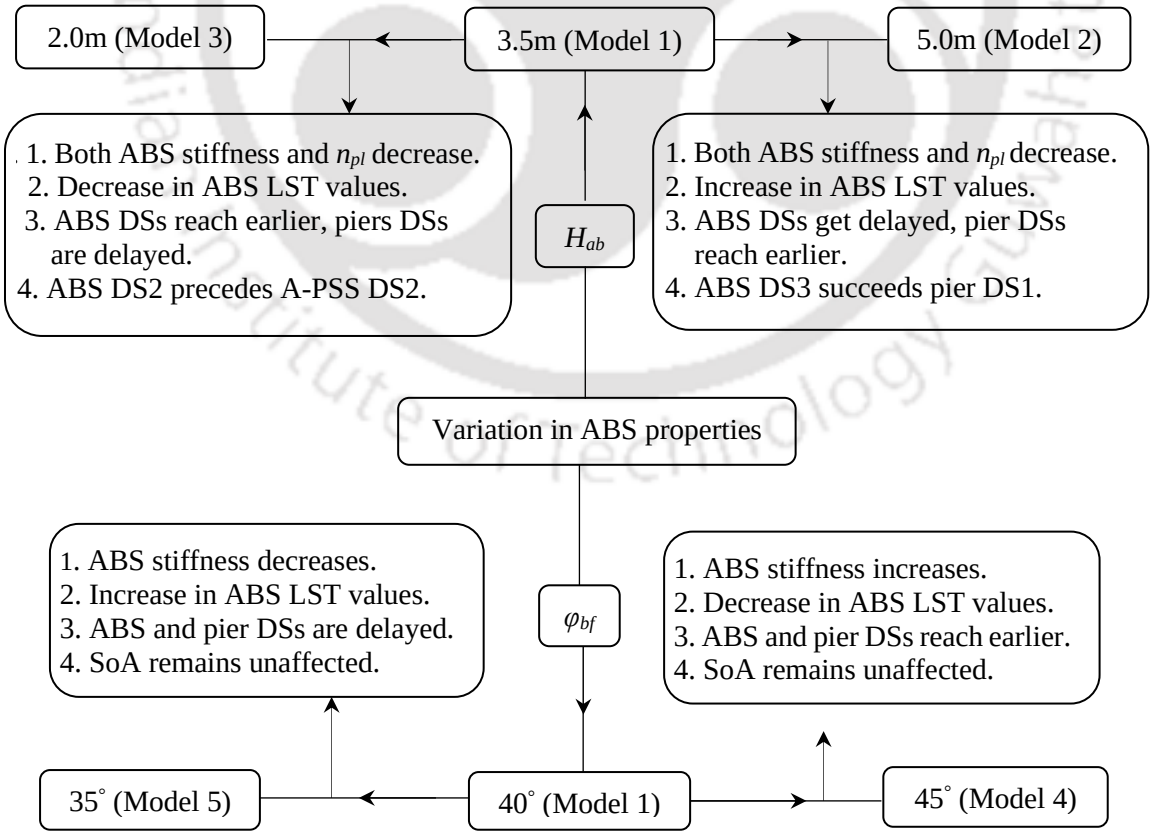

Figure 6.14 Trends of SoAs with ABS parameters in full integral bridge.

With respect to the set of values of the parameters of the components, corresponding to the BS reference model in the study, changes in these values cause shifts in the relative degrees of frailty among the components, as observed in the trends of the SoAs, which can be summarised as follows:

- In case of multispan continuous IAB, increase in h_{br} as well as H_{pr} reduces the relative frailty of bearing, rendering ABS followed by A-PSS to be the most vulnerable component. As H_{pr} decreases, bearing, upto DS2, becomes the most vulnerable of all the components. Decrease in h_{br} has no influence on the instant of attainment of the LSTs nor SoA.
- d_{brd} is influential in only hastening or delaying the bearing DSs with respect to decrease and increase in its value, without influencing the SoA.
- Increase in D_{pl} reduces relative frailty of A-PSS, while the decrease causes A-PSS to be the most vulnerable component, while φ_s has the vice versa effects.
- φ_{bf} is influential in only delaying or hastening the ABS DSs with respect to decrease and increase in its value, without influencing the SoA.
- Decrease in H_{ab} causes ABS to be the most vulnerable component at least upto DS2, while its increase is only influential in delaying ABS DSs.
- Decrease in span length delays the bearing DSs and hastens the ABS and A-PSS DSs, while the increase has the vice versa effects. While, the increase has no effect on the SoA, the decrease reduces the relative frailty of bearing.
- With increase in number of piers, ABS and PSS DSs reach earlier, while bearing DSs are delayed. Relative frailty of bearing reduces while that of pier increases.
- In case of full integral bridge, both the respective increase and decrease in D_{pr} and H_{pr} reduce and increase the respective relative vulnerabilities of pier and B-PSS, with the vice-versa effects otherwise.
- With increase in D_{pl}, B-PSS as well as A-PSS DSs are delayed and pier DSs reach earlier; relative vulnerability of B-PSS reduces, while the decrease has the vice versa effects.
- With increase in φ_s, B-PSS as well as A-PSS DSs reach earlier and pier DSs are delayed, though has no influence on SoA.
- With increase in H_{ab}, relative frailty of ABS decreases, while pier relative vulnerability increases; the decrease has the vice versa effects.
- With increase in φ_{bf}, ABS and pier DSs are delayed, while the decrease has the vice versa effects; SoA is unaffected.

6.4 SUMMARY

This chapter develops some numerical expressions, referred to as Parameterised Limit State Expressions (PLSEs), to be applicable for future use for evaluating the expected values of the Limit State Thresholds (LSTs) of the components with the variations in the influential parameters over wide ranges. Those PLSEs have been validated through the convergence of the numerical plots depicting the trends of the LSTs with the parametric variation with the sensitivity analysis results carried out earlier and through a good agreement of the pile soil system PLSE with a past test result. Thus, avoiding analysis repetition of the damage models every time, these would lead to more realistic performance assessment estimates, rather than using previous case-specific LSTs. With the component LSTs, be readily obtained for any given values of the parameters employing those PLSEs, the chronology of occurrences of the DSs of the constituent components for the IAB configuration in the study is examined. With the promptness of gauging the LSTs with the parametric variations, the trends in the SoAs of the DSs of the components with changing geometrical and soil parameters are subsequently assessed. In case of multispan continuous integral abutment bridge configuration, bearing height, pier height and diameter, abutment height are found to be significantly effecting the SoAs of component DSs, while in case of the case of full integral bridge configuration, the significant parameters are the height and diameter of pier, and abutment height. Sand friction angle is found to have moderate effects for both the configurations. The observations are presented as flowcharts, which can be used as rough guidelines to arrive at the sets of combination of values of the parameters leading to particular SoAs and thus the appropriate selection of the component parameter values at the design stage itself such that the intended functional requirements are met.

Chapter 7
CONCLUSIONS AND FUTURE RESEARCH

CONTENTS

7.1 SUMMARY

Over the last few decades, significant damages have been incurred in bridges due to major earthquakes. These have led to assessment of the seismic vulnerability of bridges becoming a major research area in earthquake engineering and its output within a probabilistic perspective, i.e., Fragility Curves (FCs), effectively helping in seismic disaster mitigation.

The present study derives the component-level and system-level FCs for a class of multispan continuous reinforced concrete Integral Abutment Bridges (IABs). For the adopted attributes, the lateral force deformation capacity characteristics are evaluated from the analytical models (a) generated in OpenSees for pier and Pile-Soil System (PSS) while simulating the pile-soil interaction, (b) developed for bearing in the study, and (c) generated for Abutment-Backfill System (ABS) while adopting a past work on the abutment-backfill interaction. Individual damage models are developed for the components, incorporating different failure modes as well as soil-structure interaction relevantly, to obtain the Limit State Threshold (LST) values, specific to the properties of the components in the study.

To make the present work generic, Bridge System (BS) samples are generated employing Latin Hypercube sampling technique on the adopted ranges of wide variations in the structural and geotechnical parameters. Analyses of the damage models for the numerical models of the samples of the components lead to the data of the respective LSTs.

Component-level demands are assessed, while evolving a few steps beyond the inverse application of the adaptive capacity spectrum method, with respect to peak ground acceleration and the spectral acceleration at 0.7s, adopted as the earthquake Intensity Measures (IMs). The capacity spectra are generated through the displacement based

adaptive pushover algorithm embedded within the numerical models (created using 'structural components' modeling' analogy) of the BS samples in OpenSees. The seismic demand spectra against the nine input Ground Motions (GMs) (selected over wide ranges of frequency contents), at each component DS, are generated using SeismoSignal for the evaluated BS damping at that DS. With the GM IMs, scaled to specified values within 0-1.8g, the demand data and demand-IM relationships are developed. Optimality of the IMs is checked using the efficiency, effectiveness, practicability and sufficiency criteria.

Owing to rough and complete misfits to lognormal form, the component-level FCs are derived through numerical computation using the actual capacity and demand distributions, and lognormal formulation. System-level FCs are derived, computing the correlations among the component demands, generating the joint demand probability distribution surface (using MATLAB) and thereby comparing the joint demand samples with the quartets of mutually independent component-level capacities, assuming system failure with the sequence in series. Extent of variation between two FCs is measured as the percentage difference in fragility relative to IM. Thus, the impact of the IMs and the fragility computation approaches are investigated and comparisons are made among the individual component FCs, and also between the FCs of the BS and the individual components.

Parameterised limit state threshold expressions (validated), numerical expressions for the bearing capacity curves, and the flowchart representations of the trends in the sequences of attainments of different component DSs with respect to the continuous and full integral configurations of IABs are developed in the study, as future applications.

7.2 CONCLUSIONS

The salient conclusions drawn from the present study are as follows:

Numerical modeling

1. Combined variations in the bearing pad and dowel parameters affect the sequence of the events regarding exceedance of pad shear capacity and dowel fracture, which in turn decide on the isolation of the bents from the Bridge System (BS). Thus, by rearranging the order of attainments of bearing and pier Damage States (DSs) (denoted with DS1, DS2, DS3 and DS4 corresponding to the first four DSs), the parametric variations can alone influence the global responses for the adopted Integral Abutment Bridge (IAB).
2. Assumption of linear elastic pile behaviour anticipates Pile-Soil System (PSS) failure only through initiation of Flow Around Failure (FAF) in sand and sufficient progression down soil depth; this may result in unrealistic over-estimation of pile capacity when the

influence of structural nonlinearities in pile are not considered as below:

a) Pile in dense sand is mostly governed by only its structural DSs, while in loose sand, FAF gets initiated and progresses quite before the pile DSs could occur.
b) FAF is initiated earlier while the occurences of pile DSs are delayed, with decrease in pile cross-sectional size D_{pl} and increase in longitudinal reinforcement ratio $\rho_{l,pl}$.
c) Increase in the pile transverse reinforcement ratio $\rho_{t,pl}$ has no influence on pile DS1 and FAF initiation, while the occurrence of the pile ultimate DS gets delayed .
d) Increase in the yield strength of reinforcement $f_{y,pl}$ in pile has no influence on FAF initiation, while the occurrences of pile DSs get delayed.
e) With increase in υ_{pl} and $f_{c,pl}$, FAF as well as the pile DSs are attained earlier.
f) Pile length L_{pl} ('flexible pile' category) is non-influential to pile-soil interaction.

Sensitivity study

1. Both the pile LSTs $d_{1,pl}$ and $d_{2,pl}$ corresponding to the pile DS1 and DS2 are most significantly and negatively influenced by φ_s, followed by the highest and positive influence of $f_{y,pl}$ in case of $d_{1,pl}$ and $\rho_{t,pl}$ in case of $d_{2,pl}$. The LST with respect to FAF is the most and least influenced by D_{pl} and υ_{pl} respectively.
2. Pier height has the highest and positive influence on all its DS LSTs. While, the LSTs corresponding to DS1 and DS4 are not influenced by the transverse $\rho_{t,pr}$ and longitudinal $\rho_{l,pl}$ reinforcement ratios respectively in flexural damage mode, effects are observed while accounting for shear and buckling failures, for low $\rho_{t,pr}$ and high $\rho_{l,pl}$ values.
3. All the ABS (Abutment-Backfill System) LSTs are significantly and positively influenced by the abutment height H_{ab} followed by abutment-backfill interface friction angle δ_{abf}, and negatively and moderately influenced by backfill friction angle φ_{bf} .
4. Bearing LSTs $d_{1,br}$ and $d_{2,br}$ corresponding to DS1 and DS2 are most significantly and positively influenced by the bearing height. $d_{1,br}$ is found to be insensitive to the yield and ultimate strengths of the bar, and $d_{2,br}$ to the bearing pad surface area.

Probabilistic seismic capacity model

1. LST data corresponding to PSS, pier and bearing DSs follow lognormal distributions approximately; exceptions are bearing DS3 and DS4 LSTs which are based on seat width. LST data corresponding to ABS DSs follow uniform distribution approximately.
2. Coefficient of variation increase with DS rank for every component except for bearing.
3. Closeness of LST data to lognormal or uniform fit increases with the DS rank.

Adaptive Capacity Spectra

1. 1-column bent type IAB model gives stiffer response than the 4-column bent type one.
2. Most 1-column bent and 4-column bent types are governed by bearing DSs and pier DSs respectively, with any of the possibilities in between for 2- and 3-column bent types.
3. Shape of the IAB capacity spectrum, which would influence the performance point (i.e., the value of the earthquake Intensity Measure (IM) causing a DS to occur), in turn depends on the sequences of attainments (SoAs) of the DSs of the components. For the cases, where the bearing DSs govern, the spectrum show steepness in its path or even dropdown. For the cases, where pier DSs govern, it follows smooth transitions in path.

Seismic demand distributions

1. Demand data of the components show approximate to very rough fit to lognormal distribution, with those of ABS exhibiting the maximum deviation.
2. Demand distributions of all the components show more refinement toward lognormal shape with respect to S_a (0.7s) (pseudo-spectral acceleration at the time period of 0.7s) compared to Peak Ground Acceleration (PGA).
3. Demand data of all the components show larger dispersions with respect to PGA compared to S_a (0.7s).

Optimality of the adopted IMs

1. S_a (0.7s) is a highly efficient IM for A-PSS (abutment-PSS) and ABS than PGA. S_a (0.7s) is also more efficient for bearing and pier, to moderate to small extent, and moderate to negligible extents respectively.
2. Both the IMs are equally effective IMs for all the components.
3. S_a (0.7s) is a more sufficient IM for A-PSS (abutment-PSS) and ABS than PGA to moderate extents. PGA is a slightly more sufficient IM than S_a (0.7s) for bearing, while PGA is a highly sufficient IM for pier than S_a (0.7s).

Correlations among the component demands

1. Demands of any two components are found to be more correlated with respect to PGA than compared to S_a (0.7s) at all DSs, except for the pier-bearing pair.
2. ABS and A-PSS demand pairs have the highest correlations than those of the other pairs of any two components, with respect to both the IMs and at all DSs; correlation slightly decreases with increase in DS rank.
3. Correlations between pier and bearing demands increase considerably with the increase in DS rank. However, these have zero correlations at higher DSs, due to non-coexistence

of their DSs together in any of the BS samples.

Fragility Curves (FCs) in general

1. Difference between any two FCs varies relative to IM and is the greatest at respective DS1s. The point of the maximum influence shifts to a higher IM value with increase in the DS rank; the shift is more in case of S_a (0.7s) as compared to PGA. These trends are observed irrespective of employed fragility computation approaches and IM types.
2. While computing the actual correlations existing among the demands of the components, the evaluated BS FCs are observed to be more reliable, thus avoiding underestimation or overestimation through the traditional series or parallel system assumption.
3. For the three-span continuous reinforced concrete IAB class, A-PSS as well as ABS are the most vulnerable components. Bearing, pier and bent-PSS follow the degree of vulnerability sequence in the decreasing order.
4. The IAB is more vulnerable as compared to the individual components at respective DSs of same ranks. It shows more or less vulnerabilities for certain ranges of the IMs and vice-versa beyond at higher DS ranks as compared to those of the components.

Impacts of the fragility computation approaches

1. Numerical Computation (NC) gives higher values of fragilities as compared to Lognormal Formulation (LF), for all the IAB components and at most of the IM values and at all DSs. NC approach reveals the actual and rugged FC profile which is not always smooth as provided by LF.
2. Differences between the fragilities obtained using LF and NC are more noticeable in case of PGA than S_a (0.7s); these can be as large as 90% and 20% for A-PSS, and 180% and 50% for ABS with respect to PGA and S_a (0.7s). Similarly, for bearing and pier, these values are 120% and 10%, and 20% and 10% respectively.
3. Influence of the LF and NC approaches is the least for A-PSS. This is because, apart from its capacity distributions, the demand distributions follow lognormal form approximately with respect to both the IMs, while showing more refinement to the form with respect to S_a (0.7s). This can be seen as the validation of the NC approach, while providing similar fragility estimates as the standard LF with respect to S_a (0.7s).
4. Influence of the LF and NC approaches is the highest for ABS, owing to the misfit of its capacity distributions and rough fit of its demand distributions to lognormal form, as compared to the other components, with respect to both the IMs.

5. NC approach results in more realistic and accurate component fragility estimates, as compared to the estimates from LF approach, as it employs the actual profiles of the evaluated capacity and demand distribution data. In fact, in most cases, use of LF underestimates the fragilities for the adopted IAB class.

Impacts of the adopted IM types on the FC evaluation

1. Fragilities estimated with respect to PGA are higher than those obtained with respect to S_a (0.7s) in most cases and at all DSs; differences are very high for both A-PSS and ABS, less for bearing and even negligible for pier. This implies that the adopted IM types have significant effects on the vulnerability assessment of A-PSS and ABS, while the effects are small and negligible respectively on bearing and pier.
2. Differences between the fragilities with respect to PGA and S_a (0.7s) are more noticeable in case of the NC approach than LF; these can be as large as 140% and 220% for A-PSS, and 90% and 250% for ABS with respect to LF and NC. Similarly, for bearing and pier, these values are 30% and 140%, and 10% and 30% respectively.
3. BS fragilities with respect to PGA are more as compared to S_a (0.7s) in most cases; the differences between fragilities with respect to the IMs can be as large as 700% at the very initial IM range, which transitions to a considerable range of 60% to 160%, within the usual expected IM range (0.10g to 0.30g).
4. S_a (0.7s) is found to be an optimal IM as compared to PGA, at least for A-PSS and ABS. Thus, the Fragility Curves (FCs) derived with respect to S_a (0.7s) are expected to be more accurate and reliable than those with respect to PGA. In fact, PGA, as the IM, overestimates the fragilities of the adopted IAB class.

Comparison among the individual fragility curves of the components

1. At respective DS1s of all the components:
   a) Bearing is more vulnerable than A-PSS, as high as 290% and 190%, and upto certain values of PGA and S_a (0.7s) such as 0.14g and 0.32g respectively; thereafter, it is less vulnerable, as low as 60% and 70% with respect to PGA and S_a (0.7s).
   b) Bearing is more vulnerable than ABS, as high as 260% and 180%, and upto certain values of PGA and S_a (0.7s) such as 0.11g and 0.26g respectively; thereafter, it is less vulnerable, as low as 90% and 70% with respect to PGA and S_a (0.7s).
   c) ABS is more vulnerable than A-PSS throughout the ranges of the IMs, to the extents of 90% and 80% with respect to PGA and S_a (0.7s); except that ABS and A-PSS are equally vulnerable beyond a certain value of S_a (0.7s) such as 0.60g.

d) Pier is less vulnerable than A-PSS, ABS and bearing, to the extent of 230%, 310% and 290% with respect to PGA, and 150%, 170% and 190% with respect to S_a (0.7s).

2. At respective DS2s of all the components:
   a) Bearing is more vulnerable than A-PSS, to the extents of 40% and 30%, and upto certain values of PGA and S_a (0.7s) such as 0.08g and 0.34g respectively; thereafter, it is less vulnerable, to the extents of 70% and 50% with respect to PGA and S_a (0.7s).
   b) Bearing is more vulnerable than ABS, to the extents of 40% with respect to both the IMs and upto certain values of PGA and S_a (0.7s) such as 0.14g and 0.41g respectively; thereafter, it is less vulnerable, to the extents of 40% and 30% with respect to PGA and S_a (0.7s).
   c) A-PSS is more vulnerable than ABS throughout the ranges of both the IMs, to the extents of 70% and 20% with respect to PGA and S_a (0.7s).
   d) Pier is less vulnerable than A-PSS, ABS and bearing, to the extent of 180%, 100% and 100% with respect to PGA, and 150%, 170% and 190% with respect to S_a (0.7s).
3. At respective DS3s of all the components:
   a) Bearing is more vulnerable than A-PSS, to the marginal extents of 10% with respect to both the IMs and upto certain values of PGA and S_a (0.7s) such as 0.10g and 0.25g respectively; thereafter, it is less vulnerable, to the extents of 50% and 40% with respect to PGA and S_a (0.7s).
   b) Pier is less vulnerable than ABS throughout the ranges of both the IMs, to the extents of 80% and 60% with respect to PGA and S_a (0.7s), except that pier is initially marginally more vulnerable upto a certain PGA value such as 0.1g.
   c) Pier is less vulnerable than bearing throughout the ranges of both the IMs, to the extents of 30% and 20% with respect to PGA and S_a (0.7s), except that pier is initially marginally more vulnerable upto a PGA value such as 0.08g.
4. At respective DS4s of all the components:
   a) Pier is less vulnerable than bearing throughout the ranges of both the IMs, to the extents of 20% and 10% with respect to PGA and S_a (0.7s), except that pier is initially marginally more vulnerable upto a PGA value such as 0.25g.

Comparison among the BS and the individual curves

1. At respective DS1s, BS is more vulnerable, as high as 880%, 880%, 650% and 880% with respect to PGA, and 460%, 450%, 240% and 460% with respect to S_a (0.7s), compared to A-PSS, ABS, bearing and pier respectively, at the very initial IM range.

2. At respective DS2s, BS is more vulnerable, as high as 150%, 150%, 140% and 220% with respect to PGA, and 100%, 100%, 110% and 190% with respect to S_a (07s), compared to A-PSS, ABS, bearing and pier respectively.
3. At respective DS3s, BS is more vulnerable, as high as 50%, 90% and 120%, with respect to PGA, and 40%, 70% and 90% with respect to S_a (0.7s), compared to ABS, bearing and pier respectively.
4. At respective DS4s, BS is more vulnerable, as high as 30% and 40% with respect to PGA, and 20% and 30% with respect to S_a (0.7s), compared to bearing and pier respectively.
5. Comparative vulnerabilities of the BS at its DS2 and the individual components at respective DS1s:
   a) BS is more vulnerable than A-PSS, to the maximum extent of 140% and upto a certain PGA value such as 0.12g; it is less vulnerable, to the maximum extent of 30% within a certain PGA range such as 0.12g to 0.32g. The BS is marginally less vulnerable, upto a certain value of S_a (0.7s) such as 0.07g; thereafter, it is more vulnerable, to the maximum extent of 55%.
   b) BS is more vulnerable than ABS, to the maximum extent of 99% within a certain PGA range such as 0.03g to 0.07g; it is less vulnerable, to the maximum extent of 99% within a certain PGA range such as 0.07g to 0.28g. The BS is less vulnerable, to the maximum extent of 29% upto a certain value of S_a (0.7s) such as 0.38g; thereafter, it is more vulnerable, to the maximum extent of 12%.
   c) BS is less vulnerable than bearing, to the maximum extent of 270% and upto a certain value of PGA such as 0.15g; thereafter, it is more vulnerable, to the maximum extent of 80%. The BS is less vulnerable, to the maximum extent of 190% upto a certain value of S_a (0.7s) such as 0.27g; thereafter, it is more vulnerable, to the maximum extent of 80%.
   d) BS is more vulnerable than pier throughout the range of both the IMs, to the maximum extents of 200% and 170% with respect of PGA and S_a (0.7s).
6. Comparative vulnerabilities of the BS at its DS3 and the individual components at respective DS1s:
   a) BS is more vulnerable than A-PSS, to the maximum extent of 20% upto a certain value of PGA such as 0.06g; thereafter, it is less vulnerable, to the maximum extent of 170%. The BS is less vulnerable than A-PSS, to the maximum extent of 100%

beyond a certain value of $S_a(0.7\text{s})$ such as 0.16g, whereas, it is more vulnerable, to the maximum extent of 30% within a certain S_a (0.7s) range such as 0.08g to 0.16g.

b) BS is less vulnerable than ABS throughout the range of both the IMs, to the maximum extents of 250% and 120% with respect to PGA and S_a (0.7s).

c) BS is less vulnerable than bearing, to the maximum extent of 270% and upto a certain value of PGA such as 0.40g; thereafter, it is more vulnerable, to the extent of 30%. The BS is less vulnerable, to the maximum extent of 190% and upto a certain value of $S_a(0.7\text{s})$ such as 0.70g; thereafter, it is more vulnerable to the extent of 30% thereafter with respect to $S_a(0.7\text{s})$.

d) BS is more vulnerable than pier throughout the range of both the IMs, to the maximum extents of 90% and 70% with respect to PGA and S_a (0.7s).

7. Comparative vulnerabilities of the BS at its DS4 and the individual components at respective DS1s:

a) BS is less vulnerable than A-PSS throughout the ranges of both the IMs, to the maximum extents of 250% and 160%, with respect to PGA and S_a (0.7s).

b) BS is less vulnerable than ABS throughout the range of both the IMs, to the maximum extents of 310% and 180% with respect to PGA and S_a (0.7s).

c) BS is less vulnerable than bearing, to the maximum extent of 290% and upto a certain value of PGA such as 1.52g; thereafter, it is more vulnerable to the maximum extent of 5% with respect to PGA. BS is less vulnerable than bearing, to the maximum extent of 190% and upto a certain value of S_a (0.7s) such as 1.79g, thereafter, it is equally vulnerable.

d) BS is less vulnerable than pier, to the maximum extent of 70% within a certain range of PGA such as 0.12g to 0.59g; thereafter, it is more vulnerable, to the maximum extent of 20%. with respect to PGA. BS is less vulnerable than pier, to the maximum extent of 9% within a certain range of S_a (0.7s) such 0.25g to 0.87g; it is more vulnerable, to the maximum extent of 19% and beyond a certain value of S_a (0.7s) such as 0.87g.

8. Comparative vulnerabilities of the BS at its DS3 and the individual components at respective DS2s:

a) BS is more vulnerable than A-PSS, to the maximum extent of 30% and upto a certain value of PGA such as 0.07g; it is less vulnerable, to the maximum extent of 96% within a certain range of PGA such as 0.07g to 0.78g. BS is more vulnerable

than A-PSS, to the maximum extent of 33% within a certain range of S_a (0.7s) such as 0.08g to 0.25g; it is less vulnerable, to the maximum extent of 47% within a certain of S_a (0.7s) such as 0.25g to 0.99g.

b) BS is more vulnerable than ABS, to the maximum extent of 40% and upto a certain value of PGA such as 0.08g; it is less vulnerable upto, to the maximum extent of 42% within a certain range of PGA such as 0.08g to 0.28g. BS is more vulnerable than ABS, to the maximum extent of 37% and upto a certain value of S_a (0.7s) such as 0.30g; it is less vulnerable, to the maximum extent of 27% within a certain range of S_a (0.7s) such as 0.30g to 0.79g.

c) BS is less vulnerable than bearing, to the maximum extent of 40% within a certain range of PGA such as 0.06g to 0.26g; thereafter, it is more vulnerable, to the maximum extent of 46%.BS is less vulnerable than bearing, to the maximum extent of 22% within a certain range of S_a (0.7s) such as 0.14g to 0.54g; thereafter, it is more vulnerable, to the extent of 37%.

d) BS is more vulnerable than pier throughout the ranges of both the IMs, to the maximum extents of 110% and 80% with respect to PGA and S_a (0.7s).

9. Comparative vulnerabilities of the BS at its DS4 and the individual components at respective DS2s:

a) BS is less vulnerable than A-PSS throughout the ranges of both the IMs, to the maximum extents of 179% and 100% with respect to PGA and S_a (0.7s).

b) BS is less vulnerable than ABS throughout the ranges of both the IMs, to the maximum extents of 108% and 100% with respect to PGA and S_a (0.7s).

c) BS is less vulnerable than bearing, to the maximum extent of 107% and upto a certain value of PGA such as 1.30g; thereafter, it is more vulnerable upto maximum extent of 11%. BS is less vulnerable than bearing throughout the range of S_a (0.7s), upto the maximum extent of 73%.

d) BS is more vulnerable than pier, to the maximum extent of 32% and upto a certain value of PGA such as 0.28g; it is marginally less vulnerable, to the maximum extent of 1.63% and within a certain range of PGA such as 0.18g to 0.33g. BS is more vulnerable than bearing throughout the S_a (0.7s) range, to the mximum extent of 26%.

10. Comparative vulnerabilities of the BS at its DS4 and the individual components at respective DS3s:

a) BS is more vulnerable than ABS, to the maximum extent of 12% and upto a certain value of PGA such as 0.11g; thereafter, it is less vulnerable than ABS, to the

maximum extent of 70%. BS is more vulnerable than ABS, to the maximum extent of 5% within a certain range of S_a (0.7s) such as 0.12g to 0.21g; thereafter, it is less vulnerable than ABS, to the maximum extent of 44%.

b) BS is less vulnerable than bearing, to the maximum extent of 19% within a certain range of PGA such as 0.12g to 0.58g; thereafter, it is more vulnerable, to the maximum extent of 19%. BS is less vulnerable than bearing, to the maximum extent of 11% within a certain range of S_a (0.7s) such as 0.16g to 0.94g; thereafter, it is more vulnerable than bearing, to the maximum extent of 17%.

c) BS is marginally less vulnerable than pier, to the maximum extent of 1.04% within a certain range of PGA such as 0.18g to 0.22g; thereafter, it is more vulnerable, to the maximum extent of 36% . BS is more vulnerable than pier throughout the range of S_a (0.7s), to the maximum extent of 30%.

Parametric influence on the SoAs of DSs

1. In case of multispan continuous IAB, bearing height, pier height, pile diameter and abutment height are found to be significantly effecting the SoAs of component DSs.
2. In case of full integral bridge, height and diameter of pier, and abutment height significantly affect the SoAs.
3. Sand friction angle is found to have moderate effects for both multispan continuous IAB and full integral bridge.

7.3 RESEARCH IMPACTS

While attempting to obtain reliable fragility estimates, the major contributions of the present study are as follows:

1. ***Pile-soil interaction and pile LSTs*** – The few prescriptions which exist on pile LSTs were specific to the adopted PSS properties and respective pile-soil interaction. Earlier formulations considered only soil unit weight γ_s, φ_s and D_{pl}, and cannot reflect the combined pile-soil nonlinear responses and damages. The present study brings out those influences and evaluates PSS LSTs, in a generalised and simplistic manner as below:

a) Instead of a complex three-dimensional continuum technique, the finite element analysis of soil spring-supported pile in OpenSees has been combined with the spreadsheet-based Strain Wedge Model (SWM) (a theoretical beam on Winkler foundation approach) analysis of the PSS. Convergence between SWM and beam on Winkler foundation parameters is performed through displacement controlled

pushover analysis while iterating with updated modulus of subgrade reaction profile to achieve the accurate pile deflection profile. This technique has been validated through a good agreement with a previous field test result.

b) From the deformed configuration of pile as OpenSees output, the structural damages in pile and the flow around failure in sandy from the spreadsheets can be ascertained. Thus, the respective LST values can be assessed.

c) The validated technique can be implemented to model and analyse PSSs over wide variations in pile parameters like D_{pl}, L_{pl}, $f_{c,pl}$, $f_{y,pl}$, $\rho_{l,pl}$, $\rho_{l,pt}$ and υ_{pl}, various pile head conditions, and soil parameters like γ_s, φ_s and coefficient of the subgrade reaction.

d) The technique, reliably bringing out parametric influences on pile-soil interaction and LSTs, can provide valuable insight to improved PSS design and behaviour in future.

2. ***Damage models*** – The present study develops individual component damage models to yield the LSTs instead of using the past case-specfic prescriptions to avoid error propagation, justified through the dispersed data (instead of a single-valued one) for LST over wide variations in component parameters. The specific contributions are:

a) Damage models built over possible failure modes as well as detailed soil structure interaction can be used to obtain LSTs specific to given component properties. Thus, implementation of LST values specific for the component attributes, as evaluated through the damage models, will provide precise bounds of fragility estimates with respect to those attributes, e.g., fragility estimates specific to the adopted IAB class.

b) In case of ABS damage model, the limit states have been quantified and prescribed as a function of the stress level SL_{bf} generated in the backfill, thus the other abutment-backfill interaction parameters influencing SL_{bf} such as φ_{bf} and δ_{abf}, apart from H_{ab}, are also incorporated. Thus, ABS DSs and the respective LSTs will be more realistically correlated with SL_{bf} compared to earlier prescriptions based on only H_{ab}.

c) Using the damage models, proper and realistic trends in SoAs of DSs of the components with the IAB geometrical and soil parameters can be easily assessed. Those trends can be used at the design stage to arrive at the parameter combinations specific to the required SoAs with respect to the intended functional requirements

d) Parameterised LST expressions have been developed based on regression on LST data evaluated employing the damage models over wide ranges of parametric variations. As generalised LST prescriptions are scanty in literature, these validated prescriptions can be readily used for application in future studies and without analysis repetition.

3. ***Mathematical expressions for evolving the bearing lateral force deformation capacity curve*** **-** Previous studies on elastomeric bearings with dowel bar have commonly considered swedge bolts (one-inch in diameter) as dowel bars and have used the past experimental results or analytical evaluation for obtaining the lateral force deformation capacity curve. The present study has developed closed-form expressions to evaluate the force and lateral displacements at the salient points on the reinforcing (dowel) bar, based on a generalised stress-strain curve. These can be used to obtain the bar lateral force deformation capacity curve and evaluate the bearing LSTs for any set of bar properties.
4. ***Fragility evaluation technique*** **-** The present study has employed a novel method for estimating fragility through the NC approach which employs the probability distribution functions, just as evaluated in the study for the component-level capacity and demand data, and can be used as alternative in case the data do not follow any specific distribution. Thus, it can also avoid the likely misjudgement of fragilities stemming from imposition of lognormal distribution on the data, when these are actually very rough fit as well as misfit, while estimating the lognormal parameters required as inputs in LF.
5. ***Method of assessing the seismic demands and obtaining the Probabilistic Seismic Demand Models (PSDMs)*** − The present study has put forward a different demand assessment method while evolving a few steps beyond the present applicability of the Inverse application of the Adaptive Capacity Spectrum Method (IACSM). IACSM traditionally evaluates the IM causing a particular DS to occur and use it in the LF to evaluate the FC and the dispersion due to the uncertainties of GMs, BS parameters etc., required as input, is based on some recommended values without going into detailed demand analysis. The present study has extended IACSM for extracting the BS pseudo-spectral demand at that DS from the demand spectrum and finally arriving at the component-level demands by utilising the modal contributions of the components to the BS mode shape. Repetition for BS samples generated over wide ranges of parametric variations against a set of GMs over varying characteristics, demand and the associated dispersion are obtained, as in nonlinear time history analysis, but with lesser efforts.
6. ***Improved IM*** **-** Apart from PGA which is traditionally used in many studies, the study employs S_a at the inelastic time period of 0.7 sec (S_a (0.7s)) as defined in the study; 0.7sec being the near average value in the regime of 0.45 to 1.3 secs, from damage initiation till collapse for the BS samples. However, this range can be generalised, as it is obtained from the analyses of the BS samples generated encompassing wide and practical ranges of the BS parameters. S_a (0.7s) is found to be a highly efficient IM than

PGA for A-PSS and ABS. S_a (0.7s) is a more efficient IM for both bearing and pier to the moderate to small, and moderate to marginal extents respectively.

7.4 SCOPE OF FUTURE RESEARCH

In continuation of the present work, the following area can be explored:

- The present work has concentrated on evaluating the FCs corresponding to a class of reinforced concrete multispan continuous IABs. Though the study has incorporated the full integral bridge configuration to study the SoAs of the DSs of the components, seismic fragility estimation has not been carried out. Thus, the future scope lies in evaluating the FCs of the same class of IABs, but with full integral configuration and comparing the respective fragilities at the component- as well as at system-level.
- During the generation of the BS samples in the present study, IAB class has been grouped as 1-, 2-, 3- and 4-column bent type samples. Though, the SoAs of these individual sub-bins of the class have been investigated, the associated fragility evaluation has not been carried out. Thus, while evaluating the FCs while considering larger number of samples, the relative vulnerabilities of the individual sub-bins as well as bridge components within each sub-bin can be investigated more elaborately.
- The present study evaluates the FCs while incorporating wide variations in the BS parameters. Thus, the generated FCs can be expressed in terms of the influential bridge parameters as well as the IM, in the same manner as done while evaluating the parameterised limit state expressions in the present study. Such parameterised FCs can be promptly employed to obtain the FCs of the BSs having different parametric attributes, without going through the entire formulation process each time.
- The present study considers dry sandy soil supporting the pile foundation and liquefaction has not been considered in the soil-structure analysis, evaluation of the PSS LSTs and estimation of fragilities. Thus, while carrying out fragility analyses incorporating the kinematic interactions, comparisons can be drawn with respect to the resulting pile-soil interaction outputs, LSTs and thus the fragility estimates for the case with liquefaction and the case without liquefaction (as in the present study). Lateral ground displacement as well as peak ground velocity can be used as demand parameter and the optimality of this parameter paired with the adopted IMs can be checked.
- The study has evaluated FCs employing IACSM due to 'more practicality while being efficient at par with time history analysis' and thus the computational complexities

of the nonlinear time history analysis are avoided. FCs can also be estimated for the adopted IAB class employing the nonlinear time history analysis and the results can be compared with those obtained using IACSM as in the present study, as a validation to the statement.

7.5 LIMITATIONS OF THE PRESENT WORK

The limitations of the present study are laid out as follows:

- The present work is limited to IABs founded on dry sandy soil sites. Thus, the effect of soil liquefaction on the seismic vulnerability of the IAB has not been studied.
- The present study has not considered stratified soil layers which is usually found in sites. The uniform profile for the sandy soil, as assumed in the study for simplicity, is a rare field condition. Though, the study could well verify the results for the pile founded in such a soil profile with a past test, using the data of the equivalent uniform sandy soil (available from another study) corresponding to the site soil of layered profile of silty sands and clayey silts, usage of the present study outputs might not provide accurate results where the soil profile grossly varies from the uniform one.
- The present work is not applicable to IABs wherein the foundation is based on the prevalent design type of using steel H-piles, pinned-head piles, bearing types other than elastomeric bearings with dowel bars and the full integral configuration (apart from the trends of the sequences of attainments of the damage states of the components as investigated herein)

This page has been left intentionally blank.

REFERENCES

AASHTO (1998). *AASHTO LRFD Bridge Design Specifications*. American Association of State Highway and Transportation Officials, Washington, D.C.

Abbasi, M. and Moustafa, M. A. (2017). "Seismic Fragility Curves for System and Individual Components of Multi-Frame Concrete Box-Girder Bridges." *Transportation Research Board 96th Annual Meeting, 2, Report No. 17-05569,* Washington DC, United States.

Abdel-Mohti, A. and Peckan, G. (2013). "Assessment of seismic performance of skew reinforced concrete box girder bridge." *International Journal of Advanced Structural Engineering,* 5(1), 1-18.

ACI 318-89 (1989). "Building Code Requirements for Reinforced Concrete and Commentary." *American Concrete Institute,* Detroit, 353.

AmiriHormozaki, E., Pekcan, G. and Itani, A. (2014). "Analytical fragility functions for horizontally curved steel I- girder highway bridges." *Earthquake Spectra*.

Antoniou, S. and Pinho, R. (2004a). "Advantages and Limitations of Adaptive and Non-Adaptive of Force-Based Pushover Procedures." *Journal of Earthquake Engineering*, 8(4), 497-522.

Antoniou, S. and Pinho, R. (2004b). "Development and Verification of a Displacement Based Adaptive Pushover Procedure." *Journal of Earthquake Engineering*, 8(5), 643-661.

Appendix C. "Properties of Soils*." https://www.sefindia.org/forum/files/appc_ soilproperties718.pdf,* Data Accessed: February 12, 2016.

API (2000). *Recommended Practice 2A-WSD-Planning, Designing, and Constructing Fixed Offshore Platforms – Worfking Stress Design*. 21st ed. American Petroleum Institute.

Article 11.6.1.3. (2008). "Design Guidelines for Integral Abutments." *apps.itd.idaho.gov/apps/Bridge/manual/11%20Abutments%20Piers%20and%20Walls/ 11.6.1.3%20Integral%20Abutments.pdf*, Data Accessed: August 31, 2017.

ASCE-ACI 426 (1974). "The shear strength of reinforced concrete members—slabs." *Journal of Structural Division, ASCE*, 100(8), 1543-1591.

ASCE (2010). *Minimum Design Loads for Buildings and Other Structures. ASCE/SEI 7-10,* American Society of Civil Engineers, Reston, Virginia.

Ashour, M., Norris, G. and Pilling, P. (1998). "Lateral loading of a pile in layered soil using the strain wedge model." *Journal of Geotechnical and Geoenvironmental Engineering*, 124(4), paper no. 16004, 303-315.

Ashour, M. and Norris, G. (2000a). "Modeling lateral soil-pile response based on soil-pile interaction." *Journal of Geotechnical and Geoenvironmental Engineering*, 126(5), paper no.19113, 420-428.

Ashour, M., Norris, G. and Shamsabadi, A. (2000). "Effect of the non-linear behaviour of pile material on the response of laterally loaded piles." *Proceedings of 4th International conference on Recent Advances in Geotechnical Earthquake Engineering and Soil Dynamics*, San Diego, California, paper no. 6.15.

Ashour, M. and Norris, G. (2000b). "Undrained lateral pile and pile group response in saturated sand." *Report No. CCEER-00-01*, State of California Department of Transportation.

Ashour, M., Norris, G. and Pilling, P. (2002). "Strain wedge model capability of analysing behaviour of laterally loaded isolated piles, drilled shafts, and pile groups." Journal of Bridge Engineering, 7(4), 245-54.

Ashour, M. and Norris, G. (2008). "Pile group program for full material modeling and progressive failure (No. CA02-0076)." California. Dept. of Transportation.

Ashour, M., Pilling, P. and Norris, G. (2004). "Lateral behaviour of pile groups in layered soils." *Journal of Geotechnical and Geoenvironmental Engineering*, 130(6), 580-92.

Ashour, M. and Ardalan, H. (2011). "Piles in fully liquefied soils with lateral spread." Computer and Geotechnics, 38(6), 821-33.

Ashour, M. and Ardalan H. (2012). "Analysis of pile stabilized slopes based on soil–pile interaction." Computer and Geotechnics, 39, 85-97.

Ashour, M and Helal, A. (2013). "Contribution of vertical skin friction to the lateral resistance of large-diameter shafts." *Journal of Bridge Engineering*, 19(2), 289-302.

ATC (1985). "Earthquake Damage Evaluation Data for California." *Report No. ATC-13*, Applied Technology Council, FEMA.

ATC (1991). "Seismic Vulnerability and Impact of Disruption of Lifelines in the Conterminous United States." *Report No. ATC-25*, Applied Technology Council Report, FEMA.

ATC (1996). "Seismic evaluation and retrofit of concrete buildings." *Report No. ATC-40*, Applied Technology Council Report, FEMA.

Avsar, O. (2009). "Fragility Based Seismic Vulnerability Assessment of Ordinary Highway Bridges in Turkey," Ph.D. Thesis, Graduate School of Natural and Applied Sciences of Middle East Technical University.

Aygun, B., Duenas-Osorio, L., Padgett, J. E., and DesRoches, R. (2011). "Efficient Longitudinal Seismic Fragility Assessment of a Multispan Continuous Steel Bridge on Liquefiable Soils." *Journal of Bridge Engineering*, 16, 93-107.

Baker, J. W. and Cornell, C. A. (2006). "Vector-Valued Ground Motion Intensity Measures for Probabilistic Seismic Demand Analysis." *PEER Report 2006/08*. Pacific Earthquake Engineering Research Center College of Engineering University of California, Berkeley.

Baker, J. W. (2010). "Conditional mean spectrum: Tool for ground-motion selection." *Journal of Structural Engineering*, 137(3), 322-331.

Baker, J. W., Lin, T., Shahi, S.K. and Jayaram, N. (2011). "New ground motion selection procedures and selected motions for the PEER transportation research program." *Peer Report 2011, 3*.

Ballard, T. A. and Sedarat, H. (1999). "SR5 Lake Washington Ship Canal Bridge pushover analysis." *Computers and Structures*, 72, 63-80.

Banerjee, S., and Chi, C. (2013). "State-dependent fragility curves of bridges based on vibration measurements." *Probabilistic Engineering Mechanics*, 33, 116–125.

Banerjee, S. and Shinozuka, M. (2008). "Mechanistic quantification of RC bridge damage states under earthquake through fragility analysis." *Probabilistic Engineering Mechanics*, 23(1), 12-22.

Basoz, N. and Kiremidjian, A. S. (1998). "Evaluation of Bridge Damage Data from the Loma Prieta and Northridge, California Earthquakes." *Technical Report MCEER- 98-0004*.

Basoz, N. and Mander, J. B., (1999), *Enhancement of the Highway Transportation Lifeline Module in HAZUS, Final Pre-Publication Draft (#7)*, National Institute of Building Sciences.

Basu, P. C., Shyiamoni, P. and Roshan, A. D. (2004). "Characterization of steel reinforcement for RC structures: An overview and related issues." *Indian Concrete Journal*, 78(1), 19- 30.

Basu, D., Salgado, R. and Prezzi, M. (2008). "Analysis of laterally loaded piles in multilayered soil deposits." *FHWA/IN/JTRP-2007/23 Final Report*, Joint Transportation Research Program.

Bahremand, A. and De Smedt, F. (2008). "Distributed Hydrological Modeling and Sensitivity Analysis in Torysa Watershed, Slovakia." *Water Resources Management*, 22(3), 293–408.

Belarbi, A. and Hsu, T. T. C. (1994) "Constitutive Laws of Concrete in Tension and Reinforcing Bars Stiffened by Concrete." *ACI Structural Journal*, 91(4).

Berry, M. and Eberhard, M. O. (2003). "Performance models for flexural damage in reinforced concrete columns," *PEER Report*, Pacific Earthquake Engineering Research Center, College of Engineering, University of California, Berkeley.

Bhawar, P. D., Wakchaure, M. R. and Nagare, P. N. (2015). "Optimization of Prestressed Concrete Girder". *International Journal of Research in Engineering and Technology*, 4(3).

Bignell, J. L., LaFave, J. M. and Hawkins, N. M. (2005). "Seismic vulnerability assessment of wall piers supported highway bridges using nonlinear pushover analyses." *Engineering Structures*, 27, 2044–2063.

Billah, A. M. and Alam, M. S. (2015). "Seismic fragility assessment of highway bridges: a state-of-the-art review." *Structure and Infrastructure Engineering*, 11:6, 804-832, DOI: 10.1080/15732479.2014.912243.

Billah, A. M., and Alam, M. S. (2016). "Performance-based seismic design of shape memory alloy-reinforced concrete bridge piers. I: Development of performance-based damage states." *Journal of Structural Engineering*, 142(12), 04016140.

Binjhwar, N. (2017). "Study of Suitability of Types of Superstructures Based on their Span Arrangement, *Indian Journal of Scientific Research*, 14 (2), 526-529.

BIS (1986). *Code of practice for design and construction of foundations in soils: General requirements, IS-1904*. Bureau of Indian Standards, New Delhi, India.

BIS (2000). *Plain and Reinforced Concrete-Code of practice, IS-456*. Bureau of Indian Standards, New Delhi, India.

BIS (2009). *Indian standard for concrete mix proportioning, IS-10262*. Bureau of Indian Standards, New Delhi, India.

BIS (2010). *Design and Construction of Pile Foundations –Code of Practice, Part 1 Concrete Piles Section 1 Driven Cast In-Situ Concrete Piles, IS-2911-Part 1/Sec 1*. Bureau of Indian Standards, New Delhi, India.

Bradley, B. A., Cubrinovski, M., Dhakal, R. P. and MacRae, G. A. (2009). "Intensity measures for the seismic response of pile foundations." *Earthquake Engineering and Soil Dynamics*, 29(6), 1046-1058.

Bradley, B. A., Cubrinovski, M., Dhakal, R. P. and MacRae, G. A. (2010). "Probabilistic seismic performance and loss assessment of a bridge–foundation–soil system." *Soil Dynamics and Earthquake Engineering*, 30(5), 395-411.

Brandenberg, S. J., Kashighandi, P., Zhang, J., Huo, Y. and Zhao, M. (2011). "Fragility Functions for Bridges in Liquefaction-Induced Lateral Spreads." *Earthquake Spectra*, 27(3), 683–717.

Burke Jr, M. P. (2009). *Integral and semi-integral bridges*. John Wiley and Sons.

Caltrans (1989). *Bridge design aids 14–1*. California Department of Transportation, Sacramento, CA, USA.

Caltrans (1999). *Caltrans seismic design criteria*. California Department of Transportation, Sacramento, CA, USA.

Calvi, G. M., Priestley, M. J. N. and Kowalsky, M. J. (2013). "Displacement-based seismic design of bridges." *Structural Engineering International*, 23(2), 112-121.

Campbell, K. W. and Bozorgnia, Y. (2008). "NGA ground motion model for the geometric mean horizontal component of PGA, PGV, PGD and 5% damped linear elastic response spectra for periods ranging from 0.01 to 10 s." *Earthquake Spectra*, 24(1), 139-171.

Cardone, D., Perrone, G. and Dolce, M. (2007). "Seismic risk assessment of highway bridges." *1st US–Italy Seismic Bridge Worksho*p, IUSS Press Ltd, Pavia (Italy).

Casarotti, C. and Pinho, R. (2007). "An adaptive capacity spectrum method for assessment of bridges subjected to earthquake action." *Bull Earthquake Engineering*, 5, 377–390.

Chai, Y. H. and Hutchinson, T. C. (2002). Flexural strength and ductility of extended pile-shafts. II: Experimental study. Journal of Structural Engineering 128(5):595-602.

Chang, D. W., Cheng, M. Y. and Chang, T. L. (2008). "Seismic Assessment and Retrofit Strategy of Taiwan Roadway Bridges." *Proc. 14th World Conference on Earthquake Engineering*, Beijing, China.

Chen, W. F. and Duan, L. (2003). Bridge engineering: Construction and maintenance. CRC Press.

Choi, E. (2002). "Seismic Analysis and Retrofit of Mid-America Bridges," PhD thesis, Georgia Institute of Technology.

Choi, E., DesRoches, R., and Nielson, B. (2004). "Seismic fragility of typical bridges in moderate seismic zones." *Engineering Structures*, 26, 187–199.

Choine, M. N., O'Connor, A. J. and Padgett, J. E. (2015). "Comparison between the Seismic Performance of Integral and Jointed Concrete Bridges." *Journal of Earthquake Engineering*, 19, 172-191.

Chopra, A. K. and Goel, R. K. (1999). "Capacity-demand-diagram methods based on inelastic design spectrum." *Earthquake Spectra*, 15(4), 637-656.

Chopra, A. K. and Goel, R. K. (2002). "A modal pushover analysis procedure for estimating seismic demands for buildings." *Earthquake Engineering and Structural Dynamics*, 31, 561–582.

Comisu, C. C. (2005). "Integral Abutment and Jointless Bridges." *The Bulletin of the Polytechnic Institute of Jassy, Construction*, Architecture Section, 51(1-2), 107-118.

Conte, E., Troncone, A. and Vena, M. (2013). Nonlinear three-dimensional analysis of reinforced concrete piles subjected to horizontal loading. Computer and Geotechnics 49:123-33.

Cornell, C. A. and Krawinkler, H. (2000). "Progress and challenges in seismic performance assessment." *PEER Center News*, 3(2).

Cornell, C. A., Jalayer, F., Hamburger, R. O. and Foutch, D. A. (2002). Probabilistic basis for 2000 SAC federal emergency management agency steel moment frame guidelines. *Journal of Structural Engineering*, 128(4), 526-533.

Coulomb, C. (1776). Essai sur une application des regles des maximis et minimis a quelues problemes de statique relatifs a l´c6architecture. Mem Acad Roy des Sci.

Cox, W. R., Reese, L. C. and Grubbs, B. R. (1974). "Field testing of laterally loaded piles in sand." *Proceedings of Offshore Technology Conference*.

Dutta, A. and Mander, J. B. (2001). "Rapid and detailed seismic fragility analysis of highway bridges." *Technical Report MCEER*.

Duncan, J. M. and Chang, C. Y. (1970). "Nonlinear analysis of stress and strain in soils." *J. Soil Mech. and Found. Div.*, 96(5), 1629–1653.

Waugh, J. D. (2009). "Nonlinear analysis of T-shaped concrete walls subjected to multi-directional displacements," A Doctor of Philosophy report, Iowa State University Ames, Iowa.

DRTH (2009). "Width of Bridges on 2-lane National Highways (with and without footpath)." *Report No. RW/NH/33044/2/88-S&R(B)*, Department of Road Transport and Highways to the Ministry of Shipping, Road Transport and Highways. www.arunachalpwd.org/pdf/WIDTH%20OF%20BRIDGES%20ON%202LANE%20NH%20(WITH%20AND%20WITHOUT%20FOOTPATH).pdf. Accessed 02 September 2018.

DesRoches, R., Choi, E., Leon, R. T., Dyke, S. J., and Aschheim, M. (2004). "Seismic Response of Multiple Span Steel Bridges in Central and South eastern United States. I: As Built." *Journal of Bridge Engineering*, 9, 464-472.

DesRoches, R., Leon, R.T. and Dyke, S. (2003). "Response modification of bridges." *Mid-America Earthquake Center CD Release 03-08*.

Dhakal, P. R., Mander, B. J. and Mashiko, N. (2006). "Identification of critical ground motions for seismic performance assessment of structures." *Earthquake Engineering and Structural Dynamics*, 35, 989–1008.

Dicleli, M. and Bruneau, M. (1995a). "Seismic Performance of Multipan Simply Supported Slab-on Girder Steel Highway Bridges." *Journal of Structural Engineering*, 121, 1497-1506.

Dicleli, M. and Bruneau, M. (1995b). "Seismic Performance of Single-Span Simply Supported and Continuous Slab-on-Girder Steel Highway Bridges." *Journal of Structural Engineering*, 121, 1497-1506.

Dicleli, M. and Bruneau, M. (1996). "Quantitative Approach to Rapid Seismic Evaluation of Slab-on-Girder Steel Highway Bridges." *Journal of Structural Engineering*, 122, 1160-1168.

DOT, Minnesota. "Superstructure Guidelines." *http://www.dot.state.mn.us/stateaid/bridge/docs/8.pdf*, Date Accessed: September 22, 2017.

Dukes, J. D. (2013). "Application of Bridge Specific Fragility Analysis In The Seismic Design Process of Bridges In California," Ph.D. Thesis, School of Civil and Environmental Engineering, Georgia Institute of Technology.

Dukes, J., DesRoches, R. and Padgett, J. E. (2012). "Sensitivity study of design parameters used to develop bridge specific fragility curves." *15th World Conf. Earthquake* Engineering (720).

Dutta, A. (1999). "On Energy Based Seismic Analysis And Design of Highway Bridges," PhD thesis, State University of New York at Buffalo.

Dutta, A. and Mander, J. B. (2001). "Rapid and detailed seismic fragility analysis of highway bridges." *Technical Report MCEER*.

EN 1998-2 (2005). *Eurocode 8: Design of structures for earthquake resistance*, *Part 2: Bridges*.

Elassaly, M. (2015) "Effects of Ground Motion Characteristics on Damage of RC Buildings: A Detailed Investigation." *World Academy of Science, Engineering and Technology, International Journal of Civil, Environmental, Structural, Construction and Architectural Engineering*, 9(6), 693-701.

Elnashai, A. S. (2001). "Advanced inelastic static (pushover) analysis for earthquake applications." *Structural engineering and mechanics*, 12(1), 51-70.

Elnashai, A. S., Borzi, B. and Vlachos, S. (2004). "Deformation-based Vulnerability functions for RC bridges." *Structural Engineering and Mechanics*, 17(2), 215-244.

Feng, Y., Kowalsky, M. J. and Nau, J. M. (2014). "Deformation Limit States for Longitudinal Bar Buckling in RC Circular Columns Considering the effect of Seismic Load History." *Proceedings. of the 10th U.S. National Conference on Earthquake Engineering Frontiers of Earthquake Engineering*, Anchorage, Alaska.

FHWA (1995). *Seismic Retrofitting Manual for Highway Bridges*, Vol. FHWA-RD-94-052. Office of Engineering and Highway Operations R&D, Federal Highway Administration, McLean, Virginia.

Firat, F. K. (2016). "Mechanical Properties of Reinforcing Steel in R/C: Uncertainty Analysis and Proposal of a New Material Factor." *Arabian Journal for Science and Engineering*, 41(10), 4019-4028.

Franchetti, P., Grendene, M., Sleiko, D. and Modena, C. (2008). "Seismic damage assessment for six RC bridges in the Veneto region (NE Italy)." *Bollettino di geofisica applicate*, 49(3-4), 513-532.

Frankovich, D. (2000). The basics of vibration isolation using elastomeric materials. *Society of Manufacturing Engineers*.

Freeman, S. A. (1998). "Development and Use of Capacity Spectrum." Proceedings of the *6th US NCEE Conference on Earthquake Engineering/EERI*, Seattle, Washington, Paper 269.

Frosch, R. J., Kreger, M. E. and Talbott, A. M. (2009). "Earthquake resistance of integral abutment bridges." *Report No: FHWA/IN/JTRP-2008/11*, INDOT & Purdue University, Indiana, US.

Fusion of Technology. "Neoprene Bearing Pad. Maruti Techno Rubber Pvt. Ltd." *www.speckw.com/upload/Neoprene_Bearing_Pad_749.pdf*, Data Accessed: April 24, 2017.

GB (2010). *Code for Seismic Design of Buildings. GB 50011-2010*, China Building Industry Press, Beijing, China.

Ger, J. and Cheng, F. Y. (2011). *Seismic Design Aids for Nonlinear Pushover Analysis of Reinforced Concrete and Steel Bridges*. 2, CRC Press.

Ghazali, A., Hasan Al-Haris A., Alih, S. C. and Vafaei, M. (2019). "Seismic fragility of concrete box girder bridges in Malaysia." In *IOP Conference Series: Materials Science and Engineering*, 513(1), 012019. IOP Publishing, 2019.

Ghosh, J., Padgett, J. E. and Dueñas-Osorio, L. (2012). "Comparative Assessment of Different Surrogate Modeling Strategies with Application to Aging Bridge Seismic Fragility Analysis." *In the Proceedings of the 11th ASCE Joint Specialty Conference on Probabilistic Mechanics and Structural Reliability (PMC 2012)*, Notre Dame, Indiana.

Gidaris, I., Padgett, J. E., Barbosa, A. R., Chen, S., Cox, D., Webb, B., and Cerato, A. (2017). "Multiple-hazard fragility and restoration models of highway bridges for regional risk and resilience assessment in the United States: state-of-the-art review." *Journal of Structural Engineering*, 143(3), 04016188.

Giovenale, P., Cornell, A. C., Esteva, L. (2004). "Comparing the adequacy of alternative ground motion intensity measures for the estimation of structural responses." *Earthquake Engineering and Structural Dynamics*, 33, 951–979.

Gupta, B. and Kunnath, S. K. (2000). "Adaptive spectra-based pushover procedure for seismic evaluation of structures." *Earthquake Spectra*, 16(2), 367-392.

Haldar, A. and Mahadevan, S. (2000). *Probability, reliability, and statistical methods in engineering design*. John Wiley.

Hajialilue-Bonab, M., Sojoudi, Y and Puppala, A. J. (2011). "Study of strain wedge parameters for laterally loaded piles." *International Journal of Geomechanics*, 13(2), 143-152.

Hamby, D.M. (1994). "A review of techniques for parameter sensitivity analysis of environmental models. *Environmental monitoring and assessment*." 32(2), 135-154.

HAZUS (1997). *Earthquake loss estimation methodology*. Technical Manual, FEMA.

HAZUS (1999). *Earthquake loss estimation methodology*. Technical Manual, FEMA.

HAZUS (2003). *Earthquake loss estimation methodology*. Technical Manual, FEMA.

Helton, J. C., Davis, F. J. and Johnson, J. D. (2005) "A comparison of uncertainty and sensitivity analysis results obtained with random and Latin hypercube sampling." *Reliability Engineering and System Safety*, 89(3), 305-330.

Hoit, M. I., McVay, M., Hays, C. and Andrade, P. W. (1996). "Nonlinear pile foundation analysis using Florida Pier." *Journal of Bridge Engineering*, 1(4), 135-42.

Hose, Y., Silva, P. and Seible, F. (2000). "Development of a Performance Evaluation Database for Concrete Bridge Components and Systems under Simulated Seismic Loads." *Earthquake Spectra*, 16(2), 413–442.

Hoshikuma, J., Kawashima, K., Nagaya, K. and Taylor, A.W. (1997). "Stress-strain model for confined reinforced concrete in bridge piers." *Journal of Structural Engineering, ASCE*, 624-633.

Huang, A. B., Hsueh, C. K., O'Neill, M. W., Chern, S. and Chen, C. (2001). "Effects of construction on laterallyloaded pile groups." *Journal of Geotechnical and Geoenvironmental Engineering*, 127(5):385-97.

Hwang, H., Liu, J. B. and Chiu, Y. (2001). "Seismic Fragility Analysis of Highway Bridges." *Technical Report*, MAECRR-4 Project.

IRC (1987). *Standard Specifications and Code of Practice for Road Bridges, Section IX Bearing, Part II Elastomeric Bearings. IRC 83-Part II*, Indian Road Congress, New Delhi, India.

IRC (2000a). *Design Criteria for Prestressed Concrete Road Bridges (Post-Tensioned Concrete). IRC 18*, Indian Road Congress, New Delhi, India.

IRC (2000b). *Standard Specifications and Code of Practice for Road Bridges. Section II loads and stresses. IRC 6*, Indian Road Congress, New Delhi, India.

IRC (2011). *Code of Practice for Concrete Road Bridges. IRC-112,* Indian Road Congress, New Delhi, India.

IRC (2014a). *Standard Specifications and Code of Practice for Road Bridges. Section VII Foundations and Substructure. IRC-78*, Indian Road Congress, New Delhi, India.

IRC (2014b). *Guidelines for Design and Construction of Cement Concrete Pavements for Low Volume Road. IRC SP 62*, Indian Road Congress, New Delhi, India.

Irvine, T. (2004). Damping Properties of Materials Revision C

Itani, A. M. and Peckan, G. (2011). "Seismic performance of steel plate girder bridges with integral abutments." *Report No: FHWA-HIF-11-043*, Federal Highway Administration.

Iervolino, I., Maddaloni, G. and Cosenza, E. (2006). "Ground motion duration effects on nonlinear seismic response." *Earthquake Engineering and Structural Dynamics,* 35, 21–38.

Iooss, B. and Lemaitre, P. (2015). "A review on global sensitivity analysis methods." *In Uncertainty management in simulation-optimization of complex systems*, Springer, Boston, MA, 101-122.

Jernigan, J. B. and Hwang, H. (2002). "Development of bridge fragility curves." *7th US National Conference on Earthquake Engineering*.

Jeon, J. S., Shafieezadeh, A., Lee, D. H., Choi, E. and DesRoches, R. (2015). "Damage assessment of older highway bridges subjected to three-dimensional ground motions:

characterization of shear–axial force interaction on seismic fragilities." *Engineering Structures*, 87, 47-57.

Kafali, C. and Grigoriu, M. (2004). "Seismic fragility analysis." *9th ASCE specialty conference on probabilistic mechanics and structural reliability*.

Kampitsis, A. E., Giannakos, S., Gerolymos, N. and Sapountzakis, E. J. (2015). "Soil–pile interaction considering structural yielding: Numerical modeling and experimental validation." *Engineering Structure*, 99, 319–33.

Khandelwal, M. (2015). 'Basic Forces Transfer Mechanism for Design of Structural Precast Connections." https://www.masterbuilder.co.in/data/edata/Articles/January 2015/96.pdf, Data Accessed: April 17, 2018.

Kappos, A., Stylianidis, K. and Pitilakis, K. (1998). "Development of Seismic Risk Scenarios Based on a Hybrid Method of Vulnerability Assessment." *Natural Hazards 17*.

Kappos, A. (2002). Dynamic loading and design of structures. Spon Press, London.

Kappos, A. J., Saiidi, M. S., Aydinoglu, M. N. and Isakovic, T. (2012). Seismic Design Assessment of Bridges, Inelastic Methods of Analysis and Case Studies. Geotechnical, Geological and Earthquake Engineering, Springer.

Karim, K. R. and Yamazaki, F. (2001). "Effect of earthquake ground motions on fragility curves of highway bridges piers based on numerical simulation." *Earthquake Engineering and Structural Dynamics*, 30, 1839–1856.

Katsanos, E. I., Sextos, A.G. and Manolis, G. D. (2010). "Selection of earthquake ground motion records: A state-of-the-art review from a structural engineering perspective." *Soil Dynamics and Earthquake Engineering*, 30(4), 157-169.

Kennedy, R., Cornell, C., Campbell, R., Kaplan, S. and Perla, H. (1980). "Probabilistic Seismic Safety Study of an Existing Nuclear Power Plant." *Nuclear Engineering and Design*, 59, 315-338.

Kibboua, A, Bechtoula, H, Mehani, Y, Naili, M. (2014). "Vulnerability assessment of reinforced concrete bridge structures in Algiers using scenario earthquakes." Bull *Earthquake Engineering*, 12, 807–827.

Kim, S. H. and Feng, M. Q. (2003). "Fragility analysis of bridges under ground motion with spatial variation." *International Journal of Non-Linear Mechanics*, 38, 705 – 721.

Kowalsky, M. J. (2000). "Deformation Limit States for Circular Reinforced Concrete Bridge Columns." *ASCE Journal of Structural Engineering*, 126(8), 869-878.

Krawinkler, H. and Seviratna, G. D. P. K. (1998). "Pros and cons of a pushover analysis for seismic performance evaluation." *Engineering Structures*, 20(4-6), 452-464.

Kumar, C. P. and Babu, S. V. V. K. (2016). "Analysis and Design of Prestressed Box Girder Bridge by IRC: 112-2011." *International Journal of Constructive Research in Civil Engineering (IJCRCE)*, 2(2), 1-10.

Kunnath, S. K., Larson, L. and Miranda, E. (2006). "Modelling considerations in probabilistic performance- based seismic evaluation: case study of the I-880 viaduct." *Earthquake Engineering and Structural Dynamics*, 35, 57–75.

Kwon, O. S. and Elnashai, A. S (2006). "The effect of material and ground motion uncertainty on the seismic vulnerability curves of RC structure." *Engineering Structures*, 28, 289–303.

Kwon, O. S. and Elnashai, A. S. (2010). "Fragility analysis of a highway over-crossing bridge with consideration of soil–structure interactions." *Structure and Infrastructure Engineering*, 6(1-2), 159–178.

Laboratory 8. "Relative Density and Load Carrying Capacity of Sands." *eng.mu.edu/ newmand/CEEN%203160%20Lab8%20RelativeDesnity.pdf*, Data Accessed: August 24, 2017.

Langroudi, B., Salehi, E., Keshani, S. and Baghersad, M. (2011). "Evaluation of Seismic Damage for Gisha Bridge in Tehran by HAZUS Methodology." *World Academy of Science,Engineering and Technology, International Journal of Civil, Environmental, Structural,Construction and Architectural Engineering*, 5(5), 255-259.

Ledezma, C. (2007). "Performance-based earthquake engineering design evaluation procedure for bridge foundations undergoing liquefaction induced lateral spreading," Ph.D. dissertation, University of California, Berkeley.

Lee, S. M., Kim, T. J. and Kang, S. L. (2007). 'Development of fragility curves for bridges in Korea." KSCE Journal of Civil Engineering, 11(3), 165-174.

Lehmann, E. L. and D'Abrera, H. J. M. (1998). Nonparametrics: Statistical methods based on ranks. Prentice Hall, Upper Saddle River, New Jersey, 463.

Lemnitzer, A., Khalili-Tehrani, P., Ahlberg, E. R., Rha, C., Taciroglu, E., Wallace, J. W. and Stewart, J. P. (2010). "Nonlinear efficiency of bored pile group under lateral loading." *Journal of Geotechnical and Geoenvironmental Engineering*, 136(12), 1673-85.

Liao, W. I. and Loh, C. H. (2004). "Preliminary Study on the Fragility Curves for Highway Bridges in Taiwan." *Journal of the Chinese Institute of Engineers*, 27(3), 367-375.

Limkatanyua, S., Kuntiyawichai, K. and Spaconec, E. (2009). "Response of reinforced concrete piles including soil pile interaction effects." *Engineering Structure*, 31,1976-86.

Mackie, K. and Stojadinovic, B. (2003). "Seismic Demands for Performance-based Design of Bridges." *PEER Report No.16*, Pacific Earthquake Engineering Research Center, University of California, Berkeley, CA.

Mackie, K. and Stojadinovic, B. (2004a). "Fragility Curves for Reinforced Concrete Highway Overpass Bridges." Proc. *13th World Conference on Earthquake Engineering*, Vancouver, B.C., Paper No. 1553, Vancouver, Canada.

Mackie, K. and Stojadinovic, B. (2004b). "Improving Probabilistic Seismic Demand Models through Refined Intensity Measures." *Proc. 13th World Conference on Earthquake Engineering*, Paper No. 1556, Vancouver, Canada.

Mackie, K. and Stojadinovic, B. (2005). "Fragility basis for California highway overpass bridge seismic decision making." Pacific Earthquake Engineering Research Center, College of Engineering, University of California, Berkeley.

Mackie, K. and Stojadinovic, B. (2007). "Performance-Based Seismic Bridge Design for Damage and Loss Limit States." *Earthquake Engineering and Structural Dynamics*, 36(13), 1953–1971.

Mahmoudi, S. N. (2015). “Seismic Fragility Assessment of Highway Bridge,” PhD dissertation, McGill University, Montreal, Quebec, Canada.

Malhotra, P. K. (2003). “Strong-motion records for site-specific analysis.” *Earthquake Spectra*, 19(3), 557-578.

Mander, J. B., Priestley, M. J. and Park, R. (1988). “Theoretical stress-strain model for confined concrete.” *Journal of structural engineering*, 114(8), 1804-1826.

Mander, J. B., Kim, D. K., Chen, S. S. and Premus, G. J. (1996). “Response of Steel Bridge Bearings to the Reversed Cyclic Loading”, *Technical Report NCEER 96-0014*, Buffalo, NY.

Mander, J. B. (1999). “Fragility curve development for assessing the seismic vulnerability of highway bridges.” *Research Progress*, 89.

Maroney, B. H. and Chai, Y. H. (1994). “Bridge abutment stiffness and strength under earthquake loadings.” *In Memorias, Second International Workshop on Seismic Design and Retrofitting of Reinforced Concrete Bridges*, University of Canterbury, Queenstown, New Zealand.

Martin, G. R. and Yan, L. (1995). “Modeling Passive Earth Pressure for Bridge Abutments.” *Earthquake-Induced Movements and Seismic Remediation of Existing Foundations and Abutments, ASCE 1995 Annual National Convention*, Vol. Geotechnical Special Publication 55, San Diego, CA. ASCE.

Masahiro, S., Kohno, T. and Nakatani, S. (2009). “Geotechnical criteria for serviceability limit state of horizontally loaded deep foundations.” *Proceedings of 2nd International Symposium on Geotechnical Risk and Safety*, 119-126.

MATLAB 8.6 (2015): MATLAB: Language of Technical Computing. MathWorks, New York, NY, R2015b edition.

Matlock, H. (1970). “Correlations for design of laterally loaded piles in soft clay.” *2nd annual offshore technology conference*, Houston, Texas, 1, 577–594.

McKenna, F. and Feneves, G. L. (2005). “Open System for Earthquake Engineering Simulation.” *Pacific Earthquake Engineering Research Center*, Version 1.6.2.

Mehanny, S. S. F., Ramadan, O. M. O. and Howary, H. A. E. (2014) “Assessment of bridge vulnerability due to seismic excitations considering wave passage effects.” *Engineering Structures*, 70, 197-207.

Meng, J. Y and Lui, E. M. (2000). “Seismic analysis and assessment of a skew highway bridge.” *Engineering Structures*, 22, 1433–1452.

Meyer B. J. and Reese L. C. (1979). “Analysis Of Single Pile Under Lateral Loading.” *Research Report 244-1*, Center for Highway Research, The University of Texas at Austin

Mirza, S. A. and MacGregor, J. G. (1979). “Variability of mechanical properties of reinforcing bars.” *Journal of Structural Division*, ASCE, 105(ST5), 921-937.

Mohtashami, E. and Shooshtari, A. (2013). “A Multimode Adaptive Pushover Procedure for Seismic Assessment of Integral Bridges”, Hindawi Publishing Corporation Advances in Civil Engineering, Article ID 941905.

Moschonas, I. F., Kappos, A. J., Panetsos, P., Papadopoulos, V., Makarios, T. and Thanopoulos, P. (2009). "Seismic fragility curves for Greek bridges: methodology and case studies." *Bull Earthquake Engineering*, 7, 439–468.

Mountford, G.L., Atkinson, P.M., Dash, J., Lankester, T. and Hubbard, S. (2017). Sensitivity of Vegetation Phenological Parameters: "From Satellite Sensors to Spatial Resolution and Temporal Compositing Period." In *Sensitivity Analysis in Earth Observation Modelling, Elsevier*, 5-90.

Mouida, A. and Alaa, N. (2011). "Sensitivity analysis of TSEB model by one-factor-at-a-time in irrigated olive orchard." *International Journal of Computer Science Issues (IJCSI)*, 8(3), 369.

Mounnarath, P., Schmitz, U. and Zhang, Ch. (2016). "Seismic fragility assessment of continuous integral bridge frames with variable expansion joint clearances." *World Academy of Science, Engineering and Technology, International Journal of Civil, Environmental, Structural, Construction and Architectural Engineering*, 10(2).

Naik, V. T. and Yashavantha (2016). "Comparative Study of Precast RCC I-Girder Configuration for Various Span Arrangements in A Bridge Super Structure". *International Research Journal of Engineering and Technology (IRJET)*, 3(8).

Nateghi, F. and Shahsavar, V. L. (2004). "Development of fragility and reliability curves for seismic evaluation of a major prestressed concrete bridge." *Proceedings of 13th World Conference on Earthquake Engineering*, Vancouver.

Newmark, N. M. and Hall, W. J. (1982) "Earthquake spectra and design." *Earthquake Research Institute*, Oakland, California.

NZS 1170.5 (2004). *Structural Design Actions Part 5 – Earthquake Actions (New Zealand)*. Committee draft DR PPCD 8, Standards New Zealand, Wellington.

Ni Choine, M., O'Connor, A. J. and Padgett, J. E. (2015). "Comparison between the seismic performance of integral and jointed concrete bridges." *Journal of Earthquake Engineering*, 19(1), 172-191.

Nicknam, A., Mosleh, A. and Jamnani, H. H. (2011). "Seismic Performance Evaluation of Urban Bridge using Static Nonlinear Procedure, Case Study: Hafez Bridge." *Procedia Engineering*, 14, 2350–2357.

Nielson, B. G. (2005). "Analytical Fragility Curves for Highway Bridges in Moderate Seismic Zones," Ph.D. Thesis, School of Civil and Environmental Engineering, Georgia Institute of Technology.

Nielson, B. G. and DesRoches, R. (2007). "Seismic fragility methodology for highway bridges using component level approach." *Earthquake Engineering and Structural Dynamics*, 36(6), 823-839.

Norris, G. M. (1986). "Theoretically based BEF laterally loaded pile analysis." *3rd International Conference on Numerical Methods in Offshore Piling*, Editions Technip, Paris, France, 361-386.

Nowak, A., S., and Collins, K., R. (2012). *Reliability of structures*. CRC Press.

Padgett, J. and DesRoches, R. (2007). "Sensitivity of seismic response and fragility to parameter uncertainty." *Journal of Structural Engineering*, 133(12), 1710–1718.

Padgett, J. E., Nielson, B. G. and DesRoches, R., (2008). "Selection of optimal intensity measures in probabilistic seismic demand models of highway bridge portfolios." *Earthquake Engineering and Structural Dynamics*, 37, 711–725.

Padgett, J. E., Ghosh, J. and Duenas-Osorio, L. (2013). "Effects of liquefiable soil and bridge modeling parameters on the seismic reliability of critical structural components." *Structure and Infrastructure Engineering*, 9(1), 59-77.

Pahlavan, H., Zakeri, B., Amiri, G. G. and Shaianfar, M. (2016). "Probabilistic vulnerability assessment of horizontally curved multiframe RC box-girder highway bridges." *Journal of Performance of Constructed Facilities*, 30(3), 04015038.

Paraschos, A. (2016) "Effects of Wingwall Configurations on the Behaviour of Integral Abutment Bridges," Ph.D. thesis, Civil Engineering Dept., University of Maryland, College Park, Maryland.

Parool, N. and Rai, D. C. (2015). "Seismic fragility of multispan simply supported bridge with drop spans and steel bearings." *Journal of Bridge Engineering*, 20(12), 04015021-11.

Pan, Y., Agrawal, A. K. and Ghosn, M. (2007). "Seismic Fragility of Continuous Steel Highway Bridges in New York State." *Journal of Bridge Engineering*, 12, 689-699.

Pan, Y., Agarwal, A. K., Ghosn, M. and Alampalli, S. (2010a). "Seismic Fragility of Multispan Simply Supported Steel Highway Bridges in New York State. I: Bridge Modeling, Parametric Analysis, and Retrofit Design." *Journal of Bridge Engineering*, 15, 448-461.

Pan, Y., Agarwal, A. K., Ghosn, M. and Alampalli, S. (2010). "Seismic Fragility of Multispan Supported Steel Highway Bridges in New York State. II: Fragility Analysis, Fragility Curves, and Fragility Surfaces." *Journal of Bridge Engineering*, 15, 462-472.

Panagiotakos, T. B., and Fardis, M. N. (2001). "Deformations of reinforced concrete members at yielding and ultimate." *Structural Journal*, 98(2), 135-148.

Palacios, S. M. (2004). "State of the art in seismic vulnerability." *Institutional repository of Alicante University*. [Online]. *Available: http://hdl. handle. net/10045/2626*.

Pathmanathan, P., Cordeiro, J. M. and Gray, R. A. (2019). "Comprehensive uncertainty quantification and sensitivity analysis for cardiac action potential models." *Frontiers in physiology*, 10.

Pavel, F. and Lungu, D. (2012). "Frequency content indicators of strong ground motions." *In Proceedings of the 15th World Conference on Earthquake Engineering*.

Pawirodikromo, W. (2017). "Simple Damage Potential of Earthquake with Low Frequency Content Based on Global Reinforced Concrete (RC) Inelastic Response." *Procedia engineering*, 171, 1060-1068.

Peera, D. G., Kumar, M. K. and Kumar, K. P. (2014). "A Study on Design of Prestressed Post-Tensioned Girder by Morice-Little Method." *International Journal of Innovative Research in Advanced Engineering (IJIRAE)*, 5(2), 160-168.

Pile Foundation Design as per IS 2911-2010. https://www.sefindia.org/forum/download.php?id=10975. Accessed February 20, 2019.

Pilling, P., Ashour, M. and Norris, G. (2001). "Strain wedge model hybrid analysis of laterally loaded pile group." Journal of Transportation Research Board,1772, 115-121.

Pinho, R., Antoniou, S., Casarotti, C. and Lopez, M. (2005). "A Displacement-Based Adaptive Pushover for Assessment of Buildings and Bridges", *NATO International Workshop on Advances in Earthquake Engineering for Urban Risk Reduction*, Istanbul, Turkey.

Popovics, S. (1973). "A Numerical Approach to the Complete Stress-Strain Curve of Concrete." *Cement and Concrete Research*, 3(4), 583-599.

Pottatheere, P. and Renault, P. (2008). "Seismic Vulnerability Assessment of Skew Bridges." *Proceedings of the 14th World Conference on Earthquake Engineering*, Beijing, China.

Poulos, H. G. (1971). "Behaviour of laterally loaded piles: I–single piles." *Journal of Soil Mechanics and Foundation Division*, 97, 711-731.

Pradeep, P. (2013). "Seismic Vulnerability Assessment of Building Stock," Master of Technology Report, Indian Institute of Technology, Madras.

Priestley, M. N., Verma, R. and Xiao, Y. (1994). Seismic shear strength of reinforced concrete columns. *Journal of Structural Engineering*, 120(8), 2310-29.

Priestley, M. J. N., Seible, F. and Calvi, G. M. (1996). *Seismic Design and Retrofit of Bridges*. John Wiley and Sons, New York.

Ramanathan, K. N., DesRoches, R. and Padgett, J. E. (2010). "Analytical fragility curves for multispan continuous steel girder bridges in moderate seismic zones." *Transportation Research Record*, 2202(1), 173-182.

Ramanathan, K. N., Padgett, J. E. and DesRoches, R. (2011). "Fragility Curves for Typical Multispan Simply Supported Bridge Classes in Moderate Seismic Zones: Pre - and Post - Seismic Design Considerations." *3rd ECCOMAS Thematic Conference on Computational Methods in Structural Dynamics and Earthquake Engineering*, Greece.

Ramanathan, K. N., DesRoches, R. and Padgett, J. E. (2012). "A comparison of pre- and post-seismic design considerations in moderate seismic zones through the fragility assessment of multispan bridge classes." *Engineering Structures*, 45, 559–573.

Ramanathan, K. N. (2012). "Next generation seismic fragility curves for California bridges incorporating the evolution in seismic design philosophy," Ph.D. Thesis, Georgia Institute of Technology.

Rankine, W. J. M. (1857). Earth pressure theory. *Phil. Trans. of the Royal Soc*.

Reese, L. C., Cox, W. R. and Koop, F. D. (1974) "Analysis of laterally loaded piles in sand." *6th offshore technology conference*, Houston, TX, Paper No. 2080, 473–483.

Reese, L. C. and Van Impe, W. F. (2010). "Single piles and pile groups under lateral loading", CRC Press.

Rossetto, T. and Elnashai, A. (2003). "Derivation of vulnerability functions for European-type RC structures based on observational data." *Engineering Structures*, 25, 1241–1263.

RDSO (2013). *Code of Practice for the Design of Sub-Structures and Foundations of Bridges*. Bridge Substructures and Foundation Code. Indian Railway Standard, Government of India, Ministry of Railways.

Skempton, A. W. and MacDonald, D. H. (1956). "The allowable settlements of buildings." *Proceedings of the Institution of Civil Engineers*, 5(6), 727-768.

Saadeghvaziri, M. A. and Yazdani-Motlagh, A. R. (2007). "Seismic behaviour and capacity/demand analyses of three multi-span simply supported bridges." *Engineering Structures*, 30, 54–66.

Sahs, S., Veletzos, M., Panagiutou, M. and Restrepo, J. (2008). "Visual Inspection and Capacity Assessment of Earthquake Damaged Reinforced Concrete Bridge Elements." *Integrate Research and Deployment Final Report*, California Department of Transportation, Sacramento, CA.

Saltelli, A., Chan, K. and Scott, M. (2008). *Sensitivity Analysis*. New York, John Wiley and Sons, New York.

Sangadji, S., Wibowo, N. A., Tropormera, E. N., Purwanto, E. and Kristiawan, S. A. (2017). "Fragility function for assessing seismic risk of typical concrete bridge by means of nonlinear static and dynamic analysis." In *MATEC Web of Conferences*, 138, 02005. EDP Sciences.

Schrage, I. (1981). "Anchoring of Bearings by Friction." *Joint Sealing and Bearing Systems for Concrete Structures, World Congress on Joints and Bearings*, 1, Niagara Falls, NY, American Concrete Institute.

SEAOC (2000). *Seismic design manual*. Structural engineering association of California.

SeismoSignal V4.3 user manual.

Seo, J. and Linzell, D. G. (2012). "Horizontally curved steel bridge seismic vulnerability assessment." *Engineering Structures*, 34, 21–32.

Seo, J. and Rogers, L.P. (2017). "Comparison of curved prestressed concrete bridge population response between area and spine modeling approaches toward efficient seismic vulnerability analysis." *Engineering Structures*, 150, 176-189

Serdar, N. and Jankovic, S. (2014). "Performance –based seismic assessment of continuous concrete bridge with lack of confining reinforcement." *Proceedings of* 2nd *European Conference on Earthquake Engineering and Seismology*, Istanbul.

Shamsabadi, A., Ashour, M. and Norris, G. (2005) "Bridge Abutment Nonlinear Force-Displacement Capacity Prediction for Seismic Design." *Journal of Geotechnical and Geoenvironmental Engineering*, 131(2), 151-161.

Shamsabadi, A. Rollins, K. M. and Kapuskar, M. (2007) "Nonlinear soil–abutment–bridge structure interaction for seismic performance-based design." *ASCE Journal of Geotechnical and Geoenvironmental Engineering*, 133(6), 707-20.

Shamsabadi, A., Khalili-Tehrani, P., Stewart, J. P., and Taciroglu, E. (2010). "Validated simulation models for lateral response of bridge abutments with typical backfills." *Journal of Bridge Engineering*, 15(3), 302-311.

Siddiquee, K.N. (2015). "Seismic vulnerability assessment of wall pier highway bridges in British Columbia," Master of Applied Science Thesis, University of British Columbia.

Siddiquee, K. and Alam, M.S., 2017. Highway bridge infrastructure in the province of British Columbia (BC), Canada. Infrastructures, *2*(2):7.

Simon, J. (2016). "Seismic performance and damage assessment of Hungarian road bridges."

Singhal, A. and Kiremidjian, A. S. (1996a). "Method for Probabilistic Evaluation of Seismic Structural Damage." *Journal of Structural Engineering*, 122(12), 1459-1467.

Singhal, A. and Kiremidjian, A. S. (1996b). "Bayesian updating of fragilities with application to RC frames." *Journal of Structural Engineering*, 124(8), 922-929.

Siqueira, G.H., Tavares, D.H. and Paultre, P. (2014). 'Seismic fragility of a highway bridge in Quebec retrofitted with natural rubber isolators." *Revista IBRACON de Estruturas e Materiais*, 7(4), 534-547.

Shinozuka, M., Feng, M. Q., Kim, H., Uzawa, T. and Ueda, T. (2001). "Statistical Analysis of Fragility Curves." *Technical Report MCEER*, University of Southern California.

Shome, N., Cornell, C. A, Bazzurro, P. and Carballo, J. E. (1998). "Earthquakes, records and nonlinear responses." *Earthquake Spectra*, 14(3), 469–500.

Song, S. T., Chai, Y. H. and Hale, T. H. (2004) "Limit state analysis of fixed-head concrete piles under lateral loads." *Proc. of the Thirteenth World Conference on Earthquake Engineering*, Vancouver, BC, Canada.

Song, S. T. and Chai, Y. H. (2018). "Seismic Response and Design of Pile Foundations. Struct Eng and Geomech." https://www.eolss.net/Sample-Chapters/C05/E6-139-24.pdf. Assessed June 8, 2018.

Sritharan, S., Werff, J. V., Abendroth, R. E., Wassef, W. G. and Greimann, L. F. (2005). "Seismic behaviour of a concrete/steel integral bridge pier system." *Journal of Structural Engineering*, 131(7), 1083–1094.

Stanton, J. F. and Roeder, C. W. (1982). "Elastomeric bearings design, construction, and materials." *NCHRP report*, (248).

Stefanidou, S. P. and Kappos, A. J. (2017b). "Methodology for the development of bridge-specific fragility curves." *Earthquake Engineering & Structural Dynamics*, 46(1), 73-93.

Sucuoglu, H. and Nurtug, A. (1995). "Earthquake ground motion characteristics and seismic energy dissipation." *Earthquake Engineering and Structural Dynamics*, 24(9), 1195-1213.

Sung, Y. C., Hsu, C. C., Hung, H. H. and Chang, Y. J. (2013). "Seismic risk assessment system of existing bridges in Taiwan." *Structure and Infrastructure Engineering*, 9(9), 903-917.

Sullivan, I. T. (2010). "Analytical Seismic Fragility Curves for Skewed Multi-Span Steel Girder Bridges," MSc. Thesis, Civil Engineering, the Graduate School of Clemson University, 2010.

Tabatabaiefar, H. and Clifton, T. (2016). "Significance of Considering Soil-Structure Interaction Effects on Seismic Design of Unbraced Building Frames Resting on Soft Soils." *Australian Geomechanics Journal*.

Tanaka, S., Kameda, H., Nojima, N. and Ohnishi, S. (2000). "Evaluation of seismic fragility for highway transportation systems." *Proc. 12th World Conference on Earthquake Engineering*, Paper No. 0546, Upper Hutt, New Zealand, January.

Taskari, O. and Sextos, A. (2015). "Multi-angle, multi-damage fragility curves for seismic assessment of bridges." *Earthquake Engineering and Structural Dynamics.*

Taylor, H. P. J. (1969). "Investigation of the Dowel Shear Forces Carried by the Tensile Steel in Reinforced Concrete Beams." *Technical Report No. TRA-431*, Cement and Concrete Association, London.

Tavares D. H., Padgett J. E. and Paultre, P. (2012). "Fragility curves of typical as-built highway bridges in eastern Canada." *Engineering Structures*, 40,107–118.

Tavares, D. H., Suescun, J. R., Paultre, P. and Padgett, J. E. (2013). "Seismic Fragility of a Highway Bridge in Quebec." *Journal of Bridge Engineering*, 18, 1131-1139.

Tecchio, G., Grendene, M. and Modena, C. (2011). "Spatial variability of earthquake ground motion: effects on seismic response of long multi-span girder bridges." *8th Intl. Conference on Structural Dynamics, EURODYN*, Leuven, Belgium.

Tehrani, P. and Mitchell, D. (2013). "Incremental dynamic analysis (IDA) applied to seismic risk assessment of bridges. In Handbook of seismic risk analysis and management of civil infrastructure systems." Woodhead Publishing, 561-596.

Terzaghi, K. (1943). *Theoretical soil mechanics*, Wiley, New York.

Terzaghi, K. and Peck, R. B. (1967). Soil Mechanics in Engineering Practice, John Wiley and Sons, pp 58-61.

Tso, W. K., Zhu, T. J. and Heidebrecht, A. C. (1992). "Engineering application of ground motion A/V ratio." *Soil Dynamics and Earthquake Engineering*, 11, 133–44.

Vamvatsikos, D. and Cornell, C. A. (2002). "Incremental dynamic analysis." *Earthquake Engineering and Structural Dynamics*, 31(3), 491-512.

Van Schepdael, A., Carlier, A. and Geris, L. (2016). "Sensitivity analysis by design of experiments." *In Uncertainty in Biology*, Springer, Cham, 327-366.

Vidic, T., Fajfar, P. and Fischinger, M. (1994). "Consistent inelastic design spectra: strength and displacement." *Earthquake Engineering and Structural Dynamics*, 23(5), 507-521.

Vosooghi, A., and Saiidi, M.S. (2012). "Experimental fragility curves for seismic response of reinforced concrete bridge columns. ACI Structural Journal, 109, 825–834.

Wang, Z., Padgett, J. E., and Dueñas-Osorio, L. (2013). "Influence of Vertical Ground Motions on the Seismic Fragility Modeling of a Bridge-Soil-Foundation System." *Earthquake Spectra*, 29(3), 937–962.

Waugh, J. D. (2009). "Nonlinear analysis of T-shaped concrete walls subjected to multi-directional displacements," Ph.D. thesis, Civil Engineering Dept., Iowa State University Ames, Iowa.

White, H. (2007). "Integral abutment bridges: Comparison of current practice between European countries and the United States of America." *Transportation Research and Development Bureau*, New York State Department of Transportation.

Whitman, R. V., Biggs, J. M., Brennan III, J. E., Cornell, A. C., de Neufville, R. L. and Vanmarcke, E. H. (1975). "Seismic Design Decision Analysis." *Journal of Structural Division*, 101(ST5), 1067-1084.

Wyss, G. D. and Jorgensen, K. H. (1998). "A user's guide to LHS: Sandia's Latin hypercube sampling software." SAND98-0210, Sandia National Laboratories, Albuquerque, NM.

Xu, L. Y., Cai, F., Wang, G. X. and Ugai, K. (2013). "Nonlinear analysis of laterally loaded single piles in sand using modified strain wedge model*." Computers and Geotechnics*, 51, 60-71.

Xu, L. Y., Cai, F., Wang, G. X., Chen, G. X. and Li, Y. Y. (2017). "Nonlinear Analysis of Single Reinforced Concrete Piles Subjected to Lateral Loading." KSCE Journal of Civil Engineering, 21(7), 2622-33.

Yang, X., Zhang, C., Huang, M. and Yuan, J. (2018). "Lateral loading of a pile using strain wedge model and its application under scouring." *Marine Georesources and Geotechnology*, 36(3), 340-50.

Yamazaki, F., Hamada, T., Motoyama, H. and Yamauchi, H. (1999). "Earthquake Damage Assessment of Expressway Bridges in Japan." *Technical Council on Lifeline Earthquake Engineering Monograph*, 16, 361-370

Yen, W. P. and Kuo, M. L. "Integral Abutment and Jointless Bridges Design Issues and Recommendations".

Yi, J. H., Kim, S. H. and Kushiyama, S. (2007). "PDF interpolation technique for seismic fragility analysis of bridges." *Engineering Structure*, 29, 1312-1322.

Yu. O., Allen, D. L., and Drnevich, V. P. (1991). "Seismic Vulnerability Assessment of Bridges on Earthquake Priority Routes in Western Kentucky." Proc. *3rd US National Conference on Lifeline Earthquake Engineering*, Los Angeles, CA.

Zakeri, B., Padgett, J. E., Amiri, G. G. (2014). "Fragility analysis of skewed single-frame concrete box-girder bridges." *Journal of Performance of Constructed Facilities*, 28(3), 571-582.

Zelaschi, C., Monteiro, R., Marques, M. and Pinho, R. (2014). "Comparative Analysis of Intensity Measures for Reinforced Concrete Bridges." *2nd European Conference on Earthquake Engineering and Seismology*, Istanbul.

Zhong, J., Gardoni, P., Rosowsky, D. and Haukaas, T. (2008). "Probabilistic Seismic Demand Models and Fragility Estimates for Reinforced Concrete Bridges with Two-Column Bents." *Journal of Engineering Mechanics*, 134, 495-504.

Zhang, X. J. and Aggour, M.S. (1996). "Damping determination of sands under different loadings." *11th World Conf. on Earthquake Engineering*. Elsevier Science.

Zhang, J., Huo, Y., Brandenberg, S. J. and Kashighandi, P. (2008). "Effects of structural characterizations on fragility functions of bridges subject to seismic shaking and lateral spreading." *Earthquake Engineering and Engineering Vibration*, 7, 369-382.

Zhang, J. and Huo, Y. (2009). "Evaluating effectiveness and optimum design of isolation devices for highway bridges using fragility function method." *Engineering Structures*, 31(8), 1648–1660.

Zhang, Y. (2006). "Probabilistic structural seismic performance assessment methodology and application to an actual bridge-foundation-ground system," Ph.D. Thesis, University of California, San Diego.

Zsarnoczay, A., Vigh, L. G. and Kollar, L. P. (2014). "Seismic Performance of Conventional Girder Bridges in Moderate Seismic Regions." *ACSE Journal of Bridge Engineering*, 19(1-9).

Appendix A
DERIVATION OF LATERAL FORCE DEFORMATION CAPACITY CURVE OF THE BEARING DOWEL BAR

Based on the numerical model of the bar (Subsection 3.2.2), the lateral forces and deformations are evaluated by monitoring the bending stress f_{brd} developing at the critical section of the bar (with modulus Z_{brd}) due to F_{brd} and following the stiffness path of the bar material as its deformation progresses with the loading.

Bending moment M_{brd} and f_{brd} due to F_{brd} at the section adjacent to the rubber pad-capbeam interface can be expressed in Equation (A.1a) as,

$$M_{brd} = F_{brd} \cdot h_{brd} \; ; \quad f_{brd} = M_{brd}/Z_{brd} \tag{A.1a}$$

where, Z_{brd} is expressed in Equation A.1(b) as,

$$Z_{brd} = (\pi d_{brd}^4 / 64) \big/ (d_{brd} / 2) = \pi d_{brd}^3 / 32 \tag{A.1b}$$

Substituting M_{brd} (Equation A.1a) and Z_{brd} (Equation A.1b) in f_{brd} (Equation A.1a) and simplifying, we have final expression for f_{brd} and thus F_{brd} in Equation (A.1c) as,

$$f_{brd} = 10.18 F_{brd} h_{br} / d_{brd}^3 \Rightarrow F_{brd} = \frac{f_{brd} d_{brd}^3}{10.18 h_{br}} \tag{A.1c}$$

Using Equation A.1(c) and Figure 3.6, the expressions for the relative shares $F_{t,brd}$, $F_{y,brd}$ and $F_{u,brd}$ of the bridge lateral loadings corresponding to the transition, yield and ultimate stresses $f_{t,brd}$, $f_{y,brd}$ and $f_{u,brd}$ respectively can be evaluated in Equation (A.2) as,

$$F_{t,brd} = \frac{f_{t,brd} d_{brd}^3}{10.18 h_{br}} = \frac{0.8 f_{y,brd} d_{brd}^3}{10.18 h_{br}} ; F_{y,brd} = \frac{f_{y,brd} d_{brd}^3}{10.18 h_{br}} ; F_{u,brd} = \frac{f_{u,brd} d_{brd}^3}{10.18 h_{br}} \quad \text{(A.2)}$$

Since, the bar deforms in a single curvature mode, its LFDR initial stiffness $k_{e,brd}$ is evaluated using the cantilever stiffness expression which implies $k_{e,brd}$ being proportional to $E_{e,brd}$, where, I_{brd} is the moment of inertia of the bar section, as in Equation (A.3a).

$$k_{e,brd} = 3E_{e,brd} I_{brd} / h_{brd}^3 ; I_{brd} = \pi d_{brd}^4 / 64 \quad \text{(A.3a)}$$

The bar deforming in the cantilever mode throughout till fracture, the stiffness path beyond the elastic portion will be similar to the steel modulus path, with the transition and post yield stiffness $k_{t,brd}$ and $k_{p,brd}$ being proportional to $E_{t,brd}$ and $E_{p,brd}$ respectively,
in Equation (A.3b) as,

$$k_{t,brd} = 3E_{t,brd} I_{brd} / h_{brd}^3 ; k_{p,brd} = 3E_{p,brd} I_{brd} / h_{brd}^3 \quad \text{(A.3b)}$$

Since, $E_{e,brd}$ value is more or less same for any grade of steel material, $k_{e,brd}$ can be readily computed for bar of any dimensions. Hence for simplicity, both $k_{t,brd}$ and $k_{p,brd}$ are expressed in terms of $k_{e,brd}$ using Equation (A.3a) in Equation (A.3b) leading to Equation (A.3c) as,

$$k_{t,brd} = \frac{E_{t,brd}}{E_{e,brd}} k_{e,brd} = b_t k_{e,brd} , \quad k_{p,brd} = \frac{E_{p,brd}}{E_{e,brd}} k_{e,brd} = b_p k_{e,brd} \quad \text{(A.3c)}$$

where, $b_t = \frac{E_{t,brd}}{E_{e,brd}}$ and $b_p = \frac{E_{p,brd}}{E_{e,brd}}$ (A.3d)

From Figure 3.6, $E_{t,brd}$ and $E_{p,brd}$ can be expressed in Equation (A.3e) as,

$$E_{t,brd} = \frac{f_{y,brd} - f_{t,brd}}{\varepsilon_{y,brd} - \varepsilon_{t,brd}} = \frac{f_{y,brd} - 0.8 f_{y,brd}}{\left(0.002 + \frac{f_{y,brd}}{E_{e,brd}}\right) - \frac{0.8 f_{y,brd}}{E_{e,brd}}}$$

$$E_{p,brd} = \frac{f_{u,brd} - f_{y,brd}}{\varepsilon_{u,brd} - \varepsilon_{y,brd}} = \frac{f_{y,brd}\left(\frac{f_{u,brd}}{f_{y,brd}} - 1\right)}{\varepsilon_{u,brd} - \left(0.002 + \frac{f_{y,brd}}{E_{e,brd}}\right)} \quad \text{(A.3e)}$$

Using Equation (A.3e), b_t and b_y (Equation (A.3d)) can be simplified in Equation (A.3f) as,

$$b_t = \frac{\frac{f_{y,brd}}{E_{e,brd}}}{0.01 + \frac{f_{y,brd}}{E_{e,brd}}} \; ; \qquad b_p = \frac{\frac{f_{y,brd}}{E_{e,brd}}\left(\frac{f_{u,brd}}{f_{y,brd}} - 1\right)}{\varepsilon_{u,brd} - \left(0.002 + \frac{f_{y,brd}}{E_{e,brd}}\right)} \tag{A.3f}$$

Deformations at the loading point of the dowel bar $y_{t,brd}$, $y_{y,brd}$ and $y_{u,brd}$ corresponding to $F_{t,brd}$, $F_{y,brd}$ and $F_{u,brd}$ respectively can be evaluated in Equation (A.4a) as,

$$\begin{aligned} y_{t,brd} &= \frac{F_{t,brd}}{k_{e,brd}}; \; y_{y,brd} = y_{t,brd} + \frac{F_{y,brd} - F_{t,brd}}{k_{t,brd}} = \frac{F_{t,brd}}{k_{e,brd}} + \frac{F_{y,brd} - F_{t,brd}}{k_{t,brd}} \; ; \\ y_{u,brd} &= y_{y,brd} + \frac{F_{u,brd} - F_{y,brd}}{k_{p,brd}} = \frac{F_{t,brd}}{k_{e,brd}} + \frac{F_{y,brd} - F_{t,brd}}{k_{t,brd}} + \frac{F_{u,brd} - F_{y,brd}}{k_{p,brd}} \end{aligned} \tag{A.4a}$$

Substituting $F_{t,brd}$ (Equation (A.2)), $k_{e,brd}$ and (Equation (A.3a)) in $y_{t,brd}$ (Equation (A.4a)), we have the final expression for $y_{t,brd}$ in Equation (A.4b) as,

$$y_{t,brd} = \frac{0.8 h_{brd}^2 f_{y,brd}}{1.5 d_{brd} E_{e,brd}} \tag{A.4b}$$

Substituting $F_{t,brd}$ and $F_{y,brd}$ (Equation (A.2)), $k_{e,brd}$ and I_{brd} (Equation (A.3a)), $k_{t,brd}$ (Equation (A.3c)) and b_t (Equation (A.3f)) for $y_{y,brd}$ (Equation (A.4a)) and simplifying, we arrive at the final expression for $y_{y,brd}$ in Equation (A.4c) as,

$$\begin{aligned} y_{y,brd} &= \frac{F_{t,brd}}{k_{e,brd}} + \frac{F_{y,brd} - F_{t,brd}}{b_t k_{e,brd}} = \frac{F_{t,brd}}{k_{e,brd}}\left(1 + \frac{\frac{F_{y,brd}}{F_{t,brd}} - 1}{b_t}\right) \\ &= \frac{0.8 h_{brd}^2 f_{y,brd}}{1.5 d_{brd} E_{e,brd}}\left\{1 + \frac{(1.25 - 1)\left(0.01 + \frac{f_{y,brd}}{E_{e,brd}}\right)}{\frac{f_{y,brd}}{E_{e,brd}}}\right\} \\ &= \frac{0.8 h_{brd}^2 f_{y,brd}}{1.5 d_{brd} E_{e,brd}}\left(1.25 + \frac{0.0025}{\frac{f_{y,brd}}{E_{e,brd}}}\right) = \frac{h_{brd}^2 f_{y,brd}}{1.5 d_{brd} E_{e,brd}} + \frac{0.00133 h_{brd}^2}{d_{brd}} \end{aligned} \tag{A.4c}$$

Substituting $F_{t,brd}$, $F_{y,brd}$ and $F_{u,brd}$ (Equation (A.2)), $k_{e,brd}$ and I_{brd} (Equation (A.3a)), $k_{t,brd}$ and $k_{p,brd}$ (Equation (A.3c)) and b_t and b_p (Equation (A.3f)) for $y_{u,brd}$ (Equation A.4a)) and simplifying, we arrive at the final expression for $y_{u,brd}$ in Equation (A.4d) as,

$$y_{u,brd} = y_{y,brd} + \frac{F_{u,brd} - F_{y,brd}}{b_p k_{e,brd}} = \frac{h_{brd}^2 f_{y,brd}}{1.5 d_{brd} E_{e,brd}} + \frac{0.00133 h_{brd}^2}{d_{brd}} + \frac{F_{y,brd}}{k_{e,brd}} \left(\frac{\frac{F_{u,brd}}{F_{y,brd}} - 1}{b_p} \right)$$

$$= \frac{h_{brd}^2 f_{y,brd}}{1.5 d_{brd} E_{e,brd}} + \frac{0.00133 h_{brd}^2}{d_{brd}} + \frac{h_{brd}^2 f_{y,brd}}{1.5 d_{brd} E_{e,brd}} \left(\frac{\frac{f_{u,brd}}{f_{y,brd}} - 1}{b_p} \right)$$

$$= \frac{0.00133 h_{brd}^2}{d_{brd}} + \frac{h_{brd}^2 f_{y,brd}}{1.5 d_{brd} E_{e,brd}} \left[1 + \left(\frac{f_{u,brd}}{f_{y,brd}} - 1 \right) \Bigg/ \left\{ \frac{\frac{f_{y,brd}}{E_{e,brd}} \left(\frac{f_{u,brd}}{f_{y,brd}} - 1 \right)}{\varepsilon_{su,brd} - \left(0.002 + \frac{f_{y,brd}}{E_{e,brd}} \right)} \right\} \right]$$

$$= \frac{0.00133 h_{brd}^2}{d_{brd}} + \frac{h_{brd}^2}{1.5 d_{brd}} \left(\varepsilon_{su,brd} - 0.002 \right) \qquad \text{(A.4d)}$$

Appendix B
CALCULATION OF SENSITIVITY INDICES

SIs of the parameters of the components on the respective LSTs are evaluated and are listed in Table B.1 and B.2, B.3, B.4 and B.5, B.6, and B.7 for bearing pad and dowel bar, ABS, pier, sand FAF, and pile respectively as below. In all the Tables, InV and AvgV imply Individual Value and Average Value, and *O* and *I* are the input and output values respectively and the model 1 (serial no. 1) represent the base model on which OFTA is applied to obtain the remaining models.

Table B.1 Calculation of sensitivity indices of bearing pad parameters

Bearing pad		*I*			*O*	sensitivity indices	
Serial no.	Variation in	h_{br} (m)	*G* (kPa)	σ_m (kPa)	($y_{u,brp_{sl}}$) (m)	values	
1		0.080	1000	5000	0.052	individual	average
2	h_{br}	0.020	1000	5000	0.013	1	1
3		0.150	1000	5000	0.098	1	
4	*G*	0.080	800	5000	0.065	-1	-1
5		0.080	1200	5000	0.043	-1	
6	σ_m	0.080	1000	2000	0.040	0.304	0.394
7		0.080	1000	10000	0.072	0.484	

Table B.2 Calculation of SIs of bearing dowel bar parameters

Dowel bar		*I*			*O*	sensitivity indices	
Serial no.	Variation in	h_{br} (m)	values	values	($y_{u,brd}$) (m)	values	
1		0.080	individual	individual	0.0212	individual	average
2	h_{br}	0.020	0.032	0.1611	0.0013	1.471	1.65
3		0.150	0.032	0.1611	0.0746	1.830	
4	d_{brd}	0.080	0.025	0.1611	0.0272	-1	-1
5		0.080	0.040	0.1611	0.0170	-1	
6	$\varepsilon_{su,brd}$	0.080	0.032	0.1450	0.0191	1.01	1.01
7		0.080	0.032	0.1770	0.0233	1.01	

Table B.3 Calculation of SIs of ABS parameters

ABS		*I*			*O*	sensitivity indices	
Serial no.	Variation in	H_{ab} (m)	φ_{bf} (°)	$\delta_{abf,f}$	($d_{3,ab}$) (m)	values	
1		3.5	40	0.7	0.157	individual	average
2	H_{ab}	0.020	40	0.7	0.080	1.19	1.19
3		0.150	40	0.7	0.241	1.19	
4	φ_{bf}	3.5	35	0.7	0.166	-0.64	-0.74
5		3.5	45	0.7	0.149	-0.84	
6	$\delta_{abf,f}$	3.5	40	0.6	0.147	0.17	0.30
7		3.5	40	0.8	0.174	0.43	

Table B.4 Calculation of SIs of pier parameters on $d_{1,pr}$

Pier		*I*	*O*	sensitivity indices	
Serial no.	Variation in	H_{pr} = 8m, D_{pr} =1.4m, υ_{pr} = 0.1 $f_{y,pr}$ = 415MPa, $f_{c,pr}$ = 30MPa, $\rho_{l,pr}$ = 2.185%, $\rho_{t,pr}$ = 0.24%	($d_{1,pr}$) (m)	values	
1			0.0376	individual	average
2	H_{pr}	6m	0.022	1.80	1.81
3		12m	0.081	1.82	
4	D_{pr}	0.846m	0.064	-0.43	-1.45
5		1.73m	0.030	-2.47	
6	υ_{pr}	0.2	0.0395	0.07	0.09
7		0.3	0.0420	0.11	
8	$f_{y,pr}$	500MPa	0.0396	0.28	0.31
9		550MPa	0.0412	0.33	
10	$f_{c,pr}$	25MPa	0.0379	-0.043	-0.04
11		40MPa	0.0371	-0.047	
12	$\rho_{l,pr}$	1.165%	0.0337	0.18	0.17
13		3.241%	0.0400	0.16	
14	$\rho_{t,pr}$	0.133%	0.0375	0.01	0.005
15		0.300%	0.0376	0	

Table B.5 Calculation of SIs of pier parameters on $d_{4,pr}$

Pier		*I*	*O* ($d_{4,pr}$) (m)	sensitivity indices	
Serial no.	Variation in	H_{pr} = 8m, D_{pr} =1.4m, υ_{pr} = 0.1 $f_{y,pr}$ = 415MPa, $f_{c,pr}$ = 30MPa, $\rho_{l,pr}$ = 2.185%, $\rho_{t,pr}$ = 0.24%		values	
1			0.212	individual	average
2	H_{pr}	6m	0.133	1.59	1.62
3		12m	0.419	1.65	
4	D_{pr}	0.846m	0.327	-0.87	-0.96
5		1.73m	0.170	-1.04	
6	υ_{pr}	0.2	0.165	-0.37	-0.42
7		0.3	0.136	-0.48	
8	$f_{y,pr}$	500MPa	0.194	-0.46	-0.59
9		550MPa	0.182	-0.71	
10	$f_{c,pr}$	25MPa	0.254	-1.00	-0.94
11		40MPa	0.164	-0.88	
12	$\rho_{l,pr}$	1.165%	0.226	-0.11	-0.12
13		3.241%	0.200	-0.14	
14	$\rho_{t,pr}$	0.133%	0.113	1.06	0.99
15		0.300%	0.259	0.91	

Table B.6 Calculation of SIs of PSS parameters on FAF

PSS		*I*	*O* (d_{FAF}) (m)	sensitivity indices	
Serial no.	Variation in	φ_s = 30°, D_{pl} = 0.52m, υ_{pl} = 0.1, $f_{y,pl}$ = 415MPa, $f_{c,pl}$ = 40MPa, $\rho_{l,pl}$ = 4.290%, $\rho_{t,pl}$ = 0.30%		values	
1			0.019	Individual	average
2	D_{pl}	0.395m	0.013	1.18	1.24
3		0.734m	0.029	1.29	
4	$f_{c,pl}$	35MPa	0.020	-0.24	-0.23
5		45MPa	0.018	-0.23	
6	$\rho_{l,pl}$	2.140%	0.021	-0.18	-0.19
7		5.360%	0.018	-0.19	
8	υ_{pl}	0.2	0.018	-0.10	-0.11
9		0.3	0.017	-0.11	

Table B.7 Calculation of SIs of PSS parameters on pile LSTs

PSS		I	O (m)		sensitivity indices			
			$d_{1,pl}$	$d_{2,pl}$	$d_{1,pl}$		$d_{2,pl}$	
Serial no.	Variation in	Base values are same as Table A.5	0.030	0.051	Values			
1					individual	average	individual	average
2 3	φ_s	40°	0.016	0.029	-2.24	-2.24	-1.91	-1.91
4	D_{pl}	0.395m	0.026	0.047	0.53	0.52	0.27	0.40
5		0.734m	0.036	0.061	0.51		0.52	
6	υ_{pl}	0.2	0.031	0.043	-0.01	-0.01	-0.26	-0.26
7		0.3	0.029	0.039	-0.01		-0.26	
8	$f_{y,pl}$	500MPa	0.036	0.055	0.91	0.91	0.44	0.43
9		550MPa	0.039	0.058	0.90		0.43	
10	$f_{c,pl}$	35MPa	0.031	0.052	-0.11	-0.11	-0.16	-0.10
11		45MPa	0.029	0.050	-0.11		-0.03	
12	$\rho_{l,pl}$	2.140%	0.022	0.048	0.44	0.46	0.09	0.11
13		5.360%	0.034	0.053	0.47		0.14	
14	$\rho_{t,pl}$	0.157%	0.030	0.042	0	0	0.30	0.92
15		0.587%	0.030	0.150	0		1.53	

LIST OF PUBLICATIONS

JOURNALS

- Ahmed, B. F. and Dasgupta, K. (2017). "Bridge Analytical Fragility Development Methodologies - A State of the Art Review." *International Journal of Bridge Engineering*, 5(3), 69-122.
- Ahmed, B. F. and Dasgupta, K. (2021). "Seismic limit states for reinforced concrete bridge pile in sand." *Structures*, Elsevier, 33, 120-140, https://doi.org/10.1016/j.istruc.2021.04.027.
- Ahmed, B. F. and Dasgupta, K. "Seismic Limit State Expressions and the Sequences of Attainment for the Components of Multispan Continuous Reinforced Concrete Integral Abutment Bridges.", submitted to *Bulletin of Earthquake Engineering* (under review since 29/10/2020).
- Ahmed, B. F. and Dasgupta, K. "A Methodology for Assessing the Component-Level Fragility Curves and its Application to a Class of Integral Abutment Bridges." (Manuscript submitted to *Journal of Risk and Uncertainty in Engineering Systems, ASCE*, dated 14/04/21, under review).
- Ahmed, B. F. and Dasgupta, K. "Impacts of Intensity Measure and Fragility Computation Approach on the Seismic Vulnerability Evaluation of a Class of Integral Abutment Bridges." (Manuscript submitted to *Journal of Risk and Uncertainty in Engineering Systems, ASCE*, dated 29/04/21, under review).
- Ahmed, B. F. and Dasgupta, K. "Comparative Seismic Fragility Curves at the Component Level and the Bridge System Level for Integral Abutment Bridges." (Manuscript to be submitted to *Journal of Risk and Uncertainty in Engineering Systems, ASCE*, under preparation).
- Ahmed, B. F. and Dasgupta, K. "Numerical Expressions for Evaluating Seismic Force Deformation Characteristics and Limit States of Bridge Rubber Bearing with Dowel Bars." (Manuscript under preparation for submission to *Frontiers of Structural and Civil Engineering*).

BOOK CHAPTER

Ahmed, B. F. and Dasgupta, K. (2020). "Seismic Damage Assessment of Integral Abutment Bridge". In *Advances in Rotor Dynamics, Control, and Structural Health Monitoring*, Springer, DOI: 10.1007/978-981-15-5693-7_26, pp 359-373

CONFERENCES

- Ahmed, B. F. and Dasgupta, K. (2017). "Seismic Damage Assessment of Integral Abutment Bridge". *13th International Conference on Vibration Problems*, Indian Institute of Technology Guwahati, Guwahati, India, 11-15 September 2017, Paper ID 294.

- Ahmed, B. F., Dasgupta, K. and Dey, A. (2017). "Behaviour of Laterally Loaded Bridge Piles in Sand". *Indian Geotechnical Conference GeoNEst*, Indian Institute of Technology Guwahati, Guwahati, India, 14-16 December 2017, Paper ID Th12_730.
- Ahmed, B. F., Dasgupta, K. (2018). "Generalised Seismic Damage Limit State Thresholds for Reinforced Concrete Circular Bridge Pier". *16th Symposium on Earthquake Engineering*, Indian Institute of Technology Roorkee, Roorkee, India, 20-22 December 2018, Paper No. 252.
- Ahmed, B. F., Dasgupta, K. (2020). "Component Level Seismic Fragility Assessment of Multispan Continuous Integral Abutment Bridges". *17thWorld Conference on Earthquake Engineering, 17WCEE, Sendai*, Japan, 13-18 September (Postponed to 2021), Paper No. 3c-0007.
- Ahmed, B. F., Dasgupta, K. (2021). "System Level Seismic Fragility Assessment of Multispan Continuous Integral Abutment Bridges". *1st Croatian Conference on Earthquake Engineering*, Zagreb, Croatia, 22 - 24 March 2021, Paper ID 157.
- Ahmed, B. F., Dasgupta, K. (2021). "Seismic Fragility Assessment of Multispan Continuous Integral Abutment Bridges". *3rd International Conference on Natural Hazards and Infrastructure*, Athens, Greece, to be held on 22 - 24 June (Postponed to 2022) (Abstract accepted, paper ID 267).